Elastic Compton Scattering from the Nucleon and Deuteron

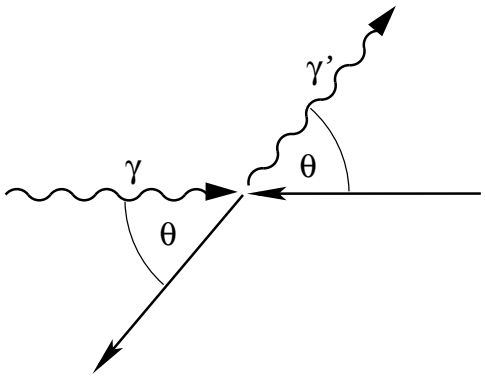

Robert P. Hildebrandt

TECHNISCHE
UNIVERSITÄT
MÜNCHEN

Physik-Department

Technische Universität München
Physik-Department
Institut für Theoretische Physik T39
Univ.-Prof. Dr. W. Weise

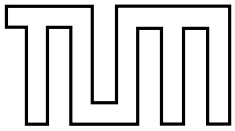

Elastic Compton Scattering from the Nucleon and Deuteron

Dipl.-Phys. Univ. Robert P. Hildebrandt

Vollständiger Abdruck der von der Fakultät für Physik der Technischen Universität München zur Erlangung des akademischen Grades eines

Doktors der Naturwissenschaften (Dr. rer. nat.)

genehmigten Dissertation.

Vorsitzender: Univ.-Prof. Dr. Reiner Krücken

Prüfer der Dissertation:

1. Univ.-Prof. Dr. Wolfram Weise
2. Univ.-Prof. Dr. Harald Friedrich

Die Dissertation wurde am 28.10.2005 bei der Technischen Universität München eingereicht und durch die Fakultät für Physik am 23.11.2005 angenommen.

Summary

Goal of this work is the consistent description of elastic Compton scattering from the single nucleon and the deuteron. The theoretical framework chosen is Chiral Perturbation Theory, which is the low-energy formulation of Quantum Chromodynamics, where we extend the spectrum of active degrees of freedom from only pions and nucleons to also the $\Delta(1232)$ resonance. In the deuteron sector, we treat the nucleon-nucleon interaction non-perturbatively. Besides the Compton cross sections, our main concern is with the nucleon polarizabilities, which are a useful tool to describe the reaction of the internal nucleonic degrees of freeedom to the external electromagnetic field. Experimentally, only a few nucleon polarizabilities are known. Especially our present knowledge of the neutron polarizabilities is not satisfying. The reason why it is so difficult to determine these quantities experimentally is the finite lifetime of the free neutron. Therefore, we want to contribute to the ongoing discussion of the neutron polarizabilities by fitting the average over proton and neutron polarizabilities to the elastic deuteron Compton-scattering data. Similarly, we determine the proton polarizabilities from fits to the single-proton Compton data. We finally combine both results in order to identify the neutron polarizabilities.

Zusammenfassung

Ziel dieser Arbeit ist die konsistente Beschreibung von elastischer Compton-Streuung am einzelnen Nukleon und am Deuteron. Als theoretischen Rahmen wählen wir chirale Störungsrechnung, die Niederenergieformulierung der Quantenchromodynamik, wobei wir das Spektrum der aktiven Freiheitsgrade von Pionen und Nukleonen um die $\Delta(1232)$-Resonanz erweitern. Im Deuteron-Sektor behandeln wir die Nukleon-Nukleon-Wechselwirkung nichtperturbativ. Neben den Compton-Streuquerschnitten gilt unser Hauptinteresse den Nukleon-Polarisierbarkeiten, einem nützlichen Instrument, um die Reaktion der inneren Freiheitsgrade des Nukleons auf das äußere elektromagnetische Feld zu beschreiben. Experimentell sind nur wenige der Nukleon-Polarisierbarkeiten bekannt. Insbesondere unsere momentane Kenntnis der Neutron-Polarisierbarkeiten ist nicht zufriedenstellend. Der Grund, warum es so schwierig ist, diese Größen experimentell zu bestimmen, ist die endliche Lebensdauer des freien Neutrons. Deshalb wollen wir zu der aktuellen Diskussion der Neutron-Polarisierbarkeiten beitragen, indem wir das Mittel von Proton- und Neutron-Polarisierbarkeiten an die elastischen Deuteron-Compton-Streudaten anfitten. Ebenso bestimmen wir die Proton-Polarisierbarkeiten aus Fits an die Proton-Compton-Streudaten. Schließlich kombinieren wir beide Ergebnisse, um die Neutron-Polarisierbarkeiten zu ermitteln.

Contents

List of Figures

List of Tables

Chapter 1

Introduction

1.1 Compton Scattering and the Nucleon Polarizabilities

The structure of protons and neutrons as analyzed with electromagnetic probes has been under experimental and theoretical investigation for a number of decades. While for photon energies below 25 MeV the experimental cross section is well described with the assumption of a point-like spin-1/2 nucleon with an additional anomalous magnetic moment κ [1], the internal structure of the nucleon starts to play a role at higher energies. In Compton scattering, the external electromagnetic field of the photon attempts to deform the nucleon. The electromagnetic polarizabilities provide a measure of the global resistance of the nucleon's internal degrees of freedom against displacement in an external electric or magnetic field, which makes them an excellent tool to study the structure of the nucleon. The most prominent two nucleon polarizabilities, the electric and magnetic dipole polarizabilities[1] $\bar{\alpha}_{E1}$ and $\bar{\beta}_{M1}$, are connected via the famous Baldin sum rule with the total photon-nucleon cross section [2]. This sum rule is derived via the Kramers-Kronig relation from the low-energy theorems, an expansion of the forward-scattering amplitude in the photon energy [3]. It reads

$$\bar{\alpha}_{E1} + \bar{\beta}_{M1} = \frac{1}{2\,\pi^2} \int_{\omega_{\rm th}}^{\infty} d\omega \, \frac{\sigma_{\rm tot}(\omega)}{\omega^2} \tag{1.1}$$

with ω the photon energy and $\omega_{\rm th}$ the threshold energy for pion photo-production.

The leading-order effective Hamiltonian, which arises due to the nucleon being polarized by the photon, is (see e.g. [4])

$$H_{\rm eff} = -\frac{1}{2}\, 4\pi \left[\bar{\alpha}_{E1}\, \vec{E}^2 + \bar{\beta}_{M1}\, \vec{B}^2 \right]. \tag{1.2}$$

This Hamiltonian, however, includes only terms of second order in ω and can be extended, as long as symmetries like gauge-, Lorentz- and isospin-invariance are respected. One of the $\mathcal{O}(\omega^4)$-terms is proportional to the square of the time derivative of the electric field:

$$\delta H_{\rm eff} = -\frac{1}{2}\, 4\pi \left[\alpha^{\nu}_{E1}\, \dot{\vec{E}}^2 \right] \tag{1.3}$$

Such corrections may be resummed to a dynamical, i.e. energy-dependent polarizability

$$\bar{\alpha}_{E1} + \alpha^{\nu}_{E1}\, \omega^2 + \cdots \to \alpha_{E1}(\omega), \tag{1.4}$$

[1] We denote the static polarizabilities, i.e. the polarizabilities in the limit of vanishing photon energy, by a bar throughout this work.

which in turn provides information on the energy dependence of the internal nucleonic degrees of freedom. In this work we deal with dynamical polarizabilities in terms of multipole expansions.

Apart from $\alpha_{E1}(\omega)$ and $\beta_{M1}(\omega)$ there exist further polarizabilities, such as the spin-dependent dipole polarizabilities and quadrupole polarizabilities. In this work we are mainly concerned with the dipole polarizabilities because we will see that in the energy range where our calculation is supposed to be valid, polarizabilities of higher multipole order are negligible in describing nucleon Compton cross sections. Stated differently, we observe a fast convergence of the Compton multipole expansion. On the other hand, the spin polarizabilities do give important contributions. Therefore, we rewrite Eq. (1.2), extended to the (energy-dependent) spin dipole polarizabilities:

$$\begin{aligned} H_{\text{eff}} = -2\pi \Big[& \alpha_{E1}(\omega)\, \vec{E}^2 + \beta_{M1}(\omega)\, \vec{B}^2 + \gamma_{E1E1}(\omega)\, \vec{\sigma} \cdot \vec{E} \times \dot{\vec{E}} \\ & + \gamma_{M1M1}(\omega)\, \vec{\sigma} \cdot \vec{B} \times \dot{\vec{B}} - 2\,\gamma_{M1E2}(\omega)\, \sigma_i\, E_{ij}\, B_j + 2\,\gamma_{E1M2}(\omega)\, \sigma_i\, B_{ij}\, E_j \Big] \end{aligned} \tag{1.5}$$

This Hamiltonian can be found e.g. in [4], with $\vec{\sigma}$ denoting the nucleon spin, $T_{ij} = \frac{1}{2}(\partial_i T_j + \partial_j T_i)$ and the indices of the spin polarizabilities chosen such that $\gamma_{TlT'l'}$ parameterizes a Tl ($T'l'$) transition at the first (second) photon vertex.

The experimentally best-known nucleon polarizabilities are the static electric and magnetic dipole polarizabilities of the proton, $\bar{\alpha}^p_{E1}$ and $\bar{\beta}^p_{M1}$. They are extracted from proton Compton-scattering data, and a large number of such experiments has been performed over the past decades, see e.g. Refs. [5-9]. In [5], a global, Baldin-sum-rule-constrained fit to the wealth of Compton-scattering data on the proton yielded

$$\begin{aligned} \bar{\alpha}^p_{E1} &= (12.1 \pm 0.3\,(\text{stat}) \mp 0.4\,(\text{syst}) \pm 0.3\,(\text{model})) \cdot 10^{-4}\ \text{fm}^3, \\ \bar{\beta}^p_{M1} &= (1.6 \pm 0.4\,(\text{stat}) \pm 0.4\,(\text{syst}) \pm 0.4\,(\text{model})) \cdot 10^{-4}\ \text{fm}^3, \end{aligned} \tag{1.6}$$

where the errors include statistical and systematic uncertainties as well as estimates of model dependence in the analysis. These numbers are very close to those recommended in a recent review [10], which were obtained as the weighted average over several experiments:

$$\begin{aligned} \bar{\alpha}^p_{E1} &= (12.0 \pm 0.6) \cdot 10^{-4}\ \text{fm}^3 \\ \bar{\beta}^p_{M1} &= (1.9 \mp 0.6) \cdot 10^{-4}\ \text{fm}^3 \end{aligned} \tag{1.7}$$

Comparing these values to the typical size of a proton ($\sim 1\,\text{fm}^3$) we find that nucleons are hard to deform, i.e. they are rather stiff objects. Note that the experiments from which the numbers of Eq. (1.6) are derived, have not been performed for near-static photons but in an energy range of about 55 - 800 MeV. Therefore theoretical input, e.g. from a Dispersion-Relation Analysis, is unavoidable in the extraction of $\bar{\alpha}_{E1}$ and $\bar{\beta}_{M1}$.

Stable single-neutron targets do not exist. It is therefore much harder to access the neutron polarizabilities experimentally. An experiment on quasi-free Compton scattering from the proton and neutron bound in the deuteron [11] gives results for the neutron polarizabilities which suggest very small isovector components[2] when compared to Eqs. (1.6, 1.7):

$$\begin{aligned} \bar{\alpha}^n_{E1} &= (12.5 \pm 1.8\,(\text{stat})\, {}^{+1.1}_{-0.6}\,(\text{syst}) \pm 1.1\,(\text{model})) \cdot 10^{-4}\ \text{fm}^3 \\ \bar{\beta}^n_{M1} &= (2.7 \mp 1.8\,(\text{stat})\, {}^{+0.6}_{-1.1}\,(\text{syst}) \mp 1.1\,(\text{model})) \cdot 10^{-4}\ \text{fm}^3 \end{aligned} \tag{1.8}$$

[2] The isovector polarizabilities are defined as $\alpha^v_{E1} \equiv \frac{1}{2}\,(\alpha^p_{E1} - \alpha^n_{E1})$, $\beta^v_{M1} \equiv \frac{1}{2}\,(\beta^p_{M1} - \beta^n_{M1})$.

The central values of Eq. (1.8) are identical to those suggested in [10], which were obtained – like the proton values given in Eq. (1.7) – as the weighted average over several experiments:

$$\begin{aligned} \bar{\alpha}^n_{E1} &= (12.5 \pm 1.7) \cdot 10^{-4} \text{ fm}^3 \\ \bar{\beta}^n_{M1} &= (2.7 \mp 1.8) \cdot 10^{-4} \text{ fm}^3 \end{aligned} \tag{1.9}$$

The two procedures entering Eq. (1.9) are quasi-free Compton scattering from the neutron and electromagnetic scattering of neutrons on lead. A similar observation for $\bar{\alpha}^n_{E1}$ has been made in [12], where the latter process was investigated:

$$\bar{\alpha}^n_{E1} = (12.6 \pm 2.5) \cdot 10^{-4} \text{ fm}^3 \tag{1.10}$$

However, the precision of this result has been questioned by the authors of [13]. Their estimate of the correct range for the result from [12] is $7 \leq \bar{\alpha}^n_{E1} \leq 19$. On the other hand, another experiment [14], using the same technique, gives a completely different result:

$$\bar{\alpha}^n_{E1} = (0.6 \pm 5.0) \cdot 10^{-4} \text{ fm}^3 \tag{1.11}$$

On the theory side, non-relativistic Chiral Perturbation Theory predicts that the proton and neutron polarizabilities are equal at leading-one-loop order [15], since the pion loops that generate these contributions are isoscalar in nature. The absence of large isovector pieces in α_{E1} and β_{M1} is therefore in accord with this picture. The isoscalar $\mathcal{O}(p^4)$-HBχPT estimate [16], $\bar{\alpha}^s_{E1} = (11.95 \pm 2.5) \cdot 10^{-4}$ fm^3, $\bar{\beta}^s_{M1} = (5.65 \pm 5.1) \cdot 10^{-4}$ fm^3, is consistent with vanishing isovector polarizabilities, when compared to the numbers given in Eq. (1.9), but no meaningful conclusion can be drawn due to the large error bars in the $\mathcal{O}(p^4)$ estimate, which in addition is cutoff dependent. The reason for the huge error bars is sensitivity to short-distance contributions that were estimated using the resonance-saturation hypothesis.

Another possible way to determine the neutron polarizabilities is elastic low-energy Compton scattering from light nuclei, e.g. from the deuteron. Several experiments have already been performed [17, 18, 19] and further proposals exist – e.g. Compton scattering on the deuteron or ^{3}He at TUNL/HIγS [20][3] and on deuteron targets at MAXlab [21]. The latter proposal has already been accepted and promises an extensive study of elastic deuteron Compton scattering below the pion-production threshold. From a theorist's point of view, extracting the neutron polarizabilities from elastic γd scattering requires an accurate description of the nucleon structure *and* of the dynamics of the low-energy degrees of freedom within the deuteron, as one has to account for the proton polarizabilities as well as for nuclear binding effects. A first attempt to fit the isoscalar polarizabilities $\bar{\alpha}^s_{E1} \equiv \frac{1}{2}(\bar{\alpha}^p_{E1} + \bar{\alpha}^n_{E1})$, $\bar{\beta}^s_{M1} \equiv \frac{1}{2}(\bar{\beta}^p_{M1} + \bar{\beta}^n_{M1})$ to the elastic deuteron Compton-scattering data from [17, 19] has been made in [22]. The extracted neutron polarizabilities $\bar{\alpha}^n_{E1} = (9.0 \pm 3.0) \cdot 10^{-4}$ fm^3, $\bar{\beta}^n_{M1} = (11.0 \pm 3.0) \cdot 10^{-4}$ fm^3 indicate the possibility of a rather *large* isovector part, in contrast to the quasi-elastic results from [11]. They also disagree with the isoscalar Baldin sum rule, $\bar{\alpha}^s_{E1} + \bar{\beta}^s_{M1} = (14.5 \pm 0.6) \cdot 10^{-4}$ fm^3, cf. Chapter 5 for details. The same pattern is observed, albeit less pronounced, in the fit of Ref. [23] to the data measured at 49 MeV [17] and 55 MeV [18] within an Effective Field Theory with pions integrated out: $\bar{\alpha}^s_{E1} = (12.3 \pm 1.4) \cdot 10^{-4}$ fm^3, $\bar{\beta}^s_{M1} = (5.0 \pm 1.6) \cdot 10^{-4}$ fm^3. On the other hand, comparing the elastic deuteron Compton calculation of Ref. [24] with the data from [17] is in good agreement with nearly vanishing isovector polarizabilities: $\bar{\alpha}^n_{E1} = (12.0 \pm 4.0) \cdot 10^{-4}$ fm^3, $\bar{\beta}^n_{M1} = (2.0 \pm 4.0) \cdot 10^{-4}$ fm^3, albeit within rather large error bars.

[3] Experiments on ^{3}He are especially well suited to investigate the spin structure of the neutron, which mainly carries the spin of the ^{3}He-nucleus.

It is obvious from these partly contradictory results that there is still a lot of work to be done in order to have reliable values for $\bar{\alpha}^n_{E1}$ and $\bar{\beta}^n_{M1}$. Therefore, in this thesis we contribute to the ongoing discussion of the neutron polarizabilities, investigating single-nucleon Compton scattering and elastic Compton scattering from the deuteron. The framework is Chiral Effective Field Theory (χEFT), allowing for non-perturbative methods in the deuteron section. In general, χEFT provides a consistent, controlled framework for elastic γp and γd scattering within which nucleon-structure effects can be disentangled from meson-exchange currents, deuteron binding, etc. It also allows for an estimate of the uncertainties arising from higher-order corrections.

We perform a multipole expansion of the Compton amplitude in the single-nucleon Compton calculation, mainly for two reasons: Firstly, we are interested in the Compton multipoles themselves, which we combine to dynamical polarizabilities, cf. Eq. (1.4). These multipole amplitudes exhibit the response of the various nucleonic degrees of freedom to the external electromagnetic field of the scattered photon and therefore provide valuable information on the structure of the nucleon. The second reason is that it is often sufficient to include only the leading terms of the multipole expansion in order to achieve a good approximation of the full calculation. We demonstrate that this scenario also holds in nucleon Compton scattering and conclude that the few contributing parameters, i.e. the six dipole polarizabilities, may be extracted from a combination of spin-averaged and polarized Compton experiments. The two parameters $\bar{\alpha}^p_{E1}$ and $\bar{\beta}^p_{M1}$, which are a priori free in our calculation, are determined via fits to proton Compton data.

The central goal of this work is to extract not only the proton but also the neutron values for $\bar{\alpha}_{E1}$ and $\bar{\beta}_{M1}$ from data. Therefore in the second main part we are concerned with elastic deuteron Compton scattering, which was introduced before as one of the possible ways to determine the isoscalar polarizabilities. We present two partly different calculations of deuteron Compton scattering. The first one agrees well with the high-energy data but it fails to describe the low-energy regime, say the region $\omega \ll 50$ MeV, correctly, a feature that we have in common with other calculations such as [25]. On the other hand, all calculations on elastic deuteron Compton scattering existing so far, which reach the correct low-energy limit, have problems to describe the high-energy data from [19], see e.g. [22, 24]. Therefore, we consider it as one of the central points of this work that in our second approach to γd scattering we obtain a consistent and novel description of all existing deuteron Compton data, which also fulfills the low-energy theorem, i.e. we obtain the well-known Thomson-limit of elastic deuteron Compton scattering. The good description of the data enables us to perform a global fit of the isoscalar polarizabilities to all data points. These numbers are combined with our fit results for the proton polarizabilities, yielding values which prove that the data basis on elastic γd scattering is in good agreement with even vanishing isovector polarizabilities.

Parts of this work have been published in our papers Refs. [26], [27] and [28]. Some elements are based on my diploma thesis [29].

1.2 Outline

This thesis is structured in the following way:

In Chapter 2 we give a brief introduction to the two versions of Chiral Effective Field Theory applied in this work, starting with "Heavy Baryon Chiral Perturbation Theory" (HBχPT, Section 2.1), which is the low-energy formulation of Quantum Chromodynamics (QCD) with pions and nucleons as active degrees of freedom. In Section 2.2 we review how this theory is modified in the so-called "Small Scale Expansion", an extension of HBχPT including the $\Delta(1232)$-resonance field as an

additional explicit degree of freedom. In both sections we write down the respective Lagrangeans relevant for this work.

Chapter 3 is dedicated to spin-averaged single-nucleon Compton scattering. We derive a multipole expansion for this process and compare the Compton cross sections, calculated in leading-one-loop order HBχPT and SSE, respectively, to a Dispersion-Relation Analysis and experiments. In the SSE description we allow for free polarizabilities $\bar{\alpha}_{E1}$ and $\bar{\beta}_{M1}$, which we fit to proton Compton data. Furthermore, we use the various multipole amplitudes to define dynamical, i.e. energy-dependent nucleon polarizabilities, cf. Section 1.1, and we compare the results achieved for these quantities within the three theoretical frameworks.

After the chapter on unpolarized cross sections we turn to polarized Compton scattering in Chapter 4, where we calculate several asymmetries, using circularly and linearly polarized photons. We demonstrate that determining the six dipole polarizabilities directly from experiment is possible, due to the strong sensitivity of selected observables to the spin polarizabilities.

Our most prominent aim is to extract the proton and the neutron values for $\bar{\alpha}_{E1}$ and $\bar{\beta}_{M1}$ from data within one consistent framework. As there are no data on Compton scattering from the neutron, we turn in Chapters 5 and 6 to elastic deuteron Compton scattering in order to determine the isoscalar polarizabilities. The main difference between the two chapters is that in Chapter 5 we restrict ourselves to photon energies of the order of 100 MeV which enables us to calculate the γd kernel strictly according to the power-counting rules of the Small Scale Expansion. In Chapter 6, we allow for non-perturbative aspects via the inclusion of the two-nucleon T-matrix in the intermediate state, which turns out to be a necessary modification in order to describe low-energy deuteron Compton scattering correctly. In both approaches we fit the isoscalar polarizabilities $\bar{\alpha}^s_{E1}$, $\bar{\beta}^s_{M1}$ and combine the respective numbers with our results for the proton polarizabilities in order to determine those of the neutron. Both extractions agree well with each other within their (small) error bars and with the results of Ref. [11], however only in Chapter 6 we are able to fit to all existing elastic deuteron Compton data.

We conclude in Chapter 7, having shifted the most technical parts of this thesis to the appendices.

Chapter 2

Chiral Effective Field Theories

In this chapter we want to give a brief survey of the two Effective Field Theories applied in this work, starting with "Heavy Baryon Chiral Perturbation Theory" (HBχPT), which is the low-energy formulation of Quantum Chromodynamics including nucleons and pions as active degrees of freedom. In the succeeding section we shortly introduce the so-called "Small Scale Expansion" (SSE), an extension of the former theory that, in addition, also includes the $\Delta(1232)$ resonance as an explicit degree of freedom.

2.1 Heavy Baryon Chiral Perturbation Theory

The theory of strong interactions, QCD, describes point-like fermions of spin $\frac{1}{2}$, the so-called quarks, which interact with each other via the exchange of gauge-bosons, the gluons. These particles couple to the "color" of the quarks, an additional degree of freedom which was introduced in order to maintain the demand of totally antisymmetric fermion wave functions, see e.g. [30]. At low momentum transfer, however, the coupling constant of QCD becomes rather strong and quarks and gluons are no longer the relevant degrees of freedom. In fact they are confined in color-neutral objects, the hadrons, which therefore are the active degrees of freedom of low-energy QCD.

When we compare the masses of the six different quark flavors, we find three flavors – "up", "down" and "strange" – which are considerably lighter than the nucleon. Their masses (at a renormalization scale of about 1 GeV) are [31]

$$m_u \approx 4 \text{ MeV}, \qquad m_d \approx 8 \text{ MeV}, \qquad m_s \approx 164 \text{ MeV}. \tag{2.1}$$

The other quark flavors ("charm", "bottom" and "top") are heavy, i.e. their masses exceed the nucleon mass. Therefore, it is sufficient for many applications to only calculate with the three light flavors, or even with only up and down quarks.

Due to the low masses of the light quark flavors, it is instructive to investigate the so-called "chiral limit", i.e. the limit of vanishing quark masses. In this limit, the QCD-Lagrangean exhibits another symmetry, the "chiral symmetry", which forbids the coupling of right-handed to left-handed quarks. In order to demonstrate this symmetry we write the Lagrangean of a free, mass-less fermion,

$$\mathcal{L} = i\bar{\psi}\gamma_\mu\partial^\mu\psi \tag{2.2}$$

in terms of right- and left-handed particles:

$$\mathcal{L} = i\bar{\psi}_R\gamma_\mu\partial^\mu\psi_R + i\bar{\psi}_L\gamma_\mu\partial^\mu\psi_L \tag{2.3}$$

with

$$\psi_R = \frac{1}{2}\left(1+\gamma_5\right)\psi, \qquad \psi_L = \frac{1}{2}\left(1-\gamma_5\right)\psi. \tag{2.4}$$

Obviously, the two kinds of fermions in Eq. (2.3) do not interact with each other, i.e. in the chiral limit the Lagrangean of QCD is invariant under the global, unitary transformations in flavor space

$$\psi_R \to U_R\,\psi_R = \exp\left[i\theta_R^a \frac{\tau_a}{2}\right]\psi_R, \qquad \psi_L \to U_L\,\psi_L = \exp\left[i\theta_L^a \frac{\tau_a}{2}\right]\psi_L \tag{2.5}$$

with τ_a the Pauli isospin matrices. Here we restrict ourselves to the lightest two quark flavors, i.e. $U_R,\ U_L \in SU(2)$. The corresponding conserved Noether currents are

$$J^\mu_{R,a} = \bar{\psi}_R \gamma^\mu \frac{\tau_a}{2}\psi_R, \qquad J^\mu_{L,a} = \bar{\psi}_L \gamma^\mu \frac{\tau_a}{2}\psi_L, \tag{2.6}$$

which can be rewritten by addition or subtraction as the often used isospin (vector) and axial-vector currents

$$V^\mu_a = \bar{\psi}\gamma^\mu \frac{\tau_a}{2}\psi, \qquad A^\mu_a = \bar{\psi}\gamma^\mu\gamma_5 \frac{\tau_a}{2}\psi. \tag{2.7}$$

Including the $SU(2)$-quark-mass matrix $\hat{m}$ in the Lagrangean explicitly breaks chiral symmetry, as such a term couples left- to right-handed quarks:

$$\mathcal{L}_m = \bar{\psi}\,\hat{m}\,\psi = \bar{\psi}_L\,\hat{m}\,\psi_R + \bar{\psi}_R\,\hat{m}\,\psi_L \tag{2.8}$$

Nevertheless, due to the small size of the quark masses, chiral symmetry might still be fulfilled to a good approximation. In this case, all hadrons would appear as doublets of nearly equal mass but opposite parity. However, investigating the hadronic spectrum we find that chiral symmetry has to be spontaneously broken, as e.g. the pseudoscalar ($J^P = 0^-$) mesons are considerably lighter than their pendants with positive parity. On the other hand, $m_u \approx m_d$, cf. Eq. (2.1), i.e. isospin symmetry is nearly exactly preserved. Therefore, the symmetry $SU(2)_L \times SU(2)_R$ is obviously broken to $SU(2)_V$.

Whenever a global, continuous symmetry of the Lagrangean is spontaneously broken, Goldstone's theorem applies and massless Goldstone-bosons occur. In the case of chiral symmetry with two active quark flavors there are three generators broken, i.e. we expect the observation of three Goldstone-bosons. These are the three pions, which are by far the lightest of the hadrons. Their quantum numbers coincide with breaking the axial-vector symmetry: Like the 0-component of the axial current they are of pseudoscalar nature [31]. Although they are the Goldstone-bosons of chiral symmetry breaking, the pions do have a small mass due to the non-vanishing quark masses, which explicitly break chiral symmetry. Nevertheless, the mass gap between the pions and all other hadrons suggests that the pions are the relevant low-energy degrees of freedom of QCD.

It is at the heart of perturbation theory to have a small expansion parameter. In Chiral Perturbation Theory (χPT), the low-energy formulation of QCD with only pions as active degrees of freedom [32], this parameter is given by the pion mass or a small momentum, divided by the characteristic scale, which is $\Lambda_\chi = 4\pi f_\pi \approx 1161$ MeV with the pion-decay constant f_π. Obviously, the expansion only converges for momenta of the external probe – in our case the scattered photon – which are much smaller than the breakdown scale Λ_χ.

In this work we are interested in processes involving one or two nucleons. Therefore we use Heavy Baryon Chiral Perturbation Theory, an extension of χPT which explicitly includes the nucleon as an additional degree of freedom [33]. Weinberg showed [34], how one can systematically include contributions from pion loops to

the tree-level diagrams. These corrections are often referred to as contributions from the "pion-cloud" around the nucleon.

In HBχPT one assumes small momenta of the heavy nucleons and therefore includes their kinetic energy only perturbatively. As long as the nucleons are on-shell, this is a valid procedure for low energies, however we will encounter a severe problem in our deuteron calculation, where even for external sources of vanishing energy the nucleons are non-static, due to their slight off-shellness.

For completeness, in the following we list all HBχPT Lagrangeans relevant for real Compton scattering up to $\mathcal{O}(p^3)$, the order to which we are working. However, except for the leading-order Lagrangeans we restrict ourselves to those parts which actually contribute to Compton scattering. We choose the Weyl-gauge, i.e. $v\cdot A = 0$ with the four-velocity v_μ of the nucleon and the photon field A_μ. Further details can be found in Ref. [35], albeit our convention differs from [35] in the sense, that we split the photon field into isoscalar and isovector parts.

The Lagrangean is composed of baryonic and purely pionic parts,

$$\mathcal{L}^{(3)}_{CS} = \mathcal{L}^{(1)}_{\pi N} + \mathcal{L}^{(2)}_{\pi N} + \mathcal{L}^{(3)}_{\pi N} + \mathcal{L}^{(2)}_{\pi\pi} + \mathcal{L}^{(4)}_{\pi\pi} \tag{2.9}$$

with

$$\mathcal{L}^{(1)}_{\pi N} = \bar{N}_v \left(iv\cdot D + g_A\, S\cdot u\right) N_v, \tag{2.10}$$

$$\mathcal{L}^{(2)}_{\pi N} = \frac{1}{2\,m_N}\bar{N}_v\Big\{(v\cdot D)^2 - D^2 - \frac{i}{2}\left[S^\mu, S^\nu\right]\Big[\left(1+\kappa_v\right) f^+_{\mu\nu} + 2\left(1+\kappa_s\right) v^{(s)}_{\mu\nu}\Big] + \ldots\Big\} N_v, \tag{2.11}$$

$$\mathcal{L}^{(3)}_{\pi N} = \frac{-1}{8\,m_N^2}\bar{N}_v\Big\{\left(1+2\kappa_v\right)\,\left[S_\mu, S_\nu\right]\,f^{\mu\sigma}_+\,v_\sigma\,D^\nu + 2\left(\kappa_s-\kappa_v\right)\,\left[S_\mu, S_\nu\right]\,v^{\mu\sigma}_{(s)}\,v_\sigma\,D^\nu + h.\,c. + \ldots\Big\} N_v. \tag{2.12}$$

g_A is the axial pion-nucleon coupling constant at leading order, m_N the nucleon mass and $\kappa_s = \kappa_p + \kappa_n$ ($\kappa_v = \kappa_p - \kappa_n$) the anomalous isoscalar (isovector) magnetic moment of the nucleon. The velocity projection operator

$$P^+_v = \frac{1}{2}(1+\not{v}) \tag{2.13}$$

projects from the relativistic nucleon Dirac field Ψ_N to the velocity-dependent nucleon field via

$$N_v = \exp\left[im_N v\cdot x\right] P^+_v \Psi_N. \tag{2.14}$$

S_μ is the Pauli-Lubanski vector (see e.g. [35]) and

$$D_\mu = \partial_\mu + \Gamma_\mu - iv^{(s)}_\mu \tag{2.15}$$

denotes the covariant derivative of the nucleon. The chiral tensors contained in the above equations are

$$U = u^2 = \exp\left[i\vec{\tau}\cdot\vec{\pi}/f_\pi\right], \tag{2.16}$$

$$\Gamma_\mu = \frac{1}{2}\left\{u^\dagger\left(\partial_\mu - i\,e\,\frac{\tau^3}{2}\,A_\mu\right)u + u\left(\partial_\mu - i\,e\,\frac{\tau^3}{2}\,A_\mu\right)u^\dagger\right\} \tag{2.17}$$

and

$$u_\mu = i\left\{u^\dagger\left(\partial_\mu - i\,e\,\frac{\tau^3}{2}\,A_\mu\right)u - u\left(\partial_\mu - i\,e\,\frac{\tau^3}{2}\,A_\mu\right)u^\dagger\right\} \tag{2.18}$$

with $\vec{\pi}$ representing the pion field. $v_\mu^{(s)} = \frac{e}{2} A_\mu$ denotes an isoscalar photon field and the corresponding field-strength tensors are

$$v_{\mu\nu}^{(s)} = \partial_\mu v_\nu^{(s)} - \partial_\nu v_\mu^{(s)}, \tag{2.19}$$

$$f_+^{\mu\nu} = u\, e\, \frac{\tau^3}{2} \left(\partial_\mu A_\nu - \partial_\nu A_\mu\right) u^\dagger + u^\dagger\, e\, \frac{\tau^3}{2} \left(\partial_\mu A_\nu - \partial_\nu A_\mu\right) u. \tag{2.20}$$

As far as the purely mesonic sector is concerned, we need

$$\mathcal{L}_{\pi\pi}^{(2)} = \frac{f_\pi^2}{4} \,\mathrm{tr}\left[(\nabla_\mu U)^\dagger \, \nabla^\mu U + \chi^\dagger U + \chi U^\dagger\right] \tag{2.21}$$

and

$$\mathcal{L}_{\pi\pi}^{(4)} = -\frac{e^2}{32\,\pi^2\, f_\pi}\, \epsilon^{\mu\nu\alpha\beta}\, f_{\mu\nu}\, f_{\alpha\beta}\, \pi^0 + \ldots, \tag{2.22}$$

where $\epsilon_{0123} = 1$. Eq. (2.22) is responsible for the decay of an uncharged pion into two photons, i.e. for the pion-pole diagram, Fig. B.1(d). For further details on this decay we refer the reader to Refs. [36, 37]. The chiral tensors in Eqs. (2.21) and (2.22) are

$$\nabla_\mu U = \partial_\mu U - i\, \frac{e}{2}\, A_\mu \left[\tau_3, U\right], \tag{2.23}$$

$$\chi = 2\,\mathcal{B}\,\hat{m} \tag{2.24}$$

with the quark-condensate parameter $\mathcal{B}$ and the $SU(2)$-quark-mass matrix $\hat{m}$ in the isospin limit $m_u = m_d$, which has already been introduced in Eq. (2.8). $f_{\mu\nu}$ is the well-known field-strength tensor

$$f_{\mu\nu} = \partial_\mu A_\nu - \partial_\nu A_\mu. \tag{2.25}$$

Now we have prepared all tools in order to calculate real Compton scattering up to leading-one-loop order in HBχPT. However, it has been known for many decades that the $\Delta(1232)$ resonance plays a crucial role in this process. Therefore, in the next section we extend the spectrum of explicit degrees of freedom for this first nucleonic resonance.

2.2 Small Scale Expansion

Concerning the mass difference Δ_0 between the $\Delta(1232)$ and the nucleon, there exist two complementary points of view: Some authors consider Δ_0 to be much larger than m_π and therefore argue that the contributions from the Δ resonance may be absorbed into higher-order contact terms [35]. In other publications the Δ resonance is included as an explicit degree of freedom because one might expect that due to the strong $N\Delta$-coupling the $\Delta(1232)$ gives as important contributions as the pion cloud. The idea to extend HBχPT in such a way has its origin in the early 1990's [38]. Whether or not it is advantageous to include the $\Delta(1232)$ explicitly of course depends on the process under investigation, e.g. the pion-mass dependence of the nucleon mass is rather weakly influenced by the $\Delta(1232)$ [39], whereas the anomalous magnetic moment of the nucleon depends strongly on the Δ resonance [40].

In nucleon Compton scattering, the $\Delta(1232)$ resonance is well-known to play a crucial role, see e.g. [9]. Therefore, in this work we include the Δ resonance explicitly, i.e. we need to specify how the ΔN mass splitting Δ_0 is treated in the power counting. Here we use the so-called Small Scale Expansion (SSE) [41, 42][1],

[1] We note that there also exist alternative approaches for Chiral Effective Field Theories with explicit π, N and Δ degrees of freedom, e.g. the δ-expansion [43], which was recently shown to describe γp cross-section data well in an energy range from $\omega = 0$ MeV to $\omega = 300$ MeV.

where the expansion parameter is called ϵ, denoting either a small momentum, the pion mass or the mass difference Δ_0 between the real part of the Δ mass and the nucleon mass:

$$\Delta_0 = \mathrm{Re}[m_\Delta] - m_N \tag{2.26}$$

We note that the SSE power counting is constructed such that up to a certain order in ϵ all HBχPT diagrams to the same order are included as well. In this work, real Compton scattering on the nucleon and on the deuteron is investigated up to third order ($\mathcal{O}(\epsilon^3)$) in the Small Scale Expansion.

In the following we summarize all parts of the SSE Lagrangean, which are relevant for our calculation and contain the explicit Δ field. The notation is adapted from [42] and [26].

$$\mathcal{L}_\Delta^{(1)} = -\bar{T}_i^\mu \, g_{\mu\nu} \, \left[iv\cdot D^{ij} - \Delta\, \delta^{ij} + \ldots \right] T_j^\nu \tag{2.27}$$

$$\mathcal{L}_{N\Delta}^{(1)} = g_{\pi N\Delta}\, \bar{T}_i^\mu \, w_\mu^i \, N + h.c. \tag{2.28}$$

$$\mathcal{L}_{N\Delta}^{(2)} = \bar{T}_i^\mu \, \left[\frac{i\, b_1}{M} \, S^\nu \, f_{+\mu\nu}^i + \ldots \right] N + h.c. \tag{2.29}$$

Here

$$T_\mu^i(x) = P_v^+ \, P_{(33)\mu\nu}^{3/2} \, \psi_i^\nu(x) \exp(iM\, v\cdot x) \tag{2.30}$$

denotes the "light" part of the spin-3/2 baryon field ψ_μ^i, which is projected from the relativistic Rarita-Schwinger field via the spin-3/2 projection operator for fields of constant "velocity",

$$P_{(33)\mu\nu}^{3/2} = g_{\mu\nu} - \frac{1}{3}\gamma_\mu\,\gamma_\nu - \frac{1}{3}\,\left(\not{v}\,\gamma_\mu\, v_\nu + v_\mu\,\gamma_\nu\,\not{v} \right), \tag{2.31}$$

whereas the remaining "heavy" parts are integrated out. For further details cf. Ref. [42]. The chiral tensors in Eqs. (2.27-2.29) are

$$D_\mu^{ij} = \partial_\mu\, \delta^{ij} - i\, \frac{e}{2}\, (1+\tau_3)\, A_\mu\, \delta^{ij} + e\, \epsilon^{i3j}\, A_\mu + \ldots\,, \tag{2.32}$$

$$w_\mu^i = -\frac{1}{f_\pi}\, \partial_\mu\, \pi^i - \frac{e}{f_\pi}\, A_\mu\, \epsilon^{i3j}\, \pi^j + \ldots\,, \tag{2.33}$$

$$f_{+\mu\nu}^i = e\, \delta^{i3}\, \left(\partial_\mu\, A_\nu - \partial_\nu\, A_\mu \right) + \ldots\,. \tag{2.34}$$

The two coupling constants in Eqs. (2.28) and (2.29) are $g_{\pi N\Delta}$, which parameterizes the leading-order $\pi N\Delta$ coupling, and b_1, the leading-order constant of the $\Delta \to N\gamma$ transition.

In the original formulation of SSE, the only contributions to a leading-one-loop order calculation of nucleon Compton scattering come from the Lagrangeans given in Section 2.1 and Eqs. (2.27-2.29). However, we found that including only these tools we are missing strong diamagnetic contributions, which are necessary to render the magnetic dipole polarizability a small number, as found in experiments such as [5, 11]. In fact, using only the above Lagrangeans, $\bar{\beta}_{M1}$ turns out to be of the same order of magnitude as the electric dipole polarizability $\bar{\alpha}_{E1}$, in clear contradiction to experiment. Therefore, we include two additional $\gamma\gamma NN$ couplings g_1, g_2 [44][2] in the leading-one-loop SSE analysis, which are formally of higher order, but will turn out to be anomalously large. The corresponding short-distance Lagrangeans are

$$\mathcal{L}_1^{sd} = \frac{2\, g_1}{(4\pi\, f_\pi)^2\, m_N}\, \bar{N}\, v^\mu\, v^\nu \left\langle \tilde{f}_{\lambda\mu}\, \tilde{f}_\nu^\lambda \right\rangle N, \tag{2.35}$$

$$\mathcal{L}_2^{sd} = \frac{2\, g_2}{(4\pi\, f_\pi)^2\, m_N}\, \bar{N} \left\langle \tilde{f}_{\mu\nu}\, \tilde{f}^{\mu\nu} \right\rangle N \tag{2.36}$$

[2] The coupling constants g_1 and g_2 correspond to g_{117} and g_{118} in [44].

with the electromagnetic field-strength tensor $\tilde{f}^{\mu\nu} = \frac{e}{2}\,\tau_3\,(\partial^\mu A^\nu - \partial^\nu A^\mu)$ [35]. To promote these two structures to leading-one-loop order modifies the power counting, as they are formally part of the next-to-leading one-loop order chiral Lagrangean [44]. However, we will see in the next chapter that due to their unnaturally strong contributions to nucleon Compton scattering we cannot avoid this modification.

Now that we have fixed – albeit very briefly – the theoretical framework of our calculation, we turn to the first main part of this work: Elastic, spin-averaged Compton scattering from the single nucleon.

Chapter 3

Unpolarized Compton Scattering and Nucleon Polarizabilities

We turn now to the first main part of this work: Compton scattering on the single nucleon. While we discuss both proton and neutron Compton scattering, we are aware of the fact that experiments using single-neutron targets are not feasible due to the finite life-time of the free neutron. Therefore the main focus will be on proton Compton cross sections, where a large amount of data exists (Section 3.3). We also discuss in detail the response of the internal degrees of freedom of the nucleon to an external electromagnetic field, represented e.g. by a photon that is scattered on the nucleon. This reaction is described in Section 3.5 in terms of dynamical nucleon polarizabilities, which show a characteristic dependence on the photon energy. These polarizabilities are defined via a multipole expansion in Compton scattering, derived in Section 3.1. One of the advantages is that the inclusion of only a few multipoles is often sufficient to obtain a good approximation of the full calculation. Only when such a reduction of the parameters can be achieved, there is hope that the unknown structure can be fitted to experimental data. We show that our full calculation is nearly indistinguishable from an approximation which includes only the six dynamical dipole polarizabilities. Therefore we conclude that determining the dipole polarizabilities of the nucleon is possible, combining spin-averaged cross sections (Chapter 3) and polarized ones (Chapter 4).

The results of this chapter are published in our Ref. [26] and partly in my diploma thesis, Ref. [29]. Throughout the chapter we will indicate new results with respect to [29].

3.1 Multipole Expansion for Nucleon Compton Scattering

3.1.1 From Amplitudes to Multipoles

The T-matrix for real Compton scattering off the nucleon is written in terms of six structure amplitudes $A_i(\omega, z),\ i = 1, \ldots, 6$:

$$\begin{aligned} T_{fi}(\omega, z) = {} & A_1(\omega, z)\, \vec{\epsilon}\,' \cdot \vec{\epsilon} + A_2(\omega, z)\, \vec{\epsilon}\,' \cdot \hat{k}\, \vec{\epsilon} \cdot \hat{k}' \\ & + i\, A_3(\omega, z)\, \vec{\sigma} \cdot (\vec{\epsilon}\,' \times \vec{\epsilon}) + i\, A_4(\omega, z)\, \vec{\sigma} \cdot (\hat{k}' \times \hat{k})\, \vec{\epsilon}\,' \cdot \vec{\epsilon} \\ & + i\, A_5(\omega, z)\, \vec{\sigma} \cdot \Big[(\vec{\epsilon}\,' \times \hat{k})\, \vec{\epsilon} \cdot \hat{k}' - (\vec{\epsilon} \times \hat{k}')\, \vec{\epsilon}\,' \cdot \hat{k} \Big] \\ & + i\, A_6(\omega, z)\, \vec{\sigma} \cdot \Big[(\vec{\epsilon}\,' \times \hat{k}')\, \vec{\epsilon} \cdot \hat{k}' - (\vec{\epsilon} \times \hat{k})\, \vec{\epsilon}\,' \cdot \hat{k} \Big] \end{aligned} \tag{3.1}$$

For the Compton multipole expansion, we follow Ritus et al. [45] and work in the center-of-mass (cm) frame, i.e. ω denotes the cm energy of a real photon scattering under the cm angle θ ($z = \cos\theta$) off a nucleon. $\vec{\sigma}$ is the vector of the Pauli spin matrices, $\hat{\vec{k}}_i = \vec{k}_i/\omega$ ($\hat{\vec{k}}_f = \vec{k}_f/\omega$) denotes the unit vector in the momentum direction of the incoming (outgoing) photon with polarization $\vec{\epsilon}$ ($\vec{\epsilon}\,'$).

Expanding the Compton-scattering amplitude into multipoles has a long tradition [45], albeit then it was common to use a slightly different basis. The connection between the amplitudes used in [45] and written in Eq. (3.4), and those of Eq. (3.1), reads

$$\begin{aligned} A_1 &= \frac{4\pi W}{m_N}(R_1 + zR_2), \\ A_2 &= \frac{4\pi W}{m_N}(-R_2), \\ A_3 &= \frac{4\pi W}{m_N}(R_3 + zR_4 + 2zR_5 + 2R_6), \\ A_4 &= \frac{4\pi W}{m_N}(R_4), \\ A_5 &= \frac{4\pi W}{m_N}(-R_4 - R_5), \\ A_6 &= \frac{4\pi W}{m_N}(-R_6) \end{aligned} \tag{3.2}$$

with $W = \sqrt{s} = \omega + \sqrt{m_N^2 + \omega^2}$ denoting the total cm energy and m_N the nucleon mass.

The multipole expansion is defined for the complete Compton amplitude. Nucleon structure effects as for example expressed in $\bar{\alpha}_{E1}$ and $\bar{\beta}_{M1}$, cf. Section 1.1, involve processes for which the particle content between the interactions of the in- and outgoing photon goes beyond the single nucleon. This corresponds to subtracting from the full amplitudes the Powell amplitudes [1] of Compton scattering on a point-like nucleon of spin $\frac{1}{2}$ and anomalous magnetic moment κ. Therefore, we separate the six amplitudes into structure-independent (pole) and structure-dependent (non-pole) parts,

$$R_i(\omega, z) = R_i^{\text{pole}}(\omega, z) + \bar{R}_i(\omega, z). \tag{3.3}$$

We specify the pole contributions as those terms which have a nucleon pole in the s- or u-channel and *in addition* as terms with a pion pole in the t-channel. Schematically, we show these three contributions in Fig. 3.1 and note that any theoretical framework utilized to calculate Compton scattering has to clearly state the separation of these pole contributions before any information on static or dynamical

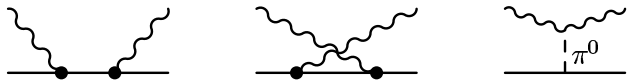

Figure 3.1: Schematic representation of the three types of pole contributions to nucleon Compton scattering in the s-, u- and t-channel (left to right).

polarizabilities can be obtained. Obviously, any Compton observable is independent of the choice of separating the amplitudes.

As the pole contributions to nucleon Compton scattering and the resulting low-energy theorems have been known for many decades [3], the main interest in Compton studies over the past few years focused on the non-pole contributions $\bar{R}_i$. Ref. [46] suggested that the Compton multipole expansion should be applied only to these structure-dependent terms. In analogy to Ref. [45], one obtains [4][1]

$$
\begin{aligned}
\bar{R}_1(\omega,z) &= \sum_{l=1}^{\infty}\Big\{\left[(l+1)\,f_{EE}^{l+}(\omega)+l\,f_{EE}^{l-}(\omega)\right]\,\left(l\,P_l'(z)+P_{l-1}''(z)\right)\\
&\quad-\left[(l+1)\,f_{MM}^{l+}(\omega)+l\,f_{MM}^{l-}(\omega)\right]\,P_l''(z)\Big\},\\
\bar{R}_2(\omega,z) &= \sum_{l=1}^{\infty}\Big\{\left[(l+1)\,f_{MM}^{l+}(\omega)+l\,f_{MM}^{l-}(\omega)\right]\,\left(l\,P_l'(z)+P_{l-1}''(z)\right)\\
&\quad-\left[(l+1)\,f_{EE}^{l+}(\omega)+l\,f_{EE}^{l-}(\omega)\right]\,P_l''(z)\Big\},\\
\bar{R}_3(\omega,z) &= \sum_{l=1}^{\infty}\Big\{\left[f_{EE}^{l+}(\omega)-f_{EE}^{l-}(\omega)\right]\,\left(P_{l-1}''(z)-l^2\,P_l'(z)\right)\\
&\quad-\left[f_{MM}^{l+}(\omega)-f_{MM}^{l-}(\omega)\right]\,P_l''(z)+2f_{EM}^{l+}(\omega)\,P_{l+1}''(z)-2f_{ME}^{l+}(\omega)\,P_l''(z)\Big\},\\
\bar{R}_4(\omega,z) &= \sum_{l=1}^{\infty}\Big\{\left[f_{MM}^{l+}(\omega)-f_{MM}^{l-}(\omega)\right]\,\left(P_{l-1}''(z)-l^2\,P_l'(z)\right)\\
&\quad-\left[f_{EE}^{l+}(\omega)-f_{EE}^{l-}(\omega)\right]\,P_l''(z)+2f_{ME}^{l+}(\omega)\,P_{l+1}''(z)-2f_{EM}^{l+}(\omega)\,P_l''(z)\Big\},\\
\bar{R}_5(\omega,z) &= \sum_{l=1}^{\infty}\Big\{\left[f_{EE}^{l+}(\omega)-f_{EE}^{l-}(\omega)\right]\,\left(l\,P_l''(z)+P_{l-1}'''(z)\right)-\left[f_{MM}^{l+}(\omega)-f_{MM}^{l-}(\omega)\right]\,P_l'''(z)\\
&\quad+f_{EM}^{l+}(\omega)\,\left[(3l+1)\,P_l''(z)+2P_{l-1}'''(z)\right]-f_{ME}^{l+}(\omega)\,\left[(l+1)\,P_{l+1}''(z)+2P_l'''(z)\right]\Big\},\\
\bar{R}_6(\omega,z) &= \sum_{l=1}^{\infty}\Big\{\left[f_{MM}^{l+}(\omega)-f_{MM}^{l-}(\omega)\right]\,\left(l\,P_l''(z)+P_{l-1}'''(z)\right)-\left[f_{EE}^{l+}(\omega)-f_{EE}^{l-}(\omega)\right]\,P_l'''(z)\\
&\quad+f_{ME}^{l+}(\omega)\,\left[(3l+1)\,P_l''(z)+2P_{l-1}'''(z)\right]-f_{EM}^{l+}(\omega)\,\left[(l+1)\,P_{l+1}''(z)+2P_l'''(z)\right]\Big\}.
\end{aligned}
\tag{3.4}
$$

The prime denotes differentiation with respect to $z=\cos\theta$ in the cm system, and $P_l(z)$ is the lth Legendre polynomial. The functions $f_{TT'}^{l\pm}(\omega)$ are the Compton multipoles and correspond to transitions $Tl\to T'l'$, where $T,T'=E,M$ labels the coupling of the incoming or outgoing photon as electric or magnetic. Here

[1] We correct here the factors of 2 in front of f_{ME}^{l+} (f_{EM}^{l+}) in R_5 (R_6), which appear in Ref. [4].

l ($l' = l \pm \{1, 0\}$) denotes the angular momentum of the initial (final) photon, whereas the total angular momentum is $j_\pm = l \pm \frac{1}{2}$, abbreviated by $l\pm$. We note that mixed multipole amplitudes $T \neq T'$ only occur in the spin-dependent amplitudes $\bar{R}_i$, $i = 3, \ldots, 6$.

Having defined the structure-dependent Compton multipoles in the cm frame, we now move on to connect them to polarizabilities.

3.1.2 Dynamical and Static Polarizabilities

In order to derive a consistent connection between the Compton multipoles $f_{TT'}$ and the polarizabilities of definite spin structure and multipolarity at a certain energy, we recall the low-energy behavior of the multipoles in the cm frame [45]:

$$\begin{aligned} f^{l\pm}_{TT'}(\omega) &\sim \omega^{2l}, \qquad & T = T', \\ f^{l+}_{TT'}(\omega) &\sim \omega^{2l+1}, \qquad & T \neq T'. \end{aligned} \tag{3.5}$$

With this information, dynamical spin-independent electric or magnetic dipole and quadrupole polarizabilities were defined as linear combinations of Compton multipoles in [46]:

$$\begin{aligned} \alpha_{E1}(\omega) &= \left[2f^{1+}_{EE}(\omega) + f^{1-}_{EE}(\omega)\right]/\omega^2 \\ \beta_{M1}(\omega) &= \left[2f^{1+}_{MM}(\omega) + f^{1-}_{MM}(\omega)\right]/\omega^2 \\ \alpha_{E2}(\omega) &= 36\left[3f^{2+}_{EE}(\omega) + 2f^{2-}_{EE}(\omega)\right]/\omega^4 \\ \beta_{M2}(\omega) &= 36\left[3f^{2+}_{MM}(\omega) + 2f^{2-}_{MM}(\omega)\right]/\omega^4 \end{aligned} \tag{3.6}$$

We note that the normalization of these linear superpositions has been chosen in such a way that the usual (static) electric and magnetic polarizabilities of the nucleon can be recovered from the dynamical dipole polarizabilities via

$$\bar{\alpha}_{E1} = \lim_{\omega\to 0} \alpha_{E1}(\omega), \qquad \bar{\beta}_{M1} = \lim_{\omega\to 0} \beta_{M1}(\omega). \tag{3.7}$$

Likewise, the static electric and magnetic quadrupole polarizabilities $\bar{\alpha}_{E2}$ and $\bar{\beta}_{M2}$ discussed in Refs. [4] and [47] can be obtained as the zero-energy limit of the corresponding dynamical quadrupole polarizabilities.

Extending Ref. [46], we also introduce dynamical *spin-dependent* dipole polarizabilities[2] via

$$\begin{aligned} \gamma_{E1E1}(\omega) &= \left[f^{1+}_{EE}(\omega) - f^{1-}_{EE}(\omega)\right]/\omega^3, \\ \gamma_{M1M1}(\omega) &= \left[f^{1+}_{MM}(\omega) - f^{1-}_{MM}(\omega)\right]/\omega^3, \\ \gamma_{E1M2}(\omega) &= 6\, f^{1+}_{EM}(\omega)/\omega^3, \\ \gamma_{M1E2}(\omega) &= 6\, f^{1+}_{ME}(\omega)/\omega^3. \end{aligned} \tag{3.8}$$

The notation is such that $\gamma_{TlT'l'}$ parameterizes a Tl ($T'l'$) transition at the first (second) photon vertex. In the limit of zero photon energy, one again recovers the four static spin polarizabilities $\bar{\gamma}_{E1E1}$, $\bar{\gamma}_{M1M1}$, $\bar{\gamma}_{E1M2}$, $\bar{\gamma}_{M1E2}$ of the nucleon:

$$\bar{\gamma}_{TlT'l'} = \lim_{\omega\to 0} \gamma_{TlT'l'}(\omega), \qquad T, T' = E, M. \tag{3.9}$$

Here, these four static spin polarizabilities are written in the so called multipole-basis [4]. The connection to the Ragusa-basis γ_i, $i = 1, \ldots, 4$ [48], is discussed

[2]The definition of the dynamical spin quadrupole polarizabilities can be found in Ref. [29].

in Ref. [49]. We note that at present there exists little information on the spin-dependent nucleon polarizabilities. Only two linear combinations – typically denoted as the forward $\bar{\gamma}_0$ and the backward $\bar{\gamma}_\pi$ spin polarizabilities of the nucleon – are constrained from experiments, e.g. see the discussion in Ref. [50]. Both quantities involve all four (dipole) spin polarizabilities:

$$\begin{aligned}\bar{\gamma}_0 &= -\bar{\gamma}_{E1E1} - \bar{\gamma}_{E1M2} - \bar{\gamma}_{M1M1} - \bar{\gamma}_{M1E2} \\ \bar{\gamma}_\pi &= -\bar{\gamma}_{E1E1} - \bar{\gamma}_{E1M2} + \bar{\gamma}_{M1M1} + \bar{\gamma}_{M1E2}\end{aligned} \tag{3.10}$$

While the static polarizabilities of the nucleon are real, we note that the dynamical polarizabilities become complex once the energy in the intermediate state is high enough to create an on-shell intermediate state, the first being the physical πN intermediate state. Below the two-pion-production threshold, the imaginary parts of the dynamical polarizabilities can be understood very easily. They are simply given by the well-known multipoles of single-pion photoproduction (see e.g. [51]). One obtains [26]

$$\begin{aligned}
&\mathrm{Im}[\alpha_{E1}] = \frac{k_\pi}{\omega^2}\sum_C (2|E_{2-}^{(C)}|^2 + |E_{0+}^{(C)}|^2), && \mathrm{Im}[\beta_{M1}] = \frac{k_\pi}{\omega^2}\sum_C (2|M_{1+}^{(C)}|^2 + |M_{1-}^{(C)}|^2), \\
&\mathrm{Im}[\alpha_{E2}] = 36\,\frac{k_\pi}{\omega^4}\sum_C (3|E_{3-}^{(C)}|^2 + 2|E_{1+}^{(C)}|^2), && \mathrm{Im}[\beta_{M2}] = 36\,\frac{k_\pi}{\omega^4}\sum_C (3|M_{2+}^{(C)}|^2 + 2|M_{2-}^{(C)}|^2), \\
&\mathrm{Im}[\gamma_{E1E1}] = \frac{k_\pi}{\omega^3}\sum_C (|E_{2-}^{(C)}|^2 - |E_{0+}^{(C)}|^2), && \mathrm{Im}[\gamma_{M1M1}] = \frac{k_\pi}{\omega^3}\sum_C (|M_{1+}^{(C)}|^2 - |M_{1-}^{(C)}|^2), \\
&\mathrm{Im}[\gamma_{E1M2}] = 6\,\frac{k_\pi}{\omega^3}\sum_C \mathrm{Re}[E_{2-}^{(C)}(M_{2-}^{(C)})^*], && \mathrm{Im}[\gamma_{M1E2}] = -6\,\frac{k_\pi}{\omega^3}\sum_C \mathrm{Re}[E_{1+}^{(C)}(M_{1+}^{(C)})^*],
\end{aligned} \tag{3.11}$$

where k_π is the magnitude of the pion momentum and $E_{l\pm}^{(C)}$ and $M_{l\pm}^{(C)}$ are the pion-photoproduction multipoles which are summed over the different isotopic or charge channels C. In the following, we therefore focus only on the real parts of the dynamical polarizabilities. The imaginary parts of our calculation can be found in Ref. [29].

This concludes our section pertaining to the definitions of the dynamical polarizabilities and their connection to static polarizabilities as well as to single-pion photoproduction. Before we discuss the numerical values of the (static) polarizabilities in the upcoming section, we first provide some background on the theoretical machinery employed to analyze nucleon Compton scattering.

3.2 Theoretical Framework

Many calculations of nucleon Compton scattering – some even up to next-to-leading one-loop order – have been performed using Chiral Effective Field Theory (χEFT) during the past decade [35, 43, 52, 53, 54]. Here, we extract information on the dynamical polarizabilities of the nucleon both from the leading-one-loop Heavy Baryon Chiral Perturbation Theory (HBχPT) calculation of Ref. [35] as well as from the leading-one-loop "Small Scale Expansion" (SSE) calculations of Refs. [55, 56]. We remind the reader of Chapter 2, where we introduced the HBχPT as well as the SSE formalism. The first one only involves explicit πN degrees of freedom, whereas the latter is one possibility to also systematically include explicit spin-3/2 nucleon-resonance degrees of freedom, i.e. the $\Delta(1232)$, in χEFT.

The pole contributions to nucleon Compton scattering at leading-one-loop order in χEFT are given in Appendix B. As discussed in Section 3.1, it is the non-pole contribution to Compton scattering which determines the polarizabilities. In HBχPT, these structure-dependent contributions are solely given by πN intermediate states (Fig. 3.2), whereas SSE takes into account in addition $\pi\Delta$ diagrams (Fig. 3.3) as well as the $\Delta(1232)$ s- and u-channel pole terms (Fig. 3.4 (a),(b)).

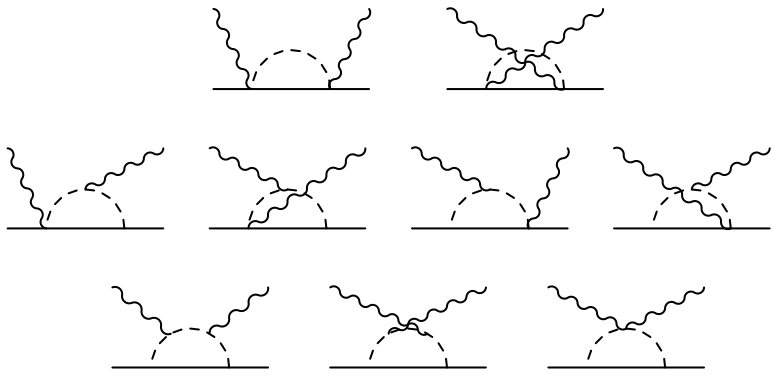

Figure 3.2: Leading-one-loop $N\pi$-continuum contributions to nucleon polarizabilities.

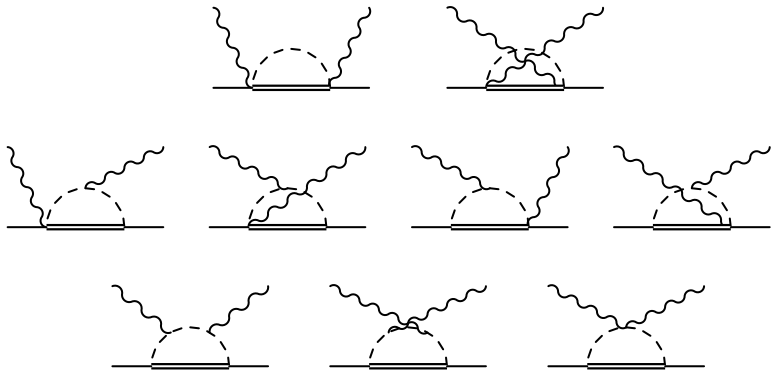

Figure 3.3: Leading-one-loop $\Delta\pi$-continuum contributions to nucleon polarizabilities.

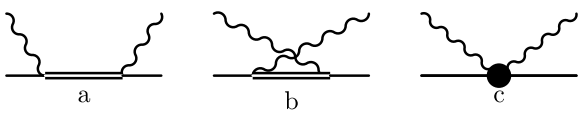

Figure 3.4: Δ-pole and short-distance contributions to nucleon polarizabilities.

We note that we go beyond the existing leading-one-loop HBχPT/SSE calculations [35, 55, 56] of nucleon Compton scattering in four aspects:

1) Both HBχPT and SSE are non-relativistic frameworks leading to a $1/m_N$ expansion of the amplitudes, where m_N is the mass of the target nucleon. In the

leading-one-loop structure amplitudes $\bar{R}_i$, the one-pion-production threshold

$$\omega_\pi = \frac{m_\pi^2 + 2\, m_\pi\, m_N}{2\,(m_\pi + m_N)} \approx 131 \text{ MeV} \tag{3.12}$$

is therefore not at the correct location. We correct for this purely kinematical effect by replacing the photon energy ω with the Mandelstam variable s via

$$\omega \to \sqrt{s(\omega)} - m_N. \tag{3.13}$$

There are various possibilities to perform such a threshold correction (cf. Ref. [16]), but it is clear that all these choices agree within the strict truncation of the χEFT employed. Obviously this replacement should only be applied in those places where an imaginary part arises above threshold. In contrast to Ref. [29], the u-channel diagrams are left unchanged. We are aware that this procedure violates crossing symmetry, but the crossing-violating effects in the u-channel are small. Formally, the terms correcting for the exact location of the pion threshold start to appear at $\mathcal{O}(p^4)$. We implement this kinematical correction in the leading-one-loop πN-continuum contribution to the χEFT amplitudes throughout all chapters of this work on single-nucleon Compton scattering. Such kinematical corrections should be employed in non-relativistic χEFTs at all particle thresholds. However, as our calculation is valid only below the $\Delta(1232)$ resonance, the one-pion-production threshold is the only one to be taken care of. The formulae for the SSE amplitudes are given in Refs. [26] and [29], albeit in Ref. [29] we also corrected the u-channel, in analogy to Eq. (3.13).

2) Another kinematical effect concerns the exact location of the $\Delta(1232)$ pole. In Ref. [51], it was determined as a T-matrix pole in the complex $W = \sqrt{s}$ plane at the location $m_\Delta = (1210 - i\,50)$ MeV. We therefore employ the same substitution prescription $\omega \to \sqrt{s} - m_N$ as in Eq. (3.13) in s-channel pole contributions of the $\Delta(1232)$ resonance, generating a pole at $\sqrt{s} = m_N + \Delta_0 = 1210$ MeV. Given that $\Delta(1232)$-pole contributions in the u-channel can also affect higher multipoles, we make an analogous replacement $\omega \to m_N - \sqrt{u}$ in the $\Delta(1232)$ u-channel-pole contributions and note that the corrections of the Δ pole are new with respect to Ref. [29]. While these kinematical details are of minor importance when one only discusses static polarizabilities (with the exception of $\bar{\beta}_{M2}$, see Section 3.4.2), they do become important in dynamical polarizabilities once the photon energy is higher than 100 MeV. We note again that via these modifications, we have not introduced any additional physics content into the χEFT calculations, as in the $m_N \to \infty$ limit all these purely kinematical modifications reduce to the strict $\mathcal{O}(\epsilon^3)$ truncation of SSE [55, 56]. The detailed form of the modified amplitudes can be found in Appendix B of our Ref. [26].

3) The parameters required for the leading-one-loop HBχPT calculation are well known. For completeness, we list them in Table A.1. Also shown are the two parameters Δ_0 and $g_{\pi N\Delta}$ utilized in the leading-one-loop SSE Compton-scattering calculation of Refs. [55, 56]. The numbers given here differ slightly from Ref. [55], as we determine them now from the exact kinematical location of the $\Delta(1232)$-pole in the complex W-plane, discussed in the previous paragraph.

   To leading-one-loop order, the HBχPT calculation for nucleon Compton scattering is therefore parameter-free (in the sense that all parameters shown in Table A.1 can be determined outside Compton scattering). On the other

hand, in the corresponding SSE calculation we are left with one free parameter b_1 – which in χEFT corresponds to the leading $\gamma N\Delta$ coupling [41, 55, 50]. In Ref. [56], b_1 was estimated from the measured $\Delta \to N\gamma$ decay width to be $|b_1| \approx 3.9$. As this determination is very sensitive to the numerical value of the parameter Δ_0 (for the value $\Delta_0 = 271$ MeV shown in Table A.1, we would obtain $|b_1| \approx 4.4$), we choose a different strategy here and determine b_1 directly from a fit to Compton cross-section data, whereas in Ref. [29] we used the Dispersion-Relation result for $\bar{\gamma}_{M1M1}$ [26] to fix this coupling.

4) With the $\gamma N\Delta$ coupling constant b_1 as a fit parameter in the SSE analysis, we can constrain the crucial paramagnetic contribution from the Δ directly from data. In [31] an estimate of its contribution to $\bar{\beta}_{M1}$, based on the $N \to \Delta$ transition matrix element from [57] gives $\beta_\Delta \approx 12 \cdot 10^{-4}$ fm^3. This number agrees with the result $\beta_\Delta = (13 \pm 3) \cdot 10^{-4}$ fm^3 from [58]. However, it has been known for a long time that there must also be substantial diamagnetism in the nucleon – otherwise the small numbers for the static magnetic polarizability of the proton cannot be understood, see e.g. Ref. [50] for details. At leading-one-loop order neither HBχPT nor SSE in their respective counting schemes, based on (naïve) dimensional analysis, allow for such a contribution [55]. Both schemes assume that this is a "small" higher-order effect, which can be accounted for at the next-to-leading one-loop order. As a side remark we remind the reader that in Ref. [16] it was shown in a next-to-leading one-loop HBχPT calculation that for "reasonable" values of the regularization scale λ, a large part of this diamagnetism could be accounted for by πN loop effects. Working only to leading-one-loop order, we cannot contribute to the discussion of the physical nature of this diamagnetism in the nucleon. However, from our combined analysis of proton and deuteron Compton data we conclude that dynamics beyond our leading-one-loop order calculation indeed strongly contributes to $\bar{\alpha}_{E1}$ and $\bar{\beta}_{M1}$. We can constrain these contributions to be of isoscalar nature and, reminiscent of short-distance dynamics, they are largely energy independent.

   As we determine the paramagnetic response of the nucleon from data and as there is a well-known delicate interplay between para- and diamagnetic contributions at small photon energy, we introduce two additional $\mathcal{O}(p^4)$ $\gamma\gamma NN$ couplings g_1 and g_2, cf. Eqs. (2.35, 2.36). If they turned out to give only small corrections, we could safely neglect them as a higher-order effect in accordance with the counting assumptions of SSE. However, as will be demonstrated in Section 3.4.1, this is not the case and these two couplings have to be included already at leading-one-loop order, modifying the naïve power counting due to their unnaturally large sizes. Two independent structures are needed to separate magnetic and electric contributions via different linear combinations of g_1 and g_2. Promoting these two structures from $\mathcal{O}(\epsilon^4)$ to leading-one-loop order obviously modifies the power counting. Nevertheless, in light of the reasoning given above, we must include them as free parameters in our SSE fit to Compton cross sections. We find that the two couplings in Eqs. (2.35, 2.36) are sufficient to parameterize any quark-mass independent unknown magnetic and electric short-distance physics in nucleon Compton scattering (cf. Fig. 3.8). The contributions of g_1, g_2 to the Compton structure-amplitudes are shown explicitly in Appendix B of our Ref. [26][3].

The leading-one-loop structure-dependent Compton amplitudes of Ref. [26] include the four modifications discussed above. In order to extract from them the dynamical polarizabilities of the nucleon in χEFT frameworks, one first projects out the

[3]We correct for a missing factor of -2 in Ref. [29].

Compton multipoles $f_{TT'}(\omega)$ of Section 3.1.1, using the formulae in Appendix C. The dynamical polarizabilities at definite multipolarity as a function of the photon energy follow then from Eqs. (3.6, 3.8).

This concludes our brief summary of leading-one-loop χEFT calculations for nucleon Compton scattering. We now move on to a determination of the three free parameters b_1, g_1 and g_2 from cross-section data.

3.3 Spin-Averaged Compton Cross Sections

3.3.1 General Remarks

In the previous section, we have briefly introduced the theoretical framework of our nucleon Compton-scattering calculation, which we now confront with actual proton Compton data. This will also serve as a check for the parameters employed (in the case of HBχPT), respectively allow us to constrain some parameters (in the case of SSE). To be precise, we compare the experimental differential cross sections with predictions from leading-one-loop HBχPT, which does not contain any additional free parameters to be determined from Compton scattering, and with the Dispersion-Relation Analysis from [26]. This method makes use of the optical theorem to deduce the imaginary part of the transition amplitude from measured break-up cross sections, in our case $\gamma N \to X$. The real part of the amplitude is derived from the imaginary part via the Kramers-Kronig dispersion relations. Although we do not show any error bands for the Dispersion-Analysis curves in our figures, we must stress that there are non-negligible uncertainties also in this framework, which arise e.g. due to error bars in the input parameters $\bar{\alpha}_{E1}$, $\bar{\beta}_{M1}$ and $\bar{\gamma}_\pi$, cf. Ref. [26]. For further details on the Dispersion-Theory formalism we refer the reader to the literature, e.g. to the review given in Ref. [50].

In the case of leading-one-loop SSE calculations, we perform a fit of the three free parameters b_1, g_1, g_2 discussed in the previous section to proton Compton data. In this section, we can therefore only check whether the two curves from Field Theory are consistent with data and Dispersion Theory. A detailed discussion of the electromagnetic structure of the proton will be given in Section 3.5.

So far, only spin-averaged cross sections on the proton have been measured. We draw from a large set of data [5, 6, 7, 8], covering proton Compton scattering from low energies to above pion-production threshold. We present the low-energy data as functions of the differential cross section in the cm system versus the photon energy (in the cm system) at different angles $\theta_{\rm lab}$. Note that in the plots we work in the cm system when comparing with the SAL data, and in the lab system for all other cases.

In the differential Compton-scattering cross sections, the artificial separation between pole and non-pole contributions is absent and both terms have to be added. The differences between lab and cm system are expressed via the flux factors

$$\Phi_{\rm cm} = \frac{m_N}{4\pi\,\sqrt{s(\omega)}}, \qquad \Phi_{\rm lab} = \frac{\omega_f}{4\pi\,\omega_i}, \tag{3.14}$$

with

$$\omega_f = \frac{m_N\,\omega_i}{m_N + \omega_i\,(1-\cos\theta_{\rm lab})}. \tag{3.15}$$

ω_f (ω_i) denote the energy of the outgoing (incoming) photon in the lab frame, ω_i being related to the photon energy in the γN cm frame by

$$\omega = \frac{\omega_i}{\sqrt{1+2\omega_i/m_N}}. \tag{3.16}$$

In the spin-averaged case, the differential cross section is then given by

$$\left.\frac{d\sigma}{d\Omega}\right|_{\rm frame} = \Phi^2_{\rm frame}\,|T|^2. \tag{3.17}$$

The absolute square of the Compton amplitude, averaged over the initial and summed over the final nucleon and photon polarizations, is [35]

$$\begin{aligned}|T|^2 = {}& \frac{1}{2}\,|A_1|^2\,\left(1+z^2\right) + \frac{1}{2}\,|A_3|^2\,\left(3-z^2\right)\\ & + \left(1-z^2\right)\,\left[4\,{\rm Re}[A_3^*\,A_6] + {\rm Re}[A_3^*\,A_4 + 2A_3^*\,A_5 - A_1^*\,A_2]\,z\right]\\ & + \left(1-z^2\right)\,\left[\frac{1}{2}\,|A_2|^2\,\left(1-z^2\right) + \frac{1}{2}\,|A_4|^2\,\left(1+z^2\right)\right.\\ & \left. + |A_5|^2\,\left(1+2z^2\right) + 3\,|A_6|^2 + 2{\rm Re}[A_6^*\,\left(A_4+3A_5\right)]\,z + 2{\rm Re}[A_4^*\,A_5]\,z^2\right]. \end{aligned}\tag{3.18}$$

After these general remarks, we now move on to the comparison with experiment.

3.3.2 Comparison to Experiments on Proton Compton Scattering

Figs. 3.5 and 3.6 compare several different cross-section data at selected angles with the third-order HBχPT prediction, the DR prediction from Ref. [26] and with the result of our SSE fit (details of the fit will be discussed in the next section). Similar pictures can already be found in Ref. [29]. In Fig. 3.5 we also give the comparison to the $\mathcal{O}(p^4)$-HBχPT result of [54] for two angles: 59° and 155°. The data of Hallin et al. [6] (Fig. 3.6) provide important constraints for the fit above pion threshold. However, we must caution that close to 200 MeV there may already be a sizeable error in the SSE calculation due to our treatment of the $\Delta(1232)$, which behaves like a stable particle in the SSE. Its width is only included perturbatively and it is zero at leading-one-loop order. We are aware that such procedure violates unitarity. However, sufficiently far below the resonance we can expand in powers of ω/Δ_0, so that unitarity and the width are built up order by order in this expansion parameter. Nevertheless, violating unitarity may cause a non-negligible uncertainty for $\omega \approx 200$ MeV. The DR calculation is only shown up to 170 MeV in Fig. 3.6, which is the upper energy limit of the plots in [26].

All four theoretical curves in Fig. 3.5 describe the available data quite well in the forward direction. The upwards trend in the data above 130 MeV related to the opening of the πN channel is also present in all three frameworks. However, while the SSE and DR results are rather similar at all angles, the HBχPT curve deviates from the data significantly in the backward direction, starting from photon energies around 80 MeV. This observation holds for both the $\mathcal{O}(p^3)$ *and* the $\mathcal{O}(p^4)$ calculation. The detailed analysis of the dynamical polarizabilities in the next section will show that this different energy dependence is due to the lack of explicit $\Delta(1232)$-resonance degrees of freedom in HBχPT. Even a broad variation of the two $\mathcal{O}(p^4)$-HBχPT counter terms, such that $\bar{\alpha}_{E1} = 8\cdot 10^{-4}$ fm^3, $\bar{\beta}_{M1} = 6\cdot 10^{-4}$ fm^3, is not sufficient to properly account for the Δ resonance, cf. Ref. [54]. We find the well-known fact that cross-section calculations in leading-one-loop order χEFT discarding the Δ as explicit degree of freedom fail for large-angle scattering $\theta > 90°$, even at energies well below pion threshold. The reason is that the Δ resonance dominates in spin-flip $M1$ processes, which are primarily observed in back-angle scattering, see e.g. [59, 9, 50].

Having shown that the full Compton amplitudes $A_1, \ldots, A_6$ of leading-one-loop SSE provide a good description of the available Compton data up to energies above

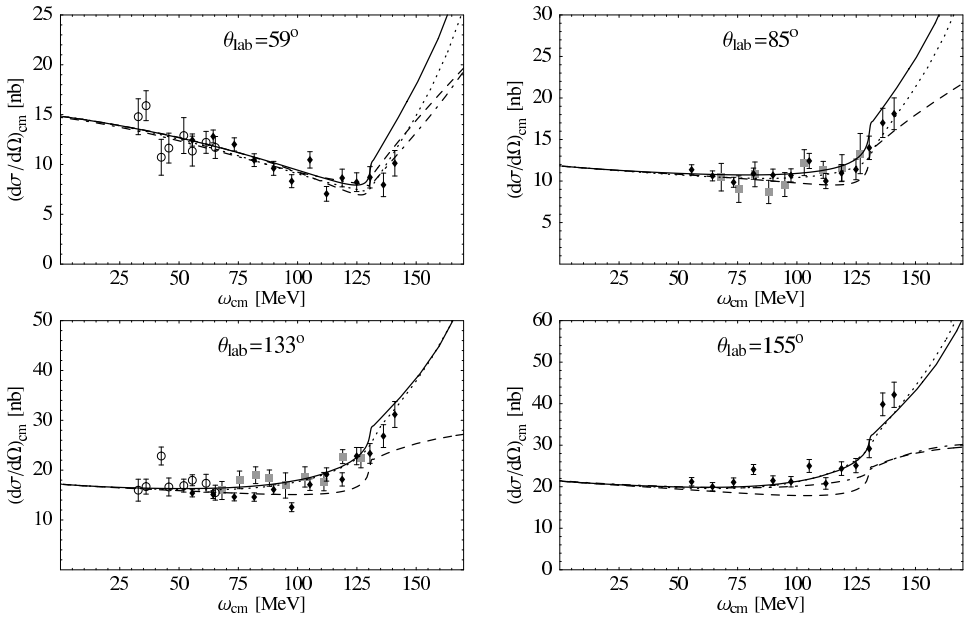

Figure 3.5: Comparison of the differential cross-section data for Compton scattering off the proton (diamonds: Olmos de Leon et al. [5], circles: Federspiel et al. [7], boxes: MacGibbon et al. [8]) with Dispersion Theory and leading-one-loop order HBχPT respectively SSE at fixed lab angle. At 59° and 155° we also compare to the $\mathcal{O}(p^4)$ HBχPT calculation of [54]. Solid line: SSE results; dashed line: $\mathcal{O}(p^3)$ HBχPT; dotted line: DR; dotdashed line: $\mathcal{O}(p^4)$ HBχPT. Note that the data of [7] are not given at 59° and 133° but at 60° and 135°; the data of [8] are not given at 85° and 133° but at 90° and 135°.

pion threshold, we now examine what kind of physics dominates in the kinematic regime considered here. A well-established procedure to answer this question is of course a systematic multipole expansion of the Compton amplitudes $A_i(\omega, z)$ as discussed in Section 3.1.1. In Fig. 3.7, we compare the contributions of the first three terms of the Compton multipole expansion to the same data as shown in Fig. 3.5. The $l = 0$ truncation only contains the pole contributions to nucleon Compton scattering as shown by the diagrams in Fig. 3.1, see also Appendix B. Truncating the multipole expansion at $l = 1$, the curve includes in addition all dynamical dipole polarizabilities. All dynamical quadrupole polarizabilities are contained in the $l = 2$ truncation. As has been known for a long time, a theoretical framework which only incorporates the pole contributions for nucleon Compton scattering gives a rather poor description of the cross sections, especially at small angles. The discrepancy between the $l = 0$ result and the data therefore is a clear indication of internal nucleon structure not contained in the standard pole terms. According to χEFT calculations, this structure can be interpreted as chiral dynamics in the nucleon: It is largely the contributions from the pions as the Goldstone Bosons of low-energy QCD (cf. Section 2.1) – or in other words the contribution from the pion cloud of the nucleon – which closes the gap between the pole contributions and the Compton data, at least for energies below the pion threshold. While this is after many years of χEFT calculations in nucleon Compton scattering a well-known fact, the surprising find from our multipole analysis is that up to energies of $\omega \approx 200$ MeV, *there is no visible difference* between the $l = 1$ and the $l = 2$ truncation. Therefore, the multipole expansion for the nucleon Compton cross section converges very fast in

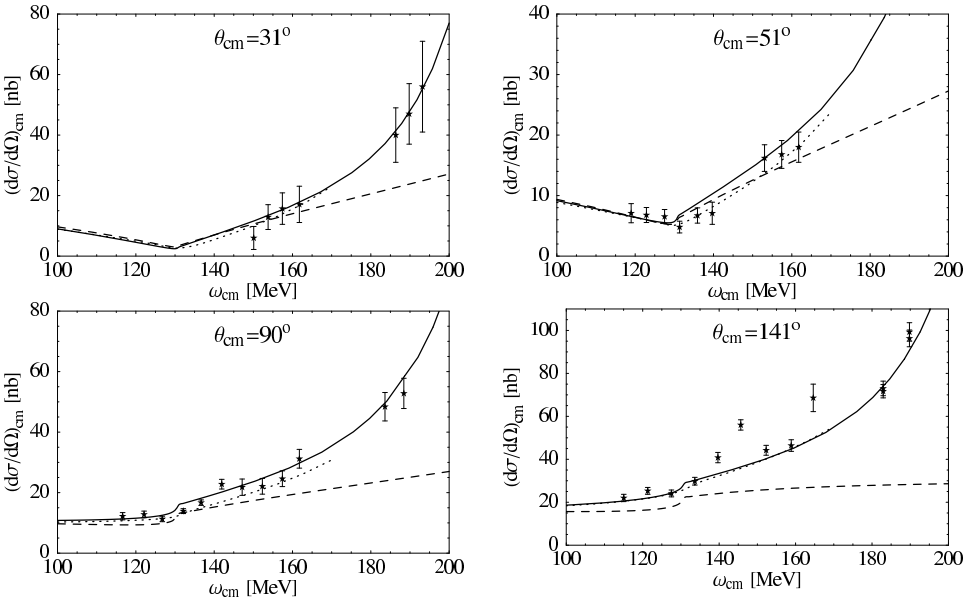

Figure 3.6: Comparison of the differential cross-section data for Compton scattering off the proton from Hallin et al. [6] with leading-one-loop order HBχPT respectively SSE and DR at fixed cm angle. Solid: SSE; dashed: HBχPT; dotted: DR.

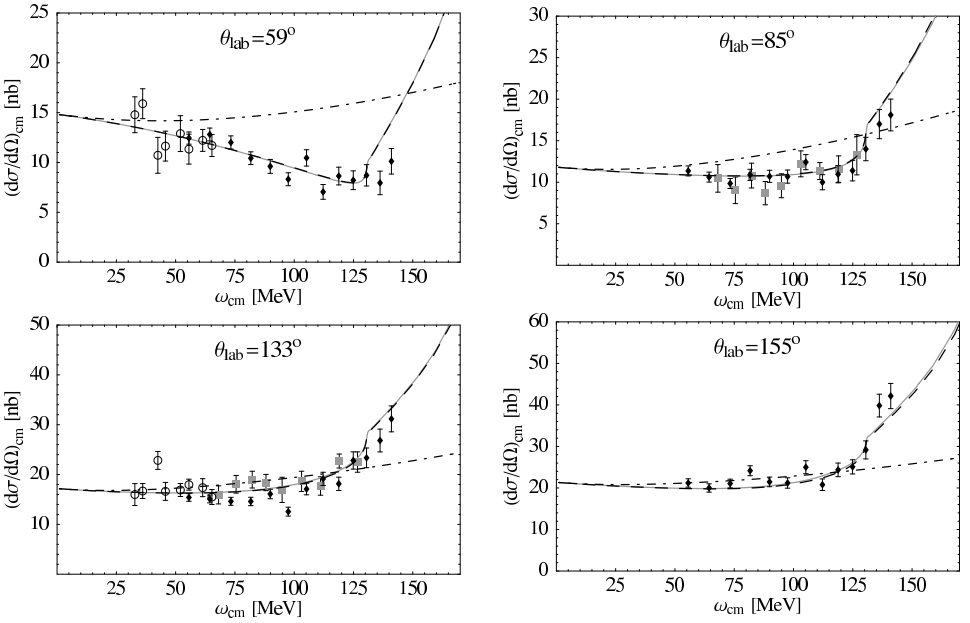

Figure 3.7: Comparison of the SSE multipole expansion to the differential cross-section data for Compton scattering off the proton. Note that the $l = 1$ and $l = 2$ truncations are indistinguishable in the energy region shown here. ($l = 0$ truncation: dash-dotted curve; $l = 1$ truncation: dashed curve; $l = 2$ truncation: solid grey curve)

the entire energy region considered. In Chapter 4, this suppression of higher-order

multipoles is also demonstrated in a variety of asymmetries in Compton scattering. Furthermore, we see that aside from the well-known standard pole terms of Fig. 3.1, all one needs to know for a good description of nucleon Compton scattering are the six dynamical dipole polarizabilities $\alpha_{E1}(\omega)$, $\beta_{M1}(\omega)$, $\gamma_{E1E1}(\omega)$, $\gamma_{M1M1}(\omega)$, $\gamma_{E1M2}(\omega)$ and $\gamma_{M1E2}(\omega)$ representing the complete $l = 1$ information. In Section 4.2 we present a proposal how to directly determine the spin-dependent polarizabilities γ_i from experiment, and in Section 4.3 we demonstrate their non-negligible contribution even to spin-averaged Compton cross sections. While χEFT calculations for nucleon Compton scattering in the past have either focused on the static values of the polarizabilities or on the (rather complicated) full Compton amplitudes, one can now dissect the role of chiral dynamics (and of explicit resonance contributions) in this process by looking at the individual multipole channels.

Before we move on to a detailed comparison of the results for these six dynamical polarizabilities derived in leading-one-loop order HBχPT, SSE and DR, respectively, we first give details regarding the three free parameters of SSE fitted to the Compton data.

3.4 Fit to Proton Compton Data and Static Polarizabilities

3.4.1 Small Scale Expansion Fit

The two energy-independent short-distance terms with couplings g_1 and g_2 of Eqs. (2.35, 2.36) give contributions only to the electric and magnetic dipole polarizabilities. The three free parameters of the leading-one-loop SSE analysis therefore correspond to a fit which determines $\bar{\alpha}_{E1}$, $\bar{\beta}_{M1}$ plus the leading $\gamma N\Delta$ coupling b_1, cf. Section 3.4.2. Note that we go beyond Ref. [29], where we only fitted the two polarizabilities. We are able to fit the two static spin-independent dipole polarizabilities because the fourth-order Lagrangeans Eqs. (2.35, 2.36) are promoted to leading-one-loop order. For the fit, we use the data from [5], which cover the low-energy region ($\omega \leq m_\pi$) very well with extremely small error bars, and those from [6], which is the only data set available in the energy regime $m_\pi \leq \omega \leq 200$ MeV. The results are displayed in Table 3.1, together with their corresponding $\chi^2/d.o.f.$-values, which we calculate using the standard definition of χ^2, i.e.

$$\chi^2 = \sum \left(\frac{\sigma_{\rm exp} - \sigma_{\rm theo}}{\Delta\sigma} \right)^2 \tag{3.19}$$

with $\sigma_{\rm exp}$ the experimental, $\sigma_{\rm theo}$ the calculated cross sections and $\Delta\sigma$ the experimental error bars. In a first step, the number of degrees of freedom ($d.o.f.$) is the number of data points (115) minus the number of free parameters (3). Note that the value of $\bar{\alpha}_{E1} + \bar{\beta}_{M1}$ from the three-parameter fit is consistent within error bars with the Baldin sum rule for the proton, $\bar{\alpha}_{E1} + \bar{\beta}_{M1} = (13.8 \pm 0.4) \cdot 10^{-4}$ fm^3 [5], cf. Section 1.1.[4] One can therefore in a second step use the value of the Baldin sum rule as additional fit constraint and thus reduce the number of free parameters to two. If not stated differently, we use these Baldin-sum-rule constrained values in all plots throughout this work. The resulting static spin-independent dipole polarizabilities, given in Table 3.1, compare very well with state-of-the-art Dispersion Analyses [50] and the values recommended in the recent review [10], cf. Eq. (1.7). Nevertheless, the $\chi^2/d.o.f.$-values of our fits are relatively large, but they are more an indication

[4] We note that an alternative extraction yielded $\bar{\alpha}_{E1} + \bar{\beta}_{M1} = (14.0 \pm 0.3) \cdot 10^{-4}$ fm^3 [22], which was combined with [5] to $(13.9 \pm 0.3) \cdot 10^{-4}$ fm^3 in Ref. [10]. The error bars of the value adopted in this work cover the whole range of this result.

of the spread in the Compton data, which we have not allowed to float with a free normalization constant. We note that at $\theta = 133^\circ$ our calculation yields values which are systematically larger than the data from [5], but agree very well with the data from [7, 8], cf. Fig. 3.5. The encouraging results of Table 3.1 therefore prove that by utilizing the SSE amplitudes of [26], one has an alternative technique to extract the static polarizabilities $\bar{\alpha}_{E1}$, $\bar{\beta}_{M1}$ from low-energy Compton data below the Δ-resonance. We note that a determination of $\bar{\alpha}_{E1}$, $\bar{\beta}_{M1}$ from Compton data using next-to-leading one-loop order HBχPT was presented in [25]. The results obtained there are comparable to ours, although the authors had to restrict their fit to the lower-energy data to exclude effects from the $\Delta(1232)$, due to the known inadequate description of the Compton cross sections in the backward direction in HBχPT, cf. Section 3.3.2.

The values we obtain in the two fits for the leading $\gamma N\Delta$ coupling b_1, cf. Table 3.1, agree with the previous analysis [56] from the radiative Δ-width as discussed in Section 3.2. Note that we could also employ the strategy to rely on the DR-results for $\bar{\alpha}_{E1}$, $\bar{\beta}_{M1}$ and $\bar{\gamma}_{M1M1}$ to determine the three unknowns. In this case, the whole energy-dependence is predicted. The values thus obtained are identical with the fit-results within the error bars, see [29].

As our leading-one-loop order SSE calculation only describes an isoscalar nucleon, we cannot contribute to the ongoing controversies over the size of the neutron polarizabilities [50, 25, 60] at this point. These quantities will be discussed in length in Chapters 5 and 6, where we fit the *isoscalar* polarizabilities, i.e. the average between proton and neutron, to elastic deuteron Compton data. From these values and the known proton numbers we are then able to deduce the elusive neutron polarizabilities.

Quantity	3-parameter fit	2-parameter fit	[5]
$\chi^2/d.o.f.$	2.87	2.83	1.14
$\bar{\alpha}_{E1}$	11.52 ± 2.43	11.04 ± 1.36	$12.4 \pm 0.6(\text{stat}) \mp 0.5(\text{syst}) \pm 0.1(\text{mod})$
$\bar{\beta}_{M1}$	3.42 ± 1.70	2.76 ∓ 1.36	$1.4 \pm 0.7(\text{stat}) \pm 0.4(\text{syst}) \pm 0.1(\text{mod})$
b_1	4.66 ± 0.14	4.67 ± 0.14	

Table 3.1: Values for $\bar{\alpha}_{E1}$, $\bar{\beta}_{M1}$ (in $10^{-4}\,\text{fm}^3$) and b_1 from a fit to MAMI- [5] and SAL-data [6], compared to the results from [5]. Note that the definition of $\chi^2/d.o.f.$ used in [5] is different from Eq. (3.19). The error bars in our fits are only statistical, i.e. the error ± 0.4 due to the Baldin sum rule in the 2-parameter fit and uncertainties from higher orders are not included.

3.4.2 Static Spin-Independent Polarizabilities

The spin-independent static dipole polarizabilities to leading-one-loop order in SSE consist of the following individual contributions:

$$\begin{aligned}
\bar{\alpha}_{E1} &= \frac{5\,\alpha\,g_A^2}{96\,f_\pi^2\,m_\pi\,\pi}\left(1-\frac{m_\pi}{m_N}\,\frac{1}{\pi}\right) - \frac{2\,\alpha\,(g_1+2g_2)}{(4\pi\,f_\pi)^2\,m_N} \\
&\quad + \frac{\alpha\,g_{\pi N\Delta_0}^2}{54\,(f_\pi\,\pi)^2}\left[\frac{9\,\Delta_0}{\Delta_0^2-m_\pi^2} + \frac{\Delta_0^2-10\,m_\pi^2}{(\Delta_0^2-m_\pi^2)^{3/2}}\,\ln R\right] \\
&= [11.87\,(N\pi) - (5.92 \pm 1.36)\,(\text{c.t.}) + 0.0\,(\Delta\text{-pole}) + 5.09\,(\Delta\pi)] \times 10^{-4}\ \text{fm}^3 \\
&= (11.04 \pm 1.36) \times 10^{-4}\ \text{fm}^3 \qquad (3.20)
\end{aligned}$$

$$\begin{aligned}\bar{\beta}_{M1} &= \frac{\alpha\, g_A^2}{192\, f_\pi^2\, m_\pi\, \pi} + \frac{4\,\alpha\, g_2}{(4\pi\, f_\pi)^2\, m_N} + \frac{2\,\alpha\, b_1^2}{9\,\Delta_0\, m_N^2} + \frac{\alpha\, g_{\pi N\Delta_0}^2}{54\,\left(f_\pi\,\pi\right)^2}\,\frac{1}{\sqrt{\Delta_0^2 - m_\pi^2}}\,\ln R \\ &= [1.25\,(N\pi) - (10.68 \pm 1.17)\,(\text{c.t.}) + (11.33 \pm 0.70)\,(\Delta\text{-pole}) \\ &\quad + 0.86\,(\Delta\pi)] \times 10^{-4}\ \text{fm}^3 = (2.76 \mp 1.36) \times 10^{-4}\ \text{fm}^3 \end{aligned} \tag{3.21}$$

where $R = \left(\Delta_0 + \sqrt{\Delta_0^2 - m_\pi^2}\right)/m_\pi$ is a dimensionless parameter [55] and the results from the Baldin-constrained fit have been used, cf. Table 3.1.

In the case of $\bar{\alpha}_{E1}$, one notices a strong cancellation between the $\pi\Delta$ contributions and the short-distance physics contained in g_1, g_2. In Section 3.5, we will demonstrate that this mutual cancellation holds throughout the low-energy region also in the case of the dynamical electric dipole polarizability, forcing us to the not surprising conclusion that for photon energies far below on-shell $\Delta\pi$ intermediate states such contributions are indistinguishable from counterterms parameterizing the short-distance physics. However, the physics content of the short-distance operators is not yet completely understood. Assuming that corrections from next-to-leading order are suppressed by m_π/m_N with respect to the leading-order result, comparing the leading-order pion-cloud contribution to $\bar{\alpha}_{E1}$ and $\delta\bar{\alpha}_{E1}^{sd}$ demonstrates that the "natural" size of g_1, g_2 is unity. Therefore, naïve dimensional analysis for next-to-leading order contributions to $\bar{\alpha}_{E1}$ and $\bar{\beta}_{M1}$ predicts that their size is

$$|\bar{\alpha}_{\text{NLO}}| \sim |\bar{\beta}_{\text{NLO}}| \sim \frac{\alpha}{\Lambda_\chi^2\, m_N} \sim 1 \cdot 10^{-4}\ \text{fm}^3 \tag{3.22}$$

with $\Lambda_\chi \sim 1$ GeV the breakdown scale of HBχPT, cf. Section 2.1, but apparently fails to give a correct estimate of their magnitudes. The numerical values of Eqs. (3.20, 3.21) tell us post factum that they must already be included in the analysis at leading order. We note that the extra, quark-mass-independent term in the πN contribution arises from our pion-threshold correction discussed in Section 3.2. This term does not appear in Ref. [29] due to the analogous correction of the u-channel applied there.

In $\bar{\beta}_{M1}$, we encounter the well-known cancellation between a large paramagnetism from the $\Delta(1232)$-pole contributions and the nucleon diamagnetism, arising from short-distance effects parameterized by the coupling g_2. Several proposals to explain this effect were put forward in the literature. One attributes it to an interplay between short-distance physics and the pion-cloud occurring from the next-to-leading order chiral Lagrangean [16], another one to the t-channel exchange of a meson or correlated two-pion exchange [61, 10]. An alternative explanation for the smallness of $\bar{\beta}_{M1}$ due to off-shell effects in the $\gamma N\Delta$-transition form factors has been presented in [62]. Whether either of these explanations gives a convincing quantitative description of the short-distance coefficients is not clear yet.

In contrast to the cancellation in $\bar{\alpha}_{E1}$ discussed above, the sum of dia- and paramagnetic effects is strongly energy dependent and therefore leads to a clear signal in the dynamical magnetic dipole polarizability $\beta_{M1}(\omega)$, see Section 3.5. Apart from the contribution proportional to g_2, Eq. (3.21) agrees with the result found in Ref. [55] (modulo the different convention for the coupling b_1), where it was already noted that the $\Delta\pi$ contributions to $\bar{\beta}_{M1}$ are considerably smaller than in the case of $\bar{\alpha}_{E1}$.

Already from this discussion, one can see that the two extra terms g_1, g_2 are not just small higher-order effects. For a consistent description both of the data and of the static polarizabilities, they are in contrast required in a leading-one-loop SSE analysis. Translating the fit results of Table 3.1 back into these two unknown couplings, one obtains

$$g_1 = 17.44 \pm 2.11\,(\text{stat}), \quad g_2 = -5.64 \pm 0.88\,(\text{stat}) \tag{3.23}$$

for the 3-parameter fit and

$$g_1 = 18.82 \pm 0.79\,(\text{stat}) \pm 0.4\,(\text{Baldin}), \quad g_2 = -6.05 \mp 0.66\,(\text{stat}) \pm 0.4\,(\text{Baldin}) \quad (3.24)$$

for the Baldin-constrained fit. Therefore, these two couplings are significantly larger than their "natural" values, which in the Lagrangean employed (Eqs. (2.35, 2.36)) would be expected to be unity. These couplings – though formally being part of the next-to-leading one-loop order Lagrangean – therefore break the naïve power counting underlying SSE and have to be taken into account already at leading-one-loop order. There are indications that this feature is not specific to SSE but occurs in all chiral calculations of $\alpha_{E1}(\omega)$ and $\beta_{M1}(\omega)$, if high-energy modes in the pion-loop graphs are to be properly accounted for, cf. [63]. Having determined g_1, g_2 from fits to Compton-scattering data, we now have fixed all our unknown parameters and have full predictive power in the determination of the energy dependence of the polarizabilities discussed in Section 3.5.

Finally, we note again that not only the energy dependence of the dynamical polarizabilities is independent of the two extra couplings g_1, g_2, but also the values of the four spin-dependent static dipole polarizabilities $\bar{\gamma}_{E1E1}$, $\bar{\gamma}_{M1M1}$, $\bar{\gamma}_{E1M2}$, $\bar{\gamma}_{M1E2}$. The results obtained in Ref. [56] are therefore reproduced[5], as expected. For better comparison with Dispersion Theory and experiment, we present in Table 3.2 the numbers for the linear combinations $\bar{\gamma}_0$, $\bar{\gamma}_\pi$ of Eq. (3.10). For more detail, we refer the interested reader to the extensive literature on these two elusive structures [50].

Quantity	SSE	experiment	DR	[10]
$\bar{\gamma}_0^p$	0.62 ∓ 0.25	$-1.01 \pm 0.08(\text{stat}) \pm 0.10(\text{syst})$	-0.7	—
$\bar{\gamma}_\pi^p$	8.86 ± 0.25	$10.6 \pm 2.1(\text{stat}) \mp 0.4(\text{syst}) \pm 0.8(\text{mod})$	9.3	8 ± 1.8
$\bar{\gamma}_0^n$	0.62 ∓ 0.25	—	-0.07	—
$\bar{\gamma}_\pi^n$	8.86 ± 0.25	—	13.7	11.9 ± 4.0

Table 3.2: Comparison of proton $\bar{\gamma}_0^p$, $\bar{\gamma}_\pi^p$ and neutron $\bar{\gamma}_0^n$, $\bar{\gamma}_\pi^n$ spin polarizabilities (in $10^{-4}\,\text{fm}^4$) between leading-one-loop SSE, experiment and fixed-t Hyperbolic Dispersion Theory [50]; the experimental values for $\bar{\gamma}_0^p$, $\bar{\gamma}_\pi^p$ are taken from [64] and [5], respectively. The last column corresponds to the averaged values recommended in Ref. [10]. Note that the $\mathcal{O}(\epsilon^3)$-SSE results are purely isoscalar.

The spin-independent static quadrupole polarizabilities $\bar{\alpha}_{E2}$, $\bar{\beta}_{M2}$ have been analyzed in Ref. [47] to leading-one-loop order in SSE. Here we present the details of our results for these $l = 2$ polarizabilities, as they include some additional features with respect to Refs. [47] and [29].

$$\begin{aligned}
\bar{\alpha}_{E2} &= \frac{\alpha\, g_A^2}{32\, f_\pi^2\, m_\pi^3\, \pi} \left(\frac{7}{5} + \frac{9}{10}\, \frac{m_\pi}{m_N}\, \frac{1}{\pi} \right) \\
&\quad + \frac{\alpha\, g_{\pi N \Delta_0}^2}{135\, (f_\pi\, \pi)^2\, m_\pi^2} \left[\frac{\Delta_0\, \left(11\, \Delta_0^2 - 41\, m_\pi^2 \right)}{\left(\Delta_0^2 - m_\pi^2 \right)^2} + \frac{3\, m_\pi^2\, \left(3\, \Delta_0^2 + 7\, m_\pi^2 \right)}{\left(\Delta_0^2 - m_\pi^2 \right)^{5/2}}\, \ln R \right] \\
&= \left[21.48\, (N\pi) + 0.0\, (\text{c.t.}) + 0.0\, (\Delta\text{-pole}) + 4.99\, (\Delta\pi) \right] \times 10^{-4}\ \text{fm}^5 \\
&= 26.47 \times 10^{-4}\ \text{fm}^5
\end{aligned} \quad (3.25)$$

[5]We note that in the case of $\bar{\gamma}_{E1E1}$ we obtain a small extra term $\delta\bar{\gamma}_{E1E1} = -\frac{\alpha g_A^2}{96 f_\pi^2 \pi m_N m_\pi}$ due to our correction of the pion threshold discussed in point 1 of Section 3.2. This term is part of the next-to-leading one-loop order contributions to this polarizability discussed in Ref. [53].

$$\begin{aligned}\bar{\beta}_{M2} &= -\frac{3\,\alpha\,g_A^2}{160\,f_\pi^2\,m_\pi^3\,\pi} - \frac{2\,\alpha\,b_1^2}{3\,\Delta_0^2\,m_N^3} + \frac{\alpha\,g_{\pi N\Delta_0}^2}{15\,(f_\pi\,\pi)^2\,m_\pi^2}\left[\frac{-\Delta_0}{\Delta_0^2-m_\pi^2} + \frac{m_\pi^2}{(\Delta_0^2-m_\pi^2)^{3/2}}\,\ln R\right] \\ &= [-8.93\,(N\pi) + 0.0\,(\text{c.t.}) - (5.18 \pm 0.32)\,(\Delta\text{-pole}) - 3.37\,(\Delta\pi)] \times 10^{-4}\ \text{fm}^5 \\ &= (-17.48 \pm 0.32) \times 10^{-4}\ \text{fm}^5 \end{aligned} \tag{3.26}$$

In particular we note the extra piece $\sim m_\pi^{-2}$ from the one-pion-threshold correction in $\bar{\alpha}_{E2}$, as well as the kinematically induced u-channel $\Delta(1232)$ contribution to $\bar{\beta}_{M2}$, which was not yet included in Ref. [29]. For details on the origin of these terms we refer to Section 3.2, items 1 and 2. Each of these effects seems to improve the agreement between SSE and Dispersion Theory, as we will see in the plots of the corresponding dynamical quadrupole polarizabilities, given in Section 3.5.1. However, as discussed in Section 3.3.2, we remind the reader that the $l = 2$ polarizabilities are in effect so small that they cannot be determined directly from state-of-the-art nucleon Compton-scattering experiments.

3.5 Chiral Dynamics and Dynamical Polarizabilities

Dynamical polarizabilities are a concept complementary to *generalized* polarizabilities of the nucleon [65, 66, 67]. The latter probe the nucleon in virtual Compton scattering, i.e. with an incoming photon of non-zero virtuality and an outgoing, soft real photon. Therefore, they provide information about the spatial distribution of charges and magnetism inside the nucleon at zero energy. Dynamical polarizabilities on the other hand test the global low-energy excitation spectrum of the nucleon at *non-zero* energy and answer the question, which internal degrees of freedom govern the structure of the nucleon at low energies.

In the following detailed discussion of the dynamical polarizabilities, the error bars for the input parameters as discussed in Section 3.3.2 induce uncertainties in the static and dynamical polarizabilities. The grey bands in the figures around the SSE curves arise from the (statistical) uncertainty in the fit parameters determined with the help of the Baldin sum rule in Section 3.4.1. Albeit only a full higher-order calculation will give a good estimate of the higher-order effects in EFT, this permits already a rough guess of their size, at least in $\alpha_{E1}^s(\omega)$ and $\beta_{M1}^s(\omega)$, given that the statistical uncertainties in Table 3.1 are at least as large as the corrections one expects from higher orders, cf. Eq. (3.22). Similar pictures of the dynamical polarizabilities have already been presented in [29], however without error bars.

3.5.1 Isoscalar Spin-Independent Polarizabilities

Turning first to $\alpha_{E1}^s(\omega)$ as shown in Fig. 3.8, it is obvious that its energy dependence in the low-energy region is entirely controlled by chiral dynamics arising from single-πN intermediate states. All three theoretical analyses agree rather well within the statistical uncertainty band of the SSE calculation. As already discussed for the static electric polarizability $\bar{\alpha}_{E1}$ in the previous section, no effects from any inherent $\pi\Delta$ intermediate states can be detected, pointing to the fact that these rather heavy degrees of freedom are effectively frozen out at low energies. This makes them – as far as the energy dependence of the dynamical polarizabilities is concerned – indistinguishable from short-distance contributions represented by the couplings g_1, g_2. We also note that the strength and shape of the cusp associated with the one-pion-production threshold is reproduced extremely well by the leading-one-loop chiral calculations. It will serve as an interesting check for the convergence properties of

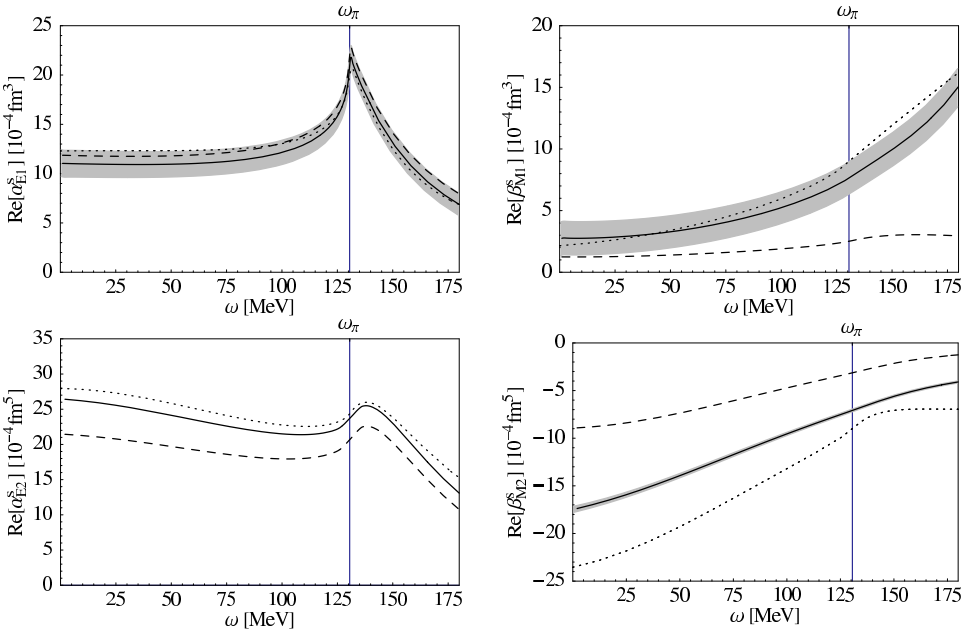

Figure 3.8: Comparison of the leading-one-loop order SSE (solid) and HBχPT (dashed) results for the real parts of the isoscalar, spin-independent dynamical electric and magnetic dipole (top) and quadrupole (bottom) polarizabilities with Dispersion Theory (dotted).

the chiral theories to see whether the rather good agreement is maintained, once the higher-order corrections are included.

The other spin-independent $l = 1$ dynamical polarizability, $\beta^s_{M1}(\omega)$, shows quite a different picture. We note that the three theoretical frameworks only agree (within the uncertainty of the SSE parameters) for the value of the static magnetic polarizability $\bar{\beta}_{M1}$. For increasing values of the photon energy, it becomes obvious from the agreement between SSE and Dispersion Theory that explicit $\Delta(1232)$ contributions via s-channel pole graphs lead to a paramagnetic behaviour quickly rising with energy. Any $\Delta\pi$ contributions remain small and are effectively frozen out. The near cancellation between para- and diamagnetic contributions for the static value discussed in the previous section is completely taken over by $\Delta(1232)$-induced paramagnetism when the photon energy goes up. We explicitly point to the scale on the y-axis of this plot, indicating a rise by a factor of four at photon energies near the one-pion-production threshold. While the leading-one-loop HBχPT calculation [15] provides a good prediction for $\bar{\beta}_{M1}$, it fails to describe the energy dependence of $\beta^s_{M1}(\omega)$, as shown in Fig. 3.8. In contrast to $\alpha^s_{E1}(\omega)$, hardly any cusp is visible in $\beta^s_{M1}(\omega)$. Beyond the static limit, the chiral πN contributions play a minor role in this polarizability. We note that while the fine details of the rising paramagnetism in $\beta^s_{M1}(\omega)$ differ between SSE and Dispersion Theory, they are consistent within the uncertainties of the SSE curve. The discrepancy between the two schemes above the one-pion-production threshold is likely to be connected to a detailed treatment of the width of the Δ resonance, which is neglected in leading-one-loop SSE.

We further note that the good agreement between SSE and Dispersion Theory for the $l = 1$ spin-independent dynamical polarizabilities provides a non-trivial check regarding the physics parameterized in the couplings g_1, g_2. Given that these two structures are energy independent, cf. Eqs. (2.35, 2.36), the fact that only

the πN and Δ degrees of freedom suffice to describe the energy dependence in the low-energy region quite well supports our idea that the physics underlying g_1, g_2 is "short-distance" from the point of view of χEFTs.

It is also interesting to look at the spin-independent $l = 2$ dynamical polarizabilities, even if in actual analyses of Compton data they only play a minor role. In $\alpha^s_{E2}(\omega)$ we observe a visible contribution from $\Delta\pi$ intermediate states. It hardly modifies the shape of the energy dependence, but does affect the overall normalization of this polarizability, as can be seen from the difference between the SSE and the HBχPT curve. The agreement between SSE and Dispersion Theory is surprisingly good throughout the entire low-energy region. Another interesting higher-order dynamical polarizability is $\beta^s_{M2}(\omega)$. The chiral πN contribution seems to play only a minor role in the energy dependence of this polarizability. $\Delta\pi$ and a surprisingly large $\Delta(1232)$ u-channel pole contribution can close a significant part of the gap between the HBχPT and the Dispersion Theory result. The remaining gap between SSE and Dispersion Theory might well be accounted for by next-to-leading one-loop chiral πN corrections, given that the slope of the energy dependence below pion threshold seems to agree between the two frameworks. Nevertheless, the energy dependence of this polarizability is quite peculiar. The magnetic quadrupole strength has decreased rather fast by more than a factor of two when the photon energy reaches the one-pion-production threshold. This shape is reminiscent of a relaxation effect typically discussed in textbook examples for dispersive effects [46]. While both in HBχPT and SSE the strengths for $\beta_{M2}(\omega)$ tend to zero for large photon energies, the DR-curve seems to point to additional physics contributions above the pion threshold.

We now move on to a discussion of the $l = 1$ spin-dependent dynamical polarizabilities.

3.5.2 Isoscalar Spin-Dependent Polarizabilities

We again remind the reader that no fit parameters analogously to g_1 and g_2 are present in the leading-one-loop SSE results for the spin-dependent polarizabilities. The only free parameter entering the dynamical spin polarizabilities is b_1, which we have determined from the fit to Compton cross sections in Section 3.4.1; however, it influences only $\gamma^s_{M1M1}(\omega)$. As Fig. 3.9 demonstrates, the contributions of the $\Delta\pi$ continuum to the spin polarizabilities are small throughout the low-energy region. The energy dependence in $\gamma^s_{E1E1}(\omega)$ is completely governed by chiral dynamics and agrees well among the three frameworks, quite analogously to the situation in $\alpha^s_{E1}(\omega)$. The $\Delta(1232)$-pole contribution – rising with energy – is visible in $\gamma^s_{M1M1}(\omega)$, but it does not rise as dramatically as in the case of $\beta^s_{M1}(\omega)$ (cf. Fig. 3.8). The HBχPT calculation for $\gamma^s_{M1M1}(\omega)$ deviates strongly from both the SSE and DR result, signaling again the need for explicit $\Delta(1232)$ degrees of freedom in resonant multipoles. The slight disagreement between SSE and DR for photon energies above pion threshold in $\gamma^s_{M1M1}(\omega)$ might be connected to a detailed treatment of the width of the Δ resonance, which is not included in leading-one-loop SSE, see Refs. [29, 26][6]. Both HBχPT and SSE predictions for the mixed spin polarizabilities are rather similar, disagreeing with the DR result. While $\gamma^s_{E1M2}(\omega)$ constitutes a rather tiny structure effect which will be hard to pin down precisely, the "large" gap between SSE and the DR result in $\gamma^s_{M1E2}(\omega)$ could possibly arise from the missing $E2$ excitation of the Δ resonance in a leading-one-loop SSE calculation. This effect can be accounted for at next-to-leading one-loop order. On the other hand, the overall shape of the energy dependence in $\gamma^s_{M1E2}(\omega)$ is rather sim-

[6] We do not include a chapter on polarizabilities in the resonance region in this work, as we did not investigate this issue further than reported in Ref. [29].

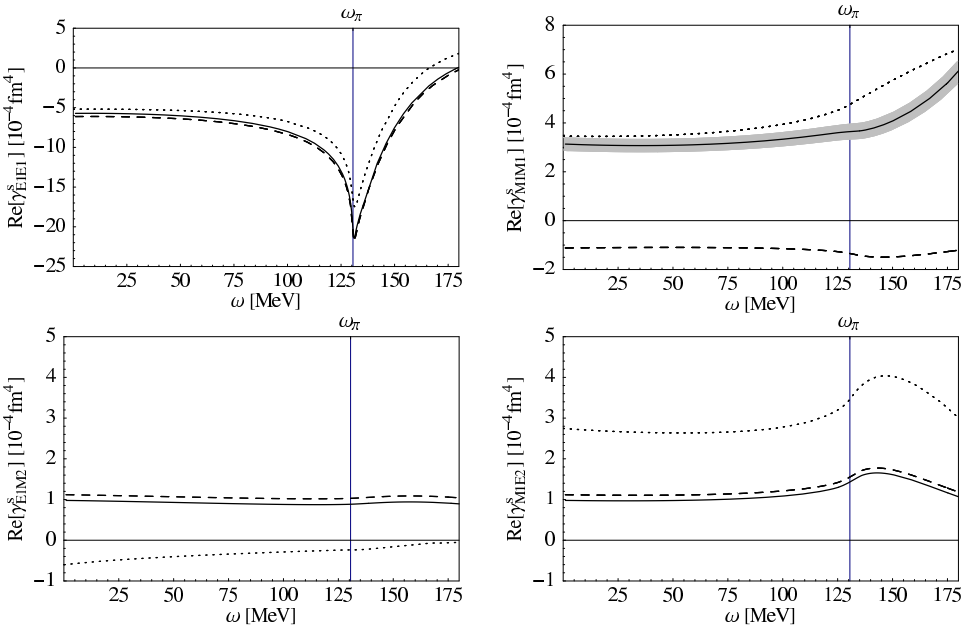

Figure 3.9: Comparison of the leading-one-loop order SSE (solid) and HBχPT (dashed) results for the real parts of the isoscalar, spin-dependent dynamical dipole polarizabilities with Dispersion Theory (dotted).

ilar between the chiral and the DR results, indicating that a πN loop contribution at the next-higher chiral order might also suffice to close the gap.

In conclusion, among the four isoscalar spin-dependent dipole polarizabilities, only $\gamma^s_{E1E1}(\omega)$ seems to be dominated by πN chiral dynamics, which can be accounted for rather well already at leading-one-loop order throughout the low-energy region. A detailed understanding of the dynamical spin dipole polarizabilities requires explicit $\Delta(1232)$-resonance degrees of freedom.

We now close our discussion of the nucleon polarizabilities, which will, however, show up several times in this work, as polarizability is one of the fundamental properties of the nucleon when tested by an external electromagnetic field. In the next chapter we turn to polarized nucleon Compton cross sections and present our predictions for various asymmetries. The aim of this investigation is to demonstrate the possibility to extract spin polarizabilities from Compton experiments. In this context, we will have another look at spin-averaged Compton cross sections, as these observables may also give important constraints on the spin-dependent polarizabilities.

Chapter 4

Polarized Nucleon Compton Scattering

In Chapter 3, we showed results for unpolarized proton Compton cross sections, which are derived by averaging over the initial and summing over the final spin states. Now, we concentrate on spin-polarized cross sections for proton and neutron, albeit we will briefly return to spin-averaged ones in Section 4.3. These investigations aim to demonstrate that determining spin polarizabilities directly from experiment is possible. They serve as a guideline for forthcoming experiments on spin-polarized Compton cross sections.

4.1 Asymmetries – Formalism

In this section we define the various quantities under investigation. These are asymmetries with the incoming photon polarized circularly, Section 4.1.1, and linearly, Section 4.1.2. Our predictions for the asymmetries using circularly polarized photons are published in Ref. [27].

4.1.1 Asymmetries with Circularly Polarized Photons

Triggered by a forthcoming proposal on polarized Compton scattering off ^{3}He at the HIγS lab of TUNL [20], we choose the incoming photon to be right-circularly polarized,

$$\vec{\epsilon} = \frac{1}{\sqrt{2}} \begin{pmatrix} 1 \\ i \\ 0 \end{pmatrix} \tag{4.1}$$

and to move along the positive z-direction, while the final polarization and nucleon spin remain undetected. The two nucleon spin configurations we investigate are

1) the difference between the target-nucleon spin pointing parallel or antiparallel to the incident photon momentum

$$\frac{d\sigma_{\uparrow\Uparrow}}{d\Omega_{\rm cm}} - \frac{d\sigma_{\downarrow\Uparrow}}{d\Omega_{\rm cm}}; \tag{4.2}$$

2) the difference between the target-nucleon spin aligned in positive or negative x-direction:

$$\frac{d\sigma_{\rightarrow\Uparrow}}{d\Omega_{\rm cm}} - \frac{d\sigma_{\leftarrow\Uparrow}}{d\Omega_{\rm cm}}. \tag{4.3}$$

The first arrow in our notation denotes the direction of the nucleon spin, the second one the direction of the incoming, right-circularly polarized photon. Both configurations are sketched in Fig. 4.1.

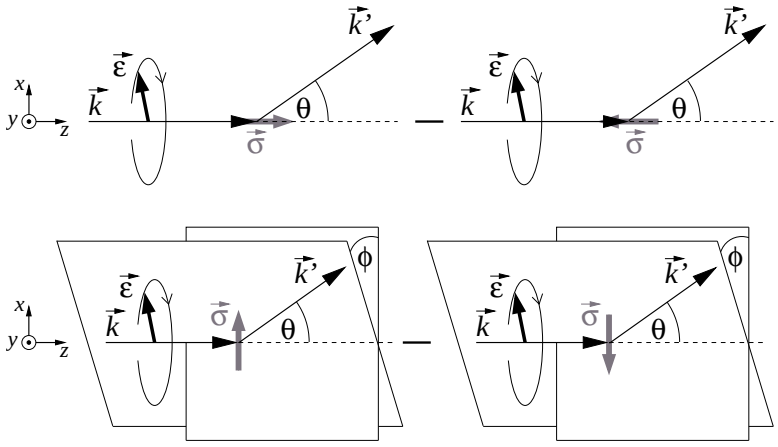

Figure 4.1: The two configurations investigated using circularly polarized photons; the nucleon spin is aligned parallel (upper panel) and perpendicular (lower panel) to the direction of the photon momentum.

The corresponding formulae for $|T|^2$ have already been derived in [35], albeit there they are given only for real amplitudes $A_1 - A_6$. However, these amplitudes become complex for photon energies above the pion-production threshold ω_π, cf. Section 3.1.2. Including the imaginary part of the amplitudes, the formulae read

$$\begin{aligned}\frac{1}{2}\left(|T|^2_{\uparrow\Uparrow} - |T|^2_{\downarrow\Uparrow}\right) = &-\mathrm{Re}[A_1\, A_3^*]\,(1+\cos^2\theta) - \Big[|A_3|^2 + 2\,|A_6|^2 + 2\,|A_5|^2\,\cos^2\theta \\ &+ \mathrm{Re}[A_6\,(A_1^* + 3\,A_3^*)] + \Big(\mathrm{Re}[A_3\,(3\,A_5^* + A_4^* - A_2^*)] + \mathrm{Re}[A_5\,(4\,A_6^* - A_1^*)]\Big)\cos\theta \\ &+ \mathrm{Re}[A_5\,(A_2^* - A_4^*)]\,\sin^2\theta\Big]\,\sin^2\theta \end{aligned} \tag{4.4}$$

and

$$\begin{aligned}\frac{1}{2}\left(|T|^2_{\rightarrow\Uparrow} - |T|^2_{\leftarrow\Uparrow}\right) = &\Big[\mathrm{Im}[A_1\,(A_3^* + 2\,A_6^* + 2\,A_5^*\,\cos\theta)]\,\cos\theta + \mathrm{Im}[A_1\,A_4^*]\,(1+\cos^2\theta) \\ &- \mathrm{Im}[A_2\,(A_3^* + 2\,A_6^*)]\,\sin^2\theta - \mathrm{Im}[A_2\,(A_4^* + 2\,A_5^*)]\,\cos\theta\,\sin^2\theta\Big]\sin\theta\,\sin\phi \\ &+ \Big[\mathrm{Re}[A_3\,(A_3^* - A_1^* + 2\,A_6^*)]\,\cos\theta + \mathrm{Re}[A_3\,A_5^*]\,(3\,\cos^2\theta - 1) \\ &+ \Big(\mathrm{Re}[A_1\,A_5^*] + \mathrm{Re}[A_2\,A_3^*] + \mathrm{Re}[A_6\,(A_2^* + A_4^* - 2\,A_5^*)]\Big)\,\sin^2\theta \\ &+ \mathrm{Re}[A_3\,A_4^*]\,(\cos^2\theta + 1) + \mathrm{Re}[A_5\,(A_2^* - A_4^* - 2\,A_5^*)]\,\cos\theta\,\sin^2\theta\Big]\sin\theta\,\cos\phi. \end{aligned} \tag{4.5}$$

Here, ϕ is the angle between the reaction plane and the plane spanned by the momentum of the incoming photon and the target-nucleon spin, cf. Fig. 4.1. Obviously, the difference Eq. (4.5) takes on the largest values – at least below the pion-production threshold – for $\phi = 0$. Therefore, we choose the nucleon spin in

the reaction plane, which simplifies Eq. (4.5) considerably. Using left- instead of right-circularly polarized photons changes the overall sign in Eqs. (4.4) and (4.5). The spin-averaged cross section can be derived by taking the sum instead of the difference in Eq. (4.4) (or as well in Eq. (4.5)). The corresponding $|T|^2$ is given in Eq. (3.18).

The asymmetries we consider[1] are

$$\Sigma_z^{\mathrm{circ}} = \frac{|T|^2_{\uparrow\Uparrow} - |T|^2_{\downarrow\Uparrow}}{|T|^2_{\uparrow\Uparrow} + |T|^2_{\downarrow\Uparrow}}, \tag{4.6}$$

$$\Sigma_x^{\mathrm{circ}} = \frac{|T|^2_{\rightarrow\Uparrow} - |T|^2_{\leftarrow\Uparrow}}{|T|^2_{\rightarrow\Uparrow} + |T|^2_{\leftarrow\Uparrow}}. \tag{4.7}$$

Σ is a frame-independent quantity, as the frame-dependent flux factor cancels in the ratio between difference and sum of the cross section, while $|T|^2$ can be written in terms of the frame-independent Mandelstam variables.

From the experimentalist's point of view, it is more convenient to measure the *asymmetry* – i.e. the difference divided by the sum – instead of the differences Eqs. (4.4) and (4.5), as the former is more tolerant to systematic errors in experiments. However, division by a small quantity, say a small spin-averaged cross section, may enhance theoretical uncertainties. Sensitivity on the nucleon structure, e.g. the spin polarizabilities, may be lost by dividing the difference by the sum. Whenever this happens in Sections 4.4 and 4.5, we will give hints in the text, but we refrain from showing our results for the differences (4.4, 4.5) for reasons of compactification, as it is questionable whether one can compare with experimental data for absolute values of polarized Compton cross sections within the next few years.

4.1.2 Asymmetries with Linearly Polarized Photons

Besides the asymmetries with circularly polarized photons in the initial state, defined in Eqs. (4.6, 4.7), we also investigate asymmetries with linearly polarized photons. Again there are two configurations to be considered. The only difference between these asymmetries is the direction of the nucleon spin, which is aligned in the positive z- or x-direction, respectively. In both cases we define ϕ as the angle between the plane perpendicular to the y-direction and the reaction plane. Our calculation shows that for fixed angle ϕ it is necessary to change the photon polarization between the two measurements, in order to obtain a non-vanishing asymmetry below the pion-production threshold. The two asymmetries read

$$\Sigma_z^{\mathrm{lin}} = \frac{|T|^2_{\uparrow\rightarrow} - |T|^2_{\uparrow\odot}}{|T|^2_{\uparrow\rightarrow} + |T|^2_{\uparrow\odot}}, \tag{4.8}$$

$$\Sigma_x^{\mathrm{lin}} = \frac{|T|^2_{\rightarrow\rightarrow} - |T|^2_{\rightarrow\odot}}{|T|^2_{\rightarrow\rightarrow} + |T|^2_{\rightarrow\odot}}. \tag{4.9}$$

Again the first arrow corresponds to the direction of the nucleon spin, whereas here the second one denotes the photon polarization, with the positive y-axis symbolised by $\odot$. Obviously, Σ_x^{lin} is equivalent to having the nucleon spin aligned in the positive y-direction – both cases emerge from each other under the rotation $\phi \rightarrow \phi + 90^\circ$. The two kinematical systems are illustrated in Fig. 4.2.

[1] Σ_z^{circ} corresponds to Σ_{2z} in the notation of [4], Σ_x^{circ} to Σ_{2x}.

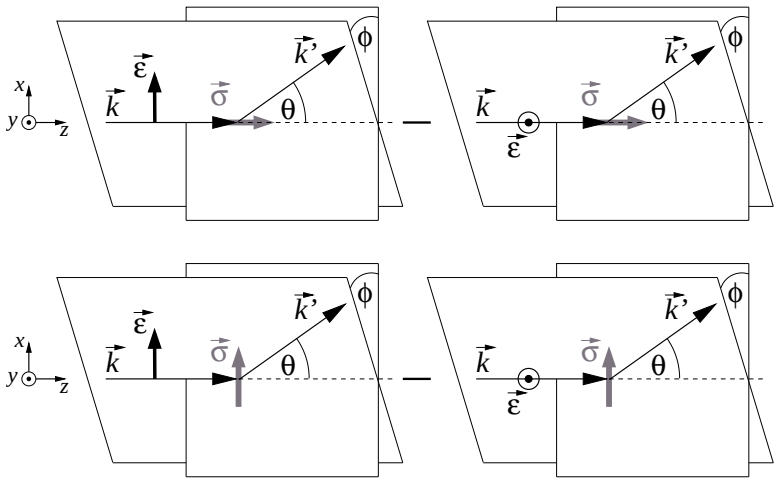

Figure 4.2: The two configurations investigated using linearly polarized photons; the nucleon spin is aligned parallel (upper panel) and perpendicular (lower panel) to the direction of the photon momentum. Note that in both systems the photon polarization is flipped between the two measurements.

The numerators of Eqs. (4.8) and (4.9) are

$$\begin{aligned}\frac{1}{2}\left(|T|^2_{\uparrow\rightarrow} - |T|^2_{\uparrow\odot}\right) = \frac{1}{2}\Bigg\{\Bigg[&\mathrm{Re}[A_3\,(A_3^* + 4\,A_6^*)] - |A_1|^2 + 4\,|A_6|^2 \\ &+ 2\,\left(\mathrm{Re}[A_3\,A_4^*] - \mathrm{Re}[A_1\,A_2^*] + 2\,\mathrm{Re}[A_3\,A_5^*] + 2\,\mathrm{Re}[(A_4 + 2\,A_5)\,A_6^*]\right)\cos\theta \\ &+ 4\,\mathrm{Re}[(A_4 + A_5)\,A_5^*]\,\cos^2\theta + \left(|A_2|^2 - |A_4|^2\right)\sin^2\theta\Bigg]\left(2\,\cos^2\phi - 1\right) \\ &+ 4\Bigg[\mathrm{Im}[(A_1 + A_3)\,A_6^*] + \mathrm{Im}[A_1\,A_3^*] + (\mathrm{Im}[A_1\,A_5^*] + \mathrm{Im}[A_2\,A_3^*] + \mathrm{Im}[A_3\,(A_4^* + A_5^*)] \\ &-2\,\mathrm{Im}[A_4\,A_6^*])\,\cos\theta - \mathrm{Im}[A_2\,A_5^*]\,\sin^2\theta - \mathrm{Im}[A_4\,A_5^*]\,(\cos^2\theta + 1)\Bigg]\sin\phi\,\cos\phi\Bigg\}\sin^2\theta\end{aligned} \tag{4.10}$$

and

$$\begin{aligned}\frac{1}{2}\left(|T|^2_{\rightarrow\rightarrow} - |T|^2_{\rightarrow\odot}\right) = \frac{1}{2}\Bigg\{\Bigg[&\mathrm{Re}[A_3\,(A_3^* + 4\,A_6^*)] - |A_1|^2 + 4\,|A_6|^2 \\ &+ 2\,\left(\mathrm{Re}[A_3\,A_4^*] - \mathrm{Re}[A_1\,A_2^*] + 2\,\mathrm{Re}[A_3\,A_5^*] + 2\,\mathrm{Re}[(A_4 + 2\,A_5)\,A_6^*]\right)\cos\theta \\ &+ 4\,\mathrm{Re}[(A_4 + A_5)\,A_5^*]\,\cos^2\theta + \left(|A_2|^2 - |A_4|^2\right)\sin^2\theta\Bigg]\left(2\,\cos^2\phi - 1\right)\,\sin\theta \\ &+ \Bigg[2\Bigg(\left(\mathrm{Im}[A_2\,A_3^*] + 2\,\mathrm{Im}[A_5\,A_6^*] + \mathrm{Im}[A_1\,A_4^*]\,(1 - 2\,\cos^2\phi) + 2\,(\mathrm{Im}[A_3\,A_4^*]\right. \\ &\left.-\mathrm{Im}[A_4\,A_6^*])\,\cos^2\phi + 2\,\mathrm{Im}[A_2\,A_6^*]\,\sin^2\phi\right)\sin^2\theta - 2\,\mathrm{Im}[A_1\,A_5^*]\,(\cos^2\theta + \cos^2\phi\,\sin^2\theta) \\ &- 2\,\mathrm{Im}[A_3\,A_5^*]\,(1 - \cos^2\phi\,\sin^2\theta)\Bigg) + 2\Bigg(\left(\mathrm{Im}[A_2\,A_4^*]\,(1 - 2\,\cos^2\phi) - 2\,\mathrm{Im}[A_4\,A_5^*]\,\cos^2\phi\right. \\ &\left.+2\,\mathrm{Im}[A_2\,A_5^*]\,\sin^2\phi\right)\sin^2\theta - \mathrm{Im}[A_1\,A_3^*] - 2\,\mathrm{Im}[(A_1 + A_3)\,A_6^*]\Bigg)\cos\theta\Bigg]\sin\phi\Bigg\}\sin\theta.\end{aligned} \tag{4.11}$$

In the first configuration the sum gives the spin-averaged cross section, however in

the latter this is not the case. Here an additional term arises above threshold:

$$\begin{aligned}\frac{1}{2}\left(|T|^2_{\rightarrow\rightarrow}+|T|^2_{\rightarrow\odot}\right) &= \frac{1}{2}\left(|T|^2_{\uparrow\Uparrow}+|T|^2_{\downarrow\Uparrow}\right)\\ &+\Big[\mathrm{Im}[A_1\,(A_3^*+2\,A_6^*)]\,\cos\theta+\mathrm{Im}[A_1\,A_4^*]\,(1+\cos^2\theta)+2\,\mathrm{Im}[A_1\,A_5^*]\,\cos^2\theta\\ &-\left(\mathrm{Im}[A_2\,(A_3^*+2\,A_6^*)]+\mathrm{Im}[A_2\,(A_4^*+2\,A_5^*)]\,\cos\theta\right)\sin^2\theta\Big]\,\sin\phi\,\sin\theta\end{aligned} \tag{4.12}$$

Comparing Eqs. (4.10) and (4.11), we find that the real parts of the various products of amplitudes contributing to the two differences are identical. Therefore there is no difference between the two configurations below the pion-production threshold. Furthermore the factor $(2\,\cos^2\phi-1)$ is largest for $\phi=0$. For this choice of ϕ, however, the real parts are the only contributions in both cases. Therefore we set $\phi\equiv 0$ and only investigate one asymmetry with linearly polarized photons in Sections 4.4 and 4.5, denoted by Σ^{lin}.

Another interesting observation in Eqs. (4.10, 4.11) is the fact that there exist no interference terms in the real parts between spin-independent ($A_1,\ A_2$) and spin-dependent (A_3-A_6) amplitudes. We are interested in the structure of the nucleon, especially in its spin structure. Therefore, we suspect that in the proton case this configuration is less suited than the other two, where such effects are amplified by interference with the strong proton pole amplitudes A_1^{pole} and A_2^{pole}, cf. Appendix B.

4.2 Extracting Spin Polarizabilities from Experiment

One of our aims in this chapter is to prove the possibility of a direct determination of dynamical spin polarizabilities from experiment. We start from our findings for the spin-independent dipole polarizabilities $\alpha_{E1}(\omega)$ and $\beta_{M1}(\omega)$, which show very good agreement with Dispersion-Relation Analysis up to about 170 MeV, cf. Fig. 3.8. Truncating the multipole decomposition at $l=1$, this leaves no unknowns in A_1 and A_2. As higher polarizabilities are negligible (cf. Sects. 4.3-4.5), the spin-dependent dipole polarizabilities could then be fitted to data sets which combine polarized and spin-averaged experimental results, taken at a fixed energy and varying the scattering angle. As starting values for the fit one may use our χEFT results (see Fig. 3.9), as indicated in Eq. (4.13), where we show the structure amplitudes up to $l=1$ with the spin polarizabilities $\gamma_i(\omega)$ replaced by $\gamma_i(\omega)+\delta_i$, introducing the fit parameters δ_i. The expansion (4.13) has been derived using Eqs. (3.2, 3.4, 3.6) and (3.8). Small fit parameters mean correct prediction of the dynamical spin-dipole

polarizabilities within the Small Scale Expansion.

$$\begin{aligned}
\bar{A}_1(\omega,z) &= \frac{4\pi W}{M}\,\left[\alpha_{E1}(\omega) + z\,\beta_{M1}(\omega)\right]\,\omega^2 \\
\bar{A}_2(\omega,z) &= -\frac{4\pi W}{M}\,\beta_{M1}(\omega)\,\omega^2 \\
\bar{A}_3^{\text{fit}}(\omega,z) &= -\frac{4\pi W}{M}\,[(\gamma_{E1E1}(\omega)+\delta_{E1E1}) + z\,(\gamma_{M1M1}(\omega)+\delta_{M1M1}) \\
&\quad + (\gamma_{E1M2}(\omega)+\delta_{E1M2}) + z\,(\gamma_{M1E2}(\omega)+\delta_{M1E2})]\,\omega^3 \\
\bar{A}_4^{\text{fit}}(\omega,z) &= \frac{4\pi W}{M}\,\left[-(\gamma_{M1M1}(\omega)+\delta_{M1M1}) + (\gamma_{M1E2}(\omega)+\delta_{M1E2})\right]\,\omega^3 \\
\bar{A}_5^{\text{fit}}(\omega,z) &= \frac{4\pi W}{M}\,(\gamma_{M1M1}(\omega)+\delta_{M1M1})\,\omega^3 \\
\bar{A}_6^{\text{fit}}(\omega,z) &= \frac{4\pi W}{M}\,(\gamma_{E1M2}(\omega)+\delta_{E1M2})\,\omega^3
\end{aligned} \tag{4.13}$$

Thus, one obtains the spin-dipole polarizabilities at a definite energy. Repeating this procedure for various energies gives the energy dependence, i.e. the dynamics of the $l = 1$ spin polarizabilities. Therefore, the amplitudes Eq. (4.13) provide one possible way to extract dynamical spin polarizabilities directly from the asymmetry observables of the previous section, using χEFT. Note that the δ_i may show a weak energy dependence. At first trial, they can be taken as energy-independent quantities. This corresponds to a free normalization of the spin-dipole polarizabilities, assuming the energy dependence derived from χEFT to be correct. This assumption is well justified, as at low energies only $\Delta(1232)$ and pion degrees of freedom are supposed to give dispersive contributions to the polarizabilities, and usually the pion-cloud dispersion is well captured in Chiral Perturbation Theory.

For certain scattering angles, the theoretical error due to the dynamical spin-independent dipole polarizabilities $\alpha_{E1}(\omega)$ and $\beta_{M1}(\omega)$ is even further reduced. In order to prove this claim we rewrite the effective Hamiltonian up to dipole order,

$$\begin{aligned}
H_{\text{eff}} = -2\pi\,\Big[&\alpha_{E1}(\omega)\,\vec{E}^2 + \beta_{M1}(\omega)\,\vec{B}^2 + \gamma_{E1E1}(\omega)\,\vec{\sigma}\cdot\vec{E}\times\dot{\vec{E}} \\
&+ \gamma_{M1M1}(\omega)\,\vec{\sigma}\cdot\vec{B}\times\dot{\vec{B}} - 2\,\gamma_{M1E2}(\omega)\,\sigma_i\,E_{ij}\,B_j + 2\,\gamma_{E1M2}(\omega)\,\sigma_i\,B_{ij}\,E_j\Big]
\end{aligned} \tag{4.14}$$

with $T_{ij} = \frac{1}{2}(\partial_i T_j + \partial_j T_i)$, cf. Section 1.1. Obviously, when the polarizations of the incoming and the outgoing photon are perpendicular to each other, i.e. $\vec{\epsilon}\perp\vec{\epsilon}\,'$, the scalar product $\vec{E}^2 \propto \vec{\epsilon}\cdot\vec{\epsilon}\,'$ vanishes and therefore $\alpha_{E1}(\omega)$ cannot contribute. This scenario is depicted in the left panel of Fig. 4.3, where the incoming photon is polarized along the x-direction and the outgoing photon is detected under this very direction, i.e. under the scattering angles $\theta = \frac{\pi}{2}$, $\phi = 0$. In the right panel, the incoming photon is polarized along the y-direction, and therefore the magnetic fields of initial and final photon are perpendicular to each other. In this case $\beta_{M1}(\omega)$ gives no contribution. One might expect that there exist similar exclusion principles for the spin polarizabilities $\gamma_{E1E1}(\omega)$ and $\gamma_{M1M1}(\omega)$, when the nucleon spin is aligned along a well-defined direction in the initial state. However, this would only be the case, if we would calculate asymmetries with polarized nucleons also in the final state. Nevertheless, for $\theta = \frac{\pi}{2}$, $\phi = 0$ and the initial nucleon polarized parallel to the x-direction, one spin polarizability vanishes, namely $\gamma_{M1E2}(\omega)$ for the incoming photon polarized parallel to the nucleon spin, $\gamma_{E1M2}(\omega)$ for $\vec{\epsilon}\parallel\vec{e}_y$. Unfortunately, these mixed spin polarizabilities are highly non-intuitive. Therefore we cannot give a heuristic explanation for this behaviour.

In the next section we confirm our claim that determining spin polarizabilities from experiment is possible by demonstrating that also spin-averaged Compton cross sections may contribute to this demanding task.

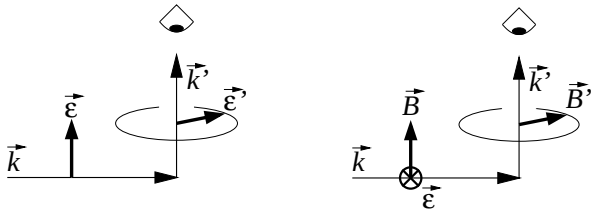

Figure 4.3: Two experimental configurations with linearly polarized photons, which exclude contributions from $\alpha_{E1}(\omega)$ (left panel) and $\beta_{M1}(\omega)$ (right panel).

4.3 Spin Contributions to Spin-Averaged Cross Sections

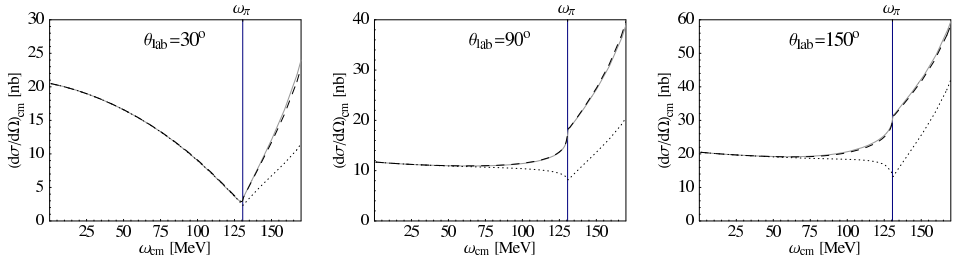

Figure 4.4: Complete $\mathcal{O}(\epsilon^3)$-SSE predictions (grey) for the spin-averaged proton cross section; dotted: spin polarizabilities not included, dashed: quadrupole polarizabilities not included.

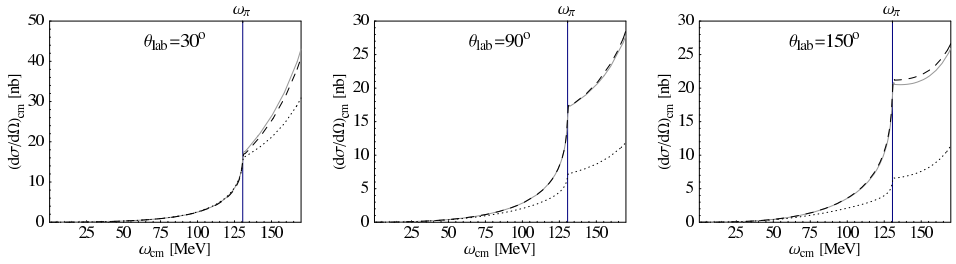

Figure 4.5: Spin-averaged neutron cross section; for notation see Fig. 4.4.

Before discussing the asymmetries in detail, we briefly turn to the question which polarizabilities are seen in unpolarized Compton cross sections. To this end we have another look at the $\mathcal{O}(\epsilon^3)$ SSE results already discussed in Section 3.3, but here we focus on the influence of the spin polarizabilities. As shown in Fig. 4.4, we find a large contribution of the dynamical spin polarizabilities to spin-averaged proton Compton cross sections above $\omega \sim 100$ MeV. We also show our results for the neutron (Fig. 4.5), exhibiting a huge sensitivity on the spin polarizabilities in the backward direction. This can be well understood, as the right hand side of Eq. (3.18) simplifies to $|A_1|^2 + |A_3|^2$ for $\theta = 0^\circ$ and $\theta = 180^\circ$. In the forward direction, the spin-independent amplitude $|A_1|^2$ dominates, in the backward direction the spin-dependent amplitude $|A_3|^2$, as can be seen in Appendix A of Ref. [27].

Recall that we found in Section 3.3 that any effects of quadrupole polarizabilities are invisible at the level of the unpolarized proton cross sections. According to Fig. 4.5, the same observation holds for the neutron. It suffices therefore to terminate the multipole expansion at the dipole level, which leaves the six dipole polarizabilities at given energy ω as parameters.

While effects from the spin polarizabilities are non-negligible in unpolarized experiments, to extract all four of them from such data is clearly impossible. Thus, double-polarized experiments as discussed in the rest of this chapter are necessary additional ingredients in a combined multipole analysis. Nevertheless, spin-averaged Compton data may give valuable constraints on such fits. As proof of principle, we show in Fig. 4.6 results from fitting the dynamical spin polarizabilities $\gamma_{E1E1}(\omega)$ and $\gamma_{M1M1}(\omega)$ to data from [5, 6, 7, 8] at fixed energy and varying angle. Note that here we extend the data base with respect to our global proton fits of Section 3.4.1, as we try to increase the number of data points per energy value as far as possible. The results are compared to the prediction from the Dispersion-Relation Analysis of [26]. However, these fits are rather unstable, as the sensitivity to $\gamma_{E1E1}(\omega)$ and $\gamma_{M1M1}(\omega)$ does not suffice to compensate for the spread in the data, cf. right panel of Fig. 4.6, which are oriented around a straight line, whereas the cross section is actually of cosine shape. In order to improve the convergence by minimizing the uncertainty in the fit amplitudes, we therefore use the multipoles from DR [26] for their construction, rather than the SSE amplitudes. Thus, Fig. 4.6 is not supposed to be considered quantitatively, but we believe to have established that spin-averaged Compton cross sections do help to pin down the dynamical spin polarizabilities.

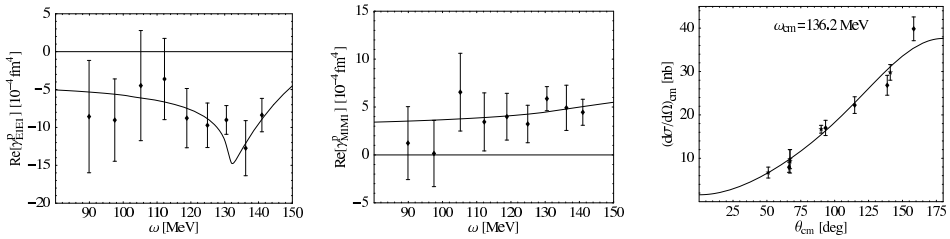

Figure 4.6: Fits of the dynamical spin polarizabilities $\gamma_{E1E1}(\omega)$ and $\gamma_{M1M1}(\omega)$ to experimental proton Compton data from [5, 6, 7, 8] at fixed energy and varying angle. The solid line in the left two panels is the prediction from the Dispersion-Relation Analysis of [26]. The right panel shows one example for the fitting procedure – for the experimental data cf. Figs. 3.5 and 3.6.

4.4 Proton Asymmetries

4.4.1 Proton Asymmetries from Circularly Polarized Photons

We turn now to the results for the asymmetries of the proton, using circularly polarized photons in the initial state. Analogously to the previous section, we confirm for each observable that the quadrupole polarizabilities are negligible. Thus, the multipole expansion of the amplitude can always be truncated at the dipole level, leaving at most six parameters. However, it will turn out that not all asymmetries are equally sensitive to the spin polarizabilities. As expected, most asymmetries are indeed governed by the pole part of the amplitudes.

In order to determine which asymmetries are most sensitive to the structure

parts of the Compton amplitudes, and which of the internal low-energy degrees of freedom in the nucleon dominate the structure-dependent part of the cross section, we will first compare three scenarios for each asymmetry: (i) the result when only the pole terms of the amplitudes are kept; (ii) the same when the effects from the pion cloud around the nucleon are added, as described by the leading-one-loop order HBχPT result; and finally (iii) a leading-one-loop order calculation in SSE, including also the $\Delta(1232)$ as dynamical degree of freedom.

An ideal asymmetry should thus fulfill three criteria: It should be large to give a good experimental signal, it should show sensitivity on the structure amplitudes, and it should allow a differentiation between the pion cloud and Δ resonance contributions in resonant channels, revealing as much as possible about the role of at least these low-energy degrees of freedom in the nucleon. In Section 4.5, we will repeat this presentation for the neutron asymmetries. To simplify connection to experiment, we give the scattering angle in the following plots in the lab frame.

Similar plots for the nucleon asymmetries are already shown in [4], using Dispersion Theory techniques. Direct comparison to those plots is however not possible, as in [4] the asymmetries are plotted against $\omega_{\rm lab}$ and because of a different choice of angles – the authors of [4] concentrated on the extreme angles 0°, 90°, 180°, whereas we show our results for 30°, 90° and 150°, as the extreme forward and backward direction is nearly impossible to access experimentally.[2] Nevertheless, qualitative agreement between our χEFT results and [4] can be deduced.

We emphasize also that our predictions are parameter free, as all constants are determined from unpolarized Compton scattering, see Section 3.4.1. In the following, the fit parameters δ_i introduced in Eq. (4.13) are all set to zero, as no measured asymmetries exist at this point.

Proton Spin Parallel to Photon Momentum

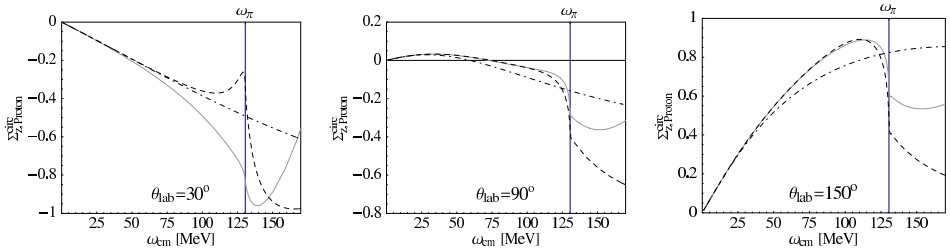

Figure 4.7: $\mathcal{O}(p^3)$-HBχPT (dashed) and $\mathcal{O}(\epsilon^3)$-SSE predictions (grey) for the proton asymmetry $\Sigma^{\rm circ}_{z,p}$; the dotdashed line describes the third-order pole contributions.

As one can see in Fig. 4.7, the proton asymmetry $\Sigma^{\rm circ}_{z,p}$ reaches values of $\mathcal{O}(1)$ and is therefore quite large, although for $\omega = 0$ it vanishes independently of the scattering angle, due to the vanishing difference and the finite static spin-averaged cross section, given by the familiar Thomson limit.

Comparing the three curves in Fig. 4.7 – third-order pole, $\mathcal{O}(p^3)$-HBχPT and $\mathcal{O}(\epsilon^3)$-SSE – one recognizes the strong influence of the pole amplitudes, given by Eq. (B.1). This is exactly what one expects for the charged proton, and can also be deduced from Eqs. (4.4, 4.13, B.1): The asymmetry starts linearly in ω, while the leading term of the structure part of $\Sigma^{\rm circ}_{z,p}$ is proportional to ω^3, as there is no term in Eq. (4.4) that contains only spin-independent amplitudes. As we are interested

[2] Note that for reasons of compactification we reduce the number of angles with respect to Ref. [27], where we present our results for 70° and 110° instead of 90°.

in information about the structure of the nucleon, i.e. in the deviation of the dashed and grey lines from the dotdashed (pole contributions only) line in Fig. 4.7, and as this deviation is not as strong as later in $\Sigma^{\rm circ}_{x,p}$ and in the neutron asymmetries, $\Sigma^{\rm circ}_{z,p}$ does not seem to be an ideal choice.

Sizeable contributions from the explicit Δ degrees of freedom exist only above ω_π. The only exception is noticed in the extreme forward direction, but this is an artifact of the asymmetry, which is extremely sensitive at small angles due to the small spin-averaged cross section at ω_π (Fig. 4.4), and neither visible in the difference, described by Eq. (4.4), nor in the spin-averaged cross section.

At ω_π, the cusp at the pion-production threshold is clearly visible for all angles. Polarized cross sections are much more sensitive on the fine structure of the nucleon than their unpolarized pendants. Therefore, our results might considerably deviate from experiment above threshold, as there are sizeable uncertainties in our imaginary parts, due to the vanishing Δ width in our leading-one-loop order SSE calculation, cf. [29]. Nevertheless, qualitative agreement should be fulfilled, so we use the same plot range as for the unpolarized results in Section 3.3, with a maximum photon energy of 170 MeV. In [4], the plots end below threshold since the Dispersion-Relation Analysis is compared to a low-energy expansion of the polarizabilities, which cannot reproduce signatures like the steep rise in $\alpha_{E1}(\omega)$, connected with the non-analyticity of the pion-production threshold, see Fig. 3.8.

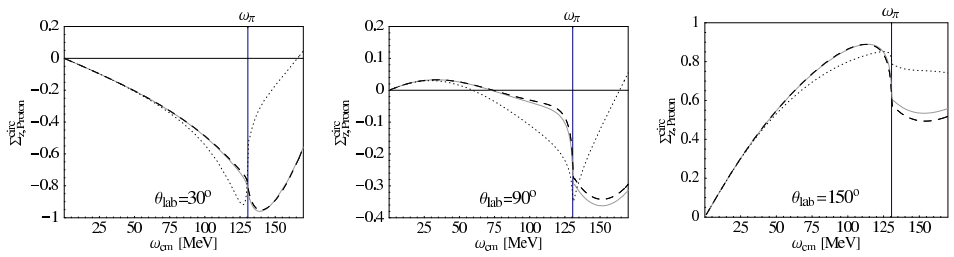

Figure 4.8: Dependence of the proton asymmetry $\Sigma^{\rm circ}_{z,p}$ on spin and quadrupole polarizabilities; for notation see Fig. 4.4.

The asymmetry $\Sigma^{\rm circ}_{z,p}$ exhibits only a weak dependence on the spin polarizabilities in the forward direction below ω_π (Fig. 4.8). The largest sensitivity is noted around 90°, whereas in the extreme backward direction the dependence on the spin polarizabilities partly cancels in the division of the difference by the sum. The sharp rise of the result without spin polarizabilities in Fig. 4.8 above the pion-production threshold in the forward direction is due to a sharply rising difference and the small spin-averaged cross section which enters the denominator presented in Fig. 4.4.

In the literature, e.g. in [68], the pion pole (Fig. B.1(d)) is often considered as one of the structure diagrams, giving the dominant contribution to the static backward spin polarizability $\bar{\gamma}_\pi$. We treat the term as pole, as it contains a pion pole in the t-channel and we assume that its contribution to nucleon Compton scattering is well understood. So the question arises why we are sensitive to the spin polarizabilities, despite of having removed this supposedly dominant part from them. The reason is that the pion pole dominates over the structure part of $\gamma_\pi(\omega)$ only for low energies. The pion-pole contribution to $\gamma_\pi(\omega)$ looks like a Lorentzian (Eq. (B.1)) and becomes smaller than the structure contribution above 100 MeV, as the latter rises due to the increasing values of $\gamma_{E1E1}(\omega)$ and $\gamma_{M1M1}(\omega)$, cf. Section 3.5.

It is crucial to notice that the quadrupole polarizabilities ($l = 2$) play again a negligibly small role, see Fig. 4.8. The most important quadrupole contribution is observed at 90° and 150° above threshold, but the relative size is still < 0.1 and

therefore presumably within the experimental error bars. As repeatedly stated, that these contributions are small is mandatory if one wants to determine spin polarizabilities via polarized cross section data, because only then can the multipole expansion be truncated at $l = 1$ as in Eq. (4.13).

Proton Spin Perpendicular to Photon Momentum

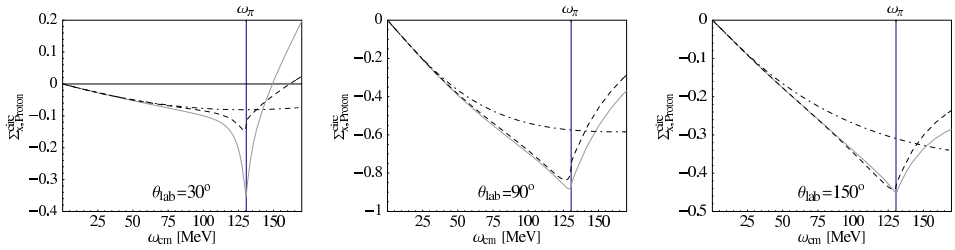

Figure 4.9: Dependence of the proton asymmetry $\Sigma^{\rm circ}_{x,p}$ on pion and Δ physics; for notation see Fig. 4.7.

The asymmetry $\Sigma^{\rm circ}_{x,p}$ in Fig. 4.9 looks quite similar for the different angles: It always starts with a falling slope and exhibits a sharp minimum at the pion cusp, therefore staying negative in a wide energy range.

Even more striking than for $\Sigma^{\rm circ}_{z,p}$ is the weak sensitivity of the asymmetry $\Sigma^{\rm circ}_{x,p}$ on explicit Δ degrees of freedom. Once again, the only exception to this rule is the extreme forward direction around ω_π because of the small spin-averaged cross section which enhances the small deviations between the HBχPT and the SSE calculation of the difference Eq. (4.5) and makes $\Sigma^{\rm circ}_{x,p}$ extremely sensitive to theoretical uncertainties. Therefore, we consider the forward angle regime as inconvenient for measuring proton asymmetries. In the other panels of Fig. 4.9, the Δ dependence cancels in the asymmetry, whereas we found the $\Delta(1232)$ resonance to give sizeable contributions to both the difference and the sum. This is demonstrated for $\theta_{\rm lab} = 150°$ in Fig. 4.10, where we show the difference $\mathcal{D}^{\rm circ}_{x,p}$, corresponding to Eq. (4.5), the spin-averaged cross section and the resulting asymmetry. This is one example that an asymmetry actually hides interesting physical information.

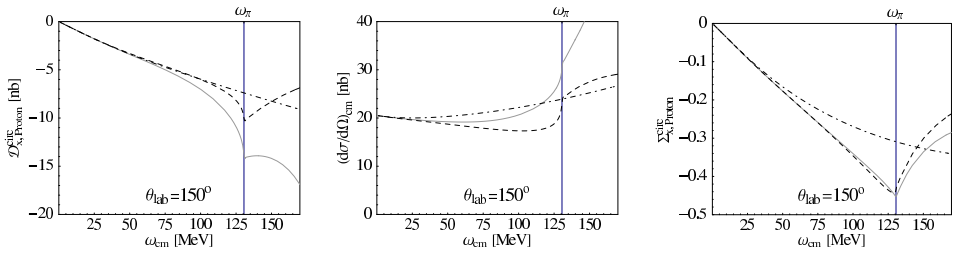

Figure 4.10: Cancellation of contributions from the Δ resonance to the asymmetry $\Sigma^{\rm circ}_{x,p}$ (right) in the division of the difference (left) by the spin-averaged cross section (middle); for notation see Fig. 4.7.

The dominance of the pole amplitudes is – as in $\Sigma^{\rm circ}_{z,p}$ – clearly visible. The argument is the same as before. Nonetheless, we find a stronger dependence of $\Sigma^{\rm circ}_{x,p}$ on the nucleon structure than for $\Sigma^{\rm circ}_{z,p}$, especially around ω_π.

As one can see in Fig. 4.11, $\Sigma^{\rm circ}_{x,p}$ is very sensitive to the spin polarizabilities for all angles. Therefore – and because of our findings in the previous subsection –

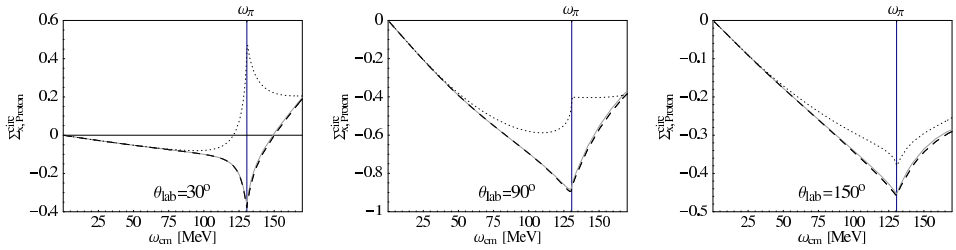

Figure 4.11: Dependence of the proton asymmetry $\Sigma_{x,p}^{\mathrm{circ}}$ on spin and quadrupole polarizabilities; for notation see Fig. 4.4.

choosing the proton spin perpendicular to the photon momentum seems to be more convenient than parallel to examine the spin structure of the proton. In the backward direction, the spin dependence of the asymmetry is less pronounced than in the forward direction.

The quadrupole contributions are extremely small.

4.4.2 Proton Asymmetries from Linearly Polarized Photons

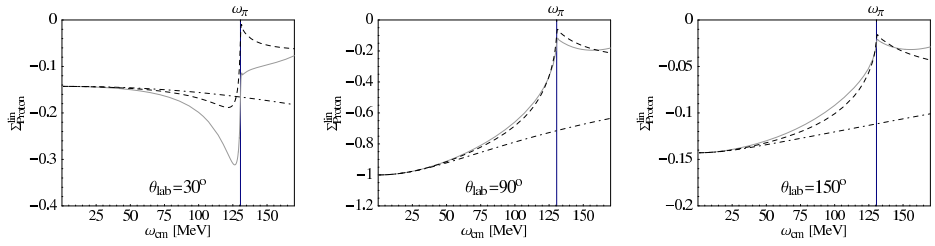

Figure 4.12: Dependence of the proton asymmetry Σ_p^{lin} on pion and Δ physics; for notation see Fig. 4.7.

The most striking difference between Fig. 4.12 and the asymmetries using circularly polarized incoming photons is the fact that the proton asymmetry Σ_p^{lin} is non-vanishing even for zero photon energy. The reason is the term $|A_1|^2$ in Eq. (4.10), which in leading order does not depend on the photon energy. The resulting formula for Σ_p^{lin} in the static limit is

$$\Sigma_p^{\mathrm{lin}}(\omega,\theta) = -\frac{\sin^2\theta}{1+\cos^2\theta}, \tag{4.15}$$

which can be derived from Eqs. (3.18, 4.4, B.1). A strong dependence on Δ physics is only observed in the forward direction, which is, however, a most delicate region with respect to theoretical errors, as already discussed.

A similar picture arises for the spin-polarizability dependence, Fig. 4.13. Except for the energy region above threshold in the extreme forward direction, these degrees of freedom are not as dominant as they are in Fig. 4.11. In the forward direction, however, we observe a relatively strong influence of the quadrupole polarizabilities. As these quantities were nearly invisible so far, this confirms our hypothesis that the forward direction is not the ideal choice to determine spin polarizabilities from asymmetries. Another disadvantage of Σ_p^{lin} is the small size of this asymmetry, except for $\theta \approx 90°$, due to the overall factor $\sin^2\theta$ in Eq. (4.10).

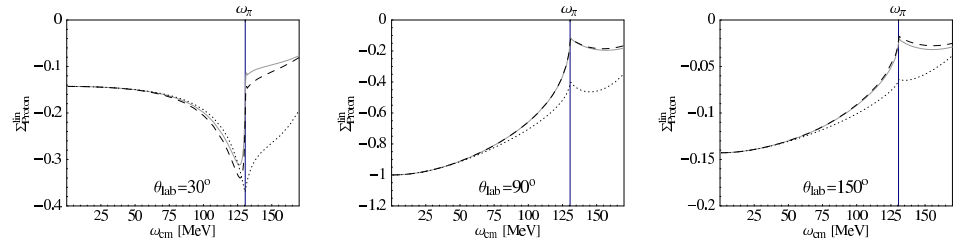

Figure 4.13: Dependence of the proton asymmetry $\Sigma_p^{\rm lin}$ on spin and quadrupole polarizabilities; for notation see Fig. 4.4.

As a short résumé of the proton asymmetries, we consider the second configuration, i.e. $\Sigma_{x,p}^{\rm circ}$, as the best choice to determine spin polarizabilities from experiments. The reasons are the clear signal of the spin polarizabilities and the nearly invisible contributions of multipole order $l > 1$. However, we have to caution that due to the very small spin-averaged proton cross section around ω_π, there may be considerable theoretical errors in our calculation in the forward direction. Therefore we consider experiments performed above 60° most promising, see also Ref. [27] for a different set of angles.

4.5 Neutron Asymmetries

4.5.1 Neutron Asymmetries from Circularly Polarized Photons

In the absence of stable single-neutron targets, the following results for the neutron have to be corrected for binding and meson-exchange effects inside light nuclei – analogously to our spin-averaged deuteron Compton calculation, described in Chapters 5 and 6. Here, we present the neutron results to guide considerations on future experiments using polarized deuterium or ^{3}He [20].

As in the proton case, the neutron asymmetries reach quite large values of $\mathcal{O}(1)$ as the photon energy increases. In the neutron, pole contributions might be expected to be small, because it is uncharged and thus only the pion pole and the anomalous magnetic moment contribute. On the other hand, spin polarizabilities are then not enhanced by interference with large pole amplitudes. Therefore, whether and which neutron asymmetries are sensitive to the structure parts, and hence to the spin polarizabilities, must be investigated carefully.

We follow the same line of presentation as outlined at the beginning of Section 4.4 for the proton asymmetries: First, we investigate which internal degrees of freedom are seen in a specific asymmetry, and then show that quadrupole polarizabilities give negligible contributions. Thus, the asymmetries most sensitive to spin polarizabilities are identified. Note that we may use the SSE parameters – $\bar{\alpha}_{E1}$, $\bar{\beta}_{M1}$ and b_1 – which we derived from proton cross sections in Section 3.4.1, because non-relativistic Chiral Perturbation Theory predicts that the proton and neutron polarizabilities are equal at leading-one-loop order [15].

Neutron Spin Parallel to Photon Momentum

Comparing Fig. 4.14 to the proton analogs, Figs. 4.7 and 4.9, we notice that the neutron is much more sensitive to the structure amplitudes. The pole curves show only a weak energy dependence, so that nearly the whole dynamics is given by the neutron polarizabilities. This minor influence of the pole amplitudes is due to the

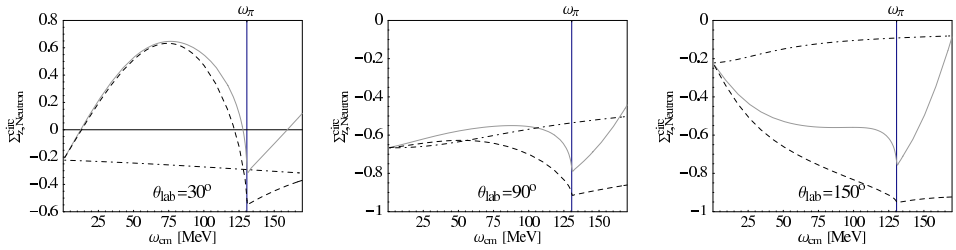

Figure 4.14: Dependence of the neutron asymmetry $\Sigma^{\rm circ}_{z,n}$ on pion and Δ physics; for notation see Fig. 4.7.

vanishing third-order pole contributions to A_1 and A_2, which make the difference Eq. (4.4) start with a term proportional to ω^2, whereas the leading structure part is $\mathcal{O}(\omega^3)$. The lowest order in ω of the spin-averaged cross section is ω^2, rendering finite static values of $\Sigma^{\rm circ}_{z,n}$. The angular dependence of this static value can be derived from Eqs. (3.18, 4.4, B.1) as

$$\Sigma^{\rm circ}_{z,n}(\omega = 0, \theta) = \frac{4\,\sin^2\theta}{-5 + \cos(2\,\theta)}. \tag{4.16}$$

The structure dependence of the neutron is also visible in the huge sensitivity of $\Sigma^{\rm circ}_{z,n}$ to the Δ resonance, which influences the polarized cross sections considerably even for very low energies. As is well known, the influence of the $\Delta(1232)$ increases with increasing angle.

Concerning the shape of the asymmetry, one recognizes a similar behaviour for the whole angular spectrum. It always reaches a local minimum at the pion cusp. A precise interpretation of the shape of $\Sigma^{\rm circ}_{z,n}$ is hard to give, as the denominator has the leading power ω^2, while it was ω^0 in the proton case.

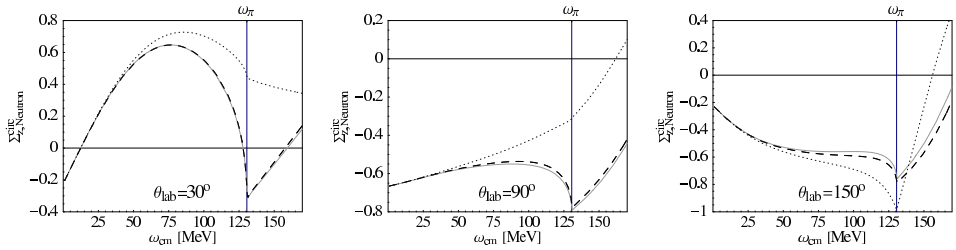

Figure 4.15: Dependence of the neutron asymmetry $\Sigma^{\rm circ}_{z,n}$ on spin and quadrupole polarizabilities; for notation see Fig. 4.4.

Fig. 4.15 exhibits that there are sizeable spin contributions to the asymmetry $\Sigma^{\rm circ}_{z,n}$ for each angle. Nevertheless, one recognizes a decreasing spin dependence with increasing angle.

As in the proton case we find the quadrupole part to be negligibly small within the accuracy of this analysis (Fig. 4.15).

Neutron Spin Perpendicular to Photon Momentum

The shape of the asymmetry $\Sigma^{\rm circ}_{x,n}$ in Fig. 4.16 with the minimum at ω_π is similar to $\Sigma^{\rm circ}_{z,n}$ (Fig. 4.14), especially in the forward direction. The curve is shifted downward with increasing angle θ. The angular dependence of the static value is determined

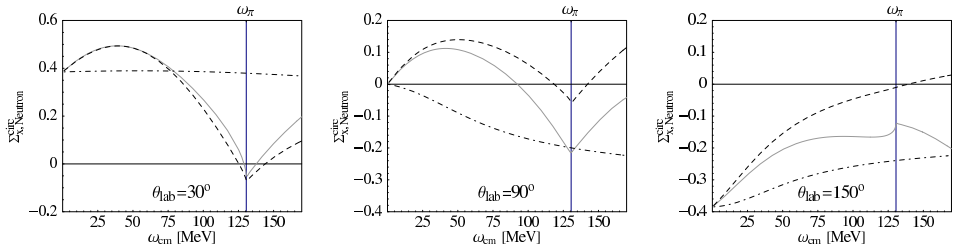

Figure 4.16: Dependence of the neutron asymmetry $\Sigma^{\rm circ}_{x,n}$ on pion and Δ physics; for notation see Fig. 4.7.

by the pole contributions. It is

$$\Sigma^{\rm circ}_{x,n}(\omega = 0, \theta) = \frac{4 \sin\theta \cos\theta}{5 - \cos(2\,\theta)}, \tag{4.17}$$

but as for $\Sigma^{\rm circ}_{z,n}$, the dynamics of $\Sigma^{\rm circ}_{x,n}$ is completely dominated by the neutron polarizabilities.

Another interesting feature in Fig. 4.16 is the fact, that the explicit Δ degrees of freedom only play a minor role in the forward direction but dominate for large angles.

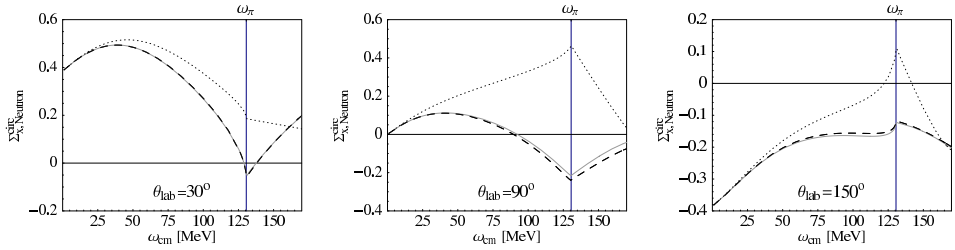

Figure 4.17: Dependence of the neutron asymmetry $\Sigma^{\rm circ}_{x,n}$ on spin and quadrupole polarizabilities; for notation see Fig. 4.4.

Turning to Fig. 4.17, $\Sigma^{\rm circ}_{x,n}$ exhibits of all asymmmetries by far the largest sensitivity to the spin polarizabilities. Therefore, and due to our observations for the proton asymmetries, an experiment with the nucleon spin aligned perpendicularly to the photon momentum seems from the theorist's point of view to be the most promising of the considered configurations to extract the spin polarizabilities.

As in $\Sigma^{\rm circ}_{z,n}$, the quadrupole polarizabilities are negligibly small in $\Sigma^{\rm circ}_{x,n}$ (Fig. 4.17).

4.5.2 Neutron Asymmetries from Linearly Polarized Photons

In the neutron asymmetries with circularly polarized photons only the leading (static) terms are identical, when we expand the pole contributions and our full $\mathcal{O}(\epsilon^3)$-calculation in the photon energy; in $\Sigma^{\rm lin}_n$ we find that also the slope at $\omega = 0$ is the same. The reason for this behaviour is that in the real parts of the various products of amplitudes in Eq. (4.10) there is no interference term between spin-independent (A_1, A_2) and spin-dependent (A_3-A_6) amplitudes, as already mentioned at the end of Section 4.1.2. Therefore there is no structure contribution at $\mathcal{O}(\omega^3)$. This missing interference term already suggests that the asymmetry $\Sigma^{\rm lin}_n$ is

not as sensitive to the neutron structure as are $\Sigma^{\rm circ}_{x,n}$ and $\Sigma^{\rm circ}_{z,n}$. In fact the three approximations in Fig. 4.18 are quite close to each other. The static limit in this configuration is described by

$$\Sigma_n^{\rm lin}(\omega = 0, \theta) = \frac{2\,\sin^2\theta}{-5 + \cos 2\theta}. \tag{4.18}$$

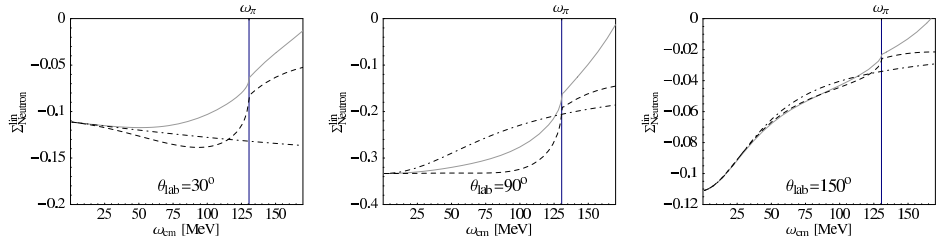

Figure 4.18: Dependence of the neutron asymmetry $\Sigma_n^{\rm lin}$ on pion and Δ physics; for notation see Fig. 4.7.

On the other hand, Fig. 4.19 suggests that the spin sensitivity of the configuration is huge, except for the forward direction. However, we have to caution that the absolute scale of the asymmetry in the backward (and also in the forward) direction is rather small – recall the factor $\sin^2\theta$ in Eq. (4.10). Nevertheless we believe that this asymmetry is able to give valuable contributions to the determination of the spin polarizabilities, at least for scattering angles close to 90°. Another disadvantage appears in $\Sigma_n^{\rm lin}$ in the forward direction, namely the surprisingly strong contributions of the dynamical quadrupole polarizabilities.

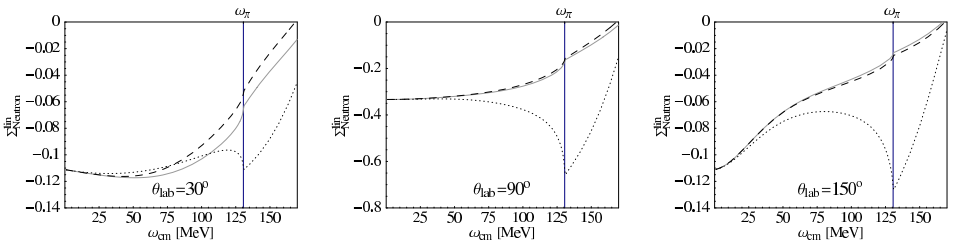

Figure 4.19: Dependence of the neutron asymmetry $\Sigma_n^{\rm lin}$ on spin and quadrupole polarizabilities; for notation see Fig. 4.4.

As a short conclusion of Sections 4.4 and 4.5 we find a much stronger sensitivity of the neutron asymmetries on the nucleon structure, while the proton asymmetries are dominated by pole terms up to at least 50 MeV. Contributions from the $\Delta(1232)$ resonance are crucial only for certain asymmetries and angles. For both nucleons, the spin configuration $\Sigma_x^{\rm circ}$ turned out as the one which is most sensitive to the nucleon spin structure, comparing to $\Sigma_z^{\rm circ}$ and $\Sigma^{\rm lin}$. However, this last configuration may give valuable contributions in the neutron case around $\theta = 90°$. Dynamical quadrupole contributions are negligible in each of the considered cases[3].

As we consider $\Sigma_x^{\rm circ}$ the most promising configuration, we investigate two aspects of this quantity in more detail: Its sensitivity to the (statistical) errors of the three SSE fit parameters, cf. Table 3.1 and Eq. (3.24), and to the four spin-dependent

[3]The only exception to this rule is $\Sigma_n^{\rm lin}$ in the forward direction, but this configuration is also for other reasons unfavorable, e.g. due to the small absolute size.

dipole polarizabilities. Fig. 4.20 tells us that the statistical errors play only a minor role in the proton asymmetry, whereas for the neutron they are considerably larger, due to the weaker constraint by the pole terms, which renders the neutron more sensitive to its structure than the proton. This behaviour is observed independently of the scattering angle θ.

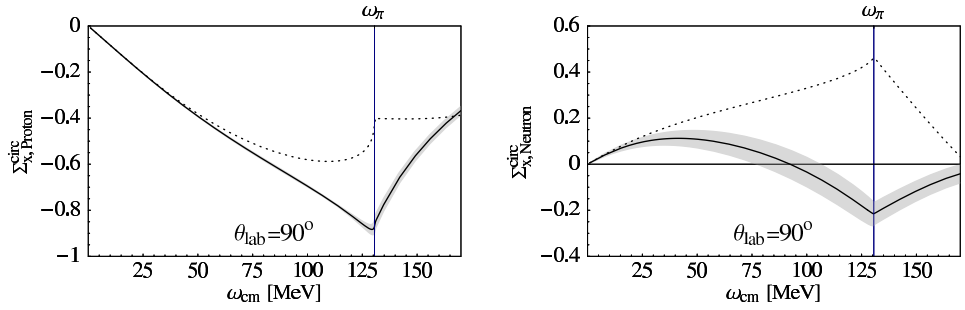

Figure 4.20: Dependence of the proton (left) and neutron (right) asymmetry Σ_x^{circ} on the statistical errors in $g_1,\ g_2,\ b_1$, denoted by the grey band around our full $\mathcal{O}(\epsilon^3)$ SSE calculation (solid); in the dotted line the spin polarizabilities are switched off.

In Fig. 4.21, we vary the four spin dipole polarizabilities successively by $+5 \cdot 10^{-4}\,\mathrm{fm}^4$, in order to investigate the dependence of Σ_x^{circ} on these quantities. For $\theta_{\mathrm{lab}} = 150°$ the asymmetry is about equally sensitive to all four of them, whereas around 90° we find that the spin dependence is dominated by $\gamma_{E1E1}(\omega)$. We also note that although the asymmetries are sensitive to all four spin polarizabilities, the dominant contribution comes from $\gamma_{E1E1}(\omega)$, which is the largest in size.

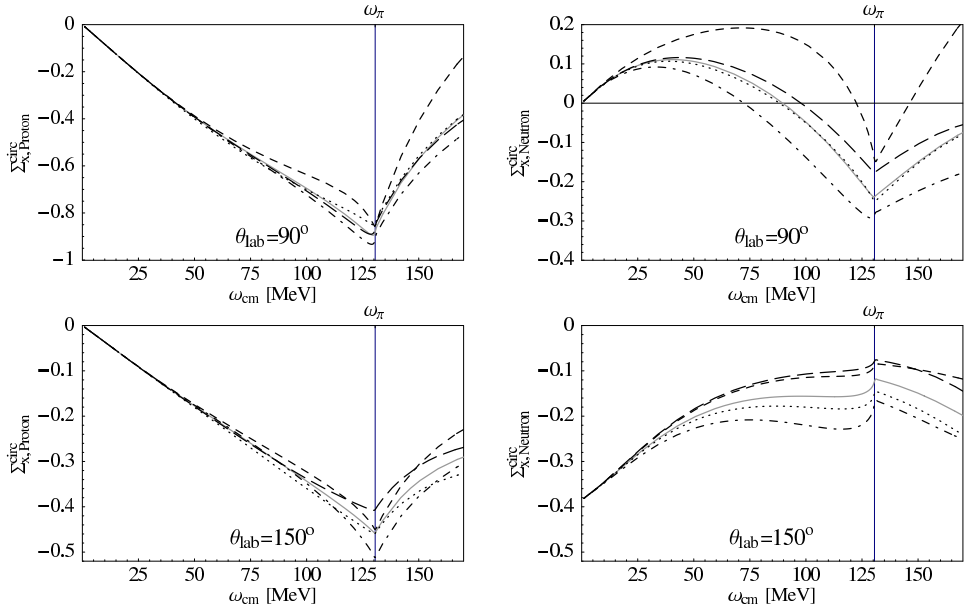

Figure 4.21: Dependence of the proton (left) and neutron (right) asymmetry Σ_x^{circ} on the various spin dipole polarizabilities. We compare our full $\mathcal{O}(\epsilon^3)$ SSE calculation (grey, solid) to the same result with a variation by $+5 \cdot 10^{-4}\,\mathrm{fm}^4$ in $\gamma_{E1E1}(\omega)$ (short-dashed), $\gamma_{M1M1}(\omega)$ (dotted), $\gamma_{E1M2}(\omega)$ (dotdashed) and $\gamma_{M1E2}(\omega)$ (long-dashed).

Before we conclude the one-nucleon part of this work, let us resume the main aspects of Chapters 3 and 4. In Chapter 3 we derived a multipole expansion for single-nucleon Compton scattering, which we use to define dynamical, i.e. energy-dependent polarizabilities. These quantities have been calculated in the framework of Chiral Effective Field Theory and are compared to predictions from a Dispersion-Relation Analysis [26] – the agreement between both approaches in most of the multipole channels was found to be very good. Before, we fixed three parameters, including the static dipole polarizabilities $\bar{\alpha}_{E1}$ and $\bar{\beta}_{M1}$, via fits to spin-averaged proton Compton cross sections, yielding results close to alternative extractions. Comparison of the resulting, fitted cross sections with experiment and Dispersion Relation looks very promising. Contributions from quadrupole polarizabilities turned out nearly invisible below 170 MeV. Nevertheless it is clear that not all of the six dipole polarizabilities can be determined via fits to spin-averaged cross sections alone. Therefore we investigated in Chapter 4 several single-nucleon asymmetries and demonstrated that neglecting quadrupole polarizabilities is a valid approximation also for spin-polarized observables. We conclude that determining the elusive spin polarizabilities from a combination of spin-polarized and spin-averaged experiments is feasible. However, such experiments are nearly impossible for the unstable neutron. So in order to investigate the neutron polarizabilities, one has to rely on light nuclei like the deuteron or ^{3}He. With this in mind we turn now to the second main part of this work, the calculation of Compton scattering from the deuteron.

Chapter 5

Deuteron Compton Scattering in Effective Field Theory

So far we were only concerned with Compton scattering from the single nucleon. We found that describing proton and neutron Compton scattering theoretically is quite similar in the framework and up to the order of the chiral expansion chosen in this work. As we saw in Section 3.3.2, our calculation gives a good description of the experimentally measured proton Compton cross sections below 200 MeV. Therefore, in Section 3.4.1, we were able to fit the (static) proton polarizabilities $\bar{\alpha}^p_{E1}$ and $\bar{\beta}^p_{M1}$ reliably to the existing data.

However, as there is no stable single-neutron target, the direct experimental investigation of neutron Compton scattering is nearly impossible. Therefore, in order to access the neutron polarizabilities, one has to rely on other experimental methods, e.g. quasi-free Compton scattering from neutrons bound in a light nucleus, scattering neutrons on heavy nuclei or elastic Compton scattering from light nuclei. In the Introduction (Section 1.1), we reviewed several attempts to extract the neutron polarizabilities from data and we found a rather broad range quoted for $\bar{\alpha}^n_{E1}$ and $\bar{\beta}^n_{M1}$, e.g. $\bar{\alpha}^n_{E1} \in [-4; 19]$. Therefore, in order to contribute to the ongoing discussion of these quantities, we are in this and the next chapter concerned with elastic deuteron Compton scattering. The cross sections resulting from our calculation are fitted to experimental data, with the isoscalar polarizabilities as fit parameters. These numbers are then combined with our fit results for $\bar{\alpha}^p_{E1}$ and $\bar{\beta}^p_{M1}$ from Section 3.4.1 in order to deduce the elusive neutron polarizabilities.

In this first chapter on deuteron Compton scattering we aim for an improved description of the elastic deuteron Compton data at $\omega \sim$ 50-100 MeV, compared to the calculations presented in [22, 24], which cannot describe the data from [19], measured at $\omega_{\rm lab} \sim 95$ MeV. In the next chapter we show how to extend the region of validity of our calculation down to the limit of vanishing photon energy.

This chapter is based on the calculations of Refs. [69, 25], where Compton scattering off the deuteron was examined for photon energies ω ranging from 50 MeV to 100 MeV. The central values for the isoscalar polarizabilities, derived in the recent $\mathcal{O}(p^4)$-HBχPT analysis [25] of the data from [17, 18, 19] are

$$\begin{aligned} \bar{\alpha}^s_{E1} &= (13.0 \pm 1.9)^{+3.9}_{-1.5} \cdot 10^{-4}\ \text{fm}^3, \\ \bar{\beta}^s_{M1} &= (-1.8 \pm 1.9)^{+2.1}_{-0.9} \cdot 10^{-4}\ \text{fm}^3. \end{aligned} \tag{5.1}$$

Comparing with Table 3.1, these results indicate a small isovector electric polarizability, but allow for values of $\bar{\beta}^v_{M1}$ which are considerably larger than $\bar{\beta}^p_{M1}$. How-

ever, the range for $\bar{\alpha}^s_{E1}$ and $\bar{\beta}^s_{M1}$ quoted in [25] is large: $\bar{\alpha}^s_{E1} = (9.6 \ldots 18.8) \cdot 10^{-4}$ fm^3, $\bar{\beta}^s_{M1} = (-4.6 \ldots 2.2) \cdot 10^{-4}$ fm^3. The authors of Refs. [69, 25] followed Weinberg's proposal [70] to calculate the irreducible kernel for the $\gamma NN \to \gamma NN$ process in Heavy Baryon Chiral Perturbation Theory, cf. Section 2.1. Proceeding in this fashion means working within an Effective Field Theory in which only nucleons and pions are active degrees of freedom. The kernel is then folded with external deuteron wave functions, derived from high-precision NN-potentials such as Nijm93 [71], CD-Bonn [72] or AV18 [73]. This combination of various elements, calculated within different theoretical frameworks, is called "hybrid" approach and has proven quite successful in describing e.g. radiative np capture [74] and πd [75], $e^- d$ [76] and also γd [69, 25] scattering. As we have seen in Chapter 3 that the $\Delta(1232)$ is an important degree of freedom in single-nucleon Compton scattering, we extend in this chapter the calculation of Ref. [69] to the framework of the Small Scale Expansion, cf. Section 2.2. The advantage of our approach with respect to the NNLO calculation of Ref. [25] is that we have a more realistic energy dependence of the Compton multipoles, which in Ref. [25] is only partially contained in the two short-distance parameters, contributing to $\bar{\alpha}_{E1}$ and $\bar{\beta}_{M1}$. As we already saw in Chapter 3, the strong energy dependence induced by the $\Delta(1232)$ plays an important role in quantities such as the magnetic dipole polarizability $\beta_{M1}(\omega)$ and in the spin-averaged Compton cross sections. It is therefore interesting to also investigate the role of these degrees of freedom in elastic γd scattering, which is the main focus in this chapter.

In Section 5.2, we discuss our predictions for the deuteron Compton cross sections for four different energies between 50 MeV and 100 MeV, comparing to data and to the $\mathcal{O}(p^3)$-HBχPT calculation [69]. Before that, we give a brief survey of the theoretical formalism in Section 5.1 and show that combining Weinberg's counting ideas with the SSE power-counting scheme leads to no additional diagrams in the two-body part of the kernel with respect to [69]. In Section 5.3, we present our results for the isoscalar polarizabilities, derived from a fit to elastic deuteron Compton-scattering data, which turn out to be in good agreement with the theoretical expectation that the isovector components are small. The corresponding curves are compared to the plots resulting from one of the $\mathcal{O}(p^4)$-HBχPT fits from Ref. [25]. All the results reported in this chapter have been published in our paper Ref. [28].

5.1 Theory of Deuteron Compton Scattering

We calculate Compton scattering off the deuteron in the framework of the Small Scale Expansion [41], cf. Section 2.2. The power-counting scheme that we use for Compton scattering off light nuclei is motivated by Weinberg's idea to count powers only in the interaction kernel. While the kernel is power counted according to the rules of the Effective Field Theory, the deuteron wave functions we use are obtained from state-of-the-art NN potentials: Nijm93 [71], the CD-Bonn potential [72], the AV18 potential [73] (see also Appendix K) and the NNLO chiral potential [77] with the cutoff chosen as $\Lambda = 650$ MeV[1]. This last potential is derived by applying the HBχPT power counting, proposed by Weinberg for the two-nucleon sector, to the NN potential V. The latter two wave functions are sketched in Appendix D. The anatomy of our deuteron Compton calculation is illustrated in Fig. 5.1.

The diagrams contributing to the scattering process considered can be classified into "one-body" pieces, in which all photon interactions take place on a single nucleon, and "two-body" pieces, in which both nucleons are involved in the Compton-

[1]We note that it has been questioned in Ref. [78], whether there is a unique 'NNLO' chiral potential due to the observed limit-cycle-like cutoff dependence of the leading-order chiral potential.

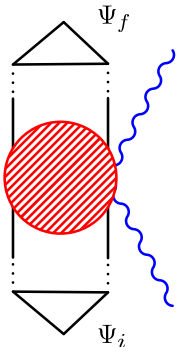

Figure 5.1: Anatomy of the deuteron Compton calculation. The blob symbolises the $\gamma\gamma d$ interaction kernel, $\Psi_{i,f}$ denote the deuteron wave function in the initial and final state, respectively.

scattering process, see Fig. 5.2. As we calculate in the γd cm frame, the two nucleon momenta in the initial state must add up to $-\vec{k}_i$. The relative momentum $\vec{p} = \frac{\vec{p}_1 - \vec{p}_2}{2}$ of the two nucleons is non-vanishing. The momenta of the outgoing nucleons depend on whether only one or both nucleons are involved in the scattering process. In the first case, they are completely determined by the momenta of the incoming nucleons and the photons, whereas momentum is transferred in the latter from one nucleon to the other, e.g. via the exchange of a pion. Of course, in both cases the momenta of the outgoing nucleons have to add up to $-\vec{k}_f$ cf. Fig. 5.2.

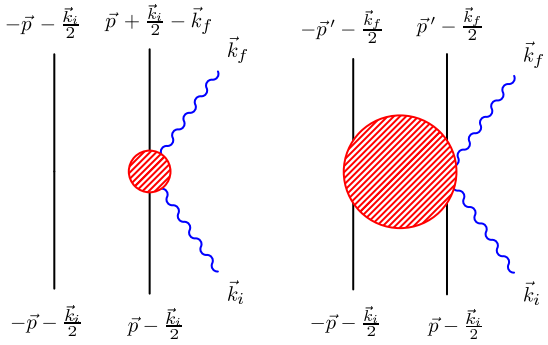

Figure 5.2: Momenta in single- and two-nucleon contributions to deuteron Compton scattering.

This, though, is not the only way to classify diagrams. They can also be divided like

$$G_{\gamma\gamma} = G\,K_\gamma\,G\,K_\gamma\,G + G\,K_{\gamma\gamma}\,G, \tag{5.2}$$

where we defined the Green's function for Compton scattering from the NN system as $G_{\gamma\gamma}$. It is the sum of all Feynman graphs which contribute to $\gamma NN \to \gamma NN$ in which the photon interacts with the NN system. G is the two-particle Green's function, constructed from the two-nucleon irreducible interaction V and the free two-nucleon Green's function. K_γ denotes the coupling of one photon to the two-nucleon system, $K_{\gamma\gamma}$ is the two-nucleon irreducible kernel for the coupling of incoming and outgoing photon.

The first piece in Eq. (5.2) is called the "two-nucleon reducible" part and the second is the "two-nucleon irreducible" part. Two-nucleon reducible diagrams are

those which contain an intermediate state with only the two nucleons as particle content. Note that, according to this classification, $K_\gamma G K_\gamma$ and $K_{\gamma\gamma}$ each contain one-body *and* two-body pieces. An example of an $\mathcal{O}(\epsilon^3)$ one-body contribution to the two-nucleon reducible part is given in Fig. 5.3(a). Two-nucleon reducible two-body contributions to $G_{\gamma\gamma}$ begin at $\mathcal{O}(\epsilon^4)$. One such diagram is given in Fig. 5.3(b), whereas Figs. 5.3(c) and (d) are two examples of two-nucleon irreducible diagrams in the one-nucleon and the two-nucleon sector, respectively.

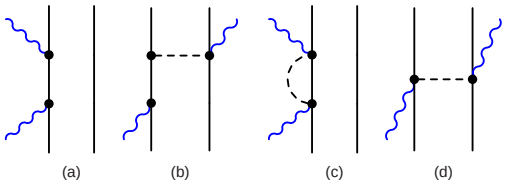

Figure 5.3: Examples of two-nucleon reducible (a, b) and two-nucleon irreducible diagrams (c, d). Except for diagram (b), which is of $\mathcal{O}(\epsilon^4)$, all graphs displayed are of third order in the Small Scale Expansion.

The amplitude for Compton scattering off the deuteron is derived as the matrix element of the interaction kernel, consisting of the two-nucleon irreducible part $K_{\gamma\gamma}$ and the two-nucleon reducible part $K_\gamma\, G\, K_\gamma$, evaluated between an initial- and final-state deuteron wave function, cf. [69]:

$$\mathcal{M} = \langle \Psi_f | K_{\gamma\gamma} + K_\gamma\, G\, K_\gamma | \Psi_i \rangle\,, \tag{5.3}$$

see also Eq. (5.10).

In this chapter, we apply the same power-counting rules to both $K_{\gamma\gamma}$ and $K_\gamma G K_\gamma$, calculating all contributions to $\mathcal{O}(\epsilon^3)$. Therefore, also the interaction between the two nucleons in the intermediate state of e.g. Fig. 5.3(a) is built up only perturbatively. Up to the order to which we work, G turns out as the Green's function of two free nucleons, while it represents the full NN-scattering Green's function in Chapter 6. We refer therefore to the approach to deuteron Compton scattering used in this chapter as the *approach without rescattering*, whereas in Chapter 6, we insert the full two-particle Green's function in the intermediate state of Fig. 5.3(a).

In order to determine which diagrams contribute to our leading-one-loop order calculation, we first remind the reader that a diagram appearing at a certain order in q in HBχPT contributes at the same order ϵ in SSE, cf. Section 2.2. In HBχPT, the leading-order propagator of a nucleon with the energy ω of the external probe flowing through it is $\frac{i}{\omega}$ [35]. Corrections from the kinetic energy of the nucleon are treated perturbatively. In the deuteron, such a perturbative treatment is not applicable for low photon energies, due to the relative momentum $\vec{p}$ between the two equally heavy nucleons. Therefore, one has to use the full non-relativistic nucleon propagator $\frac{i}{\omega - p^2/2m_N}$ in the low-energy regime. Nonetheless, the approximation $\frac{i}{\omega}$ is useful for ω much larger than the expectation value $\langle p^2/m_N \rangle$ of the kinetic energy inside the deuteron, which we found to be of the order of 20 MeV for the wave functions we are using. These considerations demonstrate that for $\omega \gg \langle p^2/m_N \rangle$, the nucleon propagator may be counted as $\mathcal{O}(\epsilon^{-1})$ like in standard HBχPT, whereas in the "nuclear" regime, i.e. $\omega \sim \mathcal{O}\left(\langle p^2/m_N \rangle\right)$, it has to be counted as $\mathcal{O}(\epsilon^{-2})$, since $p \sim \epsilon$. Therefore, from the point of view of χEFT, one has to strictly differentiate between two energy regimes: the nuclear regime $\omega \sim \mathcal{O}\left(\langle p^2/m_N \rangle\right)$ and the regime $\omega \sim \mathcal{O}(m_\pi)$. In this chapter we restrict ourselves to the latter one, as we are mainly concerned with photon energies $\omega \geq 50$ MeV, which is the energy region where one

starts to be sensitive to the nucleon polarizabilities, cf. Ref. [60]. Therefore, our calculation is only valid above some lower energy limit, which will turn out to be of the order of 50-60 MeV (cf. Section 5.2). In Chapter 6, we present an approach to deuteron Compton scattering which does not suffer from such a lower energy limit. Nevertheless, the strict perturbative calculation of this chapter has some advantages with respect to the one presented in Chapter 6: The most important point is the computational effort which as we shall see is considerably smaller. The second advantage is that it is much easier to employ a systematic expansion scheme for the interaction kernel. This systematicity leads to a high degree of transparency, which makes it easy to disentangle the various nuclear degrees of freedom from each other.

In the regime $\omega \sim \mathcal{O}(m_\pi)$, the contributions from $K_\gamma G K_\gamma$ can be treated using a perturbative chiral expansion. Heuristically, this can be easily understood, because the absorption of a high-energy photon immediately separates the nucleons from each other, so the deuteron would be destroyed if the second photon was not emitted near-instantaneously. Such a perturbative treatment is *not* valid in the nuclear regime, $\omega \sim \mathcal{O}\left(\left\langle p^2/m_N \right\rangle\right)$, as described in detail in [69, 25], and applying it there leads – not surprisingly – to violations of the low-energy theorems which govern the limit $\omega \to 0$. For example, the Thomson limit for Compton scattering from a nucleus of charge $Q\,e$ and mass $A\,m_N$,

$$A^{\text{Thomson}} = A(\omega = 0) = -\frac{Q^2\,e^2}{A\,m_N}\,\vec{\epsilon}\cdot\vec{\epsilon}\,', \tag{5.4}$$

is a direct consequence of gauge invariance [79] and cannot be recovered without the full two-nucleon Green's function in the intermediate state of diagram 5.3(a). It is one of the central results of Chapter 6 that the correct low-energy limit will be obtained (see Section 6.2). Some attempts to reach this limit at least approximately by the inclusion of $\mathcal{O}(p^4)$-pion-exchange diagrams are reported in Section 5.4.

Due to the inapplicability of our calculation at small photon energies, we strictly constrain ourselves in this chapter to $\omega \sim \mathcal{O}(m_\pi)$, where a perturbative expansion of the kernel in the standard HBχPT counting scheme, i.e. counting the nucleon propagator as $\mathcal{O}(\epsilon^{-1})$, is possible[2]. The lower limit of this power counting turns out to be $\omega \approx 50$ MeV, so we have to caution the reader that the calculation is not supposed to work in the region $\omega \ll 50$ MeV. In this energy regime, pions may be treated as "heavy" compared to the photon energy, and it can therefore be more convenient to use an Effective Field Theory approach to deuteron Compton scattering where pions are integrated out, see Refs. [60, 23]. These calculations describe the very-low-energy region well and also reach the exact Thomson limit.

As we calculate γd scattering in the Small Scale Expansion, we have to fix our counting rules also for diagrams including $\Delta(1232)$ propagators. For the one-body contributions this is straightforward, as we apply the SSE counting scheme, cf. Refs. [26, 42]. As far as the two-body physics is concerned, we combine the SSE counting rules, e.g. counting the Δ-propagator as ϵ^{-1}, with Weinberg's prescription of counting only within the interaction kernel. To $\mathcal{O}(\epsilon^3)$, the order up to which we are working, this leads to identical meson-exchange diagrams as in the $\mathcal{O}(p^3)$-HBχPT calculation. All additional diagrams are at least one order higher, an example is given in Fig. 5.4(b) (an example of an $\mathcal{O}(\epsilon^4)$-one-body diagram is sketched in Fig. 5.4(a)). Note that only nucleon propagators with the energy of the scattered photon flowing through them are supposed to be counted as ϵ^{-1}. Therefore, up to $\mathcal{O}(\epsilon^3)$ there are no diagrams with Δ excitations in outgoing lines, since the Δ propagator always has to be counted as -1.

[2] The only exception to this rule is Section 5.4, where we investigate the Thomson limit.

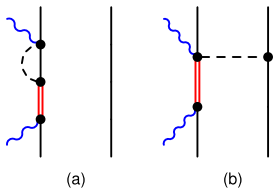

Figure 5.4: Two examples of $\mathcal{O}(\epsilon^4)$ contributions to deuteron Compton scattering with explicit $\Delta(1232)$ degrees of freedom in the one- and two-body sector.

As a side remark we note that a modified counting scheme in the two-body sector has been suggested in [75], as certain pion-exchange diagrams may be enhanced when the photon energy comes close enough to the pion mass that the pions in the two-body diagrams are almost on mass shell. We do not consider such a modification necessary for our calculation, as we restrict ourselves to photon energies $\omega \leq 100$ MeV. Therefore, the diagrams contributing to deuteron Compton scattering up to $\mathcal{O}(\epsilon^3)$ are:

- One-body contributions without explicit $\Delta(1232)$ degrees of freedom. These are the single-nucleon seagull with the two-photon vertices from $\mathcal{L}^{(2)}_{N\pi}$ and $\mathcal{L}^{(3)}_{N\pi}$ (see Fig. 5.5(a) and Appendix B). The former gives the only contribution at $\mathcal{O}(\epsilon^2)$, the latter enters at $\mathcal{O}(\epsilon^3)$. Also at $\mathcal{O}(\epsilon^3)$, the nucleon-pole terms (Fig. 5.5(b) and Appendix B) and the contributions from the leading chiral dynamics of the pion cloud around the nucleon enter (Figs. 5.5(d)-(g), see also Fig. 3.2). We note that at $\mathcal{O}(\epsilon^3)$ the nucleon s-channel pole term is the only contribution from $K_\gamma\, G\, K_\gamma$, cf. Eq. (5.2). The pion pole (Fig. 5.5(c)), i.e. the π^0-exchange in the t-channel, does not contribute to deuteron Compton scattering at this order, as it is an isovector and we neglect isospin-breaking effects.

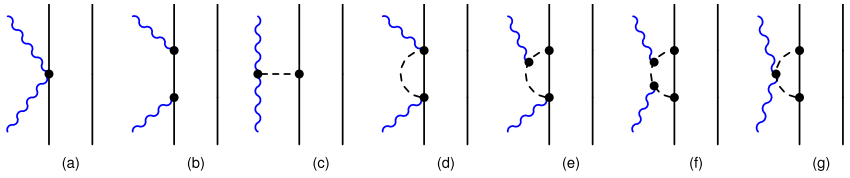

Figure 5.5: One-body interactions without a $\Delta(1232)$ propagator contributing to deuteron Compton scattering up to $\mathcal{O}(\epsilon^3)$ in SSE. Permutations and crossed graphs are not shown.

- One-body diagrams with explicit Δ degrees of freedom, as shown in Fig. 5.6: The Δ-pole diagrams (Fig. 5.6(a)) and the contributions from the pion cloud around the $\Delta(1232)$ (Figs. 5.6(b)-(e)).
- The two isoscalar short-distance one-body operators (Fig. 5.6(f)), introduced in Section 3.3. We note that except for these two contact operators, the δ-expansion [43] (cf. Section 2.2) up to NNLO is equivalent to $\mathcal{O}(\epsilon^3)$ SSE in the energy range $\omega \sim m_\pi$ considered.
- Two-body contributions with one pion exchanged between the two nucleons (Fig. 5.7). In total there are nine two-body diagrams at $\mathcal{O}(\epsilon^3)$. As discussed before, the meson-exchange diagrams are identical in third-order HBχPT and SSE.

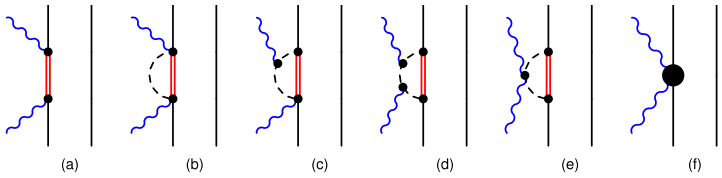

Figure 5.6: Additional one-body interactions which contribute to deuteron Compton scattering at $\mathcal{O}(\epsilon^3)$ in SSE compared to third-order HBχPT. Permutations and crossed graphs are not shown.

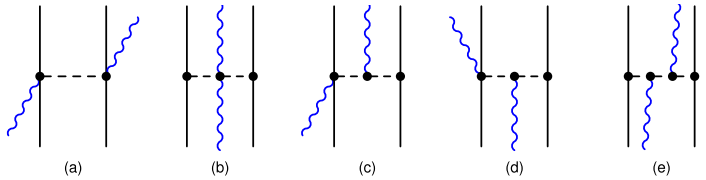

Figure 5.7: Two-body interactions contributing to the kernel for deuteron Compton scattering at $\mathcal{O}(\epsilon^3)$ in SSE. Diagrams which differ only by nucleon interchange are not shown.

All these diagrams (Figs. 5.5-5.7) make up our interaction kernel. The SSE single-nucleon amplitudes can be found in [26], however there is one difference compared to the T-matrix for Compton scattering off the single nucleon (Eq. (3.18)): The nucleon-pole amplitudes, which are given in the γN center-of-mass frame in Appendix B, have to be boosted to the γNN center-of-mass system, as our calculation is performed in the γd cm frame. This is easily accomplished by evaluating the pole diagrams (Fig. 5.5(b) plus crossed) in a frame with non-zero total γN momentum, see Fig. 5.8. We verified the resulting formula for the boost, given in Ref. [69]:

$$T_{\rm boost} = -\frac{Q^2\, e^2}{2\, m_N^2\, \omega} \left\{ (\vec{\epsilon}\cdot\vec{k}_f)\,(\vec{\epsilon}\,'\cdot\vec{k}_i) + 2\left[(\vec{\epsilon}\cdot\vec{p})\,(\vec{\epsilon}\,'\cdot\vec{k}_i) + (\vec{\epsilon}\cdot\vec{k}_f)\,(\vec{\epsilon}\,'\cdot\vec{p}) \right] \right\} \quad (5.5)$$

We note that we have simplified the expressions for the single-nucleon amplitudes given in [26] with respect to the exact position of the pion threshold, cf. Section 3.2, as we are only analysing Compton scattering for photon energies ≤ 100 MeV. For such low energies, shifting the pion threshold has only a minor effect [29]. An estimate of the (small) size of this simplification is given in Section 5.2.2.

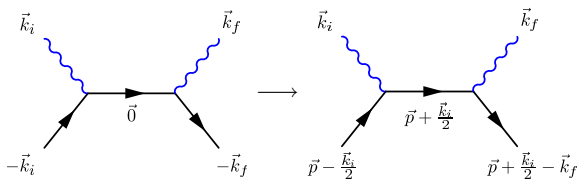

Figure 5.8: Momenta in the s-channel nucleon-pole diagram comparing the γd-cm frame (right) to the γN-cm frame (left). The analogous replacement in the u-channel is not shown.

The two-nucleon amplitude corresponding to Fig. 5.7 has been calculated in [69]

and verified by us. It reads (with $\vec{\tau}^t = (\tau^x, \tau^y, \tau^z)$)

$$T^{\gamma NN} = -\frac{e^2\, g_A^2}{2\, f_\pi^2}\, (\vec{\tau}_1 \cdot \vec{\tau}_2 - \tau_1^z\, \tau_2^z)\, \left(t^{(a)} + t^{(b)} + t^{(c)} + t^{(d)} + t^{(e)} \right) \tag{5.6}$$

with

$$\begin{aligned}
t^{(a)} &= \frac{(\vec{\epsilon}\cdot\vec{\sigma}_1)\,(\vec{\epsilon}\,'\cdot\vec{\sigma}_2)}{2\,[\omega^2 - m_\pi^2 - (\vec{p}-\vec{p}\,' + \frac{1}{2}\,(\vec{k}_i + \vec{k}_f))^2]} + (1 \leftrightarrow 2), \\
t^{(b)} &= \frac{(\vec{\epsilon}\cdot\vec{\epsilon}\,')\,(\vec{\sigma}_1\cdot(\vec{p}-\vec{p}\,' - \frac{1}{2}\,(\vec{k}_i - \vec{k}_f)))\,(\vec{\sigma}_2\cdot(\vec{p}-\vec{p}\,' + \frac{1}{2}\,(\vec{k}_i - \vec{k}_f)))}{[(\vec{p}-\vec{p}\,' - \frac{1}{2}\,(\vec{k}_i - \vec{k}_f))^2 + m_\pi^2]\,[(\vec{p}-\vec{p}\,' + \frac{1}{2}\,(\vec{k}_i - \vec{k}_f))^2 + m_\pi^2]}, \\
t^{(c)} &= -\frac{(\vec{\epsilon}\,'\cdot(\vec{p}-\vec{p}\,' + \frac{1}{2}\,\vec{k}_i))\,(\vec{\sigma}_1\cdot\vec{\epsilon})\,(\vec{\sigma}_2\cdot(\vec{p}-\vec{p}\,' + \frac{1}{2}\,(\vec{k}_i - \vec{k}_f)))}{[\omega^2 - m_\pi^2 - (\vec{p}-\vec{p}\,' + \frac{1}{2}\,(\vec{k}_i + \vec{k}_f))^2]\,[(\vec{p}-\vec{p}\,' + \frac{1}{2}\,(\vec{k}_i - \vec{k}_f))^2 + m_\pi^2]} + (1 \leftrightarrow 2), \\
t^{(d)} &= -\frac{(\vec{\epsilon}\cdot(\vec{p}-\vec{p}\,' + \frac{1}{2}\,\vec{k}_f))\,(\vec{\sigma}_1\cdot(\vec{p}-\vec{p}\,' - \frac{1}{2}\,(\vec{k}_i - \vec{k}_f)))\,(\vec{\sigma}_2\cdot\vec{\epsilon}\,')}{[\omega^2 - m_\pi^2 - (\vec{p}-\vec{p}\,' + \frac{1}{2}\,(\vec{k}_i + \vec{k}_f))^2]\,[(\vec{p}-\vec{p}\,' + \frac{1}{2}\,(\vec{k}_i - \vec{k}_f))^2 + m_\pi^2]} + (1 \leftrightarrow 2), \\
t^{(e)} &= \frac{2\,(\vec{\epsilon}\cdot(\vec{p}-\vec{p}\,' + \frac{1}{2}\,\vec{k}_f))\,(\vec{\epsilon}\,'\cdot(\vec{p}-\vec{p}\,' + \frac{1}{2}\,\vec{k}_i))\,(\vec{\sigma}_1\cdot(\vec{p}-\vec{p}\,' - \frac{1}{2}\,(\vec{k}_i - \vec{k}_f)))}{[\omega^2 - m_\pi^2 - (\vec{p}-\vec{p}\,' + \frac{1}{2}\,(\vec{k}_i + \vec{k}_f))^2]\,[(\vec{p}-\vec{p}\,' - \frac{1}{2}\,(\vec{k}_i - \vec{k}_f))^2 + m_\pi^2]} \\
&\quad \times \frac{(\vec{\sigma}_2\cdot(\vec{p}-\vec{p}\,' + \frac{1}{2}\,(\vec{k}_i - \vec{k}_f)))}{[(\vec{p}-\vec{p}\,' + \frac{1}{2}\,(\vec{k}_i - \vec{k}_f))^2 + m_\pi^2]} + (1 \leftrightarrow 2).
\end{aligned} \tag{5.7}$$

$(1 \leftrightarrow 2)$ is a shortcut for the corresponding amplitude with the two nucleons exchanged, as e.g. in Fig. 5.7(a) the incoming (outgoing) photon can couple to nucleon 1 (2) or vice versa. Such an exchange term obviously does not exist for diagram 5.7(b), which is invariant under the exchange of nucleon 1 and nucleon 2.

In order to calculate the amplitude for deuteron Compton scattering we now have to evaluate the kernel between an initial- and final-state deuteron wave function, cf. Eq. (5.3). The isospin operator $(\vec{\tau}_1 \cdot \vec{\tau}_2 - \tau_1^z\, \tau_2^z)$ in Eq. (5.6) reflects the fact that the photon couples only to charged pions. Its evaluation yields

$$\langle\, d \mid \vec{\tau}_1 \cdot \vec{\tau}_2 - \tau_1^z\, \tau_2^z \mid d \,\rangle = -2, \tag{5.8}$$

with the isospin wave function of the isospin-0 deuteron

$$\langle\, d \mid = \frac{1}{\sqrt{2}}\, \langle\, p\, n - n\, p \mid . \tag{5.9}$$

Now we write down the amplitude according to [69], separating the single-nucleon amplitude with its kernel $T^{\gamma N}$ from the two-nucleon contributions:

$$\begin{aligned}
\mathcal{M}_{fi}(\vec{k}_i, \vec{k}_f) &= \int \frac{d^3p}{(2\pi)^3}\, \Psi_f^*(\vec{p} + (\vec{k}_i - \vec{k}_f)/2)\, T^{\gamma N}(\vec{k}_i, \vec{k}_f; \vec{p})\, \Psi_i(\vec{p}) \\
&\quad + \int \frac{d^3p\, d^3p'}{(2\pi)^6}\, \Psi_f^*(\vec{p}\,')\, T^{\gamma NN}(\vec{k}_i, \vec{k}_f; \vec{p}, \vec{p}\,')\, \Psi_i(\vec{p})
\end{aligned} \tag{5.10}$$

The deuteron wave functions – explicit expressions can be found in Appendix D – depend on half of the difference between the momenta of the two nucleons, see Fig. 5.2. Due to the momentum transfer by the pion we have to integrate over momentum space twice in the two-nucleon amplitude, whereas there is only one loop integral to perform in the single-nucleon part. The indices i, f denote the dependence of the amplitude on the initial and final photon polarization and also on the projections of the total angular momentum of the deuteron M_f and M_i. Note that we have to sum over all possible combinations of spins of the two nucleons in

the initial and final state, cf. Eq. (D.9). These sums are not explicitly shown in Eq. (5.10).

The spin-averaged differential cross section for deuteron Compton scattering is calculated like the single-nucleon cross section, cf. Section 3.3.1: We take the absolute square of Eq. (5.10), average over the initial and sum over the final photon and deuteron states and multiply the result by the square of the appropriate phase-space factor, depending on the frame, in which we want to evaluate the cross section. Therefore we find, using $\sum_{i,f}$ as a shortcut for $\sum_{M_i,M_f,\lambda_i,\lambda_f}$

$$\left.\frac{d\sigma}{d\Omega}\right|_{\gamma d} = \Phi^2 \cdot \frac{1}{6} \sum_{i,f} |\mathcal{M}_{fi}|^2, \tag{5.11}$$

as there are six possible initial states: three deuteron polarizations times the two polarizations of the photon. The phase-space factors Φ read

$$\begin{aligned} \Phi_{\rm cm} &= \frac{m_d}{4\pi\sqrt{s_{\gamma d}}}, \\ \Phi_{\rm lab} &= \frac{\omega_f}{4\pi\,\omega_i}, \end{aligned} \tag{5.12}$$

with

$$\begin{aligned} \sqrt{s_{\gamma d}} &= \omega + \sqrt{\omega^2 + m_d^2}, \\ \omega_f &= \frac{m_d\,\omega_i}{m_d + \omega_i\,(1-\cos\theta_{\rm lab})}, \end{aligned} \tag{5.13}$$

cf. Eqs. (3.14, 3.15). The relation between the initial photon energy in the lab frame ω_i and the photon energy in the γd-cm frame ω is

$$\omega = \frac{\omega_i}{\sqrt{1+2\omega_i/m_d}}, \tag{5.14}$$

in analogy to Eq. (3.16).

Now that we have defined the theoretical framework for γd scattering, we compare in the next section our $\mathcal{O}(\epsilon^3)$-SSE results for the deuteron Compton cross sections to the $\mathcal{O}(p^3)$-HBχPT calculation performed in [69] and to the available data. The comparison to the $\mathcal{O}(p^4)$-HBχPT fit from Ref. [25] is postponed to Section 5.3, where we fit the isoscalar polarizabilities $\bar{\alpha}^s_{E1}$, $\bar{\beta}^s_{M1}$ to these data. Special emphasis is put on the energy and wave-function dependence of the cross sections.

5.2 Predictions for Deuteron Compton Cross Sections

In Fig. 5.9, we compare the $\mathcal{O}(\epsilon^3)$-SSE predictions to the $\mathcal{O}(p^3)$-HBχPT calculation of Ref. [69], using the wave function derived from the NNLO chiral potential with spectral-function regularization and cutoff $\Lambda = 650$ MeV [77]; this is the wave function that we always use if not stated differently. We also show the $\mathcal{O}(p^2)$ result, which consists only of the single-nucleon seagull (Fig. 5.5(a)). As we discuss only *predictions* for deuteron Compton scattering in this section, we postpone the comparison to the $\mathcal{O}(p^4)$-HBχPT fits of Ref. [25] to Section 5.3. The experiments shown have been performed at a lab energy of 49 MeV [17], 55 MeV [18], ∼67 MeV [18], 69 MeV [17] and ∼94.2 MeV [19]. (The last experiment used photons in an energy range from $84.2 - 104.5$ MeV; the deviation from the central value has been corrected for [19].)

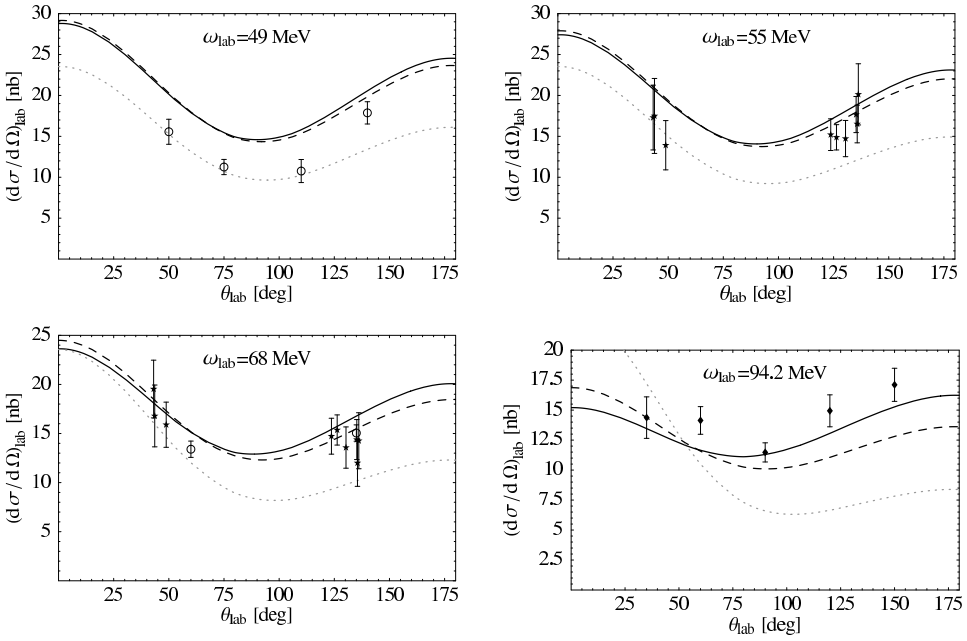

Figure 5.9: Comparison of the $\mathcal{O}(p^3)$-HBχPT (dashed) and the $\mathcal{O}(\epsilon^3)$-SSE (solid) prediction at $\omega_{\rm lab} = 49$ MeV, $\omega_{\rm lab} = 55$ MeV, $\omega_{\rm lab} = 68$ MeV and $\omega_{\rm lab} = 94.2$ MeV using the chiral NNLO wave function [77]. The data are from Illinois [17] (circle), Lund [18] (star) and SAL [19] (diamond). The dotted line is the $\mathcal{O}(p^2)$ result.

The numerical values for the various input parameters are given in Table A.1. We use for the coupling constants g_1 and g_2, connected with the two short-distance γN-operators (cf. Sections 3.3 and 5.1), and the $\gamma N\Delta$ coupling b_1 the results of the Baldin-sum-rule-constrained fit to the spin-averaged proton Compton-scattering data from Section 3.4.1. Determining the isoscalar parameters g_1, g_2 – or, eqivalently, the polarizabilities $\bar{\alpha}^s_{E1}$, $\bar{\beta}^s_{M1}$ – from proton data alone is possible, because the $\mathcal{O}(\epsilon^3)$-SSE calculation predicts $\alpha^n_{E1} \equiv \alpha^p_{E1}$, $\beta^n_{M1} \equiv \beta^p_{M1}$, as the isovector contributions only come in at $\mathcal{O}(\epsilon^4)$. This is in agreement with small isovector polarizabilities found in Dispersion-Theoretical Analyses based on pion-photoproduction multipoles (see e.g. [50]). We use the central values of the fit, which are $\bar{\alpha}^p_{E1} = 11.04 \cdot 10^{-4}$ fm^3, $\bar{\beta}^p_{M1} = 2.76 \cdot 10^{-4}$ fm^3, cf. Section 3.4.1. Therefore, like in third-order HBχPT, there are no free parameters in our deuteron Compton calculation.

From the 49 MeV, 55 MeV and 68 MeV curves shown in Fig. 5.9 it is obvious that explicit Δ degrees of freedom may well be neglected for these low energies. The two calculations – HBχPT and SSE – yield results which differ only within the uncertainties one expects from higher-order contributions. This is an important check, as it demonstrates the correct decoupling of the resonance, leading to the same low-energy limit in both theories. The 49 MeV data are best described by the $\mathcal{O}(p^2)$ calculation but we regard this as a coincidence, as the low-energy theorems are violated at this order too.

By comparing our results to data, we can now quantify the region of applicability of our calculation. The counting scheme described in Section 5.1 seems to break down for energies somewhere between 50 and 60 MeV, as both theoretical descriptions miss the 49 MeV data points, whereas the 68 MeV data are well described within both theories[3]. The 55 MeV curves are still in agreement with the

[3]We neglect the minor corrections due to the data of [18] ([17]) being measured around 67 MeV

data within the (large) error bars but lie systematically above the central values. As discussed before, we assume $\omega \sim m_\pi$ in this chapter. For $\omega \approx 20$ MeV, this counting is known to break down, see Section 5.1. In the remaining part of this chapter we are therefore only concerned with the data published for energies higher than 60 MeV.

In the high-energy regime of our calculation – i.e. for describing the 94.2 MeV data correctly – the inclusion of the explicit Δ field seems to be advantageous in a third-order calculation, as can be seen in Fig. 5.9. Here, $\mathcal{O}(p^3)$ HBχPT misses the data in the backward direction. It also fails to reproduce the shape of the data points, which shows a slight tendency towards higher cross sections in the backward than in the forward direction. This shape is very well reproduced in SSE, demonstrating once again the importance of the Δ resonance in Compton backscattering, due to the strong $M1 \to M1$ transition. This feature can be clearly seen in the dynamical magnetic dipole polarizability $\beta_{M1}(\omega)$, even for photon energies below the pion-production threshold, cf. Fig. 3.8. We believe that this is the main reason why calculations like the ones presented in Refs. [22, 24], which truncate the Compton amplitudes after the leading [22, 24] and subleading terms [22] of a Taylor expansion in ω, fail to describe the data around 95 MeV, at least without introducing an unexpectedly large magnetic dipole polarizability β_{M1} [22].

5.2.1 Energy Dependence of the γd Cross Sections

In order to decrease the statistical uncertainties, the experiment [19] had to accept scattering events in an energy range of 20 MeV. Therefore we think it worthwhile to examine the sensitivity of our results to the photon energy. In fact, our calculations suggest that the forward-angle cross section, in particular, has a sizeable energy dependence, which is, however, nearly linear. In Fig. 5.10 we show our results for three different photon energies around 68 MeV and 95 MeV, respectively, in steps of 5 MeV. This emphasizes the importance of having a well-known spectrum of the photon flux, especially in the forward direction, when one wants to examine the effects of α_{E1} and β_{M1} experimentally.

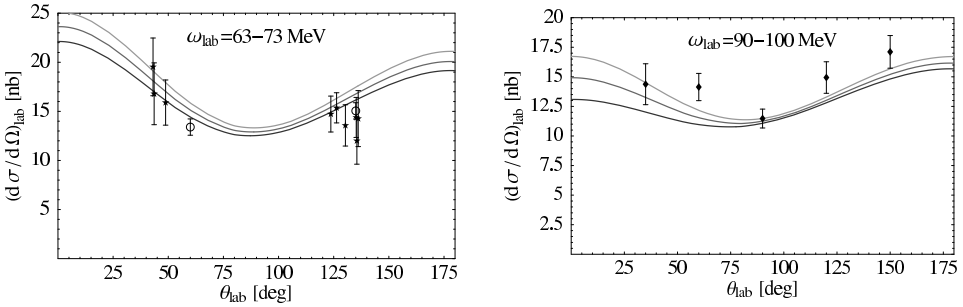

Figure 5.10: $\mathcal{O}(\epsilon^3)$-SSE results for 63 MeV, 68 MeV, 73 MeV and, respectively, 90 MeV, 95 MeV, 100 MeV (from upper to lower curve in each panel), using the χPT wave function [77].

5.2.2 Correction due to the Pion-Production Threshold

In low-order (non-relativistic) HBχPT/SSE calculations, the $\gamma d \to \pi NN$ threshold ω_π is not at the correct position as demanded by relativistic kinematics. For a

(69 MeV), and account for this deviation by calculating at the averaged energy 68 MeV.

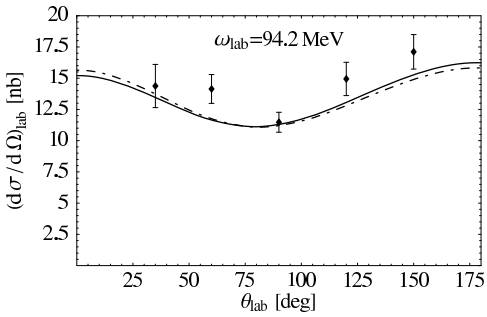

Figure 5.11: Estimate of the effect of a threshold correction (dotdashed) on the $\mathcal{O}(\epsilon^3)$-SSE results (solid), using the chiral NNLO wave function [77].

similar problem, regarding the correct position of the pion-production threshold in the single-nucleon sector, see Section 3.1.2. Thus far we have refrained from an analogous correction for γd scattering. However, in Fig. 5.11 we investigate what deviations one would expect from our present results, as indicated by an estimate which uses the single-nucleon SSE amplitudes [26] with the exact expression for $\sqrt{s}-m_N$. Obviously, even at the highest photon energies considered here, 94.2 MeV, the corrections are negligible, given the sizeable error bars of the experimental data and the theoretical uncertainties of a leading-one-loop order calculation. This is no surprise, as we found in Ref. [29] that the threshold correction is only mandatory close to ω_π, i.e. above 100 MeV. There, however, it should not be neglected anymore, see also discussion in Ref. [80].

5.2.3 Wave-Function Dependence of the γd Cross Sections

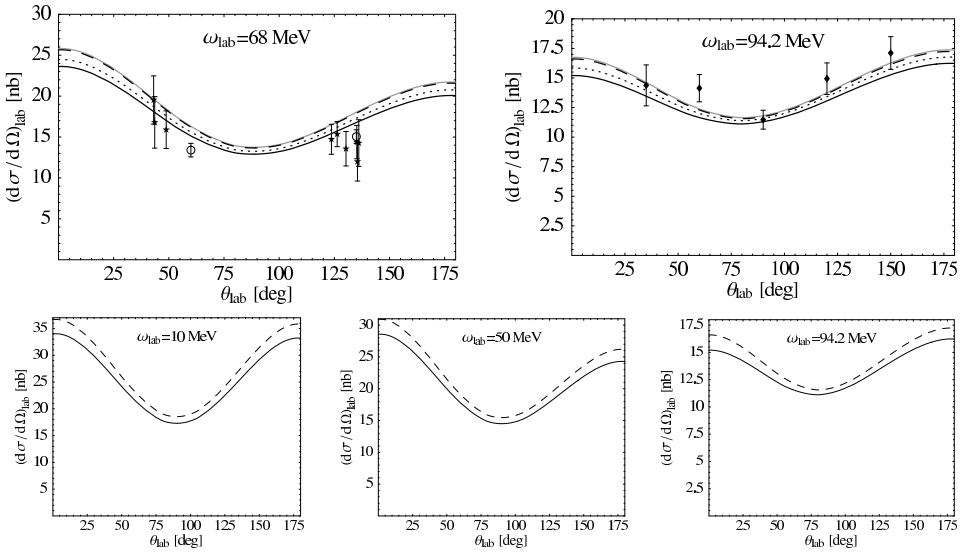

Figure 5.12: Upper panels: $\mathcal{O}(\epsilon^3)$-SSE results for 68 and 94.2 MeV, using four different wave functions: NNLO χPT with $\Lambda = 650$ MeV [77] (solid), Nijm93 [71] (grey), CD-Bonn [72] (dotted), AV18 [73] (dashed). Lower panels: $\mathcal{O}(\epsilon^3)$-SSE results for 10, 50 and 94.2 MeV, using the NNLO χPT wave function [77] (solid) and the AV18 wave function [73] (dashed).

Another interesting issue is the wave-function dependence of our results. Fig. 5.12 investigates the sensitivity to the wave function chosen, showing sizeable deviations between the NNLO χPT wave function with cutoff $\Lambda = 650$ MeV [77] on one hand and the wave function derived from the AV18 potential [73] on the other, which are both given in Appendix D. The latter yields results which are nearly indistinguishable from those obtained with the Nijm93 wave function [71], but are considerably higher than the cross sections found with the wave function from the chiral potential [77]. We note that our results using the chiral wave function from Ref. [77] with the cutoff chosen to be 450 MeV are even smaller by about 5% than those achieved with $\Lambda = 650$ MeV. With the CD-Bonn wave function [72] we obtain results in between NNLO χPT and Nijm93/AV18. This pattern is identical for both energies under investigation, 68 MeV and 94.2 MeV. In the lower three panels of Fig. 5.12, where we compare our results obtained with the NNLO chiral wave function and the AV18 wave function at 10 MeV, 50 MeV and 94.2 MeV, we demonstrate that the wave-function dependence is largely energy independent. Note that the main difference between the two curves in each panel is an angle-independent off-set, reminiscent of a systematic error.

The main contribution to the sensitivity on the deuteron wave function comes from the two-body diagrams (Fig. 5.7), as is shown in Fig. 5.13, where we calculate deuteron Compton cross sections at various energies, including only the $\mathcal{O}(\epsilon^3)$-SSE one-body diagrams. The curves in Fig. 5.13 corresponding to the NNLO χPT wave function [77] are nearly indistinguishable from those obtained with the AV18 wave function [73]. The same observation was made in Ref. [25].

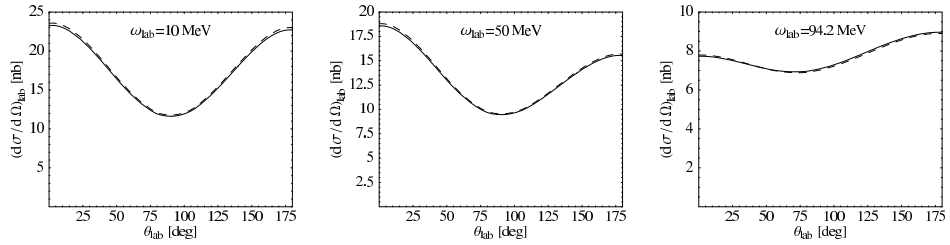

Figure 5.13: Results for 10, 50 and 94.2 MeV, including only the third-order SSE one-body diagrams, calculated with the NNLO χPT wave function [77] (solid) and the AV18 wave function [73] (dashed).

Given that our calculation is based on a low-energy Effective Field Theory of QCD, the dependence on the wave function is somewhat worrisome. Our calculation describes deuteron Compton scattering up to next-to-leading one-loop order in the Small Scale Expansion, therefore instead of the 10%-discrepancy observed in Fig. 5.12 one would rather expect such higher-order corrections to be of the order of $(m_\pi/m_N)^2 \sim 2\%$. We interpret this feature, which will be discussed further in Section 6.3.1, as an unwanted sensitivity to short-distance physics, because the long-range part of all wave functions, described by one-pion exchange, is identical. However, one must caution that the NNLO χPT potential reproduces the Nijmegen partial-wave analysis with less precision than the CD-Bonn, AV18 or Nijm93 potentials. It will be one of the major successes of our deuteron Compton calculation described in Chapter 6, that it is largely insensitive to the deuteron wave function chosen, cf. Section 6.3.1.

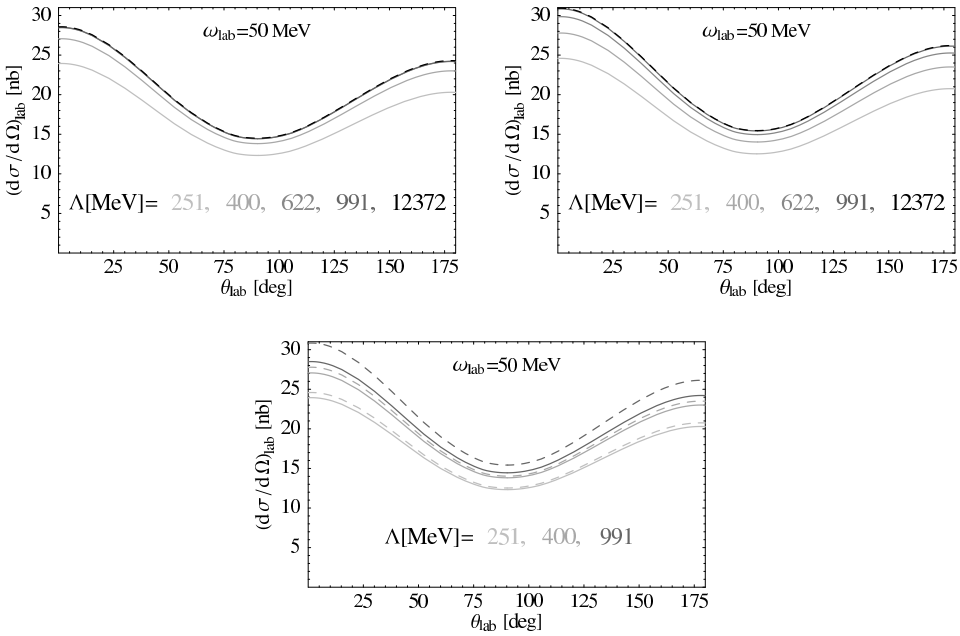

Figure 5.14: $\mathcal{O}(\epsilon^3)$-SSE results with various upper integration limits Λ. The curves in the upper left panel have been calculated with the NNLO χPT wave function [77], those in the upper right panel with the AV18 wave function [73]. In the lower panel the solid lines correspond to the chiral, the dashed lines to the AV18 wave function.

5.2.4 Dependence on the Upper Integration Limit

Here we want to investigate how fast our integrals converge, and in which energy regime the main part of the wave-function dependence enters, cf. Section 5.2.3. This question is addressed in Fig. 5.14 for an exemplary photon energy $\omega = 50$ MeV, with the respective upper integration limits Λ given in the figures. The upper left panel corresponds to the NNLO χPT wave function, the upper right one to the wave function derived from the AV18 potential. Obviously, the integrals are well saturated below 1 GeV, the one using the chiral wave function already below 620 MeV, due to the cutoff $\Lambda = 650$ MeV chosen. This observation agrees with Fig D.1, where we show the momentum-space representation of both wave functions. The only significant deviations between the two wave functions are observed in $w(p)$, corresponding to the orbital angular momentum $l = 2$. Here we notice that the χPT wave function converges faster to zero for $p \to \infty$ than the AV18 wave function, resulting in a faster saturation of the integrals entering the cross section. In the lower panel of Fig. 5.14 we give a direct comparison of our results, derived from the two wave functions for three different upper integration limits. We note that the largest part of the wave-function dependence enters between 400 MeV and 1 GeV, which is no surprise, because in this energy range the $l = 2$ wave functions differ most, cf. Fig. D.1.

In this section we presented our predictions for γd differential cross sections. These are parameter-free, as we fixed the isoscalar nucleon polarizabilities via proton Compton data. The good agreement of the SSE results with experiment at 68 MeV and 94.2 MeV leaves little room for large isovector polarizabilities, since this formalism treats the proton and neutron polarizabilities on the same footing to the order we are working. The good description of the high-energy data further encourages us to determine the isoscalar dipole polarizabilities $\bar{\alpha}^s_{E1}$ and $\bar{\beta}^s_{M1}$ di-

rectly from the deuteron Compton cross sections. The results are given in the next section, together with the results one obtains from analogous fits using the $\mathcal{O}(p^3)$ and the $\mathcal{O}(p^4)$-HBχPT [25] amplitudes, respectively.

5.3 Determining $\bar{\alpha}^s_{E1}$ and $\bar{\beta}^s_{M1}$ from γd Scattering

An accurate and systematically-improvable description of Compton scattering on deuterium offers the possibility to extract the isoscalar polarizabilities directly from deuteron Compton-scattering experiments in a well-defined way. The results can then be combined with the known numbers for the proton to draw conclusions about isovector pieces $\bar{\alpha}^v_{E1}$ and $\bar{\beta}^v_{M1}$, or, equivalently, the elusive neutron polarizabilities. As our SSE calculation provides a reasonable description of the 68 MeV and the 94.2 MeV data (see Section 5.2), we present in the following our results from a least-χ^2 fit of the isoscalar polarizabilities to these two data sets. This corresponds to fitting the coupling strengths of the two short-distance isoscalar γN-operators (Fig. 5.6(f)), which we now fit to γd rather than to γp data. In this way we can check the SSE claim that the short-distance operators are isoscalar at leading order. If their coefficients as extracted from γd data are consistent with those obtained from γp data, that argues in favour of short-distance mechanisms which are predominantly isoscalar. The value for the $\gamma N\Delta$-coupling b_1 is adopted from our Baldin-constrained 2-parameter fit, cf. Table 3.1, as there is no isovector contribution to this coupling up to third-order SSE.

Our SSE results are compared to the fit results for $\bar{\alpha}^s_{E1}$ and $\bar{\beta}^s_{M1}$ when we use modified $\mathcal{O}(p^3)$-HBχPT amplitudes. This modification consists of including in our calculation isoscalar short-distance γN operators which change both the electric and magnetic polarizability from their $\mathcal{O}(p^3)$ values. In other words, we write

$$\begin{aligned} \bar{\alpha}^s_{E1} &= \frac{5\,\alpha\,g_A^2}{96\,f_\pi^2\,m_\pi\,\pi} + \delta_\alpha, \\ \bar{\beta}^s_{M1} &= \frac{\alpha\,g_A^2}{192\,f_\pi^2\,m_\pi\,\pi} + \delta_\beta, \end{aligned} \tag{5.15}$$

where δ_α, δ_β are energy-independent quantities, connected to g_1 and g_2, cf. Ref. 2.2. Therefore, the energy dependence of the polarizabilities is still given solely by the leading-order pion cloud. Eq. (5.15) promotes the short-distance contributions to α and β from $\mathcal{O}(p^4)$ to $\mathcal{O}(p^3)$. As the loops are isoscalar, we associate purely isoscalar counter-terms which renormalize the loop integrals. In order to avoid confusion we denote the fits done with this procedure as HBχPT $\mathcal{O}(\bar{p}^3)$.

Fits similar to our $\mathcal{O}(\epsilon^3)$ and $\mathcal{O}(\bar{p}^3)$ ones have already been performed in [25], calculating in HBχPT up to $\mathcal{O}(p^4)$. The authors of [25] used all available data sets but had to exclude the two 94.2 MeV data points measured in the backward direction, due to the inadequate description of back-angle Compton scattering in fourth-order HBχPT, cf. Fig. 3.5 and Ref. [54]. As [69, 25] and the $\mathcal{O}(\epsilon^3)$-SSE calculation are not designed to work below 60 MeV, we decided to only include the data around 68 MeV [17, 18] and 94.2 MeV [19] in the fit. We do not make any cuts on the angles and, in contrast to [25], we do not allow the normalizations in the various experiments to float in the fit within their quoted systematic errors.

5.3.1 Wave-Function Dependence of the Fits

To have an estimate on the systematic error in the deuteron fits due to the wave-function dependence, we show our results when we use two different wave functions for the fit: the NNLO chiral wave function [77] and the wave function from the

Nijm93 potential [71]. These wave functions mark the two extremes in our cross sections with the CD-Bonn wave function in between (cf. Fig. 5.12). Therefore, we consider the difference between the two fits using Nijm93 and NNLO χPT as a measure of our wave-function induced error, which is typically of the order of 10 % for $\bar{\alpha}_{E1}$. Higher-order effects are expected to contribute to the systematic error by about $\pm 1 \cdot 10^{-4}$ fm^3 from naïve dimensional analysis, cf. Eq. (3.22), but we refrain for the moment from including this error explicitly into our findings. However, we are aware that it is comparable in size with our statistical error.

We fit the 16 data points using 2 free parameters ($\bar{\alpha}^s_{E1}$ and $\bar{\beta}^s_{M1}$), leaving us with 14 degrees of freedom. Averaging over the results of our 2-parameter SSE fits with the NNLO χPT [77] and the Nijm93 wave function [71], respectively, given in Table 5.1, results in the isoscalar polarizabilities

$$\begin{aligned} \bar{\alpha}^s_{E1} &= (13.2 \pm 1.3\,(\text{stat}) \pm 1.1\,(\text{wf})) \cdot 10^{-4}\ \text{fm}^3\,, \\ \bar{\beta}^s_{M1} &= (1.7 \pm 1.6\,(\text{stat}) \pm 0.2\,(\text{wf})) \cdot 10^{-4}\ \text{fm}^3\,, \end{aligned} \tag{5.16}$$

where we assume the same statistical errors as in Table 5.1. The systematic error due to the differing results when we use different wave functions (wf) is estimated to be half of the difference between the results obtained with the extreme wave functions, i.e. Nijm93 and NNLO χPT. Fitting the γd cross sections using the Nijm93 wave function yields larger results for $\bar{\alpha}_{E1}$ and smaller ones for $\bar{\beta}_{M1}$ with respect to the chiral wave function, but both extractions are in reasonable agreement with the values given in Eq. (1.8) [11].

The results for $\bar{\alpha}^s_{E1}$ and $\bar{\beta}^s_{M1}$, given in Eq. (5.16), correspond to the obviously important short-distance contributions

$$\begin{aligned} \bar{\alpha}^s_{\text{sd}} &= (-4.4 \pm 1.3\,(\text{stat}) \pm 1.1\,(\text{wf})) \cdot 10^{-4}\ \text{fm}^3, \\ \bar{\beta}^s_{\text{sd}} &= (-11.7 \pm 1.6\,(\text{stat}) \pm 0.2\,(\text{wf})) \cdot 10^{-4}\ \text{fm}^3. \end{aligned} \tag{5.17}$$

In Section 3.1.2, we already saw that they are indeed comparable in size with the other leading-order contributions to the polarizabilities, demonstrating the necessity of including the couplings g_1 and g_2 at leading-one-loop order. The plots corresponding to the fits with the chiral wave function are displayed in Fig. 5.15, together with the results of our $\mathcal{O}(\vec{p}^{\,3})$ fits.

Using the experimental values for the proton polarizabilities from [5] as input, one can derive the neutron polarizabilities from the isoscalar ones:

$$\begin{aligned} \bar{\alpha}^n_{E1} &= (14.3 \pm 1.3\,(\text{stat}) \pm 1.1\,(\text{wf})) \cdot 10^{-4}\ \text{fm}^3, \\ \bar{\beta}^n_{M1} &= (1.7 \pm 1.6\,(\text{stat}) \pm 0.2\,(\text{wf})) \cdot 10^{-4}\ \text{fm}^3. \end{aligned} \tag{5.18}$$

From these results we deduce that the isovector polarizabilities are rather small (see Table 5.1), in good agreement with χPT expectations, which predict the isovector part to be of higher than third order. Therefore we find no contradiction anymore between the results from quasi-free [11] and elastic deuteron Compton scattering. Furthermore, our calculation demonstrates that the experiments performed at Illinois [17] and Lund [18] are consistent with the SAL-data [19].

Our results for $\bar{\alpha}^s_{E1}$ and $\bar{\beta}^s_{M1}$ in SSE (cf. Eq. (5.16)) are well consistent with the isoscalar Baldin sum rule

$$\bar{\alpha}^s_{E1} + \bar{\beta}^s_{M1}\Big|_{\text{world av.}} = (14.5 \pm 0.6) \cdot 10^{-4}\ \text{fm}^3, \tag{5.19}$$

which has been a serious problem in former extractions [22, 25], cf. Eq. (5.1). The numerical value for the sum rule is derived from

$$\begin{aligned} \bar{\alpha}^p_{E1} + \bar{\beta}^p_{M1} &= (13.8 \pm 0.4) \cdot 10^{-4}\ \text{fm}^3 \quad [5], \\ \bar{\alpha}^n_{E1} + \bar{\beta}^n_{M1} &= (15.2 \pm 0.5) \cdot 10^{-4}\ \text{fm}^3 \quad [22]. \end{aligned} \tag{5.20}$$

Due to the consistency of our fit results with the sum-rule value from Eq. (5.19), one can in a second step use this number – we use the central value – as an additional fit constraint and thus reduce the number of free parameters to one. The resulting values of the 1-parameter SSE fit (see Table 5.1),

$$\begin{aligned}\bar{\alpha}^s_{E1} &= (13.1 \pm 0.7\,(\text{stat}) \pm 0.8\,(\text{wf}) \pm 0.6\,(\text{Baldin})) \cdot 10^{-4}\ \text{fm}^3\,,\\ \bar{\beta}^s_{M1} &= (1.5 \mp 0.7\,(\text{stat}) \mp 0.8\,(\text{wf}) \pm 0.6\,(\text{Baldin})) \cdot 10^{-4}\ \text{fm}^3\,,\end{aligned} \tag{5.21}$$

are in good agreement with the average of the proton numbers from Table 3.1 and the neutron polarizabilities given in Eq. (1.8).

Comparing our fit results to the isoscalar $\mathcal{O}(p^4)$-HBχPT estimate [16], $\bar{\alpha}^s_{E1} = (11.95 \pm 2.5) \cdot 10^{-4}$ fm^3, $\bar{\beta}^s_{M1} = (5.65 \pm 5.1) \cdot 10^{-4}$ fm^3, cf. Section 1.1, we see only minor deviations in $\bar{\alpha}^s_{E1}$. Our values for $\bar{\beta}^s_{M1}$ are significantly smaller, but still consistent within the (large) error bars of the $\mathcal{O}(p^4)$ estimate.

Amplitudes	Quantity	2-par. fit NNLO χPT	1-par. fit NNLO χPT	2-par. fit Nijm93	1-par. fit Nijm93
$\mathcal{O}(\epsilon^3)$ SSE	$\chi^2/d.o.f.$	1.78	1.67	2.45	2.35
	$\bar{\alpha}^s_{E1}$	12.1 ± 1.3	12.3 ± 0.7	14.3 ± 1.3	13.8 ± 0.7
	$\bar{\beta}^s_{M1}$	1.8 ± 1.6	2.2 ∓ 0.7	1.5 ± 1.6	0.7 ∓ 0.7
	$\bar{\alpha}^s_{E1} + \bar{\beta}^s_{M1}$	13.9 ± 2.1	14.5 (fit)	15.8 ± 2.1	14.5 (fit)
	$\bar{\alpha}^n_{E1}$	12.1 ± 1.3	12.5 ± 0.8	16.5 ± 1.3	15.5 ± 0.8
	$\bar{\beta}^n_{M1}$	2.0 ± 1.6	2.8 ∓ 0.8	1.4 ± 1.6	-0.2 ∓ 0.8
$\mathcal{O}(\bar{p}^3)$ HBχPT	$\chi^2/d.o.f.$	2.14	2.01	2.87	2.75
	$\bar{\alpha}^s_{E1}$	11.0 ± 1.3	11.3 ± 0.7	13.2 ± 1.2	12.7 ± 0.7
	$\bar{\beta}^s_{M1}$	2.8 ± 1.6	3.2 ∓ 0.7	2.5 ± 1.5	1.8 ∓ 0.7
	$\bar{\alpha}^s_{E1} + \bar{\beta}^s_{M1}$	13.8 ± 2.1	14.5 (fit)	15.7 ± 1.9	14.5 (fit)
	$\bar{\alpha}^n_{E1}$	9.9 ± 1.3	10.5 ± 0.8	14.3 ± 1.2	13.3 ± 0.8
	$\bar{\beta}^n_{M1}$	4.0 ± 1.6	4.8 ∓ 0.8	3.4 ± 1.5	2.0 ∓ 0.8

Table 5.1: Values for the isoscalar and neutron polarizabilities (in 10^{-4} fm^3) from a fit to the full 68 MeV and 94.2 MeV data sets [17, 18, 19], using the $\mathcal{O}(\epsilon^3)$-SSE and the $\mathcal{O}(\bar{p}^3)$-HBχPT amplitudes, respectively. The neutron results are derived using the proton values from [5] (Table 3.1) as input. All error bars displayed are only statistical (and added in quadrature).

In the next section we demonstrate that even without an explicit Δ field a good fit of the data can be achieved, however at the cost of an enhanced $\bar{\beta}^s_{M1}$.

5.3.2 Comparison of $\mathcal{O}(\epsilon^3)$-SSE and $\mathcal{O}(\bar{p}^3)$-HBχPT Fits

When we compare the $\mathcal{O}(\epsilon^3)$-SSE fit results for $\bar{\alpha}^s_{E1}$ and $\bar{\beta}^s_{M1}$ with the corresponding $\mathcal{O}(\bar{p}^3)$-HBχPT results (Table 5.1), we see that in the HBχPT fit (cf. Eq. (5.15)) the electric dipole polarizability is smaller, whereas $\bar{\beta}^s_{M1}$ turns out to be larger. The reason for the systematic shift of the magnetic polarizability is that due to the missing $\Delta(1232)$ resonance in HBχPT the static value of $\beta_{M1}(\omega)$ is inflated in order to compensate for the paramagnetic rise of the resonance, which can be clearly seen in Figs. 3.8 and 5.9.

As we see in Fig. 5.15, this compensation works very well in the γd cross sections: the curves, which correspond to the $\mathcal{O}(\epsilon^3)$-SSE and to the $\mathcal{O}(\bar{p}^3)$-HBχPT fits are nearly indistinguishable, i.e. the two fit results only differ in the associated pairs $\bar{\alpha}_{E1}$, $\bar{\beta}_{M1}$. Therefore, from the available γd data alone one cannot draw any firm conclusion regarding the importance of explicit $\Delta(1232)$ degrees of freedom.

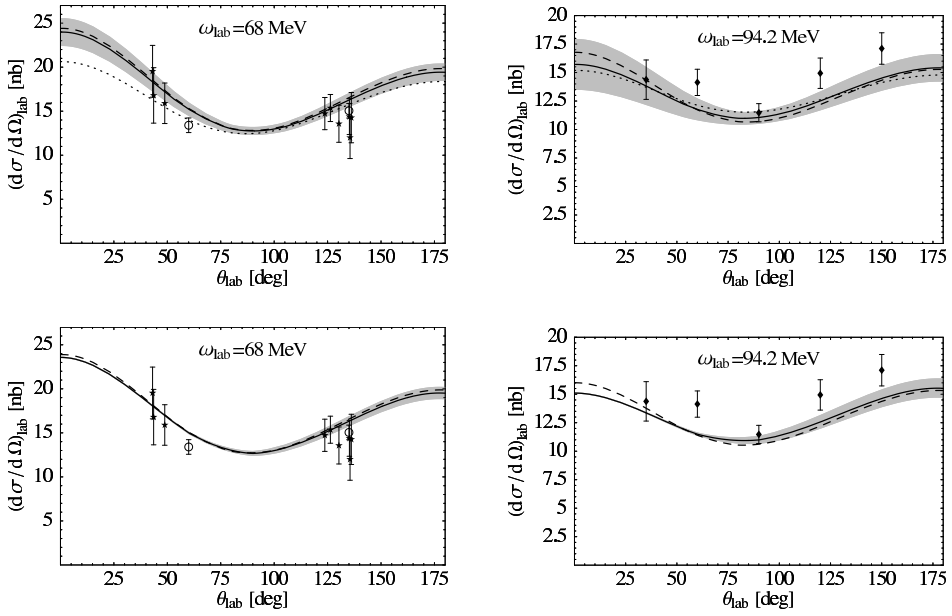

Figure 5.15: $\mathcal{O}(\epsilon^3)$-SSE (solid) and $\mathcal{O}(\bar{p}^3)$-HBχPT (dashed) results with $\bar{\alpha}^s_{E1}$, $\bar{\beta}^s_{M1}$ from Table 5.1, using the chiral NNLO wave function [77]. The upper panels correspond to a fit of both polarizabilities, in the lower panels the Baldin sum rule (cf. Eq. (5.19)) is used as additional fit constraint. The grey bands are derived from our (statistical) errors. The dotted line in the upper panels represents "fit IV", one of the $\mathcal{O}(q^4)$-HBχPT fits from Ref. [25], with central values $\bar{\alpha}^s_{E1} = 11.5$, $\bar{\beta}^s_{M1} = 0.3$. For the $\mathcal{O}(q^4)$ calculation the NLO chiral wave function of Ref. [81] has been used.

However, as we demonstrated in Section 3.1.2, it is clear from γp scattering experiments that third-order HBχPT does not describe the dynamics in the γd process correctly. Given that the SSE calculation describes both the γp and the γd experiments we have shown that a Chiral Effective Field Theory which includes the explicit Δ field is an efficient framework to identify the relevant physics underlying low-energy Compton scattering.

5.3.3 Comparison of $\mathcal{O}(\epsilon^3)$-SSE and $\mathcal{O}(p^4)$-HBχPT Fits

In Fig. 5.15, we also show the $\mathcal{O}(p^4)$-HBχPT fit of Ref. [25]. We consider the quality of our $\mathcal{O}(\bar{p}^3)$ fit to be comparable to those curves. Note that the numbers used for $\bar{\alpha}^s_{E1}$ and $\bar{\beta}^s_{M1}$ in the $\mathcal{O}(p^4)$ curves differ from Eq. (5.1), as they were derived from fitting a different set of data. The values from Eq. (5.1) are the best fit results of Ref. [25] in the sense of the least χ^2, which excluded, however, the two data points at 94.2 MeV in the backward direction. As here we are concerned with all five data points at this energy, we compare to "Fit IV" of Ref. [25] where all of the γd data were fitted.

5.3.4 Why Equal Statistics at all Energies would be Useful

There are eleven data points at $\omega_{\rm lab} \approx 68$ MeV, centered around only two different angles, and five points at $\omega_{\rm lab} \approx 94.2$ MeV, distributed over the whole angular spectrum. Especially at $\theta_{\rm lab} \approx 130^\circ$, the experimental efforts at Lund and Illinois

angle [deg]	$d\sigma/d\Omega$ [nb]
45.6	17.3 ± 1.9
130.5	14.1 ± 1.4

Table 5.2: Effective data points gained by rebinning the 67 MeV data from [18].

to get a large integrated number of counts around 65-69 MeV mean that there is a wealth of data at these energies (six points from [18] and one from [17]), which gives a strong constraint to our fit routines.

In the following we demonstrate what would happen if there were comparable statistics at 94.2 MeV and 68 MeV. Of course we cannot generate data at higher energies. Therefore, we replace in this subsection the Lund data [18] by two "effective" data points (cf. Table 5.2 and Fig. 5.16), which represent the data in the forward and backward direction, respectively. These data have been obtained by *rebinning*[4] the data from [18], and thus the statistical error of the effective data points is reduced with respect to the errors of the individual data points published in [18]. In order to calculate the rebinned data we weight the angles and the differential cross-section values and also the systematic errors of the represented data points by the inverse of their errors, e.g. the cross sections are derived via

$$\frac{d\bar{\sigma}}{d\Omega} = \sum_i \left(\frac{d\sigma}{d\Omega}\right)_i \cdot \frac{1}{\Delta\left(\frac{d\sigma}{d\Omega}\right)_i} \Big/ \sum_i \frac{1}{\Delta\left(\frac{d\sigma}{d\Omega}\right)_i} \tag{5.22}$$

with $\Delta\left(\frac{d\sigma}{d\Omega}\right)_i$ denoting the statistical errors of the rebinned data points. The statistical error of the effective data is obtained as

$$\Delta\left(\frac{d\bar{\sigma}}{d\Omega}\right) = \frac{d\bar{\sigma}}{d\Omega} \Big/ \sqrt{\sum_i \left[\left(\frac{d\sigma}{d\Omega}\right)_i \Big/ \Delta\left(\frac{d\sigma}{d\Omega}\right)_i\right]^2} \,. \tag{5.23}$$

Therefore, the remaining data are the two data points from [17] at 69 MeV, the two "effective" data at $\sim$67 MeV, shown in Table 5.2, representing [18], and the five data points from [19] around 94.2 MeV. With these nine data points we perform the same fits as we did before for the complete data sets. The resulting values for $\bar{\alpha}_{E1}$ and $\bar{\beta}_{M1}$ are presented in Table 5.3. The plots (including the two effective data points), shown in Fig. 5.16, exhibit better agreement with the 94.2 MeV data than the fits of Section 5.3.2 (Fig. 5.15); that is exactly what we expected, because due to the reduced number of data points at 68 MeV, the sensitivity of the fits to the 94.2 MeV data is increased.

The results for the static isoscalar polarizabilities, averaged as before over the two wave functions are

$$\begin{aligned} \bar{\alpha}^s_{E1} &= (12.8 \pm 1.4\,(\text{stat}) \pm 1.1\,(\text{wf})) \cdot 10^{-4}\ \text{fm}^3\,, \\ \bar{\beta}^s_{M1} &= (2.1 \pm 1.7\,(\text{stat}) \pm 0.1\,(\text{wf})) \cdot 10^{-4}\ \text{fm}^3\,. \end{aligned} \tag{5.24}$$

Including the Baldin constraint we get

$$\begin{aligned} \bar{\alpha}^s_{E1} &= (12.6 \pm 0.8\,(\text{stat}) \pm 0.7\,(\text{wf}) \pm 0.6\,(\text{Baldin})) \cdot 10^{-4}\ \text{fm}^3\,, \\ \bar{\beta}^s_{M1} &= (1.9 \mp 0.8\,(\text{stat}) \mp 0.7\,(\text{wf}) \pm 0.6\,(\text{Baldin})) \cdot 10^{-4}\ \text{fm}^3\,. \end{aligned} \tag{5.25}$$

The results of all four extraction methods, given in Eqs. (5.16, 5.21, 5.24, 5.25), agree well with each other, albeit we note that the central values for $\bar{\alpha}_{E1}$ ($\bar{\beta}_{M1}$)

[4] We are indebted to Bent Schröder for valuable comments made on this point.

given in Eqs. (5.24/5.25) are slightly smaller (slightly larger), comparing to the results from our fits to all data points. However, we consider the result from the rebinned data set as more reliable as the procedure weights the 69 MeV data and the 94.2 MeV data in a more equal fashion.

We also see in Table 5.3 once again that the theory without explicit Δ degrees of freedom leads to a systematically larger value for $\bar{\beta}^s_{M1}$ than obtained in the $\mathcal{O}(\epsilon^3)$ fit, supporting our hypothesis that this enhancement is due to insufficient dynamics in the multipoles (cf. Table 5.1). In HBχPT, the static value is artificially enlarged by the fit constraint from the 94.2 MeV data in order to compensate for the missing dynamics. Both in Fig. 5.15 and Fig. 5.16 the enhanced static magnetic dipole polarizability $\bar{\beta}_{M1}$ cures the γd cross sections and makes the resulting curves very similar to the plots from the SSE fits, albeit the resulting picture in the Compton multipoles is very different (see Fig. 3.8).

Therefore, for understanding the available γd data via fits of $\bar{\alpha}^s_{E1}$ and $\bar{\beta}^s_{M1}$, it is essential to combine the pairs $\bar{\alpha}_{E1}$, $\bar{\beta}_{M1}$ resulting from the γd analysis with an energy-dependent multipole analysis of γp scattering. From the information available on Compton multipoles from γp scattering experiments, it is clear that third-order HBχPT is too simplistic a picture for the dynamics of the γd process at energies of $\mathcal{O}$(100 MeV). It is therefore crucial that deuteron and proton Compton experiments are available at comparable energies and that they are analyzed within the same framework.

Putting equal statistical weight on the 68 and the 94.2 MeV data can be seen as a demonstration of the importance of obtaining comparable statistics at all energies. We therefore urge for more experimental information at photon energies around 100 MeV. With such information, deuteron Compton cross sections below the pion mass provide an excellent window to investigate which internal nucleonic degrees of freedom contribute in both processes, $\gamma p \to \gamma p$ and $\gamma d \to \gamma d$.

Amplitudes	Quantity	2-par. fit NNLO χPT	1-par. fit NNLO χPT	2-par. fit Nijm93	1-par. fit Nijm93
$\mathcal{O}(\epsilon^3)$ SSE	$\chi^2/d.o.f.$	2.79	2.47	3.97	3.59
	$\bar{\alpha}^s_{E1}$	11.7 ± 1.4	11.9 ± 0.8	13.8 ± 1.3	13.3 ± 0.7
	$\bar{\beta}^s_{M1}$	2.2 ± 1.7	2.6 ∓ 0.8	2.0 ± 1.6	1.2 ∓ 0.7
	$\bar{\alpha}^s_{E1} + \bar{\beta}^s_{M1}$	13.9 ± 2.2	14.5 (fit)	15.8 ± 2.1	14.5 (fit)
	$\bar{\alpha}^n_{E1}$	11.3 ± 1.4	11.7 ± 0.9	15.5 ± 1.3	14.5 ± 0.8
	$\bar{\beta}^n_{M1}$	2.8 ± 1.7	3.6 ∓ 0.9	2.4 ± 1.6	0.8 ∓ 0.8
$\mathcal{O}(\bar{p}^3)$ HBχPT	$\chi^2/d.o.f.$	3.38	2.98	4.69	4.24
	$\bar{\alpha}^s_{E1}$	10.6 ± 1.3	10.8 ± 0.8	12.7 ± 1.3	12.2 ± 0.8
	$\bar{\beta}^s_{M1}$	3.3 ± 1.7	3.7 ∓ 0.8	3.1 ± 1.6	2.3 ∓ 0.8
	$\bar{\alpha}^s_{E1} + \bar{\beta}^s_{M1}$	13.9 ± 2.1	14.5 (fit)	15.8 ± 2.1	14.5 (fit)
	$\bar{\alpha}^n_{E1}$	9.1 ± 1.3	9.5 ± 0.9	13.3 ± 1.3	12.3 ± 0.9
	$\bar{\beta}^n_{M1}$	5.0 ± 1.7	5.8 ∓ 0.9	4.6 ± 1.6	3.0 ∓ 0.9

Table 5.3: Values for the isoscalar and neutron polarizabilities (in $10^{-4}\,\mathrm{fm}^3$) from a fit to the 68 MeV and 94.2 MeV data sets [17, 19], using the $\mathcal{O}(\epsilon^3)$-SSE and the $\mathcal{O}(\bar{p}^3)$-HBχPT amplitudes, respectively. The data from [18] have been replaced by two effective data points, specified in Table 5.2. The neutron results are derived using the proton values from [5] as input. All error bars displayed are only statistical (and added in quadrature).

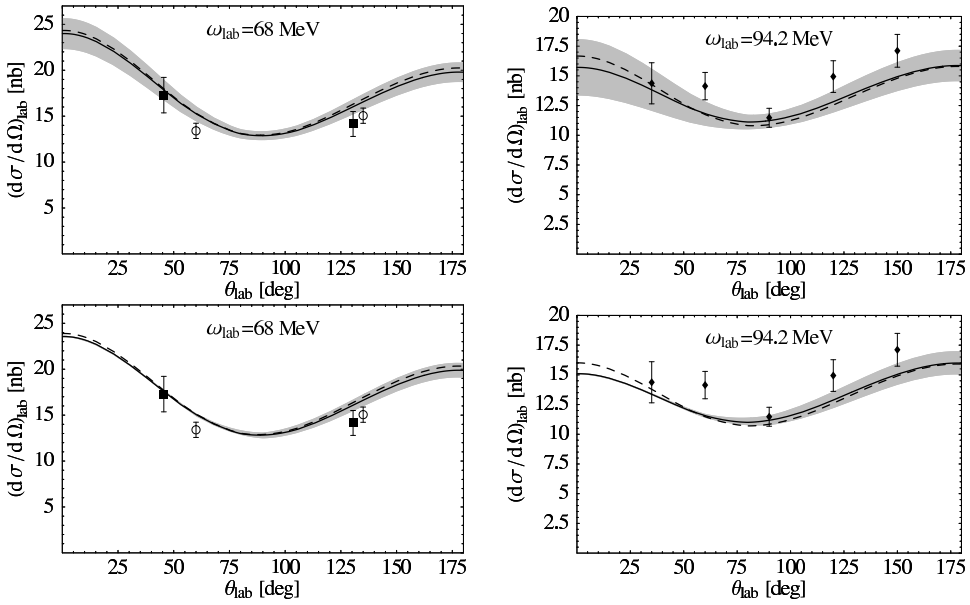

Figure 5.16: $\mathcal{O}(\epsilon^3)$-SSE (solid) and $\mathcal{O}(\bar{p}^3)$-HBχPT (dashed) results with $\bar{\alpha}^s_{E1}$, $\bar{\beta}^s_{M1}$ from Table 5.3, using the chiral NNLO wave function [77]. The upper panels correspond to a fit of both polarizabilities, in the lower panels the Baldin sum rule (cf. Eq. (5.19)) is used as additional fit constraint. The grey bands are derived from our (statistical) errors. The two data points plotted as boxes are the effective data that we use as representatives for the data from [18], cf. Table 5.2.

5.4 Attempts to Restore the Thomson Limit

In Section 5.2, we demonstrated that our calculation provides a good description of the data measured around 68 and 94.2 MeV. However, below a certain energy limit, which we found to be of the order of 50-60 MeV, the approach used in this chapter is not valid anymore. This observation is no surprise, as the power-counting scheme that we apply has been designed for photon energies of the order of the pion mass. Only for such large energies it is possible to approximate the nucleon propagator inside the deuteron by i/ω, whereas the kinetic energy of the nucleon is treated perturbatively. Such a perturbative treatment is always possible in single-nucleon calculations. However, the two nucleons bound in the deuteron have a non-vanishing momentum relative to each other and therefore cannot be treated as static, even if the energy of the external probe is zero. Therefore, only for large photon momenta it is possible to approximate the non-relativistic nucleon propagator $\frac{i}{\omega - p^2/2m_N}$ by i/ω, as already explained in Section 5.1.

From these considerations it becomes obvious that – unlike e.g. the Effective Field Theory with pions integrated out [60, 23] – our calculation cannot reach the correct static limit, i.e. the limit of vanishing photon energy, Eq. (5.4). There are only two contributions to our calculation in this limit: The proton seagull, Fig. 5.5(a), and the pion-exchange diagrams from Fig. 5.7. The first one gives the Thomson limit of the proton, which is larger by a factor of 4 than the correct deuteron limit, cf. Eqs. (5.4) and (5.11). Therefore, one might assume that the pion-exchange diagrams partly cancel this contribution, which is, however, not the case. In contrast, they even enhance the static limit and render the result too large by a factor of 6, a clear signal that gauge invariance is violated [79]. This is shown in Fig. 5.17 by comparing the static cross section of our calculation to

the correct limit as dictated by gauge invariance, given in Eq. (5.4). Although we

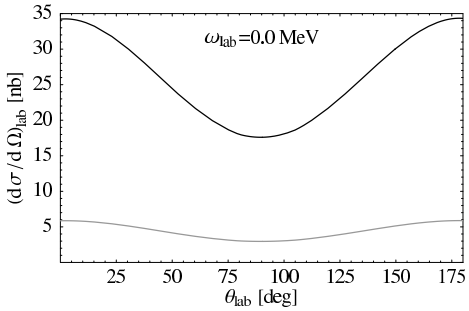

Figure 5.17: Comparison of the static limit of our deuteron Compton calculation (black) to the correct Thomson limit for the deuteron, Eq. (5.4) (grey).

know that our calculation cannot work for small photon energies, this enhancement is surprising. Therefore we undertook some efforts to – at least approximately – restore the correct Thomson limit, which we describe in the following.

So far we used the leading HBχPT approximation i/ω for the nucleon propagator, which is, however, not valid for low photon energies, as explained above. Therefore, we replace the expression i/ω by the full non-relativistic nucleon propagator. We do so in the nucleon-pole diagrams, Fig. 5.5(b), which we sketch once again in Fig. 5.18.

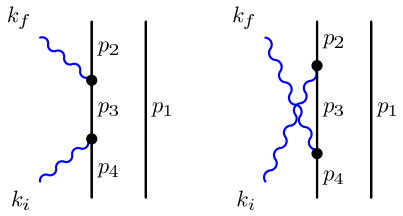

Figure 5.18: Nucleon-pole terms in the s-channel (left) and in the u-channel (right).

In order to calculate the pole diagrams with the full non-relativistic nucleon propagator, we first write down the nucleon 4-momenta corresponding to Fig. 5.18:

$$p_1 = \begin{pmatrix} -\frac{B}{2} + \frac{\omega^2}{8m_N} - p_0 \\ -\vec{p} - \frac{\vec{k}_i}{2} \end{pmatrix}, \quad p_2 = \begin{pmatrix} -\frac{B}{2} + \frac{\omega^2}{8m_N} + p_0 \\ \vec{p} + \frac{\vec{k}_i}{2} - \vec{k}_f \end{pmatrix}, \quad p_4 = \begin{pmatrix} -\frac{B}{2} + \frac{\omega^2}{8m_N} + p_0 \\ \vec{p} - \frac{\vec{k}_i}{2} \end{pmatrix},$$

$$p_3^s = \begin{pmatrix} \omega - \frac{B}{2} + \frac{\omega^2}{8m_N} + p_0 \\ \vec{p} + \frac{\vec{k}_i}{2} \end{pmatrix}, \quad p_3^u = \begin{pmatrix} -\omega - \frac{B}{2} + \frac{\omega^2}{8m_N} + p_0 \\ \vec{p} - \frac{\vec{k}_i}{2} - \vec{k}_f \end{pmatrix}. \tag{5.26}$$

The photon-nucleon vertex is taken from $\mathcal{L}_{\pi N}^{(2)}$, cf. [35]. However, as we are only interested in contributions which do not vanish in the static limit, we may restrict ourselves to

$$\frac{i\,e}{4\,m_N}\,(1+\tau^z)\,\epsilon\cdot(p_a+p_b), \tag{5.27}$$

whereas we neglect the term

$$\frac{i\,e}{2\,m_N}\,[S\cdot\epsilon, S\cdot k]\,(1+\kappa_s+(1+\kappa_v)\,\tau^z)\,. \tag{5.28}$$

After evaluating the p_0-integral (we close the contour via the four-momentum p_1), we find for the two amplitudes

$$T^s(\vec{k}_i,\vec{k}_f;\vec{p}) = -\frac{e^2}{m_N^2}\,\vec{\epsilon}\,'\cdot(\vec{p}+\vec{k}_i/2)\,\vec{\epsilon}\cdot\vec{p}\,\frac{1}{\omega - B - \frac{\vec{p}^{\,2}+\vec{p}\cdot\vec{k}_i}{m_N}}, \tag{5.29}$$

$$T^u(\vec{k}_i,\vec{k}_f;\vec{p}) = -\frac{e^2}{m_N^2}\,\vec{\epsilon}\cdot(\vec{p}-\vec{k}_f)\,\vec{\epsilon}\,'\cdot(\vec{p}-\vec{k}_i/2)\,\frac{1}{-\omega - B - \frac{\omega^2+\vec{k}_i\cdot\vec{k}_f+2\vec{p}^{\,2}-2\vec{p}\cdot\vec{k}_f}{2m_N}}. \tag{5.30}$$

Note that Eqs. (5.29, 5.30) do give non-vanishing contributions in the static limit, whereas in the approximation i/ω they cancel each other exactly for $\omega = |\vec{k}| = 0$.

So far, we have been counting the nucleon propagator as $\mathcal{O}(\epsilon^{-1})$. However, when we look at the propagator of e.g. Eq. (5.29), we see that for small photon energies this counting is not justified anymore. For $\omega \to 0$, the dominant part in the denominator of the propagator is $\vec{p}^{\,2}/m_N$. Therefore, in the low-energy regime one has to count the nucleon propagator as $\mathcal{O}(\epsilon^{-2})$, as already discussed in Section 5.1. In this counting scheme, however, there are many additional pion-exchange diagrams at $\mathcal{O}(\epsilon^3)$, which contribute in the static limit. All these diagrams are sketched in Fig. 5.19, distributed into several classes (class 1 corresponds to the diagrams of Fig. 5.7).

The calculation of the amplitudes corresponding to Fig. 5.19 is straightforward. Again we only include the part of the photon-nucleon coupling which does not vanish with the photon energy, Eq. (5.27), and of course we use the full nucleon propagator. The results are given in Appendix E. Including them in our calculation, together with the corrected nucleon-pole terms, leads to the static limit shown in Fig. 5.20. We see that these contributions help to come closer to the Thomson limit, but still we lack a factor of nearly 2. In Chapter 6 we show that this discrepancy is resolved when we include the full two-nucleon Green's function G in the intermediate state, cf. Eq. (5.2), i.e. we allow the two nucleons to rescatter. Therefore we now close our efforts to reach the exact static limit and postpone this challenge to Chapter 6 (Section 6.2).

In this chapter we reported a calculation of elastic deuteron Compton scattering, using a so-called hybrid approach, i.e. we calculated the interaction kernel according to the rules of perturbative Effective Field Theory in the Small Scale Expansion, and folded this kernel with deuteron wave functions derived from modern NN-potentials. We found good agreement with experimental data at photon energies above 60 MeV and thus fitted the Compton cross sections to these data in order to determine the isoscalar nucleon polarizabilities. The results are in good agreement with the expectation that the isovector polarizabilities are small. However, there are also certain shortcomings of this approach: As it is designed for photon energies of the order of the pion mass, our calculation fails to describe the data below 60 MeV and also violates the well-known low-energy theorem for deuteron Compton scattering. Furthermore, our results show a stronger sensitivity on the deuteron wave function than we expected. Therefore we turn now to a partly different approach to deuteron Compton scattering, including rescattering of the two nucleons, and we will find that all three disadvantages can be cured within this framework.

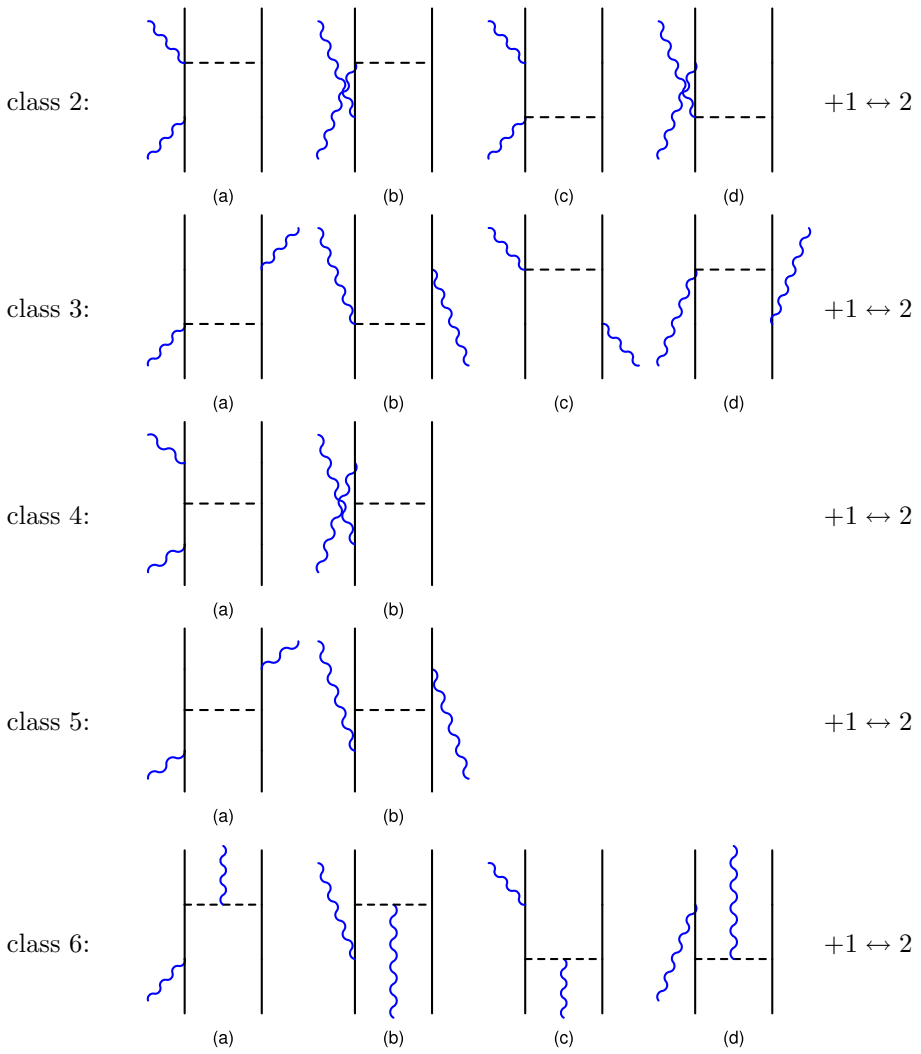

Figure 5.19: Additional pion-exchange diagrams which appear at $\mathcal{O}(\epsilon^3)$ in the low-energy regime.

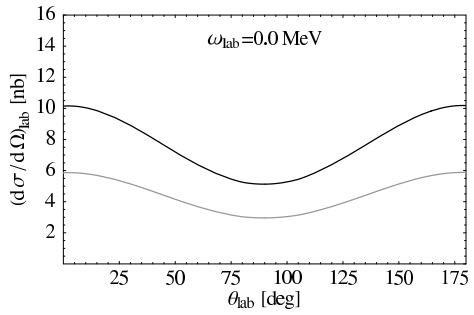

Figure 5.20: Attempt to restore the Thomson limit. The grey line marks the correct static limit for the deuteron, Eq. (5.4). The black line is our result with the nucleon-pole diagrams calculated with the exact nucleon propagator and also including the diagrams of Fig. 5.19.

Chapter 6

Non-Perturbative Approach to Deuteron Compton Scattering

In this chapter we go beyond the strictly perturbative approach to deuteron Compton scattering described in the previous chapter, in which gauge invariance was not manifest, leading to a violation of the low-energy theorem and a surprisingly strong dependence on the deuteron wave function. We do so by use of non-perturbative methods, summing over all possible np-intermediate states, in combination with coupling the photon field to the two nucleons in a more complete manner than in Chapter 5. This part of our calculation follows closely the work of J. Karakowski and G.A. Miller [24][1]. The results of this chapter are contained in Ref. [82].

6.1 Theoretical Framework

The main difference to the previous, perturbative expansion of the interaction kernel is that we now allow the two nucleons in the intermediate state to interact with each other, i.e. to rescatter, whereas such processes contribute only at higher orders in the power counting applied in Chapter 5. Diagrammatically, this difference is expressed by replacing the nucleon pole diagrams (cf. Fig. 5.5(b)) by analogous diagrams with interacting nucleons between the two photon vertices. We distinguish between the two scenarios – with and without rescattering – in Fig. 6.1 by a square, denoting the np-potential. In other words, we no longer do a perturbative treatment of the two-nucleon Green's function G which is contained in the two-nucleon reducible part of the interaction kernel $K_\gamma G K_\gamma$, cf. Eq. (5.2). In the next two sections we explain how to calculate the thus modified nucleon-pole diagrams.

6.1.1 Dominant Diagrams with Intermediate NN-Scattering

The diagrams shown in Fig. 6.1 are calculated using second-order time-ordered perturbation theory in the two-photon interaction, while the intermediate two-nucleon system is treated non-perturbatively. In general, the scattering amplitude for these

[1] We note that the sign convention of Ref. [24] for the deuteron Compton amplitude is different from ours. This difference will show up several times in our work. We fix the relative sign via the proton seagull diagram, Fig. 5.5(a).

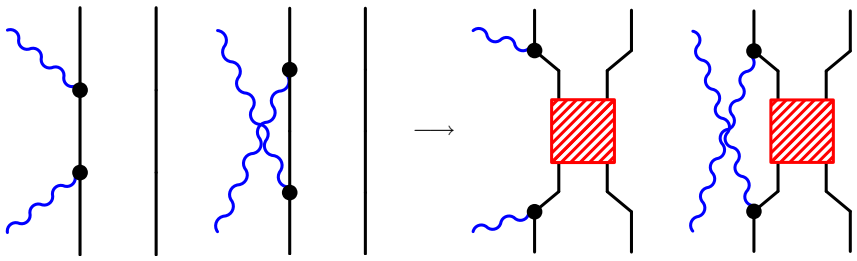

Figure 6.1: Sketch of the main difference between the purely perturbative approach to the deuteron Compton kernel used in Chapter 5 and the non-perturbative calculation described in this chapter. The square symbolises the possible interaction of the two nucleons.

processes can be written as

$$\mathcal{M}_{fi} = \sum_C \left\{ \frac{\langle\, d_f, \gamma_f \mid H^{\rm int} \mid C \,\rangle \langle\, C \mid H^{\rm int} \mid d_i, \gamma_i \,\rangle}{\omega + \frac{\omega^2}{2m_d} - B - E_C - \frac{\vec{P}_C^{\,2}}{2m_C}} + \frac{\langle\, d_f, \gamma_f \mid H^{\rm int} \mid C, \gamma_f, \gamma_i \,\rangle \langle\, C, \gamma_f, \gamma_i \mid H^{\rm int} \mid d_i, \gamma_i \,\rangle}{-\omega + \frac{\omega^2}{2m_d} - B - E_C - \frac{\vec{P}_C^{\,2}}{2m_C}} \right\} . \tag{6.1}$$

The amplitude is constructed by writing down (from right to left) the deuteron in the initial state, the interaction Hamiltonian which describes the coupling of the incoming (outgoing) photon, intermediate states C which are summed over, another interaction Hamiltonian and the final-state deuteron. In the denominator, the energy of the intermediate nucleons appears. Note that – as in Chapter 5 – we calculate the amplitudes in the γd-cm frame. Therefore, the incoming and outgoing photons have the same energy. The energies appearing in the intermediate state of the s-channel diagram (the first diagram on both sides of Fig. 6.1, corresponding to the first amplitude in Eq. (6.1)) are as follows:

- the photon energy $+\omega$
- the deuteron energy $-B$ with $B \approx 2.225$ MeV denoting the deuteron binding energy
- the excitation energy of the intermediate state C, $-E_C$
- the kinetic energy of the incoming deuteron $+\frac{\omega^2}{2m_d}$ with $m_d = 2m_N - B$ the deuteron mass (in the γd-cm frame, $\vec{P}_i = -\vec{k}_i$ with $\vec{P}_i$ ($\vec{k}_i$) the initial deuteron (photon) momentum)
- the kinetic energy $-\frac{\vec{P}_C^{\,2}}{2m_C}$ of the intermediate two-nucleon system (for our numerical evaluations we use $m_C = 2m_N$)

In the u-channel, the same energy denominator appears, except for the replacement $\omega \to -\omega$. As we calculate in the cm frame of the γd system, we have $\frac{\vec{P}_C^{\,2}}{2m_C} = 0$ in the s-channel diagram, whereas $\vec{P}_C = -\vec{k}_i - \vec{k}_f$ in the u-channel, i.e. $\frac{\vec{P}_C^{\,2}}{2m_C} = \frac{\omega^2}{m_C}(1 + \cos\theta)$. Therefore, an amplitude containing $\vec{P}_C^{\,2}$ always corresponds to a u-channel diagram throughout this work.

The interaction Hamiltonian is given by

$$H^{\rm int} = -\int \vec{J}(\vec{\xi}\,)\cdot\vec{A}(\vec{\xi}\,)\,d^3\xi. \tag{6.2}$$

For the photon field $\vec{A}(\vec{\xi}\,)$, we use the multipole expansion derived in [24] in analogy to Chapter 7 of Ref. [83], see also Appendix F. The result is

$$\begin{aligned}\hat{\epsilon}_\lambda\,{\rm e}^{i\vec{k}\cdot\vec{\xi}} = \sum_{L=1}^{\infty}\sum_{M=-L}^{L} d^L_{M,\lambda}(\theta)\,i^L\sqrt{\frac{2\pi\,(2L+1)}{L\,(L+1)}} \\ \times\left\{-\frac{i}{\omega}\,\vec{\nabla}_\xi\,\psi_L(\omega\xi)\,Y_{L\,M}(\hat{\xi}) - i\,\omega\,\vec{\xi}\,j_L(\omega\xi)\,Y_{L\,M}(\hat{\xi}) - \lambda\,\vec{L}\,Y_{L\,M}(\hat{\xi})\,j_L(\omega\xi)\right\},\end{aligned} \tag{6.3}$$

cf. Eq. (F.28). Note that in this chapter we use photon polarization-vectors given in the spherical basis, Eq. (L.10), which we denote by $\hat{\epsilon}$, whereas so far we used Cartesian polarization vectors, written as $\vec{\epsilon}$. The functions $d^L_{M,\lambda}(\theta)$ are part of the Wigner D-functions, as explained in detail in Appendix F, $Y_{L\,M}$ denote the spherical harmonics and $\psi_L(\omega r) = (1 + r\,\frac{d}{dr})\,j_L(\omega r)$ with the spherical Bessel functions $j_L(z)$ defined in Eq. (L.29). In the static (long-wavelength) limit only the gradient term in Eq. (6.3) survives, as for $\omega \to 0$, $j_1(\omega r) \to \frac{1}{3}\,\omega r$ and $\psi_1(\omega r) \to \frac{2}{3}\,\omega r$. This term will turn out to be the dominant part of the photon field for all energies under consideration. Therefore, we define two scalar functions

$$\begin{aligned}\phi_i(\vec{r}) &= -\sum_{L=1}^{\infty}\sum_{M=-L}^{L}\delta_{M,\lambda_i}\,\frac{i^{L+1}}{\omega}\sqrt{\frac{2\pi\,(2L+1)}{L\,(L+1)}}\,\psi_L(\omega r)\,Y_{L\,M}(\hat{r}), \\ \phi_f(\vec{r}) &= \sum_{L'=1}^{\infty}\sum_{M'=-L'}^{L'}(-1)^{L'-\lambda_f}\,d^{L'}_{M',-\lambda_f}(\theta)\,\frac{i^{L'+1}}{\omega}\sqrt{\frac{2\pi\,(2L'+1)}{L'\,(L'+1)}}\,\psi_{L'}(\omega r)\,Y_{L'\,M'}(\hat{r}),\end{aligned} \tag{6.4}$$

which allow us to write

$$\begin{aligned}\hat{\epsilon}_{\lambda_i}\,{\rm e}^{i\vec{k}_i\cdot\vec{\xi}} &\approx \vec{\nabla}\phi_i(\vec{\xi}), \\ \hat{\epsilon}^*_{\lambda_f}\,{\rm e}^{-i\vec{k}_f\cdot\vec{\xi}} &\approx \vec{\nabla}\phi_f(\vec{\xi}),\end{aligned} \tag{6.5}$$

cf. Eqs. (F.29) and (F.32). The largest contributions to Eq. (6.1) are thus the ones where we replace $\vec{A}(\vec{\xi}\,) \to \vec{\nabla}\phi(\vec{\xi}\,)$ in both interaction Hamiltonians. Further terms, where the replacement $\vec{A}(\vec{\xi}\,) \to \vec{\nabla}\phi(\vec{\xi}\,)$ is made only once, are calculated in Appendices H and I. Only a few combinations of interactions without the gradient part of $\vec{A}$ give sizeable contributions. These are also calculated in Appendices H and I.

In this section, however, we calculate Eq. (6.1) with $H^{\rm int} \to -\int \vec{J}(\vec{\xi}\,)\cdot\vec{\nabla}\phi(\vec{\xi}\,)\,d^3\xi$ simultaneously at both vertices, i.e. we restrict ourselves to the terms arising from minimal coupling. In order to simplify the calculation on one hand, and to ensure gauge invariance and the correct Thomson limit on the other, we integrate by parts and use current conservation:

$$-\int \vec{J}(\vec{\xi}\,)\cdot\vec{\nabla}\phi(\vec{\xi}\,)\,d^3\xi = \int \vec{\nabla}\cdot\vec{J}(\vec{\xi}\,)\,\phi(\vec{\xi}\,)\,d^3\xi \tag{6.6}$$

$$\vec{\nabla}\cdot\vec{J}(\vec{\xi}\,) = -\frac{\partial\rho(\vec{\xi}\,)}{\partial t} = -i\left[H, \rho(\vec{\xi}\,)\right] \tag{6.7}$$

The fact that we only need to know the charge density ρ in order to calculate the amplitude in the long-wavelength limit is referred to as "Siegert's theorem" [84].

For $\rho(\vec{\xi})$ one can find in Section 8.3 of Ref. [57] the general separation

$$\rho(\vec{\xi}) = \rho^{(0)}(\vec{\xi}) + \rho^{\rm ex}(\vec{\xi}; \vec{x}_1, \vec{x}_2) \tag{6.8}$$

with $\rho^{(0)}$ the charge density of the two nucleons and $\vec{x}_1$, $\vec{x}_2$ the position of nucleon 1 and 2, respectively. $\rho^{\rm ex}(\vec{\xi}; \vec{x}_1, \vec{x}_2)$ is the charge density due to meson-exchange currents. The dominant term in Eq. (6.8) is

$$\rho^{(0)}(\vec{\xi}) = \sum_{j=n,p} e_j \, \delta(\vec{\xi} - \vec{x}_j) = e \, \delta(\vec{\xi} - \vec{x}_p), \tag{6.9}$$

which is the only non-vanishing contribution to $\rho(\vec{\xi})$ in the static limit ("Siegert's hypothesis" [84]). Note that the δ-functions in Eq. (6.9) indicate that the two nucleons are treated as pointlike particles, i.e. we do not introduce any form factors as e.g. the authors of Ref. [22]. We also performed calculations including $\rho^{\rm ex}(\vec{\xi}; \vec{x}_1, \vec{x}_2)$. From these investigations, which are reported in Appendix J, we conclude that $\rho^{\rm ex}$ is negligible in the energy range considered. Therefore in the following we are only concerned with $\rho^{(0)}(\vec{\xi})$.

Albeit it is not obvious, meson-exchange currents (cf. Fig. 6.2) are also implicitly included in the calculation, as by the continuity equation (6.7)

$$\vec{\nabla} \cdot \vec{J}^{\rm ex} = -i \left[V^{\rm ex} \, \vec{\tau}_1 \cdot \vec{\tau}_2, \rho^{(0)} \right] - i \, [H, \rho^{\rm ex}] \tag{6.10}$$

with the np-potential from one-pion exchange $V^{\rm ex}$ [57], which is part of the Hamiltonian H. $\vec{\tau}_i$ is the isospin operator of the ith nucleon. Therefore, the diagrams

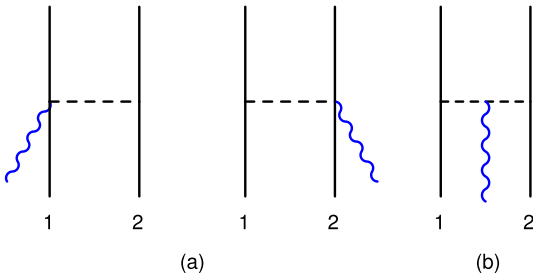

Figure 6.2: One-pion-exchange currents contributing to our calculation: the "Kroll-Ruderman current" (a) and the "pion-pole current" (b).

sketched in Fig. 6.1, which show only one-body currents, are to be replaced by Fig. 6.3, which includes the two-body exchange currents, Fig. 6.2. The np-potential is again sketched as a square.

Substituting $\vec{\nabla} \cdot \vec{J}$ by $-i \left[H, \rho^{(0)} \right]$ in Eq. (6.6), the integral over the dummy variable $\vec{\xi}$ can easily be performed to yield

$$H^{\rm int} \approx - \int \vec{J}(\vec{\xi}) \cdot \vec{\nabla} \phi(\vec{\xi}) \, d^3\xi = -i \, [H, e \, \phi(\vec{x}_p)] \, , \tag{6.11}$$

where H is the full Hamiltonian of the np-system

$$H = \frac{\vec{p}_p^{\,2}}{2m_p} + \frac{\vec{p}_n^{\,2}}{2m_n} + V \tag{6.12}$$

with the np-potential V including $V^{\rm ex}$, cf. Eq. (6.10). With $\vec{p}_p = -i\vec{\nabla}_{x_p}$ and $\vec{\nabla}^2_{x_p} \phi(\vec{x}_p) \approx 0$ for real photons (cf. Eq. (6.5)), the part of the commutator containing

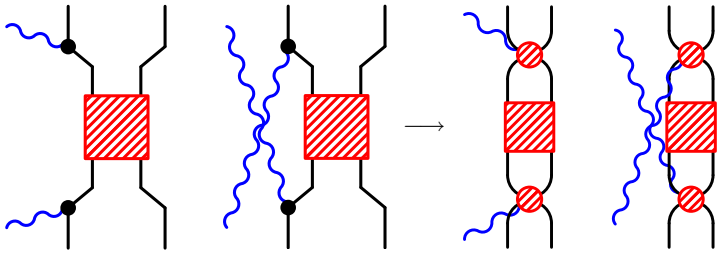

Figure 6.3: Sketch of the diagrams arising from the replacement $\vec{A} \to \vec{\nabla}\phi$ at both vertices simultaneously. The blobs denote coupling to the one-body current and possible one-pion exchange, the square symbolises the *np*-potential.

the proton kinetic energy yields

$$H^{\mathrm{int},p} = -i\left[\frac{\vec{p}_p^{\,2}}{2m_p}, e\,\phi(\vec{x}_p)\right] = -\frac{e}{m_p}\,\vec{\nabla}_{x_p}\phi(\vec{x}_p)\cdot\vec{p}_p \approx -\frac{e}{m_p}\,\vec{A}(\vec{x}_p)\cdot\vec{p}_p. \tag{6.13}$$

This approximate relation becomes exact in the extreme long-wavelength limit, where only the gradient part of $\vec{A}$ contributes, as explained after Eq. (6.3). Therefore, the operators responsible for electric dipole ($E1$) transitions are contained in the commutators of H and ϕ. In order to evaluate the commutator (6.11), we now switch to cm variables, i.e.

$$\vec{p} = \frac{\vec{p}_p - \vec{p}_n}{2}, \quad \vec{P} = \vec{p}_p + \vec{p}_n, \quad \vec{r} = \vec{x}_p - \vec{x}_n, \quad \vec{R} = \frac{\vec{x}_p + \vec{x}_n}{2}. \tag{6.14}$$

Omitting the *np*-potential V for the moment we find

$$\begin{aligned} H^{\mathrm{int}}_{\mathrm{kin}} &= -i\left[\frac{\vec{p}_p^{\,2}}{2m_p} + \frac{\vec{p}_n^{\,2}}{2m_n}, e\,\phi(\vec{x}_p)\right] = -i\left[\frac{\vec{p}_p^{\,2}}{2m_p}, e\,\phi(\vec{x}_p)\right] \\ &= -\frac{e}{m_p}\,\vec{\nabla}_{x_p}\phi(\vec{x}_p)\cdot\left(\vec{p} + \vec{P}/2\right). \end{aligned} \tag{6.15}$$

The term including the total momentum operator $\vec{P}$ is a recoil correction and has been calculated in [24]. Our evaluation of this term showed that its contribution to the cross section is invisibly small. Therefore we neglect such corrections throughout this work.

The cm coordinate $\vec{R}$ only gives rise to a momentum-conserving δ-function, which has to be separated off the scattering amplitude, cf. [24]. Therefore we may set $\vec{R} = \vec{0}$, i.e. we neglect the cm velocity of the two nucleons, which means that $\vec{x}_p = \frac{\vec{r}}{2}$, $\vec{x}_n = -\frac{\vec{r}}{2}$. Note that this procedure is consistent with neglecting the recoil corrections in Eq. (6.15). Now we can simplify this equation further:

$$\begin{aligned} -\frac{e}{m_p}\,\vec{\nabla}_{x_p}\phi(\vec{x}_p)\cdot\vec{p} &= -\frac{e}{m_p}\left(\vec{\nabla}_{x_p} - \vec{\nabla}_{x_n}\right)\phi(\vec{x}_p)\cdot\vec{p} \\ &= -i\frac{e}{m_p}\,2\vec{p}\,\phi(\vec{r}/2)\cdot\vec{p} = -i\left[\frac{\vec{p}^{\,2}}{m_p}, e\,\phi(\vec{r}/2)\right] \end{aligned} \tag{6.16}$$

Defining the "internal" Hamiltonian

$$H^{np} = \frac{\vec{p}^{\,2}}{m_p} + V, \tag{6.17}$$

which is identical to Eq. (6.12) under the assumption $\vec{p}_p = -\vec{p}_n$, we end up with

$$H^{\rm int} = -i\,[H^{np}, e\,\phi(\vec{r}/2)]\,. \tag{6.18}$$

This expression is equivalent to Eq. (6.11), neglecting the cm motion of the deuteron. Inserting the commutator (6.18) into Eq. (6.1) and defining $\hat{\phi}_i = e\,\phi_i(\vec{r}/2)$, $\hat{\phi}_f = e\,\phi_f(\vec{r}/2)$ in analogy to [24] we get (remember, $\frac{\vec{P}_C^{\,2}}{2m_C} = 0$ in the s-channel diagram)

$$\begin{aligned}\mathcal{M}_{fi}^{\phi\phi} = -\sum_C \Bigg\{ & \frac{\langle\, d_f \mid \left[H^{np}, \hat{\phi}_f\right] \mid C\,\rangle\langle\, C \mid \left[H^{np}, \hat{\phi}_i\right] \mid d_i\,\rangle}{\omega + \frac{\omega^2}{2m_d} - B - E_C} \\ & + \frac{\langle\, d_f \mid \left[H^{np}, \hat{\phi}_i\right] \mid C\,\rangle\langle\, C \mid \left[H^{np}, \hat{\phi}_f\right] \mid d_i\,\rangle}{-\omega + \frac{\omega^2}{2m_d} - B - E_C - \frac{\vec{P}_C^{\,2}}{2m_C}} \Bigg\}. \end{aligned} \tag{6.19}$$

In order to keep track of the various combinations of interaction Hamiltonians we have labelled the double-ϕ transition matrix '$\phi\phi$'; the photon states have been skipped for brevity. Now the commutators are expanded and, as $\mid d_{i,f}\,\rangle$, $\mid C\,\rangle$ are eigenstates of H^{np}, we can act with H^{np} on these states. Looking only at the s-channel term for the moment we find that

$$\begin{aligned}\mathcal{M}_{fi}^{\phi\phi,s} = -\sum_C \Bigg\{ & \frac{1}{2}\frac{\langle\, d_f \mid (-B - E_C)\,\hat{\phi}_f \mid C\,\rangle\langle\, C \mid \left[H^{np}, \hat{\phi}_i\right] \mid d_i\,\rangle}{\omega + \frac{\omega^2}{2m_d} - B - E_C} \\ & + \frac{1}{2}\frac{\langle\, d_f \mid \left[H^{np}, \hat{\phi}_f\right] \mid C\,\rangle\langle\, C \mid (E_C + B)\,\hat{\phi}_i \mid d_i\,\rangle}{\omega + \frac{\omega^2}{2m_d} - B - E_C} \Bigg\}. \end{aligned} \tag{6.20}$$

Now we add and subtract terms in order to perform some cancellations against the denominator. In the resulting expressions without energy denominator, the sum over C can be collapsed. In the other terms, the remaining commutator is expanded and again some cancellations against the energy denominator are made. We find

$$\begin{aligned}\mathcal{M}_{fi}^{\phi\phi,s} = & \frac{1}{2}\langle\, d_f \mid \left[H^{np}, \hat{\phi}_f\right]\,\hat{\phi}_i \mid d_i\,\rangle - \frac{1}{2}\langle\, d_f \mid \hat{\phi}_f\,\left[H^{np}, \hat{\phi}_i\right] \mid d_i\,\rangle \\ & - \left(\omega + \frac{\omega^2}{2m_d}\right)\langle\, d_f \mid \hat{\phi}_f\,\hat{\phi}_i \mid d_i\,\rangle + \left(\omega + \frac{\omega^2}{2m_d}\right)^2 \sum_C \frac{\langle\, d_f \mid \hat{\phi}_f \mid C\,\rangle\langle\, C \mid \hat{\phi}_i \mid d_i\,\rangle}{\omega + \frac{\omega^2}{2m_d} - B - E_C}. \end{aligned} \tag{6.21}$$

The u-channel amplitude is derived via $\omega + \frac{\omega^2}{2m_d} \to -\omega - \frac{\vec{P}_C^{\,2}}{2m_C} + \frac{\omega^2}{2m_d}$, $\hat{\phi}_i \leftrightarrow \hat{\phi}_f$ as

$$\begin{aligned}\mathcal{M}_{fi}^{\phi\phi,u} = & \frac{1}{2}\langle\, d_f \mid \left[H^{np}, \hat{\phi}_i\right]\,\hat{\phi}_f \mid d_i\,\rangle - \frac{1}{2}\langle\, d_f \mid \hat{\phi}_i\,\left[H^{np}, \hat{\phi}_f\right] \mid d_i\,\rangle \\ & + \left(\omega + \frac{\vec{P}_C^{\,2}}{2m_C} - \frac{\omega^2}{2m_d}\right)\langle\, d_f \mid \hat{\phi}_i\,\hat{\phi}_f \mid d_i\,\rangle \\ & + \left(\omega + \frac{\vec{P}_C^{\,2}}{2m_C} - \frac{\omega^2}{2m_d}\right)^2 \sum_C \frac{\langle\, d_f \mid \hat{\phi}_i \mid C\,\rangle\langle\, C \mid \hat{\phi}_f \mid d_i\,\rangle}{-\omega - \frac{\vec{P}_C^{\,2}}{2m_C} + \frac{\omega^2}{2m_d} - B - E_C}. \end{aligned} \tag{6.22}$$

Adding the amplitudes (6.21) and (6.22) we get ($\hat{\phi}_i\,\hat{\phi}_f = \hat{\phi}_f\,\hat{\phi}_i$)

$$\mathcal{M}_{fi}^{\phi\phi 1} = \left(\omega + \frac{\omega^2}{2m_d}\right)^2 \sum_C \frac{\langle\, d_f \mid \hat{\phi}_f \mid C\,\rangle\langle\, C \mid \hat{\phi}_i \mid d_i\,\rangle}{\omega + \frac{\omega^2}{2m_d} - B - E_C}, \tag{6.23}$$

$$\mathcal{M}_{fi}^{\phi\phi 2} = \left(\omega + \frac{\vec{P}_C^{\,2}}{2m_C} - \frac{\omega^2}{2m_d}\right)^2 \sum_C \frac{\langle\, d_f \mid \hat{\phi}_i \mid C\,\rangle\langle\, C \mid \hat{\phi}_f \mid d_i\,\rangle}{-\omega - \frac{\vec{P}_C^{\,2}}{2m_C} + \frac{\omega^2}{2m_d} - B - E_C}, \tag{6.24}$$

$$\mathcal{M}_{fi}^{\phi\phi 3} = \left(\frac{\vec{P}_C^{\,2}}{2m_C} - \frac{\omega^2}{m_d}\right) \langle\, d_f \mid \hat{\phi}_f\,\hat{\phi}_i \mid d_i\,\rangle, \tag{6.25}$$

$$\mathcal{M}_{fi}^{\phi\phi 4} = \frac{1}{2}\langle\, d_f \mid \left[\left[H^{np}, \hat{\phi}_i\right], \hat{\phi}_f\right] + \left[\left[H^{np}, \hat{\phi}_f\right], \hat{\phi}_i\right] \mid d_i\,\rangle. \tag{6.26}$$

These four amplitudes have already been derived in [24], albeit in the lab frame. $\mathcal{M}_{fi}^{\phi\phi 4}$ is the only one which contributes in the static limit, since for $\omega = 0$ also $\vec{P}_C^{\,2} = 0$. It is responsible for the correct low-energy behaviour of the calculation, as will be discussed in great detail in Section 6.2.

$\mathcal{M}_{fi}^{\phi\phi 1}$ will be calculated first. Defining the shortcut $E_0 \equiv \omega + \frac{\omega^2}{2m_d} - B$ and neglecting prefactors for the moment we can write this amplitude as

$$\mathcal{M}_{fi}^{\phi\phi 1} \propto \sum_C \frac{\langle\, d_f \mid \psi_{L'}\, Y_{L'\,M'} \mid C\,\rangle\langle\, C \mid \psi_L\, Y_{L\,M} \mid d_i\,\rangle}{E_0 - E_C}, \tag{6.27}$$

where we suppressed the sums over L, M and L', M' for brevity, cf. Eq. (6.4). Each wave function can be separated into a radial part, denoted by the index 'rad', and an angular part, denoted by a hat. Furthermore, $\mid C\,\rangle$ is an eigenstate to H^{np} with eigenvalue E_C, so we can write

$$\mathcal{M}_{fi}^{\phi\phi 1} \propto \sum_{C_{\mathrm{rad}}\,\hat{C}} \langle\, d_{f\,\mathrm{rad}}\,\hat{d}_f \mid \psi_{L'}\, Y_{L'\,M'}\, \frac{1}{E_0 - H^{np}_{\hat{C}}} \mid C_{\mathrm{rad}}\,\hat{C}\,\rangle\langle\, C_{\mathrm{rad}}\,\hat{C} \mid \psi_L\, Y_{L\,M} \mid d_{i\,\mathrm{rad}}\,\hat{d}_i\,\rangle. \tag{6.28}$$

$\hat{C}$ is used as a shorthand notation for all angular quantum numbers of the intermediate state, i.e. $\mid \hat{C}\,\rangle = \mid L_C\, S_C\, J_C\, M_C\,\rangle$. After acting with the Hamiltonian on the angular state $\mid \hat{C}\,\rangle$, which will be explained in detail in Eq. (6.37), H^{np} depends on the quantum numbers of the intermediate state $\mid C\,\rangle$. However, the only differential operator in H^{np} is a radial one. Therefore we may separate the radial from the angular part of $\mid C\,\rangle$. Finally we insert two complete sets of radial states $\mid r\,\rangle$ and $\mid r'\,\rangle$ to get

$$\begin{aligned}\mathcal{M}_{fi}^{\phi\phi 1} \propto \sum_{C_{\mathrm{rad}}\,\hat{C}} \int_0^\infty \int_0^\infty r^2 dr\, r'^2 dr' \langle\, \hat{d}_f \mid Y_{L'\,M'} \mid \hat{C}\,\rangle\langle\, d_{f\mathrm{rad}} \mid \psi_{L'} \mid r'\,\rangle \\ \times \langle\, r' \mid \frac{1}{E_0 - H^{np}_{\hat{C}}} \mid C_{\mathrm{rad}}\,\rangle\langle\, C_{\mathrm{rad}} \mid r\,\rangle\langle\, r \mid \psi_L \mid d_{i\,\mathrm{rad}}\,\rangle\langle\, \hat{C} \mid Y_{L\,M} \mid \hat{d}_i\,\rangle.\end{aligned} \tag{6.29}$$

Now we replace the deuteron wave function by the position-space expression given in Eq. (D.5), $\Psi_{1m}(\vec{r}) = \sum_{l=0,2} \frac{u_l(r)}{r} \mathcal{Y}_m^{l11}(\hat{r})$ with $u_0(r) \equiv u(r)$ and $u_2(r) \equiv w(r)$, see e.g. Section 3.4 of [57]. The indices $l11$ of the angular wave functions $\mathcal{Y}$ denote orbital angular momentum, spin and total angular momentum of the deuteron state, $m \in \{-1, 0, 1\}$ is the projection of the total angular momentum of the deuteron onto

the quantization axis. Using this notation we can write Eq. (6.29) as

$$\mathcal{M}_{fi}^{\phi\phi 1} \propto \sum_{\hat{C}} \sum_{l=0,2} \sum_{l'=0,2} \langle\, l'\,1\,1\,M_f \mid Y_{L'\,M'} \mid \hat{C}\,\rangle\langle\, \hat{C} \mid Y_{L\,M} \mid l\,1\,1\,M_i\,\rangle \tag{6.30}$$
$$\times \iint r dr\, r' dr' u_{l'}(r')\, \psi_{L'}(\frac{\omega r'}{2})\, \langle\, r' \mid \frac{1}{E_0 - H_{\hat{C}}^{np}} \mid r\,\rangle\, \psi_L(\frac{\omega r}{2})\, u_l(r),$$

where we have removed the sum over $C_{\rm rad}$. Integrals without limits are always integrated from 0 to infinity throughout this work.

We now have to evaluate the double integral in Eq. (6.30), including the Green's function

$$G_{\hat{C}}(r, r'; E_0) = \langle\, r' \mid \frac{1}{E_0 - H_{\hat{C}}^{np}} \mid r\,\rangle. \tag{6.31}$$

However, we need to evaluate the integral for arbitrary functions of r. Therefore we describe how to calculate

$$\mathcal{I}_{fi}^{ll'\hat{C}} = \iint r dr\, r' dr'\, u_{l'}(r')\, J_f(r')\, G_{\hat{C}}(r, r'; E_0)\, J_i(r)\, u_l(r). \tag{6.32}$$

We do so in two steps and define

$$\chi_f^{l'\hat{C}}(r) \equiv \int r' dr'\, u_{l'}(r')\, J_f(r')\, G_{\hat{C}}(r, r'; E_0). \tag{6.33}$$

Once we have solved this first part of the integral, it is easy to numerically calculate the remaining integral

$$\mathcal{I}_{fi}^{ll'\hat{C}} = \int r dr\, u_l(r)\, J_i(r)\, \chi_f^{l'\hat{C}}(r). \tag{6.34}$$

In order to find the function $\chi_f^{l'\hat{C}}(r)$ – in the following we use the abbreviation $\chi_{\hat{C}}(r)$ for simplicity – we first note that

$$\left(E_0 - H_{\hat{C}}^{np}\right)\, G_{\hat{C}}(r, r'; E_0) = \langle\, r' \mid r\,\rangle = \frac{\delta(r' - r)}{r^2}. \tag{6.35}$$

Eq. (6.35) defines the Green's function corresponding to Schrödinger's equation with a central potential and the Hamiltonian

$$H = \frac{\vec{p}^{\,2}}{2m} + V(r) = -\frac{1}{2m}\, \left(\frac{1}{r}\frac{d^2}{dr^2} r\right) + \frac{\vec{L}^{\,2}}{2m\, r^2} + V(r), \tag{6.36}$$

where $\vec{L}$ denotes the orbital angular momentum operator. Note that the neutron-proton potential contains a tensor part and therefore not only depends on the distance r but on the vector $\vec{r}$. The tensor force mixes e.g. the deuteron s- and d-states in Schrödinger's equation. Nevertheless, on the level of the Green's function this matrix equation decouples, cf. Section 3.7 of Ref. [57]. Therefore, we may replace the Hamiltonian in Eq. (6.35) by

$$H_{\hat{C}}^{np} = \frac{\vec{p}^{\,2}}{m_p} + V_{\hat{C}}(r) = -\frac{1}{m_p}\, \left(\frac{1}{r}\frac{d^2}{dr^2} r\right) + \frac{L_C\,(L_C+1)}{m_p\, r^2} + V_{\hat{C}}(r), \tag{6.37}$$

where we explicitly show the dependence of the potential on the quantum numbers of the interim state $\mid C\,\rangle$. The decoupling of Eq. (6.35) guarantees that only the diagonal terms of the tensor force contribute. Therefore, the orbital angular momentum is well defined, which allows us to replace $\vec{L}^{\,2} \to L_C\,(L_C+1)$ in Eq. (6.37).

Usually we use the AV18 potential as published in [73], one of the modern phenomenological high-precision potentials. An explicit expression for this potential is given in Appendix K. In Section 6.3.2, however, we compare to results with the LO chiral potential, and we demonstrate that our calculation is rather insensitive to this choice.

Eqs. (6.35) and (6.37) combine to

$$\left[E_0 + \frac{1}{m_p}\frac{d^2}{dr^2} - \frac{L_C\,(L_C+1)}{m_p\,r^2} - V_{\hat{C}}(r)\right]\, r\,G_{\hat{C}}(r,r';E_0) = \frac{\delta(r'-r)}{r}, \tag{6.38}$$

which e.g. in the deuteron case reduces to the two differential equations

$$\left[E_0 + \frac{1}{m_p}\frac{d^2}{dr^2} - V_{\rm cent}(r)\right]\, r\,G_0(r,r';E_0) = \frac{\delta(r'-r)}{r}, \tag{6.39}$$

$$\left[E_0 + \frac{1}{m_p}\frac{d^2}{dr^2} - \frac{6}{m_p\,r^2} - V_{\rm cent}(r) + 2\,V_{\rm ten}(r)\right]\, r\,G_2(r,r';E_0) = \frac{\delta(r'-r)}{r} \tag{6.40}$$

with $V_{\rm cent}(r)$ the central part and $V_{\rm ten}(r)$ the tensor part of the potential. The indices of the Green's functions in Eqs. (6.39, 6.40) reflect the orbital angular momentum state, whereas $J=1,\ S=1$ is not written down explicitly. The factor -2 in front of $V_{\rm ten}(r)$ in Eq. (6.40) can be read off Table K.1.

Returning to the calculation of the double-integral (6.32), we act now with the operator given in square brackets in Eq. (6.38) on $\chi_{\hat{C}}(r)$. The integral over r' collapses due to the δ-function and we find

$$\left[\frac{d^2}{dr^2} + m_p\,\left(E_0 - V_{\hat{C}}(r)\right) - \frac{L_C\,(L_C+1)}{r^2}\right]\, r\,\chi_{\hat{C}}(r) = m_p\,u_{l'}(r)\,J_f(r). \tag{6.41}$$

This is a second-order differential equation in r with an inhomogeneity, which can be interpreted as a source term. Its solutions are real for $E_0 < 0$ and complex for $E_0 > 0$. The latter case corresponds to $\omega > B$, i.e. the photon carries enough energy to break up the deuteron into its two constituents. Whenever such a new channel opens, an imaginary part starts to exist. Another example of an amplitude becoming complex at a particle-production threshold is the single-nucleon Compton amplitude for $\omega \sim m_\pi$, cf. Section 3.1.2. There, the imaginary part signals that the photon energy suffices to put a pion on-shell; here it indicates that there is enough energy to split the deuteron into two free nucleons. Like in Section 3.1.2, such an imaginary part appears only in the s-channel diagrams, where the incoming photon is absorbed before the other one is emitted. In Section 6.4 we will use the imaginary part of the amplitudes to derive total deuteron-photodisintegration cross sections via the optical theorem.

For $r \to \infty,\ \ u_{l'}(r)J_f(r) \to 0$ due to $u_{l'}(r) \to 0$, i.e. Eq. (6.41) reduces to a homogeneous differential equation. Furthermore, $V_{\hat{C}}(r) \to 0$ for $r \to \infty$ because of the finite range of the NN-potential, see Appendix K. Therefore, we are for large distances left with

$$\left[\frac{d^2}{dr^2} + E_0\,m_p - \frac{L_C\,(L_C+1)}{r^2}\right]\, r\,\chi_{\hat{C}}(r) = 0. \tag{6.42}$$

This equation is known to be solved by a linear combination of the spherical Bessel functions of the first and second kind, $j_{L_C}(Qr)$ and $n_{L_C}(Qr)$ with $Q = \sqrt{m_p\,E_0}$, see e.g. Section 17.3 in [85]. Note that Q can be real or imaginary[2] depending on

[2] In order to fix the sign of the imaginary solution, one has to add an infinitesimal imaginary part to $-B$, i.e. $B \to B - i\epsilon$. The sign of this imaginary part follows from the pole structure of the nucleon propagators.

E_0. In our case the boundary condition is that $\chi_{\hat{C}}(r)$ must be an outgoing spherical wave for large r, cf. e.g. Section 7.1 of [86]. Therefore we may write

$$\lim_{r\to\infty} \chi_{\hat{C}}(r) \propto h^{(1)}_{L_C}(Qr), \tag{6.43}$$

with $h^{(1)}_{L_C}(Qr)$ the spherical Hankel function of the first kind, defined as

$$h^{(1)}_{L_C}(Qr) = j_{L_C}(Qr) + i n_{L_C}(Qr). \tag{6.44}$$

We now have to find solutions for the homogeneous and the inhomogeneous differential equation (6.41). Numerically, this can be easily done. As the equation is of second order, we have to specify two initial conditions, e.g. $\chi_{\hat{C}}(r=0)$ and $\frac{d}{dr}\chi_{\hat{C}}(r)|_{r=0}$. In order to improve the stability of the numerics routine it is worth thinking about proper values for these conditions, which are, however, not to be confused with the boundary condition (6.43), that the final solution has to fulfill. For $r \to 0$ the right-hand side of Eq. (6.41) vanishes due to the wave function $u_{l'}(r)$. Furthermore, as $V_{\hat{C}}(r)$ is regular at the origin, cf. Fig. K.2, $\frac{L_C\,(L_C+1)}{r^2} \gg m_p \left(E_0 - V_{\hat{C}}(r)\right)$ for $L_C > 0$ and sufficiently small r. Therefore, for $r \to 0$ Eq. (6.41) can be approximated by

$$\left[\frac{d^2}{dr^2} - \frac{L_C\,(L_C+1)}{r^2}\right] r\,\chi_{\hat{C}}(r) = 0. \tag{6.45}$$

The general solution of Eq. (6.45) is given by $r\,\chi_{\hat{C}}(r) = A\,r^{L_C+1} + B\,r^{-L_C}$. As we want $\chi_{\hat{C}}(r)$ to be regular at the origin, i.e. $r\,\chi_{\hat{C}}(r) = 0$ for $r \to 0$, we find $B = 0$ and therefore close to the origin $r\,\chi_{\hat{C}}(r)$ is of order r^{L_C+1} plus higher powers in r, which means that the leading contribution to $\chi_{\hat{C}}(r)$ is proportional to r^{L_C}. Therefore it is advantageous to choose $\chi_{\hat{C}}(r=0) \neq 0$, $\frac{d}{dr}\chi_{\hat{C}}(r)|_{r=0} \neq 0$ for $L_C = 0$, $\chi_{\hat{C}}(r=0) = 0$, $\frac{d}{dr}\chi_{\hat{C}}(r)|_{r=0} \neq 0$ for $L_C = 1$ and $\chi_{\hat{C}}(r=0) \approx 0$, $\frac{d}{dr}\chi_{\hat{C}}(r)|_{r=0} \approx 0$ for higher angular momenta[3].

Once we have solutions for the homogeneous and the inhomogeneous differential equation, we need to find the correct linear combination which satisfies the condition (6.43). In other words we have to determine the coefficient λ which fulfills

$$\lim_{r\to\infty} \left\{\chi^{\text{in}}_{\hat{C}}(r) + \lambda\,\chi^{\text{hom}}_{\hat{C}}(r)\right\} \propto h^{(1)}_{L_C}(Qr), \tag{6.46}$$

where $\chi^{\text{in}}_{\hat{C}}(r)$ ($\chi^{\text{hom}}_{\hat{C}}(r)$) denote the solution to the inhomogeneous (homogeneous) differential equation. In the asymptotic limit, $\chi_{\hat{C}}(r)$ must be a linear combination of $j_{L_C}(Qr)$ and $n_{L_C}(Qr)$ or, equivalently, of $j_{L_C}(Qr)$ and $h^{(1)}_{L_C}(Qr)$. Therefore we can write the general solutions in the following way:

$$\chi^{\text{hom}}_{\hat{C}}(r) = C^{\text{hom}}_{\hat{C}}(r)\,\left[j_{L_C}(Qr) + t^{\text{hom}}_{\hat{C}}(r)\,h^{(1)}_{L_C}(Qr)\right], \tag{6.47}$$

$$\chi^{\text{in}}_{\hat{C}}(r) = C^{\text{in}}_{\hat{C}}(r)\,\left[j_{L_C}(Qr) + t^{\text{in}}_{\hat{C}}(r)\,h^{(1)}_{L_C}(Qr)\right] \tag{6.48}$$

with functions $C^{\text{in/hom}}_{\hat{C}}(r)$, $t^{\text{in/hom}}_{\hat{C}}(r)$ which become the constants $C^{\text{in/hom}}_{\hat{C}}$, $t^{\text{in/hom}}_{\hat{C}}$ for large r. With the choice $\lambda = -C^{\text{in}}_{\hat{C}}/C^{\text{hom}}_{\hat{C}}$ we find

$$\lim_{r\to\infty} \left\{\chi^{\text{in}}_{\hat{C}}(r) + \lambda\,\chi^{\text{hom}}_{\hat{C}}(r)\right\} = C^{\text{in}}_{\hat{C}}\,\left(t^{\text{in}}_{\hat{C}} - t^{\text{hom}}_{\hat{C}}\right)\,h^{(1)}_{L_C}(Qr), \tag{6.49}$$

which satisfies the condition (6.43). Therefore we need to determine the coefficients $C^{\text{in}}_{\hat{C}}$, $C^{\text{hom}}_{\hat{C}}$. This has to be done in the region where $C_{\hat{C}}(r)$, $t_{\hat{C}}(r)$ are constant, i.e. their derivatives vanish. In this region

$$\ln \chi^{\text{in/hom}}_{\hat{C}}(r) = \ln C^{\text{in/hom}}_{\hat{C}} + \ln\left[j_{L_C}(Qr) + t^{\text{in/hom}}_{\hat{C}}\,h^{(1)}_{L_C}(Qr)\right]. \tag{6.50}$$

[3]The choice 0 in both cases is impossible, as it would give the trivial solution $\chi_{\hat{C}}(r) \equiv 0$ for the homogeneous equation.

Defining $D^{\text{in/hom}} = \frac{d}{dr} \ln \chi_{\hat{C}}^{\text{in/hom}} = \frac{\chi_{\hat{C}}'^{\text{in/hom}}}{\chi_{\hat{C}}^{\text{in/hom}}}$ we find

$$D^{\text{in/hom}} = \frac{d}{dr} \ln \left[j_{L_C}(Qr) + t_{\hat{C}}^{\text{in/hom}} \, h_{L_C}^{(1)}(Qr) \right] = \frac{\frac{d}{dr} j_{L_C}(Qr) + t_{\hat{C}}^{\text{in/hom}} \, \frac{d}{dr} h_{L_C}^{(1)}(Qr)}{j_{L_C}(Qr) + t_{\hat{C}}^{\text{in/hom}} \, h_{L_C}^{(1)}(Qr)}. \tag{6.51}$$

This equation is easily solved for $t_{\hat{C}}^{\text{in/hom}}$:

$$t_{\hat{C}}^{\text{in/hom}} = \frac{D^{\text{in/hom}} \, j_{L_C}(Qr) - \frac{d}{dr} j_{L_C}(Qr)}{\frac{d}{dr} h_{L_C}^{(1)}(Qr) - D^{\text{in/hom}} \, h_{L_C}^{(1)}(Qr)} \tag{6.52}$$

Using these results we can solve Eqs. (6.47, 6.48) for $C_{\hat{C}}^{\text{in/hom}}$ and so determine λ.

Numerically, this is one of the most involved parts of this work. Fortunately, a nice and valuable cross-check to the routine can be performed. For this we consider again the double integral to be calculated, Eq. (6.32). This integral is obviously invariant under the interchange $r \leftrightarrow r'$. A general feature of Green's functions is that they are symmetric under $r \leftrightarrow r'$, i.e. $G_{\hat{C}}(r', r; E_0) = G_{\hat{C}}(r, r'; E_0)$ [87]. Therefore

$$\mathcal{I}_{fi}^{ll'\hat{C}} = \iint r' dr' \, r dr \, u_{l'}(r) \, J_f(r) \, G_{\hat{C}}(r, r'; E_0) \, J_i(r') \, u_l(r'). \tag{6.53}$$

This expression is identical to $\mathcal{I}_{fi}^{ll'\hat{C}}$, Eq. (6.32), with $i \leftrightarrow f$, $l \leftrightarrow l'$, i.e. our results must be symmetric under $i \leftrightarrow f$, $l \leftrightarrow l'$. This is a non-trivial check, because for $J_f(r) \neq J_i(r)$ completely different functions $\chi_f^{l'\hat{C}}(r)$ are generated. Our routine agrees well with this symmetry – the deviation caused by numerical uncertainties is less than 1%.

Now all tools to calculate $\mathcal{M}_{fi}^{\phi\phi 1,2}$ are prepared. However, as the algebraic manipulations are not too complicated, we shift this rather technical part to Appendix G. There we also calculate $\mathcal{M}_{fi}^{\phi\phi 3}$ and $\mathcal{M}_{fi}^{\phi\phi 4}$.

We turn now to the calculation of those contributions where the replacement $\vec{A}(\vec{\xi}) \to \vec{\nabla}\phi(\vec{\xi})$ (cf. the beginning of this section) is made at most once.

6.1.2 Subleading Terms

So far we only considered contributions arising from minimal coupling of the photon field to the two-nucleon system at both vertices. In the following we describe how to calculate the amplitudes given in Eq. (6.1), when the replacement

$$H^{\text{int}} = -\int \vec{J}(\vec{\xi}) \cdot \vec{A}(\vec{\xi}) \, d^3\xi \to -\int \vec{J}(\vec{\xi}) \cdot \vec{\nabla}\phi(\vec{\xi}) \, d^3\xi \tag{6.54}$$

is made only once, again drawing substantially from Ref. [24]. The term 'subleading' refers to the fact that the resulting amplitude is numerically less important than

that of Section 6.1.1. It is denoted by $\mathcal{M}^{\phi}_{fi}$ and follows immediately from Eq. (6.1):

$$\begin{aligned}\mathcal{M}^{\phi}_{fi} = \sum_C \Bigg\{ & \frac{\langle\, d_f \mid \int \vec{J}(\vec{\xi}\,)\cdot\vec{\nabla}\phi_f(\vec{\xi}\,)\, d^3\xi \mid C\,\rangle\langle\, C \mid \int \vec{J}(\vec{\xi}\,)\cdot\vec{A}(\vec{\xi}\,)\, d^3\xi \mid d_i\,\rangle}{\omega + \frac{\omega^2}{2m_d} - B - E_C} \\ & + \frac{\langle\, d_f \mid \int \vec{J}(\vec{\xi}\,)\cdot\vec{A}(\vec{\xi}\,)\, d^3\xi \mid C\,\rangle\langle\, C \mid \int \vec{J}(\vec{\xi}\,)\cdot\vec{\nabla}\phi_i(\vec{\xi}\,)\, d^3\xi \mid d_i\,\rangle}{\omega + \frac{\omega^2}{2m_d} - B - E_C} \\ & + \frac{\langle\, d_f \mid \int \vec{J}(\vec{\xi}\,)\cdot\vec{\nabla}\phi_i(\vec{\xi}\,)\, d^3\xi \mid C\,\rangle\langle\, C \mid \int \vec{J}(\vec{\xi}\,)\cdot\vec{A}(\vec{\xi}\,)\, d^3\xi \mid d_i\,\rangle}{-\omega + \frac{\omega^2}{2m_d} - \frac{\vec{P}_C^{\,2}}{2m_C} - B - E_C} \\ & + \frac{\langle\, d_f \mid \int \vec{J}(\vec{\xi}\,)\cdot\vec{A}(\vec{\xi}\,)\, d^3\xi \mid C\,\rangle\langle\, C \mid \int \vec{J}(\vec{\xi}\,)\cdot\vec{\nabla}\phi_f(\vec{\xi}\,)\, d^3\xi \mid d_i\,\rangle}{-\omega + \frac{\omega^2}{2m_d} - \frac{\vec{P}_C^{\,2}}{2m_C} - B - E_C} \Bigg\} \end{aligned} \tag{6.55}$$

Now we perform the same steps as described in Eqs. (6.11-6.21), i.e. we first replace $\int \vec{J}(\vec{\xi}\,)\cdot\vec{\nabla}\phi(\vec{\xi}\,)\, d^3\xi$ by $i\,[H^{np}, e\,\phi(\vec{r}/2)]$, then act with H^{np} on $\mid d\,\rangle$ and $\mid C\,\rangle$, respectively, and finally add and subtract terms in order to do some cancellations against the denominator. We find, again neglecting recoil terms and the deuteron velocity,

$$\begin{aligned}\mathcal{M}^{\phi}_{fi} = i \sum_C \Bigg\{ & \langle\, d_f \mid \hat{\phi}_f \mid C\,\rangle\langle\, C \mid \int \vec{J}(\vec{\xi}\,)\cdot\vec{A}(\vec{\xi}\,)\, d^3\xi \mid d_i\,\rangle \\ & - \left(\omega + \frac{\omega^2}{2m_d}\right) \frac{\langle\, d_f \mid \hat{\phi}_f \mid C\,\rangle\langle\, C \mid \int \vec{J}(\vec{\xi}\,)\cdot\vec{A}(\vec{\xi}\,)\, d^3\xi \mid d_i\,\rangle}{\omega + \frac{\omega^2}{2m_d} - B - E_C} \\ & - \langle\, d_f \mid \int \vec{J}(\vec{\xi}\,)\cdot\vec{A}(\vec{\xi}\,)\, d^3\xi \mid C\,\rangle\langle\, C \mid \hat{\phi}_i \mid d_i\,\rangle \\ & + \left(\omega + \frac{\omega^2}{2m_d}\right) \frac{\langle\, d_f \mid \int \vec{J}(\vec{\xi}\,)\cdot\vec{A}(\vec{\xi}\,)\, d^3\xi \mid C\,\rangle\langle\, C \mid \hat{\phi}_i \mid d_i\,\rangle}{\omega + \frac{\omega^2}{2m_d} - B - E_C} \\ & + \langle\, d_f \mid \hat{\phi}_i \mid C\,\rangle\langle\, C \mid \int \vec{J}(\vec{\xi}\,)\cdot\vec{A}(\vec{\xi}\,)\, d^3\xi \mid d_i\,\rangle \\ & + \left(\omega - \frac{\omega^2 - \vec{P}_C^{\,2}}{2m_C}\right) \frac{\langle\, d_f \mid \hat{\phi}_i \mid C\,\rangle\langle\, C \mid \int \vec{J}(\vec{\xi}\,)\cdot\vec{A}(\vec{\xi}\,)\, d^3\xi \mid d_i\,\rangle}{-\omega + \frac{\omega^2}{2m_d} - \frac{\vec{P}_C^{\,2}}{2m_C} - B - E_C} \\ & - \langle\, d_f \mid \int \vec{J}(\vec{\xi}\,)\cdot\vec{A}(\vec{\xi}\,)\, d^3\xi \mid C\,\rangle\langle\, C \mid \hat{\phi}_f \mid d_i\,\rangle \\ & - \left(\omega - \frac{\omega^2 - \vec{P}_C^{\,2}}{2m_C}\right) \frac{\langle\, d_f \mid \int \vec{J}(\vec{\xi}\,)\cdot\vec{A}(\vec{\xi}\,)\, d^3\xi \mid C\,\rangle\langle\, C \mid \hat{\phi}_f \mid d_i\,\rangle}{-\omega + \frac{\omega^2}{2m_d} - \frac{\vec{P}_C^{\,2}}{2m_C} - B - E_C} \Bigg\}. \end{aligned} \tag{6.56}$$

In those terms in which the energy denominator has been cancelled, the sum over C may be collapsed. As $\hat{\phi}\left(\int \vec{J}(\vec{\xi}\,)\cdot\vec{A}(\vec{\xi}\,)\, d^3\xi\right) = \left(\int \vec{J}(\vec{\xi}\,)\cdot\vec{A}(\vec{\xi}\,)\, d^3\xi\right)\hat{\phi}$, these four terms cancel exactly, and only the terms including an energy denominator remain.

Now we have to specify the current $\vec{J}(\vec{\xi}\,)$ and the relevant parts of the photon field $\vec{A}(\vec{\xi}\,)$, which are the non-gradient terms in Eq. (6.3). We want to decompose the photon field in its electric and magnetic part. Therefore, we write schematically

$\vec{A} = \vec{\nabla}\phi + \vec{A}^{(1)} + \vec{A}^{(2)}$ with

$$\vec{A}^{(1)}(\vec{\xi}) = -\sum_{\vec{k},\lambda=\pm1}\sum_{L=1}^{\infty}\sum_{M=-L}^{L}\lambda\sqrt{\frac{2\pi\,(2L+1)}{L\,(L+1)}}\,i^L\,j_L(\omega\xi)\,\vec{L}\,Y_{L\,M}(\hat{\xi}) \times\left[a_{\vec{k},\lambda}\,\delta_{M,\lambda} - a^{\dagger}_{\vec{k},\lambda}\,(-1)^{L+\lambda}\,d^L_{M,-\lambda}(\theta)\right], \tag{6.57}$$

$$\vec{A}^{(2)}(\vec{\xi}) = -\sum_{\vec{k},\lambda=\pm1}\sum_{L=1}^{\infty}\sum_{M=-L}^{L}\sqrt{\frac{2\pi\,(2L+1)}{L\,(L+1)}}\,i^{L+1}\,\omega\,\vec{\xi}\,j_L(\omega\xi)\,Y_{L\,M}(\hat{\xi}) \times\left[a_{\vec{k},\lambda}\,\delta_{M,\lambda} - a^{\dagger}_{\vec{k},\lambda}\,(-1)^{L+\lambda}\,d^L_{M,-\lambda}(\theta)\right], \tag{6.58}$$

cf. Eqs. (F.29), (F.32) and (L.1). $\vec{A}^{(1)}$ constitutes the magnetic part of the photon field, $\vec{\nabla}\phi + \vec{A}^{(2)}$ is the electric field, cf. e.g. Chapter 7 of Ref. [83]. The operators $a^{\dagger}_{\vec{k},\lambda}$ ($a_{\vec{k},\lambda}$) create (destroy) a photon with momentum $\vec{k}$ and polarization λ.

Now we specify which currents we include in our calculation. The one-body current is considered first. It consists of two parts, which we call $\vec{J}^{(\sigma)}$ and $\vec{J}^{(p)}$, with

$$\vec{J}^{(\sigma)}(\vec{\xi}) = \frac{e}{2m_N}\sum_{j=n,p}\left[\vec{\nabla}_\xi \times \mu_j\,\vec{\sigma}_j\,\delta(\vec{\xi}-\vec{x}_j)\right], \tag{6.59}$$

$$\vec{J}^{(p)}(\vec{\xi}) = \frac{1}{2m_N}\sum_{j=n,p}\left\{e_j\,\delta(\vec{\xi}-\vec{x}_j), \vec{p}_j\right\}, \tag{6.60}$$

cf. e.g. [57], Section 8.2. μ_j is the magnetic moment, $\vec{\sigma}_j$ the spin operator and $\vec{p}_j$ the momentum of the jth nucleon; as in the previous chapter we neglect isospin-breaking effects, i.e. we set $m_p \equiv m_n \equiv m_N$. All possible combinations of $\vec{A}^{(1)}$, $\vec{A}^{(2)}$ and $\vec{J}^{(\sigma)}$, $\vec{J}^{(p)}$ have been calculated in [24]. We also evaluated all these amplitudes, however we found that only $\vec{J}^{(\sigma)}$ gives visible contributions to the deuteron Compton cross sections. The reason is that in the amplitudes resulting from the replacement $\vec{J}\cdot\vec{A} \to \vec{J}^{(p)}\cdot\vec{A}^{(1)}$ in Eq. (6.56), the leading multipoles of the photon field $L = L' = 1$ are forbidden due to the matrix elements involved. The amplitudes including $\vec{J}^{(p)}\cdot\vec{A}^{(2)}$, on the other hand, cancel exactly for $L, L' \le 2$ in the γd-cm frame. Therefore, we may restrict ourselves to the following combinations: ($\vec{J}^{(\sigma)}$, $\vec{A}^{(1)}$), denoted by $\sigma 1$, and ($\vec{J}^{(\sigma)}$, $\vec{A}^{(2)}$), denoted by $\sigma 2$.

We now calculate $\int \vec{J}^{(\sigma)}(\vec{\xi})\cdot\vec{A}^{(1,2)}(\vec{\xi})\,d^3\xi$. We start with the derivation for $\vec{A}^{(1)}$, writing only the ξ-dependent terms for simplicity.

$$\begin{aligned}\int \vec{J}^{(\sigma)}(\vec{\xi})\cdot\vec{A}^{(1)}(\vec{\xi})\,d^3\xi &\propto \int\sum_{j=n,p}\left[\vec{\nabla}_\xi\times\mu_j\,\vec{\sigma}_j\,\delta(\vec{\xi}-\vec{x}_j)\right]\,j_L(\omega\xi)\cdot\vec{L}\,Y_{L\,M}(\hat{\xi})\,d^3\xi\\ &= \int\sum_{j=n,p}\left[\varepsilon_{ikl}\,\partial_k\,\mu_j\,\sigma_{j,l}\,\delta(\vec{\xi}-\vec{x}_j)\right]\,j_L(\omega\xi)\,L_i\,Y_{L\,M}(\hat{\xi})\,d^3\xi\\ &= -\int\sum_{j=n,p}\left[\varepsilon_{ikl}\,\mu_j\,\sigma_{j,l}\,\delta(\vec{\xi}-\vec{x}_j)\right]\,\partial_k\,j_L(\omega\xi)\,L_i\,Y_{L\,M}(\hat{\xi})\,d^3\xi\\ &= \int\sum_{j=n,p}\mu_j\,\vec{\sigma}_j\,\delta(\vec{\xi}-\vec{x}_j)\cdot\vec{\nabla}_\xi\times\left(j_L(\omega\xi)\,\vec{L}\,Y_{L\,M}(\hat{\xi})\right)\,d^3\xi,\end{aligned} \tag{6.61}$$

where one partial integration has been performed. Now we evaluate the integral

and afterwards replace $\vec{x}_p \to \frac{\vec{r}}{2}$, $\vec{x}_n \to -\frac{\vec{r}}{2}$, as in Eq. (6.16), yielding

$$\int \vec{J}^{(\sigma)}(\vec{\xi}) \cdot \vec{A}^{(1)}(\vec{\xi})\, d^3\xi \propto 2 \left[\vec{\nabla}_r \times \left(j_L(\frac{\omega r}{2})\, \vec{L}\, Y_{L\,M}(\hat{r}) \right) \right] \cdot \left(\mu_p\, \vec{\sigma}_p - (-1)^L\, \mu_n\, \vec{\sigma}_n \right), \tag{6.62}$$

where we used $\vec{\nabla}_{\pm r/2} = \pm 2 \vec{\nabla}_r$ and Eq. (L.27). By the help of Eq. (F.17), this becomes

$$\int \vec{J}^{(\sigma)}(\vec{\xi}) \cdot \vec{A}^{(1)}(\vec{\xi})\, d^3\xi \propto 2\sqrt{L\,(L+1)} \left[\vec{\nabla}_r \times j_L(\frac{\omega r}{2})\, \vec{T}_{L\,L\,M}(\hat{r}) \right] \cdot \left(\mu_p\, \vec{\sigma}_p - (-1)^L\, \mu_n\, \vec{\sigma}_n \right). \tag{6.63}$$

Now we can use the curl formula (L.44) and the recursion relations for spherical Bessel functions, Eq. (L.30), to write

$$\begin{aligned} \int \vec{J}^{(\sigma)}(\vec{\xi}) \cdot \vec{A}^{(1)}(\vec{\xi})\, d^3\xi \propto \Bigg[& i\,\omega\, j_{L-1}(\frac{\omega r}{2}) \sqrt{\frac{L\,(L+1)^2}{2L+1}}\, \vec{T}_{L\,L-1\,M}(\hat{r}) \\ & - i\,\omega\, j_{L+1}(\frac{\omega r}{2}) \sqrt{\frac{L^2\,(L+1)}{2L+1}}\, \vec{T}_{L\,L+1\,M}(\hat{r}) \Bigg] \cdot \left(\mu_p\, \vec{\sigma}_p - (-1)^L\, \mu_n\, \vec{\sigma}_n \right). \end{aligned} \tag{6.64}$$

We found that the numerical importance of the various contributions rapidly decreases with increasing photon multipolarity L. A similar observation has been made in Chapters 3 and 4 for our multipole expansion of single-nucleon Compton scattering. Therefore, the term proportional to $\vec{T}_{L\,L+1\,M}(\hat{r})$ may be neglected. Defining $\vec{S} = \frac{\vec{\sigma}_p + \vec{\sigma}_n}{2}$ and $\vec{t} = \frac{\vec{\sigma}_p - \vec{\sigma}_n}{2}$ and including all prefactors, we get the result

$$\begin{aligned} & \int \vec{J}^{(\sigma)}(\vec{\xi}) \cdot \vec{A}^{(1)}(\vec{\xi})\, d^3\xi = \\ & \quad - \sum_{\vec{k},\lambda=\pm 1} \sum_{L=1}^{\infty} \sum_{M=-L}^{L} \lambda \sqrt{2\pi\,(L+1)}\, \frac{e\,\omega}{2m_N}\, i^{L+1}\, j_{L-1}(\frac{\omega r}{2})\, \vec{T}_{L\,L-1\,M}(\hat{r}) \\ & \quad \times \left[\left(\mu_p - (-1)^L\, \mu_n \right) \vec{S} + \left(\mu_p + (-1)^L\, \mu_n \right) \vec{t} \right] \cdot \left[a_{\vec{k},\lambda}\, \delta_{M,\lambda} - a^{\dagger}_{\vec{k},\lambda}\, (-1)^{L+\lambda}\, d^L_{M,-\lambda}(\theta) \right]. \end{aligned} \tag{6.65}$$

The scalar products are replaced according to the relation

$$\vec{T}_{J\,L\,M}(\hat{r}) \cdot \vec{V} = [Y_L \otimes V]_{J\,M}\,, \tag{6.66}$$

which holds for any vector (rank 1) operator ($\otimes$ denotes the irreducible tensor product). An explicit proof of this identity is given in Appendix H. We use it to finally rewrite Eq. (6.65):

$$\begin{aligned} \int \vec{J}^{(\sigma)}(\vec{\xi}) \cdot \vec{A}^{(1)}(\vec{\xi})\, d^3\xi = & - \sum_{\vec{k},\lambda=\pm 1} \sum_{L=1}^{\infty} \sum_{M=-L}^{L} \lambda \sqrt{2\pi\,(L+1)}\, \frac{e\,\omega}{2m_N}\, i^{L+1}\, j_{L-1}(\frac{\omega r}{2}) \\ & \times \left\{ \left(\mu_p - (-1)^L\, \mu_n \right) [Y_{L-1} \otimes S]_{L\,M} + \left(\mu_p + (-1)^L\, \mu_n \right) [Y_{L-1} \otimes t]_{L\,M} \right\} \\ & \times \left[a_{\vec{k},\lambda}\, \delta_{M,\lambda} - a^{\dagger}_{\vec{k},\lambda}\, (-1)^{L+\lambda}\, d^L_{M,-\lambda}(\theta) \right] \end{aligned} \tag{6.67}$$

We turn now to the calculation of $\int \vec{J}^{(\sigma)}(\vec{\xi}) \cdot \vec{A}^{(2)}(\vec{\xi})\, d^3\xi$. Again we restrict

ourselves in the derivation to the ξ-dependent terms, finding

$$\begin{aligned}\int \vec{J}^{(\sigma)}(\vec{\xi}\,)\cdot\vec{A}^{(2)}(\vec{\xi}\,)\,d^3\xi &\propto \int \sum_{j=n,p}\left[\vec{\nabla}_\xi\times\mu_j\,\vec{\sigma}_j\,\delta(\vec{\xi}-\vec{x}_j)\right]\cdot\vec{\xi}\,j_L(\omega\xi)\,Y_{L\,M}(\hat{\xi})\,d^3\xi\\ &= \int\sum_{j=n,p}\mu_j\,\vec{\sigma}_j\,\delta(\vec{\xi}-\vec{x}_j)\cdot\vec{\nabla}_\xi\times\left(\vec{\xi}\,j_L(\omega\xi)\,Y_{L\,M}(\hat{\xi})\right)\,d^3\xi\\ &= \vec{\nabla}_r\times\left(\vec{r}\,j_L(\frac{\omega r}{2})\,Y_{L\,M}(\hat{r})\right)\cdot\left(\mu_p\,\vec{\sigma}_p+(-1)^L\,\mu_n\,\vec{\sigma}_n\right),\end{aligned} \tag{6.68}$$

where we have performed the same steps as in the derivation of Eq. (6.62). From Eq. (F.25) we know that

$$\vec{r}\,j_L(\frac{\omega r}{2})\,Y_{L\,M}(\hat{r}) = \sqrt{L\,(L+1)}\,r\,j_L(\frac{\omega r}{2})\,\left[\frac{\vec{T}_{L\,L-1\,M}(\hat{r})}{\sqrt{(L+1)\,(2L+1)}}-\frac{\vec{T}_{L\,L+1\,M}(\hat{r})}{\sqrt{L\,(2L+1)}}\right], \tag{6.69}$$

which we plug into Eq. (6.68). Using the curl formulae Eqs. (L.45) and (L.46) we find

$$\vec{\nabla}_r\times\left(r\,j_L(\frac{\omega r}{2})\,\left[\frac{\vec{T}_{L\,L-1\,M}(\hat{r})}{\sqrt{(L+1)\,(2L+1)}}-\frac{\vec{T}_{L\,L+1\,M}(\hat{r})}{\sqrt{L\,(2L+1)}}\right]\right) = -i\,j_L(\frac{\omega r}{2})\,\vec{T}_{L\,L\,M}(\hat{r}). \tag{6.70}$$

Combining Eqs. (6.68-6.70), together with the definitions of $\vec{S}$ and $\vec{t}$, cf. Eq. (6.65), yields

$$\begin{aligned}\int \vec{J}^{(\sigma)}(\vec{\xi}\,)\cdot\vec{A}^{(2)}(\vec{\xi}\,)\,d^3\xi \propto -i\,\sqrt{L\,(L+1)}\,j_L(\frac{\omega r}{2})\,\vec{T}_{L\,L\,M}(\hat{r})\\ \cdot\left[(\mu_p+(-1)^L\,\mu_n)\,\vec{S}+(\mu_p-(-1)^L\,\mu_n)\,\vec{t}\right].\end{aligned} \tag{6.71}$$

Including all prefactors, we get

$$\begin{aligned}\int \vec{J}^{(\sigma)}(\vec{\xi}\,)\cdot\vec{A}^{(2)}(\vec{\xi}\,)\,d^3\xi &= -\sum_{\vec{k},\lambda=\pm1}\sum_{L=1}^{\infty}\sum_{M=-L}^{L}\sqrt{2\pi\,(2L+1)}\frac{e\,\omega}{2m_N}\,i^L\,j_L(\frac{\omega r}{2})\vec{T}_{L\,L\,M}(\hat{r})\\ &\cdot\left[(\mu_p+(-1)^L\,\mu_n)\,\vec{S}+(\mu_p-(-1)^L\,\mu_n)\,\vec{t}\right]\cdot\left[a_{\vec{k},\lambda}\,\delta_{M,\lambda}-a^\dagger_{\vec{k},\lambda}\,(-1)^{L+\lambda}\,d^L_{M,-\lambda}(\theta)\right]\\ &= -\sum_{\vec{k},\lambda=\pm1}\sum_{L=1}^{\infty}\sum_{M=-L}^{L}\sqrt{2\pi\,(2L+1)}\,\frac{e\,\omega}{2m_N}\,i^L\,j_L(\frac{\omega r}{2})\,\left\{(\mu_p+(-1)^L\,\mu_n)\,[Y_L\otimes S]_{L\,M}\right.\\ &\left.+(\mu_p-(-1)^L\,\mu_n)\,[Y_L\otimes t]_{L\,M}\right\}\cdot\left[a_{\vec{k},\lambda}\,\delta_{M,\lambda}-a^\dagger_{\vec{k},\lambda}\,(-1)^{L+\lambda}\,d^L_{M,-\lambda}(\theta)\right],\end{aligned} \tag{6.72}$$

where we again used Eq. (6.66).

We are now ready to calculate the amplitudes $\mathcal{M}_{fi}^{\phi\,\sigma1}$ and $\mathcal{M}_{fi}^{\phi\,\sigma2}$. The results are given in Appendix H, together with the amplitudes $\mathcal{M}_{fi}^{\sigma1\,\sigma1}$ and $\mathcal{M}_{fi}^{\sigma2\,\sigma2}$, which do not contain the gradient part of the photon field. Nevertheless, these contributions are strong, cf. Fig. 6.7, due to the numerically large factor $(\mu_p-\mu_n)^2\approx 22$. As the amplitudes with both photons coupling to the current $\vec{J}^{(p)}$, Eq. (6.60), are not supported by this factor, these contributions are tiny. Therefore, they are not included in our work. We also found the mixed amplitudes $\mathcal{M}_{fi}^{\sigma1\,\sigma2}$, $\mathcal{M}_{fi}^{\sigma2\,\sigma1}$ negligibly small, which is no surprise, as explained in Appendix H.

So far we (explicitly) only considered one-body currents. However, there are also non-negligible contributions from pion-exchange currents, cf. Fig. (6.2). The corresponding expressions for the currents in coordinate-space representation are

$$\vec{J}^{\rm KR}_{\rm stat}(\vec{\xi};\vec{x}_1,\vec{x}_2) = \frac{e\,f^2}{m_\pi^2}\,(\vec{\tau}_1\times\vec{\tau}_2)_z\,\left[\vec{\sigma}_1\,\delta(\vec{x}_1-\vec{\xi})\,(\vec{\sigma}_2\cdot\hat{r})+\vec{\sigma}_2\,\delta(\vec{x}_2-\vec{\xi})\,(\vec{\sigma}_1\cdot\hat{r})\right]\,\frac{\partial}{\partial r}\frac{{\rm e}^{-m_\pi r}}{r} \tag{6.73}$$

for the Kroll-Ruderman (pair) current (Fig. 6.2(a)), and

$$\vec{J}^{\rm pole}_{\rm stat}(\vec{\xi};\vec{x}_1,\vec{x}_2) = -\frac{e\,f^2}{4\pi}\,(\vec{\tau}_1\times\vec{\tau}_2)_z\cdot\left(\vec{\nabla}_1-\vec{\nabla}_2\right)\,(\vec{\sigma}_1\cdot\vec{\nabla}_1)\,(\vec{\sigma}_2\cdot\vec{\nabla}_2)\,\frac{{\rm e}^{-m_\pi|\vec{x}_1-\vec{\xi}|}}{m_\pi\,|\vec{x}_1-\vec{\xi}|}\,\frac{{\rm e}^{-m_\pi|\vec{x}_2-\vec{\xi}|}}{m_\pi\,|\vec{x}_2-\vec{\xi}|} \tag{6.74}$$

for the so-called pion-pole current (Fig. 6.2(b)), cf. e.g. [57], Section 8.3[4]. $\vec{\tau}_i$ denotes the isospin operator of the ith nucleon, $\vec{x}_i$ its position. The relative vector $\vec{r}$ is defined as $\vec{r}=\vec{x}_1-\vec{x}_2$.

Our numerical evaluations show that the explicit inclusion of the pole current is well negligible in the process and energies under consideration. Therefore we are only concerned with the Kroll-Ruderman current, Eq. (6.73). This expression, however, is derived in the limit of static nucleons (denoted by the index 'stat' in Eq. (6.73)), i.e. the correction due to the photon energy is neglected. This being a rather crude approximation for $\omega\sim 100$ MeV, which is close to the pion mass, we use instead of Eq. (6.73)

$$\vec{J}^{\rm KR}(\vec{\xi};\vec{x}_1,\vec{x}_2) = \frac{e\,f^2}{m_\pi^2}\,(\vec{\tau}_1\times\vec{\tau}_2)_z\,\left[\vec{\sigma}_1\,\delta(\vec{x}_1-\vec{\xi})\,(\vec{\sigma}_2\cdot\hat{r})+\vec{\sigma}_2\,\delta(\vec{x}_2-\vec{\xi})\,(\vec{\sigma}_1\cdot\hat{r})\right]\,\frac{\partial}{\partial r}f^{\rm KR}(r). \tag{6.75}$$

The function $f^{\rm KR}(r)$ depends on the photon energy and is defined in Appendix I, where we derive Eq. (6.75).

Now we have another current at hand, which we can use to replace $\vec{J}(\vec{\xi})$ in Eq. (6.1). However, one has to be careful in order not to double-count[5] certain contributions; e.g. it is not allowed to combine $H^{\rm int}=-\int\vec{J}^{\rm KR}(\vec{\xi})\cdot\vec{A}^{\rm full}(\vec{\xi})\,d^3\xi$ at one vertex with $H^{\rm int}=-\int\vec{J}(\vec{\xi})\cdot\vec{\nabla}\phi(\vec{\xi})\,d^3\xi$ at the other, because $\vec{J}^{\rm KR}$ is part of $\vec{J}$. Therefore, this combination is already included – at least partly – in the dominant terms of Section 6.1.1, cf. discussion around Eq. (6.10).

First we note that the Kroll-Ruderman current changes isospin, i.e. $H^{\rm int}=-\int\vec{J}^{\rm KR}(\vec{\xi})\cdot\vec{A}(\vec{\xi})\,d^3\xi$ transforms the isospin-0 deuteron into an isospin-1 object. This can easily be seen when we act with $(\vec{\tau}_1\times\vec{\tau}_2)_z$ on the deuteron isospin wave function (Eq. (5.9)):

$$(\vec{\tau}_1\times\vec{\tau}_2)_z\,\frac{1}{\sqrt{2}}\,\mid p\,n-n\,p\,\rangle = (\tau_1^x\,\tau_2^y-\tau_1^y\,\tau_2^x)\,\frac{1}{\sqrt{2}}\,\mid p\,n-n\,p\,\rangle = -2\,i\,\frac{1}{\sqrt{2}}\,\mid p\,n+n\,p\,\rangle \tag{6.76}$$

Therefore we need another isospin-changing interaction at the second vertex. Pauli's principle guarantees that the total wave function of the two-nucleon system has to be antisymmetric under the exchange of the two constituents, as nucleons are fermions. Stated differently, the wave function has to fulfill $(-1)^{S+L+T}=-1$, i.e. in order to have $T=1$ we need $S+L$ even. The operators at our disposal are Y_L from $\hat{\phi}_{i,f}$ (Eq. (6.4)), $[Y_{L-1}\otimes S]_L$ and $[Y_{L-1}\otimes t]_L$ from $\int\vec{J}^{(\sigma)}\cdot\vec{A}^{(1)}$ (Eq. (6.67)) and $[Y_L\otimes S]_L$, $[Y_L\otimes t]_L$ from $\int\vec{J}^{(\sigma)}\cdot\vec{A}^{(2)}$ (Eq. (6.72)). Y_L and $[Y_{L'}\otimes S]_L$ are spin-conserving operators, $[Y_{L'}\otimes t]_L$ is spin-changing, i.e. this operator corresponds to $S_C=0$, cf. Eqs. (L.37-L.39). When we restrict ourselves to L, $L'=1$, which is a reasonable

[4] We note that our convention for the pion-nucleon coupling f^2 differs by a factor 4π from that used in [57].

[5] We are grateful to W. Weise for useful comments made on this point.

approximation as higher multipoles are strongly suppressed, we find Y_1 – remember, the expansion $\phi(\vec{\xi})$ starts with $L = 1$ (Eq. (6.4)), $[Y_0 \otimes S]_1$, $[Y_1 \otimes S]_1$, $[Y_0 \otimes t]_1$ and $[Y_1 \otimes t]_1$. The operator $[Y_0 \otimes S]_1$ is isospin-conserving, as it transforms the deuteron into an $S = 1$-state with even orbital angular momentum, cf. Eq. (L.38)[6]. So is the spin-changing operator $[Y_1 \otimes t]_1$. Therefore the possible candidates are Y_1, $[Y_1 \otimes S]_1$ and $[Y_0 \otimes t]_1$. We found that the numerically most important operator is $[Y_0 \otimes t]_1$. The same observation was made in [24]. Nevertheless, also the operator Y_1, which stems from $\hat{\phi}_i$, $\hat{\phi}_f$, gives non-negligible contributions, whereas we found the amplitudes including $[Y_1 \otimes S]_1$ invisibly small and therefore these terms are not written down in our work. However, in the amplitudes including $\hat{\phi}_i$ or $\hat{\phi}_f$ at the non-KR vertex, one is not allowed to use the full photon field in $H^{\rm int} = -\int \vec{J}^{\rm KR}(\vec{\xi}) \cdot \vec{A}(\vec{\xi})\, d^3\xi$, as explained after Eq. (6.75). Therefore we are left with $\mathcal{M}_{fi}^{\rm KR\,full\,\sigma 1}$, $\mathcal{M}_{fi}^{\phi\,\rm KR1}$ and $\mathcal{M}_{fi}^{\phi\,\rm KR2}$, where 'KR full' denotes the integral over the Kroll-Ruderman current, multiplied by the full photon field. There is no danger of double-counting in $\mathcal{M}_{fi}^{\rm KR\,full\,\sigma 1}$, as we only take into account the operator $[Y_{L-1} \otimes t]_L$. This operator, however, changes the deuteron spin, cf. Eq. (L.39), whereas the matrix elements arising from $\phi_{i,f}$ are spin-conserving, see Eq. (L.37). Further contributions, like the one where $\vec{J}(\vec{\xi}) = \vec{J}^{\rm KR}(\vec{\xi})$ at both vertices, turned out to be small. Therefore we only have to consider the three combinations above. The evaluation of these contributions is given in Appendix I.

Two-body currents with explicit $\Delta(1232)$ degrees of freedom, as displayed in Fig. 6.4, are suppressed by one order in ϵ with respect to the Kroll-Ruderman current, due to the $\gamma N\Delta$ vertex being part of $\mathcal{L}_{N\Delta}^{(2)}$, see Eq. (2.29). This is in agreement with the findings of [22], where such contributions to elastic deuteron Compton scattering below 100 MeV were claimed to be negligibly small (of the order of 2%). A similarly strong influence of the $\Delta(1232)$ current to the process $np \to d\gamma$ is reported in Section 8.5 of [57], where the contributions from these currents turn out considerably smaller than those from pionic exchange currents. Therefore and due to the excellent agreement of the total deuteron-photodisintegration cross section, extracted from our elastic Compton amplitude, with experimental data up to $\omega = 100$ MeV, cf. Section 6.4, we so far refrain from including these terms into our calculation. Nevertheless, it would be an interesting future task to perform a detailed investigation of their size.

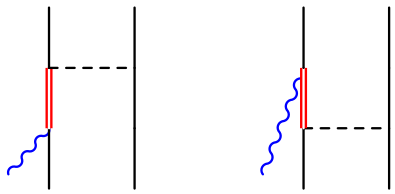

Figure 6.4: Exemplary one-pion-exchange currents with explicit $\Delta(1232)$ degrees of freedom.

In the last two subsections we prepared all ingredients of our deuteron Compton calculation, which are new with respect to Chapter 5. In the next section we demonstrate that our non-perturbative approach fulfills the well-known low-energy theorem, i.e. we reach the exact static limit in this approach. In Section 6.3, we present our results at non-zero energies and compare them to those from the strictly perturbative approach of Chapter 5 and to data.

[6] The latter claim follows from the fact that the deuteron has even orbital angular momentum and from Eq. (L.21).

6.2 Low-Energy Limit in the Non-Perturbative Approach

One of the aims to be achieved with the approach to deuteron Compton scattering described in this chapter is to extend the calculation of Chapter 5 to lower energies. In this section we prove that we have indeed *removed* the limitations of Chapter 5 at low energies, i.e. our so-called non-perturbative approach to deuteron Compton scattering reaches the correct limit of vanishing photon energy.

We remind the reader that the strictly perturbative expansion of the interaction kernel up to third order in the SSE counting scheme, used in Chapter 5, leads to a low-energy cross section that is too large by a factor of 6. The amplitude in this limit, which is the well-known Thomson term for scattering of an electromagnetic wave from a charged particle, cf. Eq. (5.4), is

$$A^{\text{Thomson}} = \frac{Q^2\, e^2}{A\, m_N}\, \hat{\epsilon}_{\lambda_i} \cdot \hat{\epsilon}^*_{\lambda_f}. \tag{6.77}$$

The overall sign of the amplitude is convention and differs e.g. in Ref. [24] from this work. As already discussed in Section 5.1, Friar showed that Eq. (6.77) is a consequence of gauge invariance [79]. Therefore the ansatz used in Chapter 5 obviously violates gauge invariance, which is one of the shortcomings that we cure – at least approximately – in this chapter. The violation appears when evaluating the kernel between the deuteron wave functions, without allowing the two nucleons in the intermediate state to interact with each other. The reason is that the deuteron wave function implies this interaction, which can be interpreted as the exchange of mesons, e.g. of pions, between the two nucleons. In order to really achieve gauge invariance, it is therefore mandatory to include rescattering of the two nucleons on one hand and to couple the photons to these meson-exchange currents on the other, cf. Figs. 6.2 and 6.3 and Refs. [22, 24]. Full gauge invariance will however not be obtained within our calculation, as the np-potential we use (AV18 [73], cf. Appendix K), contains more than only the one-pion exchange. The short-distance part of such a phenomenological potential may be interpreted as the exchange of mesons heavier than the pion (e.g. the ω- or ρ-meson). As we only allow for explicit pion-exchange currents, gauge invariance will not be fulfilled exactly [22].

For a deuteron target, Eq. (6.77) reads

$$A_d^{\text{Thomson}} = \frac{e^2}{m_d}\, \hat{\epsilon}_{\lambda_i} \cdot \hat{\epsilon}^*_{\lambda_f} \approx \frac{e^2}{2m_N}\, \hat{\epsilon}_{\lambda_i} \cdot \hat{\epsilon}^*_{\lambda_f}. \tag{6.78}$$

This is a non-trivial result because the deuteron mass is involved, whereas the Thomson seagull for Compton scattering from the proton, Fig. 5.5(a), yields the amplitude

$$A_p^{\text{Thomson}} = \frac{e^2}{m_p}\, \hat{\epsilon}_{\lambda_i} \cdot \hat{\epsilon}^*_{\lambda_f}, \tag{6.79}$$

cf. Eq. (B.1). The neutron amplitude is zero in the static limit. Therefore, all other contributions to deuteron Compton scattering in the limit $\omega \to 0$ have to cancel half of the proton amplitude (6.79). The only non-vanishing terms in the low-energy limit, except for the proton seagull, are two-body diagrams, namely the explicit pion-exchange diagrams, Fig. 5.7, and the double-commutator term, Eq. (6.26), as explained in Appendix G. This double-commutator involves the internal Hamiltonian $H^{np} = \frac{\vec{p}^{\,2}}{m_N} + V$, cf. Eq. (6.17), and therefore can be separated into a kinetic energy and a potential part, cf. Appendix G. Arenhövel [88] showed analytically that in the static limit the potential energy part, using the one-pion-exchange potential, cancels exactly the contributions from explicit pion exchange,

Fig. 5.7. It is this consistency between the diagrams explicitly included in the interaction kernel and the potential used in the double-commutator, Eq. (6.26), which guarantees the correct low-energy behaviour of our calculation. Therefore we only include the one-pion exchange in the amplitude (6.26). Since two-nucleon contact terms, which parameterize the exchange of heavier particles than pions, are of higher than third order in the SSE scheme, we do not include such diagrams explicitly, and therefore they are also not included in the double-commutator. While this procedure is strictly speaking not consistent with the NN-potential [73] that we use for constructing the np-Green's function, it is nevertheless a legitimate prescription, as we show in Section 6.3.2 that using only the one-pion-exchange potential does not change our results significantly.

As the sum of the explicit pion-exchange diagrams from Fig. 5.7 and the potential energy part of Eq. (6.26) gives no contribution in the low-energy limit, it is clear that the kinetic energy part of the double-commutator has to cancel half of the proton seagull amplitude (6.79). This can easily be shown to be true: in the long-wavelength limit, i.e. for $|\vec{k}| \to 0$, the photon field reduces to the polarization vector (dipole approximation), as $\hat{\epsilon}_\lambda \, \mathrm{e}^{i\vec{k}\vec{r}} \to \hat{\epsilon}_\lambda$. As we already know that only the gradient part of the photon field survives in the static limit, cf. Section 6.1.1, we find

$$\vec{\nabla}_\xi \phi(\vec{\xi})\Big|_{\omega\to 0} = \hat{\epsilon}_\lambda. \tag{6.80}$$

Therefore, $\phi(\vec{\xi})|_{\omega\to 0} = \hat{\epsilon}_\lambda \cdot \vec{\xi}$ and, using $\hat{\phi} = e\,\phi(\vec{r}/2)$,

$$\hat{\phi}\Big|_{\omega\to 0} = e\,\frac{\vec{r}}{2}\cdot\hat{\epsilon}_\lambda. \tag{6.81}$$

Now we need to evaluate the double-commutator in this limit, finding

$$\begin{aligned}
\lim_{\omega\to 0}\left[[\frac{\vec{p}^{\,2}}{m_N},\hat{\phi}_i],\hat{\phi}_f\right] &= \frac{e^2}{4m_N}\,\left[[\vec{p}^{\,2},\vec{r}\cdot\hat{\epsilon}_{\lambda_i}],\vec{r}\cdot\hat{\epsilon}^*_{\lambda_f}\right] \\
&= \frac{e^2}{2m_N}\,\left[(\vec{p}\,(\vec{r}\cdot\hat{\epsilon}_{\lambda_i}))\cdot\vec{p},\vec{r}\cdot\hat{\epsilon}^*_{\lambda_f}\right] \\
&= \frac{-i\,e^2}{2m_N}\,\left[\hat{\epsilon}_{\lambda_i}\cdot\vec{p},\vec{r}\cdot\hat{\epsilon}^*_{\lambda_f}\right] \\
&= -\frac{e^2}{2m_N}\,\hat{\epsilon}_{\lambda_i}\cdot\hat{\epsilon}^*_{\lambda_f},
\end{aligned} \tag{6.82}$$

where we used $\vec{p} = \frac{\vec{p}_p - \vec{p}_n}{2} = -i\,\frac{\vec{\nabla}_{x_p} - \vec{\nabla}_{x_n}}{2}$ and $\vec{r} = \vec{x}_p - \vec{x}_n$, cf. Eq. (6.14). Eq. (6.82) is obviously symmetric under $i \leftrightarrow f$. Therefore the second double-commutator in Eq. (6.26) gives the same result. Adding both commutators cancels the factor $\frac{1}{2}$ in front of the matrix element and we see that the result accounts for exactly half of the negative Thomson amplitude of the proton. Note that this result is independent of the deuteron wave function and the np-potential chosen.

Our numerical evaluation agrees well with the Thomson limit (6.77), as demonstrated in Fig. 6.5, where we see a comparison between the proton Compton cross section, $\left(\frac{1}{2}\right)^2 = \frac{1}{4}$ of this cross section and the deuteron Compton cross section at zero photon energy (we remind the reader that $\frac{d\sigma}{d\Omega} \propto |\mathcal{M}_{fi}|^2$, cf. Eq. (5.11)); the latter two curves are nearly indistinguishable. In the right panel of Fig. 6.5, where we show the relative error $\left(\frac{d\sigma}{d\Omega}\right)_d \Big/ \left(\frac{1}{4}\frac{d\sigma}{d\Omega}\right)_p - 1$, we see that the deviation is less than 2% and angle-independent. Therefore it can be accounted for by a constant factor. When we use the AV18 wave function [73], the curve in the right panel of Fig. 6.5 turns out of about the same absolute size, but with opposite sign. This observation suggests that the main part of this discrepancy is due to numerical uncertainties in the normalization of the wave function within our code.

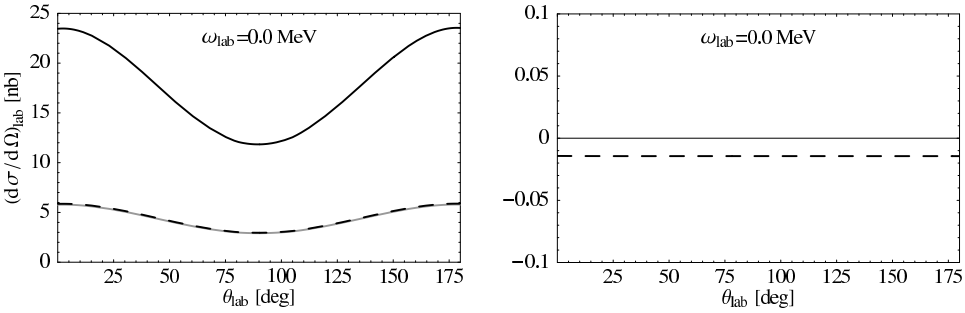

Figure 6.5: Left panel: Comparison of the proton (black, solid), deuteron (grey, solid) and 1/4 of the proton (black, dashed) Compton cross section in the static limit. The function plotted in the right panel is $\left(\frac{d\sigma}{d\Omega}\right)_d / \left(\frac{1}{4}\frac{d\sigma}{d\Omega}\right)_p - 1$.

In this section we showed that the approach to deuteron Compton scattering, that we use in this chapter, fulfills the low-energy theorem and therefore guarantees at least approximate gauge invariance of the calculation. In the next section we present our results for non-zero photon energies, demonstrating that we have achieved a consistent description of γd scattering for photon energies ranging from 0 MeV up to $\omega \sim 100$ MeV.

6.3 Predictions for Deuteron Compton Cross Sections

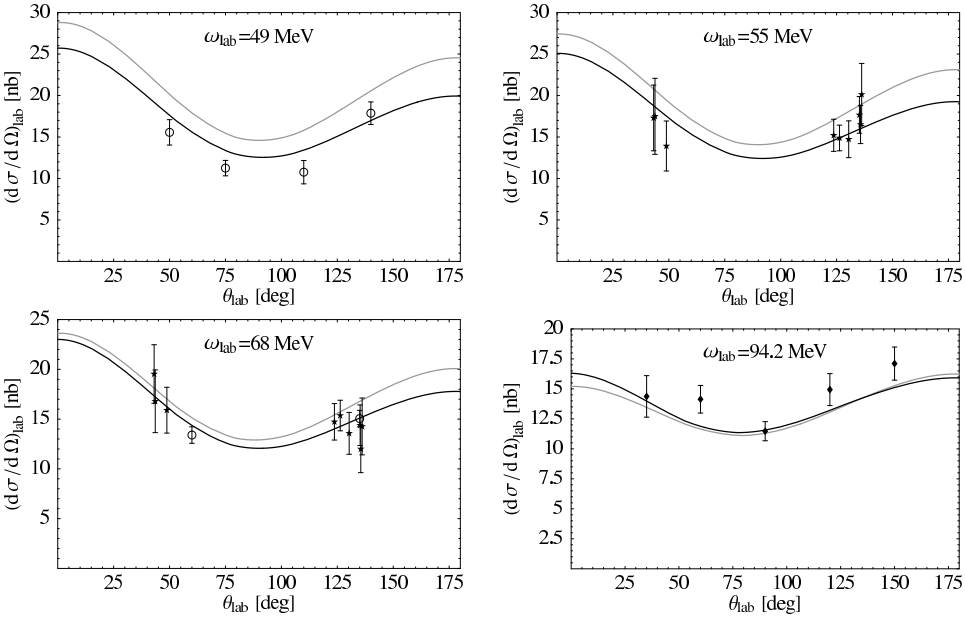

Figure 6.6: Comparison of our results from the two different approaches to deuteron Compton scattering: The black lines are the results of the non-perturbative approach, Chapter 6, the grey lines are the SSE-results of Fig. 5.9. The data are from [17] (circle), [18] (star) and [19] (diamond).

In Fig. 6.6, we show our parameter-free predictions for the elastic deuteron Compton cross sections, achieved with the "non-perturbative" calculation of this chapter. These results are compared to the predictions from Section 5.2 and to the data from Illinois [17], Lund [18] and SAL [19]. Obviously we have reached our final goal: we have achieved a (chirally) consistent calculation for elastic deuteron Compton scattering, which describes all existing data reasonably well and also satisfies the low-energy theorem exactly, cf. Section 6.2. In both calculations presented in Fig. 6.6 we use for the isoscalar polarizabilities the numbers from our 2-parameter SSE fit to proton data, given in Table 3.1, which is justified by the fact that the isovector polarizabilities vanish at leading-one-loop order in the Small Scale Expansion.

There are still minor deviations from the experiments, e.g. our calculation lies slightly above the three 49 MeV data from [17], which have been measured at angles below 120°. However, this is a feature that our calculation has in common with other approaches, which also reach the correct static limit, e.g. [22, 24, 60]. At higher energies the two calculations of Chapters 5 and 6 approach each other. A heuristic explanation of this behaviour, based on the fact that a high-energy photon immediately separates the two nucleons from each other, is given in Section 5.1. This is another important cross-check as it demonstrates that the power-counting applied in Chapter 5 is indeed suited for calculating deuteron Compton scattering at photon energies of $\omega \sim 100$ MeV. Consequently, both curves in Fig. 6.6 describe the 94.2 MeV data from [19] equally well – in fact they nearly lie on top of each other.

Because of the many contributions to the curves in Fig. 6.6 we resume all amplitudes contained in our calculation. These are:

- The single-nucleon Heavy Baryon Chiral Perturbation Theory (HBχPT) contributions from Fig. 5.5, except for the nucleon pole diagrams (Fig. 5.5(b) and its u-channel analog). These two diagrams are discussed under the final item. As in Chapter 5, the pion pole, Fig. 5.5(c), gives no contribution because isospin-breaking effects like the mass difference between proton and neutron are neglected.

- The single-nucleon contributions sketched in Fig. 5.6, which include the explicit $\Delta(1232)$ resonance and occur at third order in the Small Scale Expansion in addition to third-order HBχPT. For the coupling constants of the two isoscalar short-distance operators, Fig. 5.6(f), we use the numbers derived from our Baldin-constrained fit to the proton Compton data, cf. Section 3.3.

- The nine two-body diagrams with both photons coupling to the exchanged pion, see Fig. 5.7.

- All terms with an intermediate two-nucleon state, which replace the nucleon-pole diagrams in this chapter, cf. Figs. 6.1 and 6.3. These include the amplitudes $\mathcal{M}_{fi}^{\phi\phi}$ given in Eqs. (6.23)-(6.26), which have been derived from minimal coupling, i.e. by replacing the photon field in the interaction Hamiltonian by the gradient term at both vertices, cf. Eqs. (6.2, 6.3). Our results for these amplitudes are given in Appendix G. Further contributions are the amplitudes calculated in Appendices H and I, where the above replacement is done at only one or even at none of the photon vertices, whereas in the other interaction Hamiltonians we replace the photon field by $\vec{A}^{(1)}$ or $\vec{A}^{(2)}$, respectively, cf. Eqs. (6.57) and (6.58). $\vec{A}^{(1)}$ is the magnetic part of the photon field in our notation, the other two parts are of electric nature. The currents that we use for these interactions are the spin current $\vec{J}^{(\sigma)}$ (Eq. (6.59)) and the Kroll-Ruderman current $\vec{J}^{\rm KR}$ (Eq. (6.75), see also Fig. 6.2(a)), which are the

only currents that we found to give non-negligible contributions. The corresponding amplitudes are called $\mathcal{M}_{fi}^{\phi\,\sigma 1}$, $\mathcal{M}_{fi}^{\phi\,\sigma 2}$, $\mathcal{M}_{fi}^{\sigma 1\,\sigma 1}$, $\mathcal{M}_{fi}^{\sigma 2\,\sigma 2}$, $\mathcal{M}_{fi}^{\mathrm{KR}\,\sigma 1}$, $\mathcal{M}_{fi}^{\phi\,\mathrm{KR}1}$ and $\mathcal{M}_{fi}^{\phi\,\mathrm{KR}2}$. The indices are '$\phi$' for the vertex arising from minimal coupling, '$\sigma 1$' ('$\sigma 2$') for the coupling of $\vec{A}^{(1)}$ ($\vec{A}^{(2)}$) to the spin current and analogously for the Kroll-Ruderman current 'KR'. For example, $\mathcal{M}_{fi}^{\sigma 1\,\sigma 1}$ describes the coupling of a magnetic photon to the spin current at both vertices. This amplitude dominates the deuteron-photodisintegration cross section at threshold, cf. Section 6.4.

It is straightforward to combine the contributions from Chapter 5 with those from this chapter. The only modification necessary is to replace the Cartesian polarization vectors $\vec{\epsilon}$, used in Chapter 5, by spherical ones, cf. Eq. (L.10). Of course, one also has to make sure that the convention adopted for the overall sign of the amplitude is the same in both parts. We use the proton-seagull diagram (Fig. 5.5(a)) in order to fix the sign. The convention we chose is such that the Thomson amplitude is given by Eq. (5.4).

We now discuss the strength of several contributions separately. However, there are certain amplitudes which are closely related to each other: The kinetic energy part of the double commutator, Eq. (G.16), cancels half of the proton seagull in the static limit, cf. Section 6.2. The sum of the potential energy part of the commutator (G.37) and the nine two-body contributions from Fig. 5.7 is zero in the limit of vanishing photon energy. It stays small in the whole energy range considered in this work, as already observed in Refs. [24, 89]. Therefore we do not separate these contributions from each other. Nevertheless, there are a few issues worth investigating in more detail:

1) The prominent role of the amplitudes $\mathcal{M}_{fi}^{\phi\phi 1,2}$, which include the case of an $E1$-interaction at both vertices.

2) The importance of the amplitudes $\mathcal{M}_{fi}^{\phi\,\sigma}$ and $\mathcal{M}_{fi}^{\sigma\sigma}$, with σ denoting the coupling to the spin current.

3) The strength of the amplitudes with the explicit Kroll-Ruderman current at one vertex, $\mathcal{M}_{fi}^{\mathrm{KR}}$.

In the upper two panels of Fig. 6.7 – we investigate the two extreme energies of Fig. 6.6 – these contributions are successively added to the remaining terms: The single-nucleon amplitudes from Figs. 5.5 and 5.6 (except for the nucleon-pole diagrams Fig. 5.5(b)), the two-nucleon diagrams from Fig. 5.7 and the double-commutator amplitude $\mathcal{M}_{fi}^{\phi\phi 4}$, cf. Eq. (6.26). The amplitude $\mathcal{M}_{fi}^{\phi\phi 3}$ (Eq. (6.25)) is a small correction and has been added to the leading amplitudes $\mathcal{M}_{fi}^{\phi\phi 1,2}$.

Obviously, the amplitudes $\mathcal{M}_{fi}^{\phi\phi}$ are the dominant ones in Fig. 6.7. This observation holds for both energies considered. However, also the amplitudes $\mathcal{M}_{fi}^{\sigma\sigma}$ give important contributions. The same pattern occurs in the calculation of total deuteron-photodisintegration cross sections, cf. Section 6.4. The contributions from $\mathcal{M}_{fi}^{\phi\sigma}$ are nearly negligible. The small size of these terms is due to the fact that the amplitudes $\mathcal{M}_{fi}^{\phi\sigma 1}$ and $\mathcal{M}_{fi}^{\phi\sigma 2}$ largely cancel each other, cf. Appendix H. The diagrams with one photon explicitly coupling to the Kroll-Ruderman current are tiny for low energies, but give a sizeable correction at 94.2 MeV. Their contribution is stronger in our calculation than it appears in Ref. [24]. This discrepancy may be attributed to the use of a different pion propagator in the Kroll-Ruderman current, cf. Appendix I. The difference is that we do not neglect the photon energy in the denominator, which is a crude approximation for $\omega \sim 100$ MeV. However, we have to caution that comparing cross sections is sometimes misleading, as they are

non-additive quantities and strongly affected by interference between the various amplitudes, cf. Eq. (5.11).

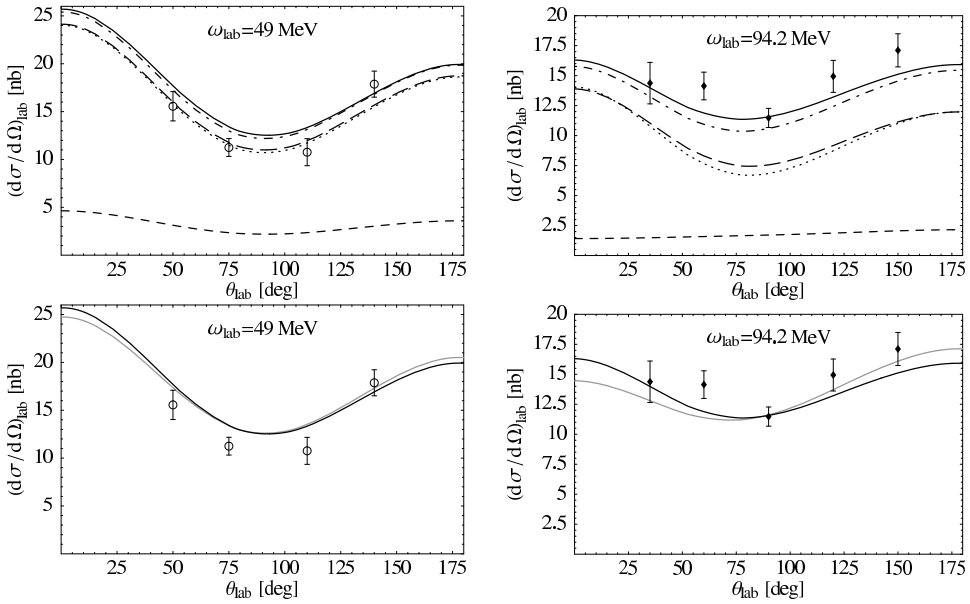

Figure 6.7: Comparison of separate contributions to our deuteron Compton-scattering results. In the upper panels we compare the full result (solid) to curves with several amplitudes subtracted; the subtracted amplitudes are: $\mathcal{M}_{fi}^{\mathrm{KR}}$ (dot-dashed), $\mathcal{M}_{fi}^{\mathrm{KR}}+\mathcal{M}_{fi}^{\sigma\sigma}$ (dotted), $\mathcal{M}_{fi}^{\mathrm{KR}}+\mathcal{M}_{fi}^{\sigma\sigma}+\mathcal{M}_{fi}^{\phi\sigma}$ (longdashed), $\mathcal{M}_{fi}^{\mathrm{KR}}+\mathcal{M}_{fi}^{\sigma\sigma}+\mathcal{M}_{fi}^{\phi\sigma}+\mathcal{M}_{fi}^{\phi\phi 1,2,3}$ (shortdashed). In the lower panels we compare our full result (black) to a curve where the amplitudes $\mathcal{M}_{fi}^{\sigma\sigma}$ and $\mathcal{M}_{fi}^{\phi\phi}$ have been replaced by their $L = L' = 1$-approximations (grey). The data are from [17] (circle) and [19] (diamond).

We also estimate the strength of those contributions where the photons coupling to the NN-rescattering diagrams, Fig. 6.1, have multipolarity $L = 2$. In Ref. [24], these next-to-leading terms in the multipole expansion of the photon field are claimed to be small and therefore have been neglected. However, we slightly disagree from this statement, as can be seen in the lower two panels of Fig. 6.7. There we show our full results compared to curves which only include the $L = L' = 1$-approximation of the dominant amplitudes $\mathcal{M}_{fi}^{\phi\phi 1,2,3}$ and $\mathcal{M}_{fi}^{\sigma\sigma}$. For low energies these corrections are certainly negligible, however in the high-energy regime of our calculation they are of the order of 10% in the forward and in the backward direction.

Comparing to Ref. [24], we see the main difference of our calculation to this work in our more involved description of the single-nucleon structure. In [24] the structure of the nucleon is respected only via the static polarizabilities $\bar{\alpha}_{E1}$ and $\bar{\beta}_{M1}$, i.e. via the leading terms of a Taylor expansion of the single-nucleon Compton multipoles, cf. Section 3.1.2. In our work, these multipoles have been calculated up to third order in the Small Scale Expansion, as explained in detail in Chapters 3 and 5, and are included with their full energy dependence. Another advantage of our approach with respect to [24] is the treatment of the pion propagator in the pion-exchange diagrams of Fig. 5.7. We calculate these diagrams using the full pion propagator, whereas the authors of [24] always make the assumption that the photon energy is small compared to the energy of the virtual pion and therefore may be neglected.

This, however, is no longer a good approximation as soon as the photon energy comes close to the pion mass. A similar difference occurs in the Kroll-Ruderman amplitudes, as discussed above. Finally we do not agree with the statement of [24] that $L = 2$-contributions are negligible for all amplitudes and energies considered, see Fig. 6.7.

We believe to have proven, in the last two sections, that our calculation provides a consistent description of elastic deuteron Compton scattering below $\omega \sim 100$ MeV. We can trust that it also gives reasonable results for even higher energies, say up to the pion mass. There, however, threshold corrections in analogy to Eq. (3.13) should not be neglected anymore. Therefore the 120 MeV curve in Fig. 6.8, where we show our results at various energies, is only a qualitative statement about the behaviour of the differential cross section for $\omega \to m_\pi$. We also show our prediction at $\omega_{\rm lab} = 30$ MeV, which is comparable in magnitude to the 49 MeV curve, but its shape is already closer to the forward-backward symmetry exhibited by the static cross section, cf. Fig. 6.5.

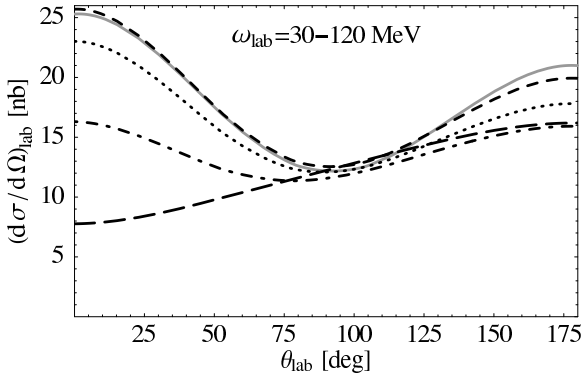

Figure 6.8: Comparison of our results for differential deuteron Compton cross sections at various energies: 30 MeV (grey), 49 MeV (shortdashed), 68 MeV (dotted), 94.2 MeV (dotdashed), 120 MeV (longdashed).

In the next section we investigate the sensitivity of our results on the deuteron wave function, which is another shortcoming of the approach presented in Chapter 5, where the observed influence turned out unexpectedly strong.

6.3.1 Dependence on the Deuteron Wave Function

As demonstrated in Section 6.2, our calculation fulfills the low-energy theorem, Eq. (6.77), independently of the wave function chosen. Therefore and because of the nearly energy-independent offset between the cross sections calculated with the chiral wave function [77] and the AV18-wave function [73], which we observe in Fig. 5.12, it is not surprising that also at non-zero energies the wave-function dependence is reduced with respect to our previous approach, where we did not have this low-energy constraint. In fact, the remaining dependence is of the order of 1% and therefore nearly invisible, cf. Fig. 6.9, where we compare our cross sections calculated with two of the extreme wave functions of Fig. 5.12: the AV18 [73] and the NNLO χPT [77] wave function (the same observation holds for other state-of-the-art deuteron wave functions). This is another important success of the non-perturbative approach, as it demonstrates that our calculation is not sensitive to details of short-distance physics anymore. The 10%-effect observed in Fig. 5.12, however, manifests a much stronger sensitivity to short-distance effects of the wave function than would be expected from a low-energy Effective Field Theory, as discussed in Section 5.2.3.

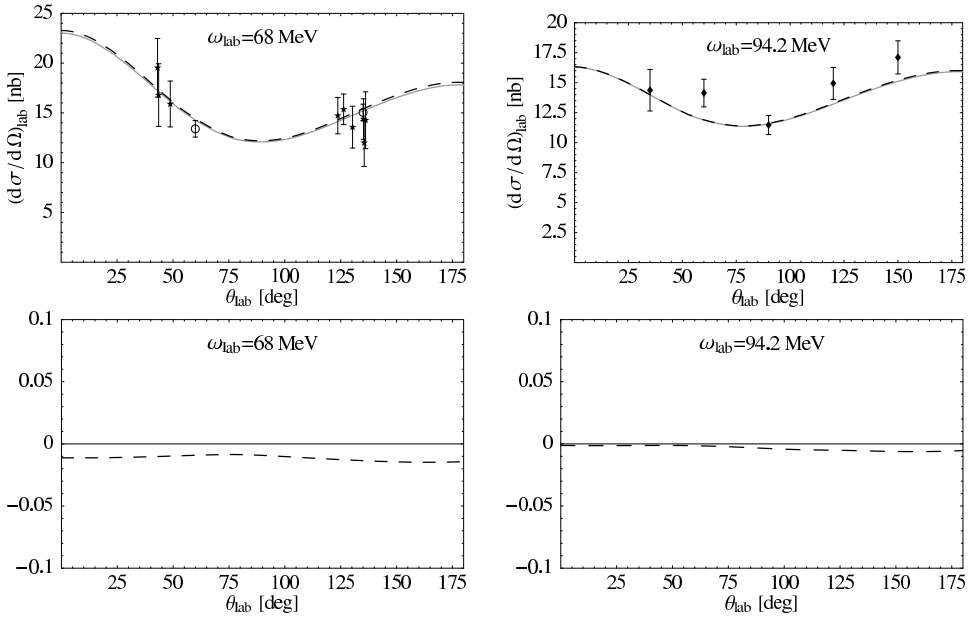

Figure 6.9: Comparison of our deuteron Compton cross-section results for 68 and 94.2 MeV, using two different wave functions: NNLO χPT (grey) [77] and AV18 (dashed) [73]. In the lower two panels we show $\left(\frac{d\sigma}{d\Omega}\right)_{\rm NNLO} / \left(\frac{d\sigma}{d\Omega}\right)_{\rm AV18} - 1$.

6.3.2 Dependence on the Potential

In this subsection we investigate briefly the sensitivity of our calculation to the *np*-potential. Usually we use the AV18-potential [73], given in App. K, which provides an excellent theoretical description of the Nijmegen partial-wave analysis. Here we compare our results achieved with this modern 'high-precision' potential to those when we use the leading-order chiral potential, which includes only the one-pion exchange and a simple parameterization of short-distance effects via two point-like, momentum-independent contact operators. This potential is given e.g. in [74] as

$$\begin{aligned} V_{\rm LO}^{^1S_0}(\vec{r}) &= -f^2\, v_\Lambda(r) + \frac{4\pi}{m_N}\, C_0^{^1S_0}\, \delta_\Lambda^3(r), \\ V_{\rm LO}^{d}(\vec{r}) &= -f^2\, [v_\Lambda(r) + S_{12}(\hat{r})\, t_\Lambda(r)] + \frac{4\pi}{m_N}\, C_0^{d}\, \delta_\Lambda^3(r) \end{aligned} \tag{6.83}$$

for the $^1S_0$ and the (deuteron) $^3S_1$-$^3D_1$ channel, respectively. $S_{12}(\hat{r}) = 3\,(\vec{\sigma}_1\cdot\hat{r})\,(\vec{\sigma}_2\cdot\hat{r}) - \vec{\sigma}_1\cdot\vec{\sigma}_2$ is the tensor operator, see also Appendix K.

The authors of Ref. [74] use a Gaussian regulator in order to render the pion-exchange potential finite at the origin. The resulting central and tensor potential reads

$$v_\Lambda(r) = \frac{1}{2r}\left[{\rm e}^{-m_\pi r}\,{\rm erfc}\left(\frac{-\Lambda r + \frac{m_\pi}{\Lambda}}{\sqrt{2}}\right) - {\rm e}^{m_\pi r}\,{\rm erfc}\left(\frac{\Lambda r + \frac{m_\pi}{\Lambda}}{\sqrt{2}}\right)\right], \tag{6.84}$$

$$t_\Lambda(r) = \frac{r}{m_\pi^2}\frac{\partial}{\partial r}\frac{1}{r}\frac{\partial}{\partial r}\, v_\Lambda(r) \tag{6.85}$$

with

$${\rm erfc}(x) = 1 - {\rm erf}(x) = 1 - \frac{2}{\sqrt{\pi}}\int_0^x dt\, {\rm e}^{-t^2}.$$

The functions given in Eqs. (6.84, 6.85) become Yukawa functions for large distances:

$$v_\Lambda(r)\Big|_{r\to\infty} = \frac{\mathrm{e}^{-m_\pi r}}{r} \tag{6.86}$$

$$t_\Lambda(r)\Big|_{r\to\infty} = \left(1+\frac{3}{m_\pi r}+\frac{3}{(m_\pi r)^2}\right)\frac{\mathrm{e}^{-m_\pi r}}{r} \tag{6.87}$$

$\delta^3_\Lambda(r)$ is the Fourier transform of the regulator,

$$\delta^3_\Lambda(r) = \int \frac{d^3q}{(2\pi)^3}\,\mathrm{e}^{i\vec{q}\cdot\vec{r}}\,\mathrm{e}^{-\frac{q^2}{2\Lambda^2}} = \frac{\Lambda^3\,\mathrm{e}^{-\frac{\Lambda^2 r^2}{2}}}{(2\pi)^{3/2}}. \tag{6.88}$$

At leading order, there are two free parameters, $C_0^{^1S_0}$ and C_0^d, cf. Eq. (6.83). $C_0^{^1S_0}$ has been fixed in [74] via the $^1S_0$ scattering length, $a_0 \approx -23.75$ fm, C_0^d at the deuteron binding energy. We use these two constants to parameterize any short-distance physics in the spin-singlet and -triplet channel, respectively. The results for $C_0^{^1S_0}$ and C_0^d, achieved in [74] for the cutoff-value $\Lambda = 600$ MeV, are given in Table 6.1.

$C_0^{^1S_0}$	C_0^d
-0.422 fm	0.795 fm

Table 6.1: Parameters of the LO chiral potential as determined in [74] for $\Lambda = 600$ MeV.

Even with this rather crude approximation of the neutron-proton interaction we obtain results close to those of the AV18-potential, cf. Fig. 6.10. The observed deviations are small (of the order of $\leq 4\%$), even for photon energies close to 100 MeV. Obviously the one-pion-exchange potential, adequately regulated for $r \to 0$, together with the simplest parameterization of the hard core gives an approximation of the potential which is well sufficient for the process under consideration. We conclude that we are mainly sensitive to the long-range part of the potential. Nevertheless, there are minor deviations visible in Fig. 6.10, which justify the application of a more sophisticated potential than the leading-order chiral one. Not surprisingly, these deviations, which arise due to the poor description of high-energy dynamics in the LO chiral potential, increase with increasing photon energy.

6.4 Total Deuteron-Photodisintegration Cross Section

Besides complying with the low-energy theorem, cf. Section 6.2, another important check on our calculation is to extract total deuteron-photodisintegration cross sections from the Compton amplitude via the optical theorem. This process has been studied more extensively than elastic deuteron Compton scattering and there is plenty of data below 100 MeV to compare with. In [24], a comparison to an older calculation of the process [90] is given, not only of the sum of all contributions, but also of several terms separately, which we use to cross-check our results for certain amplitudes.

The optical theorem in our normalization reads

$$\sigma^{\mathrm{tot}} = \frac{1}{\omega}\cdot\frac{1}{6}\sum_{i=f}\mathrm{Im}[\mathcal{M}_{fi}(\theta=0)], \tag{6.89}$$

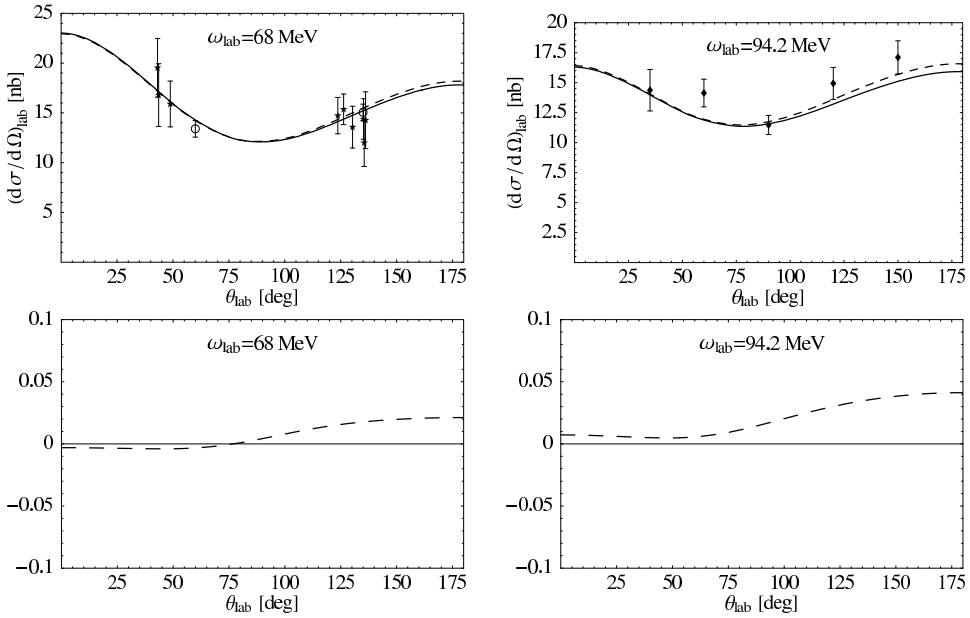

Figure 6.10: Upper panels: Comparison of our result at 68 MeV and 94.2 MeV using two different np-potentials: the AV18-potential [73] (solid) and the LO chiral potential [74] (dashed). For both curves the chiral wave function [77] has been used. Lower panels: Corresponding error plots, calculated in analogy to Fig. 6.5.

i.e. the total cross section is the sum over the imaginary part of all deuteron Compton amplitudes in the forward direction with identical initial and final states ($\lambda_f = \lambda_i$, $M_f = M_i$), divided by the photon energy ω. Like in Eq. (5.11), this sum is divided by 6, as we have to average over the initial states.

We calculate this cross section in the lab frame, in order to be able to compare to data and the theoretical works [90, 24][7]. The amplitudes given in the appendix have been derived in the γd-cm frame, but they are easily transformed into the lab frame. First we note that we only need to sum over the s-channel diagrams, as only they become complex for photon energies above the deuteron binding energy B, while the u-channel amplitudes stay real for all photon energies, cf. Section 6.1.1. As the authors of Ref. [24] calculate in the lab frame, we convert our calculation according to their work. In the s-channel the only change is $\omega + \frac{\omega^2}{2m_d} \leftrightarrow \omega - \frac{\omega^2}{2m_d}$, because in the lab frame, the deuteron's initial kinetic energy vanishes, whereas the total intermediate momentum is $\vec{P}_C = \vec{k}_i$. In the cm frame we have $\vec{P}_i = -\vec{k}_i$ and $\vec{P}_C = \vec{0}$ in the s-channel.

Our result for the total deuteron-photodisintegration cross section is shown in Fig. 6.11, together with data from [93-100], which are described well by our calculation. In the lower left panel the low-energy regime is enlarged, in order to emphasize the non-vanishing value at threshold. The by far most important contribution at threshold stems from the singlet $M1$-transition of $\mathcal{M}_{fi}^{\sigma 1\, \sigma 1\, a}$, see Appendix H. It corresponds to the operator $[Y_0 \otimes t]_1$, which transforms the deuteron into a (singlet) $S_C = 0$-state, cf. Eq. (L.39). $M1$ is the shorthand notation for the magnetic coupling of a photon with $L = 1$. Nevertheless, as is well-known, already 1 MeV above threshold the cross section is completely dominated by the amplitude $\mathcal{M}_{fi}^{\phi\phi\, 1}$, where for $L, L' = 1$ we have an $E1$-interaction at each vertex, and this dominance holds

[7] We note that many more authors have been working on this process, see e.g. [91] or [92] and references therein.

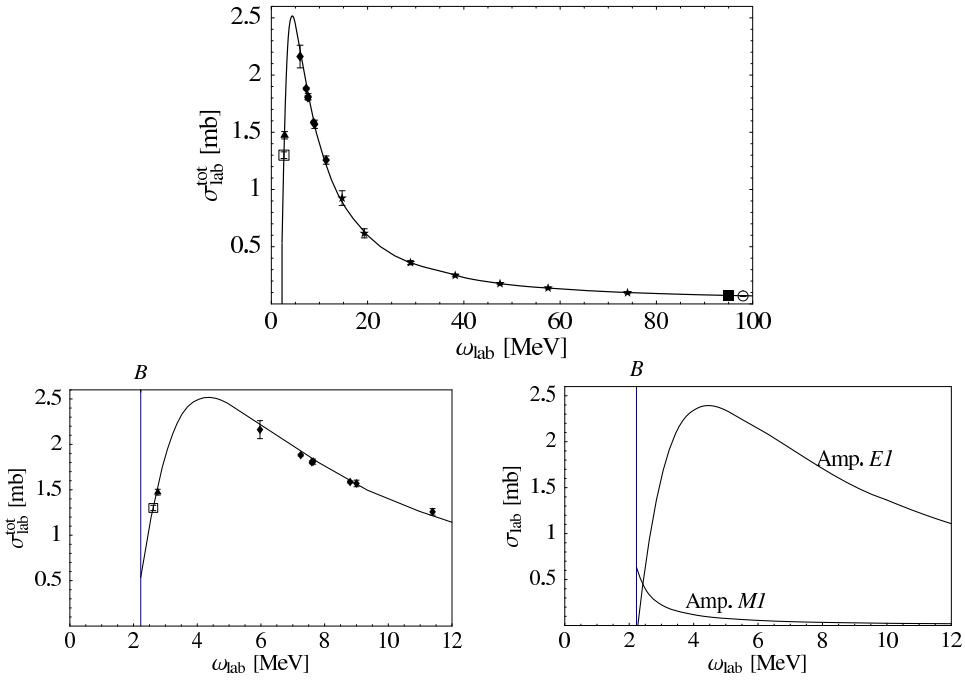

Figure 6.11: Total deuteron-photodisintegration cross section derived from our deuteron Compton amplitudes, together with data from [93] (open box), [94] (diamond), [95] (star), [96] (box), [97] (circle). The triangle corresponds to the weighted average of the data measured at 2.76 MeV [98, 99, 100], as determined in [92]. 'Amp. $E1$, $M1$' denotes the contributions from the $E1$- and the singlet $M1$-transition, respectively. B is the binding energy of the deuteron.

for all higher energies. In [90], the $E1$-contribution is called 'Approximation A', whereas 'Approximation B' is the singlet $M1$ amplitude added to this first approximation. We simplify the notation and call the $E1$-transition 'Amp. $E1$', the singlet $M1$-amplitude 'Amp. $M1$'. These two (most important) contributions to the total photodisintegration cross section are plotted in the lower right panel of Fig. 6.11, demonstrating the well-known rise of 'Amp. $M1$', as ω approaches the breakup threshold, cf. e.g. [92, 101], whereas 'Amp. $E1$' is zero for $\omega = B$. Note that Amp. $E1$ not only consists of $\mathcal{M}_{fi}^{\phi\phi\,1}$ but of all amplitudes with an $E1$-interaction at the vertex of the incoming photon. Another example for such an amplitude is $\mathcal{M}_{fi}^{\phi\sigma 2\,b}$ (Appendix H).

Strictly speaking there are also contributions from the one-body current $\vec{J}^{(p)}(\vec{\xi})$, Eq. (6.60). The corresponding amplitudes are given in [24] but are not written down in this work, as we found that their contributions to the elastic deuteron Compton cross sections are tiny (of the order of 1%) and so is their effect on the total disintegration cross section. Nevertheless, in the high-energy regime of our calculation, say for $\omega \sim 100$ MeV, they do give visible contributions to Amp. $E1$, but these cancel nearly exactly against other terms which also contain $\vec{J}^{(p)}$. Therefore, when we only look at the sum of all amplitudes contributing to $\sigma^{\rm tot}$, we may well neglect the current $\vec{J}^{(p)}$, cf. Table 6.2. However, in this table we compare our results for Amp. $E1$, Amp. $M1$ with those of [90, 24], where $\vec{J}^{(p)}$ was included. Therefore we give two numbers for Amp. $E1$ and $\sigma^{\rm tot}$, the one in bracket including $\vec{J}^{(p)}$, the other one not including this current. We report contributions from $\vec{J}^{(p)}$ only for reasons of cross-checking our calculation, and we find that the deviations from

[90, 24] may well be attributed to the use of different wave functions and potentials. This also holds for $\sigma^{\rm tot}$, which does, however, not include the two-body (Kroll-Ruderman) current diagrams of Appendix I, as explicit meson-exchange currents have been neglected in [90].

	[90]	[24]	this work
	20 MeV		
Amp. $E1$ $[\mu b]$	579.1	583.3	580.0 (583.5)
Amp. $M1$ $[\mu b]$	10.1	9.9	9.4
$\sigma^{\rm tot}$ $[\mu b]$	588.2	591.2	594.4 (594.7)
	80 MeV		
Amp. $E1$ $[\mu b]$	77.2	80.5	75.8 (79.1)
Amp. $M1$ $[\mu b]$	6.4	5.3	5.9
$\sigma^{\rm tot}$ $[\mu b]$	87.4	86.4	87.4 (88.2)
	140 MeV		
Amp. $E1$ $[\mu b]$	34.0	34.6	33.2 (36.1)
Amp. $M1$ $[\mu b]$	5.7	4.0	4.7
$\sigma^{\rm tot}$ $[\mu b]$	44.5	39.5	44.5 (44.9)

Table 6.2: Comparison of our results for the two dominant amplitudes contributing to the total deuteron-photodisintegration cross section with former works at three different energies. The total cross section is also compared, however excluding diagrams with exlicit pion exchange. Amp. $E1$ denotes the contribution due to an $E1$-, Amp. $M1$ due to a singlet $M1$-transition. The numbers in brackets include contributions from $\vec{J}^{(p)}(\vec{\xi})$.

We also compare our results with predictions for the strengths of electric and magnetic transitions close to threshold from the *Effective Range Expansion* [102, 103], given by

$$\sigma_{\rm ER}^{\rm el} = \frac{2}{3}\,\frac{e^2}{\gamma^2}\,\frac{(\frac{\omega}{B}-1)^{3/2}}{(\frac{\omega}{B})^3\,(1-\gamma\,r_t)}, \tag{6.90}$$

$$\sigma_{\rm ER}^{\rm mag} = \frac{1}{6}\,\frac{e^2}{m_N^2}\,(\mu_p-\mu_n)^2\,\frac{k\,\gamma}{k^2+\gamma^2}\,\frac{(1-\gamma\,a_s+\frac{1}{4}\,a_s\,(r_s+r_t)\,\gamma^2-\frac{1}{4}\,a_s\,(r_s-r_t)\,k^2)^2}{(1+k^2\,a_s^2)\,(1-\gamma\,r_t)} \tag{6.91}$$

with $\gamma = \sqrt{m_N\,B}$. The final-state relative momentum is $k = |\vec{p}_p - \vec{p}_n|/2 = \sqrt{m_N\,(\omega - B)}$, and for the singlet scattering length a_s and the singlet (triplet) effective range r_s (r_t) we use $a_s = -23.749$ fm, $r_s = 2.81$ fm, $r_t = 1.76$ fm given in [73]. The explicit form of Eqs. (6.90, 6.91) is adopted from [92].

In order to determine which amplitudes correspond to electric and magnetic transitions, we recall that the gradient part of the photon field, cf. Eq. (F.28), as well as $\vec{A}^{(2)}$, given in Eq. (6.58), are of electric nature. $\vec{A}^{(1)}$ (Eq. (6.57)) constitutes the magnetic part of $\vec{A}$. Therefore, except for two-body-current contributions, $\sigma^{\rm el}$ is made up by the amplitudes $\mathcal{M}_{fi}^{\phi\phi\,1}$, $\mathcal{M}_{fi}^{\phi\,\sigma1,2\,b}$, $\mathcal{M}_{fi}^{\phi\,\sigma2\,a}$ and $\mathcal{M}_{fi}^{\sigma2\,\sigma2\,a}$, cf. Appendices G and H, whereas $\sigma^{\rm mag}$ consists of the amplitudes $\mathcal{M}_{fi}^{\phi\,\sigma1\,a}$ and $\mathcal{M}_{fi}^{\sigma1\,\sigma1\,a}$, given in Appendix H.

The only non-negligible contributions to the total disintegration cross section at low energies including the Kroll-Ruderman current are the amplitudes $\mathcal{M}_{fi}^{{\rm KR}\,\sigma1\,a,b}$, cf. Appendix I. $\mathcal{M}_{fi}^{{\rm KR}\,\sigma1\,b}$ contributes to $\sigma^{\rm mag}$, but as we use the full photon field for $H^{\rm int\,KR}$, a unique assignment of $\mathcal{M}_{fi}^{{\rm KR}\,\sigma1\,a}$ is not possible. However, as the amplitudes $\mathcal{M}_{fi}^{{\rm KR}\,\sigma1}$ have a singlet intermediate state, the magnetic part of the

photon field dominates because flipping the spin is a typical magnetic effect, and therefore we assign both relevant KR amplitudes to $\sigma^{\rm mag}$.

In Fig. 6.12 we compare our results with Eqs. (6.90, 6.91), finding excellent agreement between both approaches. We also demonstrate – in the right panel – the non-negligible size of the KR diagrams.

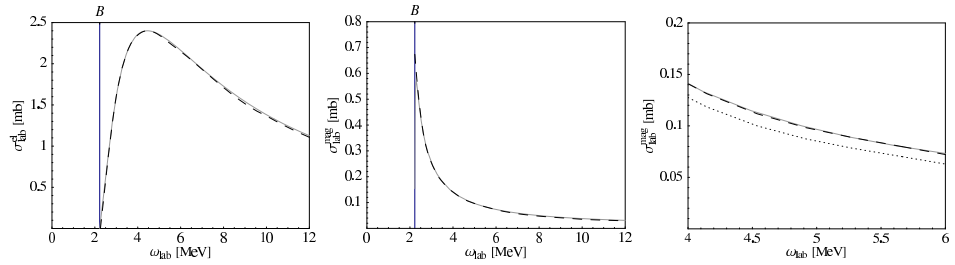

Figure 6.12: Comparison of our results (dashed) for the contributions of electric (left panel) and magnetic (middle and right panel) transitions to the total deuteron-photodisintegration cross section with predictions from the *Effective Range Expansion* (grey). The dotted curve in the right panel does not include the Kroll-Ruderman diagrams.

The cross-check described in this section, together with the exact reproduction of the low-energy theorem, cf. Section 6.2, gives a strong hint that the numerically most important amplitudes have been calculated correctly. Therefore, and due to the good agreement of our calculation with the elastic deuteron Compton data, which we observed in Section 6.3, we now fit the isoscalar nucleon polarizabilities to all existing elastic γd data in the next section.

6.5 Fits of the Isoscalar Polarizabilities

Our results for the elastic deuteron Compton cross sections obtained with the non-perturbative approach give a good description of all existing data, cf. Section 6.3. Therefore, as in Section 5.3, we use our deuteron Compton cross sections to fit the static isoscalar nucleon polarizabilities $\bar{\alpha}^s_{E1}$ and $\bar{\beta}^s_{M1}$ to these data. This time, however, we may use *all* data for the fits, whereas in Section 5.3 we had to restrict ourselves to the experiments performed around 68 and 94.2 MeV.

The fitting procedure used here is the same as in Section 5.3, i.e. we do a least-χ^2 fit, cf. Eq. (3.19), using the chiral NNLO wave function [77]. Our results for the isoscalar polarizabilities from the global fit to all data read

$$\begin{aligned}\bar{\alpha}^s_{E1}\Big|_{\rm global} &= (11.5 \pm 1.4\,({\rm stat})) \cdot 10^{-4}\ {\rm fm}^3,\\ \bar{\beta}^s_{M1}\Big|_{\rm global} &= (3.4 \pm 1.6\,({\rm stat})) \cdot 10^{-4}\ {\rm fm}^3.\end{aligned} \tag{6.92}$$

We only give the statistical error as we neglect further uncertainties, e.g. the error induced by the dependence on the deuteron wave function. This error may well be set to zero, due to the tiny wave-function dependence observed in Fig. 6.9, whereas the wave function introduces a sizeable uncertainty in Chapter 5, see Fig. 5.12 and Tables 5.1 and 5.3. Theoretical errors from higher orders are also neglected, albeit we are aware that they may be comparable in size with our statistical error: in Eq. (3.22), they were estimated to be $|\bar{\alpha}_{\rm NLO}| \sim |\bar{\beta}_{\rm NLO}| \sim 1 \cdot 10^{-4}$ fm^3 from naïve dimensional analysis. The corresponding χ^2 per degree of freedom is dramatically

reduced with respect to Table 5.1:

$$\left.\frac{\chi^2}{d.o.f.}\right|_{\text{global}} = 0.98 \tag{6.93}$$

with 27 degrees of freedom (4 data points from [17] at 49 MeV, 9 from [18] at 55 MeV, 2 from [17] and 9 from [18] around 68 MeV and 5 from [19] around 94.2 MeV, along with two fit parameters). In Fig. 6.13 we give a contour plot of the achieved χ^2, together with the ellipse corresponding to the 70% confidence level.

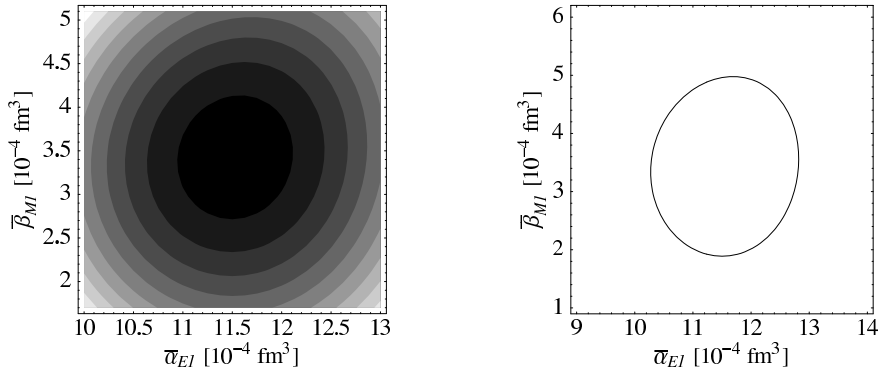

Figure 6.13: Contour plot of the χ^2 achieved in our global 2-parameter fit for $\bar{\alpha}^s_{E1}$ and $\bar{\beta}^s_{M1}$ (left panel) and the 70% confidence ellipse (right panel).

The corresponding plots, together with the (statistical) error bands, are given in Fig. 6.14. Our predictions, using our results for $\bar{\alpha}^p_{E1}$ and $\bar{\beta}^p_{M1}$ for the proton *and* the neutron polarizabilities, describe the data already well, see Fig. 6.6. It is therefore no surprise that also the fitted curves are in good agreement with experiment. Like in Section 5.3 we compare our fit results to "fit IV" from Ref. [25], which is the $\mathcal{O}(q^4)$ HBχPT fit to all data with central values $\bar{\alpha}^s_{E1} = 11.5$, $\bar{\beta}^s_{M1} = 0.3$. The only sizeable deviations are again observed at 94.2 MeV in the backward direction, due to the Δ-resonance diagram, Fig. 5.6(a), which is not included in the calculation of Ref. [25], as explained in detail in Section 5.3. In the lower two panels of Fig. 6.14, we also compare to our 2-parameter fit from Section 5.3.4, which was performed within the strictly perturbative approach, using the chiral wave function [77] and the effective data set, cf. Table 5.2. Here we observe a constant offset at 68 MeV, similarly to Fig. 6.6, whereas at 94.2 MeV the two curves are quite close to each other.

The value of our global fit for $\bar{\alpha}^s_{E1}$ is slightly smaller, the one for $\bar{\beta}^s_{M1}$ slightly larger than the fit results of Eq. (5.24). Nevertheless, both extractions agree well with each other within their error bars, and there is also very good agreement of Eq. (6.92) with the values quoted in [11] and those recommended in [10]. Furthermore, we find that the numbers given in Eq. (6.92) add up nearly exactly to the isoscalar Baldin sum rule, $\bar{\alpha}^s_{E1} + \bar{\beta}^s_{M1} = (14.5 \pm 0.6) \cdot 10^{-4}$ fm^3, cf. Eq. (5.19). Therefore, in order to reduce the statistical error, we repeat our global fit, using the central sum-rule value as an additional fit constraint like in Section 5.3. The results are

$$\begin{aligned}
\left.\bar{\alpha}^s_{E1}\right|_{\text{global Baldin}} &= (11.3 \pm 0.7\,(\text{stat}) \pm 0.6\,(\text{Baldin})) \cdot 10^{-4}\ \text{fm}^3, \\
\left.\bar{\beta}^s_{M1}\right|_{\text{global Baldin}} &= (3.2 \mp 0.7\,(\text{stat}) \pm 0.6\,(\text{Baldin})) \cdot 10^{-4}\ \text{fm}^3
\end{aligned} \tag{6.94}$$

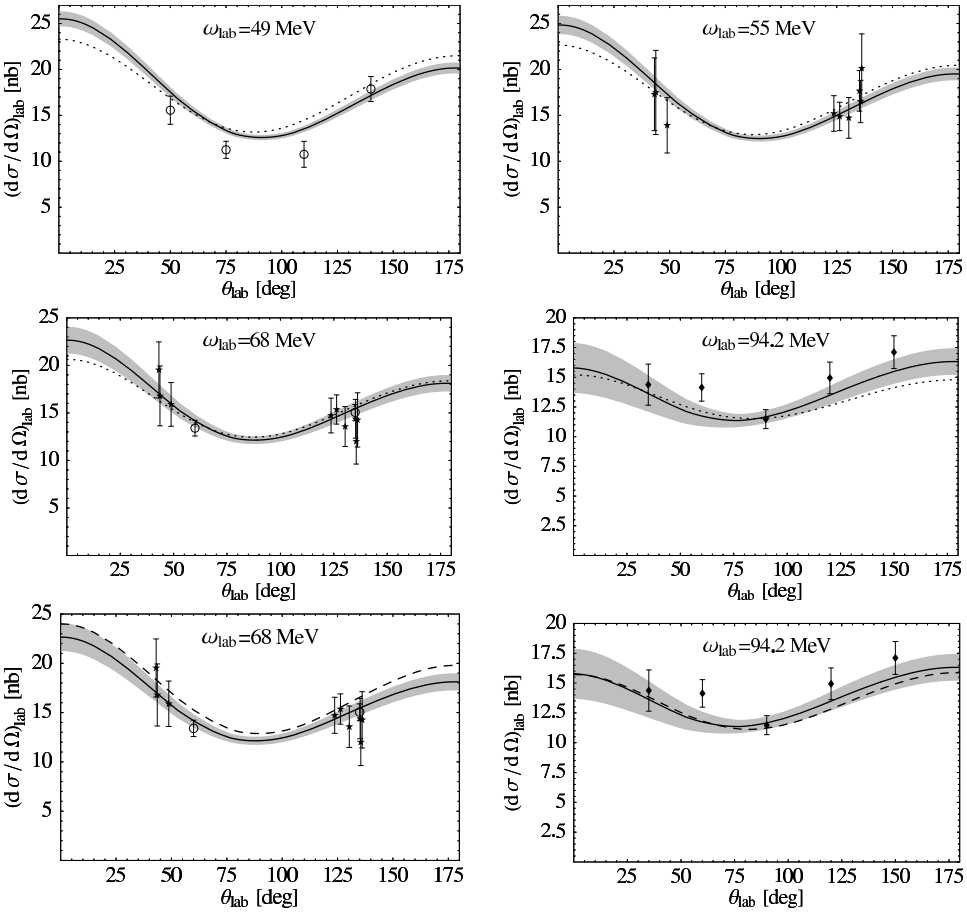

Figure 6.14: Results from a global fit of $\bar{\alpha}^s_{E1}$ and $\bar{\beta}^s_{M1}$ to all existing elastic γd data (solid). The grey bands are derived from our statistical errors. The dotted line represents "fit IV", one of the $\mathcal{O}(q^4)$-HBχPT fits from Ref. [25], with central values $\bar{\alpha}^s_{E1} = 11.5$, $\bar{\beta}^s_{M1} = 0.3$. For the $\mathcal{O}(q^4)$ calculation the NLO chiral wave function of Ref. [81] has been used, whereas our results were derived with the NNLO-version of this wave function [77]. In the lower two panels we compare to our 2-parameter-fit results from Section 5.3, using the chiral wave function [77] (dashed).

with $\chi^2/d.o.f. = 0.95$. Of course the central values of Eq. (6.94) are very similar to the ones of Eq. (6.92), due to the nearly perfect agreement of the 2-parameter-fit result with the sum-rule value. However, the statistical error is reduced by about 50%.

The plots arising from the global, Baldin-constrained fit, together with the corresponding error bars are shown in Fig. 6.15. The central curves are nearly indistinguishable from the ones of Fig. 6.14.

Combining Eqs. (6.92) or (6.94), respectively, with the (Baldin-constrained) 2-parameter-fit results of Table 3.1, we calculate the values for the neutron polarizabilities as

$$\begin{aligned}
\bar{\alpha}^n_{E1}\Big|_{\text{global}} &= (12.0 \pm 2.0\,(\text{stat}) \pm 0.4\,(\text{Baldin})) \cdot 10^{-4}\ \text{fm}^3, \\
\bar{\beta}^n_{M1}\Big|_{\text{global}} &= (4.0 \pm 2.1\,(\text{stat}) \pm 0.4\,(\text{Baldin})) \cdot 10^{-4}\ \text{fm}^3
\end{aligned} \tag{6.95}$$

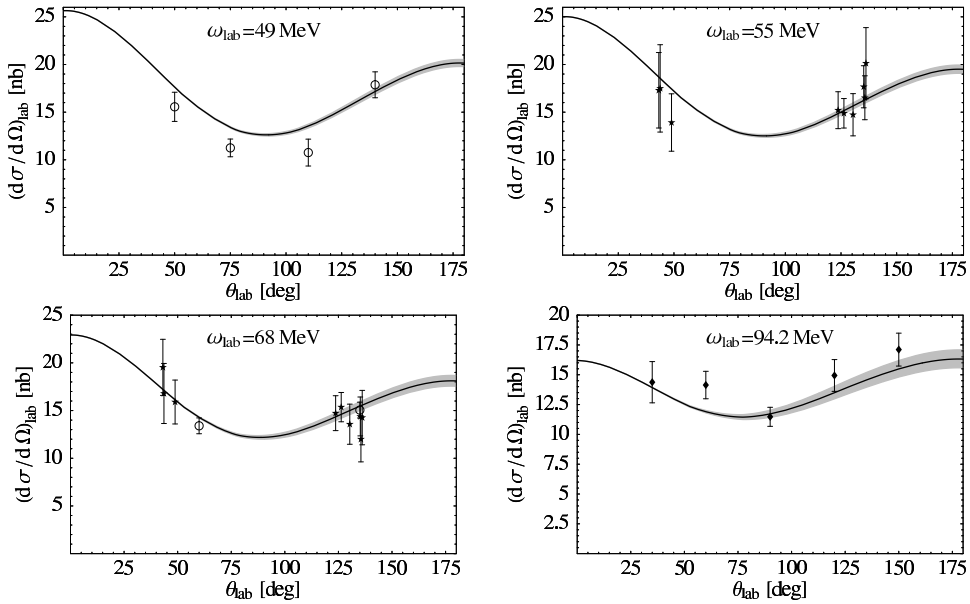

Figure 6.15: Results from a global fit of $\bar{\alpha}^s_{E1}$ to all existing elastic γd data, using the chiral wave function [77]. $\bar{\beta}^s_{M1}$ is fixed via the Baldin sum rule $\bar{\alpha}^s_{E1} + \bar{\beta}^s_{M1} = 14.5 \cdot 10^{-4}$ fm^3. The grey bands are derived from our statistical errors.

for the 2-parameter fit and

$$\begin{aligned} \bar{\alpha}^n_{E1}\Big|_{\text{global Baldin}} &= (11.6 \pm 1.5\,(\text{stat}) \pm 0.6\,(\text{Baldin})) \cdot 10^{-4}\ \text{fm}^3, \\ \bar{\beta}^n_{M1}\Big|_{\text{global Baldin}} &= (3.6 \mp 1.5\,(\text{stat}) \pm 0.6\,(\text{Baldin})) \cdot 10^{-4}\ \text{fm}^3 \end{aligned} \tag{6.96}$$

for the fit of the isoscalar polarizabilities including the Baldin constraint. We regard these values to be the most reliable ones of this work, as the isoscalar polarizabilities, from which they are derived, have been determined by fitting our deuteron Compton calculation, which fulfills the low-energy theorem, to all existing elastic deuteron Compton-scattering data. That means there is no restriction on either the energy, as in Section 5.3, or on the angle, like in [25]. From these values we deduce that the neutron is paramagnetic and that the isovector polarizabilities are considerably smaller than the isoscalar ones. In other words, our analysis shows that within the precision of the published data, elastic Compton scattering from the proton and the deuteron is in agreement with

$$\begin{aligned} \bar{\alpha}^p_{E1} &\approx \bar{\alpha}^n_{E1}, \\ \bar{\beta}^p_{M1} &\approx \bar{\beta}^n_{M1}. \end{aligned} \tag{6.97}$$

These findings agree with those of Section 5.3 and of Refs. [10, 11].

Chapter 7

Conclusion

In this work, Compton scattering from the single nucleon and the deuteron has been studied theoretically. The framework that we choose for our investigations is a Chiral Effective Field Theory based on Heavy Baryon Chiral Perturbation Theory, extended for the $\Delta(1232)$ resonance as an explicit degree of freedom. We also treat important non-perturbative aspects of the NN-system in Chapter 6 on the deuteron.

One of the central aims of our studies is to extract both the proton and the neutron polarizabilities from experiments. For the proton polarizabilities one can rely on the wealth of elastic proton Compton-scattering data, see e.g. [5, 6, 7, 8]. A single-neutron target does not exist, however. Therefore, in order to extract the neutron polarizabilities one depends on other methods, such as quasi-free Compton scattering from the neutron bound in the deuteron, or elastic deuteron Compton scattering. In this work we have chosen the latter process for our extraction of the neutron polarizabilities. Strictly speaking, from such experiment one cannot directly determine the neutron polarizabilities, because the deuteron, i.e. the bound state of a proton and a neutron, is an isoscalar target. Therefore we use the experiments performed at Illinois, Lund and Saskatoon [17, 18, 19] to extract the isoscalar polarizabilities, i.e. the average over proton and neutron. These numbers may then be combined with the proton values in order to derive $\bar{\alpha}^n_{E1}$ and $\bar{\beta}^n_{M1}$.

Our study of elastic proton Compton scattering is based on a multipole analysis of this process: a systematic expansion of the proton Compton cross sections in the multipole order (dipole, quadrupole, ...) by projecting the Compton amplitude on the various multipoles. We are not only interested in cross sections, but also in the multipole amplitudes themselves which we combine to so-called *dynamical polarizabilities*, first introduced in Ref. [46]. These quantities turn out to be a useful tool for studying the internal nucleonic degrees of freedom in their response to the external electromagnetic field. We find in Chapter 3 that in the energy range where we expect our calculation to be valid, contributions to the spin-averaged Compton cross sections from $l \geq 2$ are negligible. This observation also holds in spin-polarized quantities, as demonstrated by our calculation of several asymmetries in Chapter 4.

Our results for the dynamical polarizabilities are compared to a Dispersion-Relation Analysis [26]. Both frameworks agree well with each other in most multipole channels – albeit the upper energy limit of our calculation is lower than that of the Dispersion-Relation approach, because up to third order in SSE, which is the order chosen in this work, the $\Delta(1232)$ is treated as a stable particle. Therefore, our calculation is certainly invalid above 170-200 MeV, where the finite width of the Δ resonance cannot be neglected anymore. Predictions from Dispersion Theory are at least reliable up to the two-pion threshold.

Not all of our results for the dynamical polarizabilities are predictions. In the

original formulation of the Small Scale Expansion there is no free parameter up to third order. Nevertheless, in our procedure of fitting the static dipole polarizabilities $\bar{\alpha}_{E1}$ and $\bar{\beta}_{M1}$ to proton Compton data, we include two energy-independent short-distance operators into our calculation, which provide the desired two free parameters. The energy dependence of the (dynamical) polarizabilities is therefore still predicted.

Our fit results for $\bar{\alpha}^p_{E1}$ and $\bar{\beta}^p_{M1}$ are in good agreement with the Baldin sum rule for the proton. Therefore we use this sum-rule value in order to further reduce the number of free parameters. The proton polarizabilities thus achieved,

$$\begin{aligned}\bar{\alpha}^p_{E1} &= (11.04 \pm 1.36\,(\text{stat}) \pm 0.4\,(\text{Baldin})) \cdot 10^{-4}\ \text{fm}^3,\\ \bar{\beta}^p_{M1} &= (2.76 \mp 1.36\,(\text{stat}) \pm 0.4\,(\text{Baldin})) \cdot 10^{-4}\ \text{fm}^3,\end{aligned} \tag{7.1}$$

agree well with the analysis from [5] within statistical error bars. Systematic uncertainties from higher orders are not included in Eq. (7.1). They have been estimated in Section 3.4.2 as $|\bar{\alpha}_{\text{NLO}}| \sim |\bar{\beta}_{\text{NLO}}| \sim 1 \cdot 10^{-4}$ fm^3 from naïve dimensional analysis and are suppressed also in the following equations.

From the good agreement between our results for the Compton multipoles and the Dispersion-Relation Analysis, and from the fact that our fits describe the low-energy proton Compton data well over the whole range of scattering angles, we conclude that all relevant nucleonic degrees of freedom are included in our calculation. Comparison with third-order HBχPT demonstrates that it is advantageous and in fact necessary to include the explicit $\Delta(1232)$ resonance in a leading-one-loop-order calculation. Otherwise one misses the data in the backward direction and fails to reproduce the shape of the resonant multipole channels, such as $\beta_{M1}(\omega)$.

In Chapter 3 we demonstrate that an $l = 1$-approximation of the multipole expansion suffices to describe spin-averaged Compton cross sections. In Chapter 4 the same feature is confirmed for spin-polarized observables, namely for various asymmetries using circularly and linearly polarized photons. This observation suggests that it is possible to directly determine the six dipole polarizabilities from experiment – apart from the two spin-independent ones, $\alpha_{E1}(\omega)$ and $\beta_{M1}(\omega)$, there are four spin polarizabilities at dipole order. This suggestion is further confirmed as we observe a non-negligible influence of the spin polarizabilities on the spin-averaged Compton cross sections. We show that this dependence suffices to determine – at least qualitatively – two of the four spin polarizabilities, but it is obvious that spin-averaged experiments alone are not enough to extract all six dipole polarizabilities. Therefore we investigate which configurations are especially well suited in order to access the spin polarizabilities experimentally. We also propose a model-independent way to extract the dynamical spin polarizabilities from a combination of spin-averaged and polarized experimental data.

We investigate not only proton observables but also the corresponding quantities for the neutron. Direct Compton experiments on the neutron are however not possible. Therefore, in the second main part of this work we focus on the theoretical description of elastic Compton scattering from the deuteron, which we use to extract the isoscalar analogues to Eq. (7.1) from experiments.

Our deuteron Compton calculation is performed in two steps. First, we calculate the γd interaction kernel strictly following the power-counting rules of the Small Scale Expansion. This first attempt provides a good description of the experimental data above 60 MeV, but it breaks down for lower energies. The two main reasons for this breakdown are the applied power-counting scheme and the approximation of the nucleon propagator used in this scheme. Both are only valid in the energy regime $\omega \gg 20$ MeV. Nevertheless, encouraged by the good agreement at higher energies, we fit the isoscalar polarizabilities $\bar{\alpha}^s_{E1}$ and $\bar{\beta}^s_{M1}$ to the data from [17, 18, 19], which have been measured around 68 MeV and 94.2 MeV, yielding results in good

agreement with the quasi-elastic experiment from Ref. [11] and with the numbers recommended in Ref. [10], which both suggest rather small isovector polarizabilities. Motivated by the statistical imbalance between experimental data around 94.2 MeV and 68 MeV, we reduce in a second fit the nine data points given in [18] at ∼68 MeV to only two points by rebinning, in order to obtain an equal weighting between the two energy sets. The results from this fit, which we consider as the more reliable of the two, confirm our findings of small values for $\bar{\beta}^s_{M1}$, also implying small isovector components. As we observe a relatively strong dependence of this first approach on the deuteron wave function, we fit twice, using the two extreme wave functions, which are the chiral NNLO wave function [77] and the Nijm93 wave function [71]. Averaging over the results of our two 2-parameter SSE fits to the reduced set of data results in the isoscalar polarizabilities

$$\begin{aligned}\bar{\alpha}^s_{E1} &= (12.8 \pm 1.4\,(\text{stat}) \pm 1.1\,(\text{wf})) \cdot 10^{-4}\ \text{fm}^3\,,\\ \bar{\beta}^s_{M1} &= (2.1 \pm 1.7\,(\text{stat}) \pm 0.1\,(\text{wf})) \cdot 10^{-4}\ \text{fm}^3\,.\end{aligned} \tag{7.2}$$

The systematic error due to the wave-function dependence (wf) is estimated to be half of the difference between the results obtained with the extreme wave functions. As the numbers presented in Eq. (7.2) are in very good agreement with the isoscalar Baldin sum rule, we also use the central sum-rule value as an additional fit constraint, obtaining

$$\begin{aligned}\bar{\alpha}^s_{E1} &= (12.6 \pm 0.8\,(\text{stat}) \pm 0.7\,(\text{wf}) \pm 0.6\,(\text{Baldin})) \cdot 10^{-4}\ \text{fm}^3\,,\\ \bar{\beta}^s_{M1} &= (1.9 \mp 0.8\,(\text{stat}) \mp 0.7\,(\text{wf}) \pm 0.6\,(\text{Baldin})) \cdot 10^{-4}\ \text{fm}^3\,.\end{aligned} \tag{7.3}$$

Combining the numbers of Eq. (7.2) with our results for the proton polarizabilities, given in Eq. (7.1), we obtain a consistent Effective Field Theory determination of the neutron polarizabilities with a precision comparable to [11]:

$$\begin{aligned}\bar{\alpha}^n_{E1} &= (14.6 \pm 2.0\,(\text{stat}) \pm 1.1\,(\text{wf}) \pm 0.4\,(\text{Baldin})) \cdot 10^{-4}\ \text{fm}^3\\ \bar{\beta}^n_{M1} &= (1.4 \pm 2.2\,(\text{stat}) \pm 0.1\,(\text{wf}) \pm 0.4\,(\text{Baldin})) \cdot 10^{-4}\ \text{fm}^3\end{aligned} \tag{7.4}$$

The isoscalar input of Eq. (7.4) does not include the Baldin-sum-rule constraint, whereas the one-parameter fit using the Baldin sum rule gives

$$\begin{aligned}\bar{\alpha}^n_{E1} &= (14.2 \pm 1.6\,(\text{stat}) \pm 0.7\,(\text{wf}) \pm 0.6\,(\text{Baldin})) \cdot 10^{-4}\ \text{fm}^3\,,\\ \bar{\beta}^n_{M1} &= (1.0 \mp 1.6\,(\text{stat}) \mp 0.7\,(\text{wf}) \pm 0.6\,(\text{Baldin})) \cdot 10^{-4}\ \text{fm}^3\,.\end{aligned} \tag{7.5}$$

Eqs. (7.4) and (7.5) prove that small isovector nucleon polarizabilities are not in contradiction with elastic deuteron Compton-scattering data. This finding is in good agreement with [11], where quasi-elastic Compton scattering off the proton and neutron was measured.

Furthermore we use the $\mathcal{O}(p^3)$-HBχPT amplitudes for analogous fits, finding similar values for $\bar{\alpha}_E$ but larger ones for $\bar{\beta}_M$, which is not surprising, as the dynamics of the resonant Compton multipoles is not well captured in third-order HBχPT. Therefore, the static value becomes large, since it must correct for the missing Δ resonance, leading $\mathcal{O}(p^3)$ HBχPT to a disagreement with the single-nucleon Compton multipoles as observed in Chapter 3. Obviously, γd scattering alone is not sufficient to investigate the relevant low-energy degrees of freedom in nuclear Compton scattering, but one has to combine information from γd and γp scattering and analyze both in the same framework.

The results for the isoscalar polarizabilities, extracted in our first chapter on deuteron Compton scattering, along with the good description of the high-energy data is certainly a first success. However, as already explained, there are severe

shortcomings of this way of calculating γd scattering: the unexpectedly strong sensitivity on the deuteron wave function and, even more importantly, the fact that the calculation completely fails in the low-energy regime, which is a clear indication that gauge invariance is violated [79]. We report on several attempts to restore gauge invariance and the Thomson limit by inclusion of additional diagrams and the full non-relativistic nucleon propagator. Although we are able to improve on the static limit – we reduce the factor of 6 that our previous "power-counting" calculation is off to less than 2 – we cannot restore it exactly. Therefore, in Chapter 6 we turn to a refined approach to deuteron Compton scattering, following closely Ref. [24]. This calculation is based on second-order perturbation theory in the interaction of the photon with the two-nucleon system, with summation over all possible intermediate two-nucleon states. For the photon coupling we make use of Siegert's theorem [84], which is well-known to guarantee the exact static limit [24].

Besides the compliance with the low-energy theorem, this approach provides another valuable cross-check of our calculation: the extraction of the total deuteron-photodisintegration cross section from the Compton amplitude via the optical theorem. There is a wealth of experimental data on this process, see e.g. [93-100], and we demonstrate in Section 6.4 that our calculation agrees well with these data. Nevertheless, our primary goal is to have a consistent description of elastic deuteron Compton scattering in the whole range from 0 MeV up to $\omega \sim 100$ MeV or even up to the pion mass. In Section 6.3, we show that we have largely achieved this aim. We are able to improve the low-energy regime of our calculation, i.e. in this second approach we obtain a good description of the data published below 60 MeV. This improvement is of course connected to the correct static limit. Other calculations, reaching this limit, are also able to describe the low-energy data well, see e.g. [22, 24, 60]. However, unlike most of these calculations, we achieve good agreement also with the high-energy data, i.e. we have resolved the so-called 'SAL-puzzle'. In fact, at 94.2 MeV both calculations of ours are very close to each other. In this energy regime the work of Ref. [24] fails, the theory of [60] is inapplicable and even the authors of [22] have problems to describe the data in the backward direction, at least without introducing unrealistically large isovector polarizabilities. The main difference between their approach and ours is in the dynamics of the resonant multipoles, which is well captured in our calculation due to the inclusion of the Δ-resonance diagram.

Having achieved a good description of all elastic deuteron Compton-scattering data enables us to perform a global fit of the isoscalar polarizabilities to all existing data points, published in [17, 18, 19]. Our 2-parameter-fit results are

$$\begin{aligned} \bar{\alpha}^s_{E1}\Big|_{\text{global}} &= (11.5 \pm 1.4\,(\text{stat})) \cdot 10^{-4}\ \text{fm}^3, \\ \bar{\beta}^s_{M1}\Big|_{\text{global}} &= (3.4 \pm 1.6\,(\text{stat})) \cdot 10^{-4}\ \text{fm}^3. \end{aligned} \tag{7.6}$$

We only need to give the statistical error in this case since we have demonstrated in Section 6.3.1 that the wave-function dependence of our "non-perturbative" approach is tiny. This source of uncertainty discussed in Chapter 5 has therefore also been removed. We notice that the numbers of Eq. (7.6) are very close to our results for the proton (Eq. (7.1)), which leaves little space for large isovector polarizabilities. Furthermore they are consistent within the error bars with our previous extraction, Eq. (7.2), and agree extraordinarily well with the isoscalar Baldin-sum-rule value, cf. Eq. (5.19). Therefore, in order to reduce the statistical error, we repeat our fits

including this additional constraint, achieving

$$\begin{aligned}\bar{\alpha}^s_{E1}\Big|_{\text{global Baldin}} &= (11.3 \pm 0.7\,(\text{stat}) \pm 0.6\,(\text{Baldin})) \cdot 10^{-4}\ \text{fm}^3,\\ \bar{\beta}^s_{M1}\Big|_{\text{global Baldin}} &= (3.2 \mp 0.7\,(\text{stat}) \pm 0.6\,(\text{Baldin})) \cdot 10^{-4}\ \text{fm}^3. \end{aligned} \tag{7.7}$$

Combining Eqs. (7.6) or (7.7), respectively, with the Baldin-constrained proton results of Eq. (7.1), we find the neutron polarizabilities

$$\begin{aligned}\bar{\alpha}^n_{E1}\Big|_{\text{global}} &= (12.0 \pm 2.0\,(\text{stat}) \pm 0.4\,(\text{Baldin})) \cdot 10^{-4}\ \text{fm}^3,\\ \bar{\beta}^n_{M1}\Big|_{\text{global}} &= (4.0 \pm 2.1\,(\text{stat}) \pm 0.4\,(\text{Baldin})) \cdot 10^{-4}\ \text{fm}^3 \end{aligned} \tag{7.8}$$

for the 2-parameter fit and

$$\begin{aligned}\bar{\alpha}^n_{E1}\Big|_{\text{global Baldin}} &= (11.6 \pm 1.5\,(\text{stat}) \pm 0.6\,(\text{Baldin})) \cdot 10^{-4}\ \text{fm}^3,\\ \bar{\beta}^n_{M1}\Big|_{\text{global Baldin}} &= (3.6 \mp 1.5\,(\text{stat}) \pm 0.6\,(\text{Baldin})) \cdot 10^{-4}\ \text{fm}^3 \end{aligned} \tag{7.9}$$

for the fit including the Baldin constraint also in the extraction of the isoscalar polarizabilities. We consider the values given in Eqs. (7.1) and (7.9) to be most reliable because of the fact that our second approach to deuteron Compton scattering fulfills the low-energy theorem and enables us to include all experimental data into our fit of the isoscalar polarizabilities. From these results we deduce that the magnetic response of the neutron is comparable to that of the proton and that both nucleons are paramagnetic. We also conclude that the proton and neutron polarizabilities are identical within the precision of our analysis. In both points our two deuteron Compton calculations agree with each other.

Nevertheless, we strongly advocate enlarging the deuteron Compton data base. If further experiments, as planned at TUNL/HIγS or at MAXlab, provide additional data below the pion mass, an improved global fit with increased statistics would be possible, which would reduce the statistical error in our determination of the neutron polarizabilities.

Appendix A

Numerical Values of Physical Constants

In Table A.1 we list the numerical values that we use for all parameters, except for those which are determined within this work: b_1, g_1, g_2, cf. Section 3.4.1. The numbers are from [73, 74, 104].

Parameter	Value	Comment
m_π	139.6 MeV	charged pion mass
m_{π^0}	135.0 MeV	neutral pion mass
m_N	938.9 MeV	isoscalar nucleon mass
m_C	1877.8 MeV	twice the isoscalar nucleon mass
f^2	0.075	pion-nucleon coupling constant
g_A	1.267	axial coupling constant
f_π	92.4 MeV	pion-decay constant
α	1/137	QED fine-structure constant
μ_p	2.795	magnetic moment of the proton
μ_n	-1.913	magnetic moment of the neutron
Δ_0	271.1 MeV	$N\Delta$ mass splitting
$g_{\pi N\Delta}$	1.125	$\pi N\Delta$ coupling constant
m_d	1875.58 MeV	deuteron mass
B	2.2246 MeV	deuteron binding energy

Table A.1: χEFT parameters determined independently of this work. Magnetic moments are given in nuclear magnetons.

The pion-nucleon coupling constant f^2 is at leading order connected to g_A, m_π and f_π via the Goldberger-Treiman relation [105]:

$$f^2 \approx \left(\frac{g_A\, m_\pi}{2\, f_\pi}\right)^2 \cdot \frac{1}{4\pi} = 0.073. \tag{A.1}$$

Appendix B

Pole Contributions to Nucleon Compton Scattering

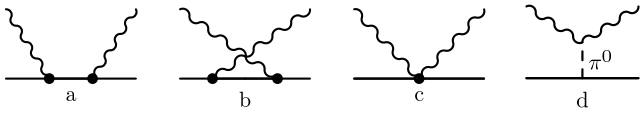

Figure B.1: Pole contributions to nucleon Compton scattering in the s-channel (a), u-channel (b) and t-channel (d). The proton seagull (c) occurs in the non-relativistic reduction of diagrams (a), (b).

In this appendix we explicitly write down the non-structure or pole amplitudes of nucleon Compton scattering in the cm frame up to third order in the Small Scale Expansion[1], corresponding to Fig. B.1. These are (with the charge $Q = 1$ (0) for a proton (neutron) target)

$$
\begin{aligned}
A_1^{\rm pole}(\omega,\theta) &= -\frac{Q\,e^2}{m_N} + \mathcal{O}(\epsilon^4),\\
A_2^{\rm pole}(\omega,\theta) &= \frac{Q^2\,e^2\,\omega}{m_N^2} + \mathcal{O}(\epsilon^4),\\
A_3^{\rm pole}(\omega,\theta) &= \frac{e^2\,\omega\,\left(Q\,(1+2\kappa) - (Q+\kappa)^2\,\cos\theta\right)}{2\,m_N^2}\\
&\quad - (2\,Q-1)\,\frac{e^2\,g_A}{4\,\pi^2\,f_\pi^2}\,\frac{\omega^3\,(1-\cos\theta)}{m_{\pi^0}^2 + 2\,\omega^2\,(1-\cos\theta)} + \mathcal{O}(\epsilon^4),\\
A_4^{\rm pole}(\omega,\theta) &= -\frac{e^2\,\omega\,(Q+\kappa)^2}{2\,m_N^2} + \mathcal{O}(\epsilon^4),\\
A_5^{\rm pole}(\omega,\theta) &= \frac{e^2\,\omega\,(Q+\kappa)^2}{2\,m_N^2} - (2\,Q-1)\,\frac{e^2\,g_A}{8\,\pi^2\,f_\pi^2}\,\frac{\omega^3}{m_{\pi^0}^2 + 2\,\omega^2\,(1-\cos\theta)} + \mathcal{O}(\epsilon^4),\\
A_6^{\rm pole}(\omega,\theta) &= -\frac{e^2\,\omega\,Q\,(Q+\kappa)}{2\,m_N^2} + (2\,Q-1)\,\frac{e^2\,g_A}{8\,\pi^2\,f_\pi^2}\,\frac{\omega^3}{m_{\pi^0}^2 + 2\,\omega^2\,(1-\cos\theta)} + \mathcal{O}(\epsilon^4).
\end{aligned}
\tag{B.1}
$$

[1]We note that these amplitudes are identical in third-order HBχPT and SSE.

For the numerical values of the various parameters and their meaning, cf. Appendix A ($\kappa = \mu - Q$). The proton seagull, Fig. B.1(c), contributes to $A_1^{\rm pole}$ and $A_3^{\rm pole}$. The contribution to $A_1^{\rm pole}$ stems from the two-photon vertex from $\mathcal{L}_{N\pi}^{(2)}$. The seagull term in $A_3^{\rm pole}$, which is the one proportional to $Q\,(1+2\kappa)$, is the leading relativistic correction from spin-orbit coupling and part of $\mathcal{L}_{N\pi}^{(3)}$. The terms depending on the axial coupling constant g_A are the contributions from the pion pole, Fig. B.1(d). All other terms correspond to the nucleon-pole diagrams, Figs. B.1(a) and (b).

Appendix C

Projection Formulae

The connection between the Compton structure amplitudes $\bar{A}_i(\omega, z),\ i = 1, \ldots, 6$, given in Appendix B of Ref. [26], and the cm Compton multipoles $f^{l\pm}_{XX'}(\omega),\ X, X' = E, M$, introduced in Section 3.1.1, has been derived in [29]. It reads:

$$
\begin{aligned}
f^{1+}_{EE}(\omega) = \int_{-1}^{1} \frac{m_N}{16 \cdot 4\pi\, W} \Big[& \bar{A}_3(\omega, z)\ \left(-3 + z^2\right) + 4\bar{A}_6(\omega, z)\ \left(-1 + z^2\right) \\
& + \left(2\bar{A}_2(\omega, z) + \bar{A}_4(\omega, z) + 2\bar{A}_5(\omega, z)\right)\ z\ \left(-1 + z^2\right) + 2\bar{A}_1(\omega, z)\ \left(1 + z^2\right) \Big] dz \\
f^{1-}_{EE}(\omega) = \int_{-1}^{1} \frac{m_N}{8 \cdot 4\pi\, W} \Big[& - \bar{A}_3(\omega, z)\ \left(-3 + z^2\right) - 4\bar{A}_6(\omega, z)\ \left(-1 + z^2\right) \\
& - \left(-\bar{A}_2(\omega, z) + \bar{A}_4(\omega, z) + 2\bar{A}_5(\omega, z)\right)\ z\ \left(-1 + z^2\right) + \bar{A}_1(\omega, z)\ \left(1 + z^2\right) \Big] dz \\
f^{1+}_{MM}(\omega) = \int_{-1}^{1} \frac{m_N}{16 \cdot 4\pi\, W} \Big[& 2\bar{A}_2(\omega, z)\ \left(-1 + z^2\right) \\
& + \bar{A}_4(\omega, z)\ \left(-1 + z^2\right) + 2\left(\bar{A}_5(\omega, z)\ \left(1 - z^2\right) + \bar{A}_1(\omega, z)\, 2z - \bar{A}_3(\omega, z)\, z\right) \Big] dz \\
f^{1-}_{MM}(\omega) = \int_{-1}^{1} \frac{m_N}{8 \cdot 4\pi\, W} \Big[& \bar{A}_4(\omega, z)\ \left(1 - z^2\right) \\
& + \bar{A}_2(\omega, z)\ \left(-1 + z^2\right) + 2\left(\bar{A}_5(\omega, z)\left(-1 + z^2\right) + \bar{A}_1(\omega, z)\, z + \bar{A}_3(\omega, z)\, z\right) \Big] dz \\
f^{2+}_{EE}(\omega) = \int_{-1}^{1} \frac{m_N}{72 \cdot 4\pi\, W} \Big[& \bar{A}_4(\omega, z)\ \left(-1 - 3z^2 + 4z^4\right) + \bar{A}_2(\omega, z)\ \left(3 - 9z^2 + 6z^4\right) + 2\left(\bar{A}_5(\omega, z)\right. \\
& \times \left(-1 - 3z^2 + 4z^4\right) + \bar{A}_1(\omega, z)\, 3z^3 + \bar{A}_3(\omega, z)\ \left(2z^3 - 3z\right) + \bar{A}_6(\omega, z)\ \left(6z^3 - 6z\right)\Big) \Big] dz \\
f^{2-}_{EE}(\omega) = \int_{-1}^{1} \frac{m_N}{48 \cdot 4\pi\, W} \Big[& \bar{A}_4(\omega, z)\ \left(1 + 3z^2 - 4z^4\right) + \bar{A}_2(\omega, z)\ \left(2 - 6z^2 + 4z^4\right) + 2\left(\bar{A}_5(\omega, z)\right. \\
& \times \left(1 + 3z^2 - 4z^4\right) + \bar{A}_1(\omega, z)\, 2z^3 + \bar{A}_3(\omega, z)\ \left(3z - 2z^3\right) + \bar{A}_6(\omega, z)\ \left(6z - 6z^3\right)\Big) \Big] dz
\end{aligned}
$$

$$
\begin{aligned}
f^{2+}_{MM}(\omega) &= \int_{-1}^{1} \frac{m_N}{72 \cdot 4\pi\, W} \Big[\bar{A}_3(\omega, z)\, \left(1 - 3z^2\right) \\
&\quad + \left(3\bar{A}_2(\omega, z) + 5\bar{A}_4(\omega, z) - 2\bar{A}_5(\omega, z)\right)\, z\, \left(-1 + z^2\right) + \bar{A}_1(\omega, z)\, \left(-3 + 9z^2\right) \Big] dz \\
f^{2-}_{MM}(\omega) &= \int_{-1}^{1} \frac{m_N}{48 \cdot 4\pi\, W} \Big[\bar{A}_3(\omega, z)\, \left(-1 + 3z^2\right) \\
&\quad + \left(2\bar{A}_2(\omega, z) - 5\bar{A}_4(\omega, z) + 2\bar{A}_5(\omega, z)\right)\, z\, \left(-1 + z^2\right) + \bar{A}_1(\omega, z)\, \left(-2 + 6z^2\right) \Big] dz \\
f^{1+}_{EM}(\omega) &= \int_{-1}^{1} \frac{m_N}{16 \cdot 4\pi\, W} \Big[\bar{A}_3(\omega, z)\, \left(1 - 3z^2\right) \\
&\quad - 2\bar{A}_6(\omega, z)\, \left(-1 + z^2\right) - \left(\bar{A}_4(\omega, z) + 4\bar{A}_5(\omega, z)\right)\, z\, \left(-1 + z^2\right) \Big] dz \\
f^{1+}_{ME}(\omega) &= \int_{-1}^{1} \frac{m_N}{16 \cdot 4\pi\, W} \Big[\bar{A}_4(\omega, z)\, \left(1 - z^2\right) - 2z\, \left(\bar{A}_3(\omega, z) + \bar{A}_6(\omega, z)\, \left(1 - z^2\right)\right) \Big] dz
\end{aligned}
\tag{C.1}
$$

Appendix D

The Deuteron Wave Function

For the deuteron Compton calculation of Chapters 5 and 6 we need an explicit expression for the deuteron wave function (total angular momentum $j = 1$). This can in momentum space be written as, see e.g. Section 3.4 in [57],

$$\Psi_{1m}(\vec{p}) = u(p)\,\mathcal{Y}_m^{011}(\hat{p}) + w(p)\,\mathcal{Y}_m^{211}(\hat{p}), \tag{D.1}$$

where the radial wave functions $u(p),\ w(p)$ fulfill the normalization condition

$$\int_0^\infty dp\, p^2\,\left(u(p)^2 + w(p)^2\right) = 1. \tag{D.2}$$

The indices of the angular wave functions $\mathcal{Y}$ are $l11$ for orbital angular momentum, spin and total angular momentum of the deuteron state. $m \in \{-1, 0, 1\}$ denotes the projection of the total angular momentum of the deuteron onto the quantization axis. We know from experiment that the deuteron is composed of an s-wave ($l = 0$) and a d-wave state ($l = 2$), cf. Eq. (D.1) – however, the s-wave part is by far the dominant one, see Fig. D.1.

In position space the wave function is usually written as [57]

$$\Psi_{1m}(\vec{r}) = \frac{u(r)}{r}\,\mathcal{Y}_m^{011}(\hat{r}) + \frac{w(r)}{r}\,\mathcal{Y}_m^{211}(\hat{r}), \tag{D.3}$$

with the normalization

$$\int_0^\infty dr\,\left(u(r)^2 + w(r)^2\right) = 1. \tag{D.4}$$

However, as we want to write down a sum over the two orbital angular momentum states we use the notation

$$\Psi_{1m}(\vec{r}) = \sum_{l=0,2} \frac{u_l(r)}{r}\mathcal{Y}_m^{l11}(\hat{r}), \tag{D.5}$$

with $u_0(r) \equiv u(r)$ and $u_2(r) \equiv w(r)$.

The angular wave functions are built of the spherical harmonics, multiplied with the corresponding Clebsch-Gordan coefficients $C^{j_3\,m_3}_{j_1\,m_1\,j_2\,m_2}$, cf. Eq. (L.14) [57]. In order to determine these coefficients, we first write down the non-vanishing Clebsch-Gordan coefficients for combining the spins of the two nucleons to the total spin $S = 1$:

$$C^{1\,-1}_{\frac{1}{2}\,-\frac{1}{2}\,\frac{1}{2}\,-\frac{1}{2}} = 1 \qquad C^{1\,0}_{\frac{1}{2}\,-\frac{1}{2}\,\frac{1}{2}\,\frac{1}{2}} = C^{1\,0}_{\frac{1}{2}\,\frac{1}{2}\,\frac{1}{2}\,-\frac{1}{2}} = \frac{1}{\sqrt{2}} \qquad C^{1\,1}_{\frac{1}{2}\,\frac{1}{2}\,\frac{1}{2}\,\frac{1}{2}} = 1 \tag{D.6}$$

In the s-wave state ($l = 0$), we have $m_l = 0$ and therefore $m_j = m_s$. The corresponding Clebsch-Gordan coefficients are

$$C^{1\,m_j}_{0\,0\;1\,m_s} = \delta_{m_s,m_j}, \tag{D.7}$$

always assuming that the projections m only take on physical values, i.e. $m_L \in \{-L, -L+1, .., L\}$.

We also need the d-wave coefficients, which project the states $l = 2, m_l$, $s = 1, m_s$ onto $j = 1, m_j$. The relation $m_l + m_s = m_j$ guarantees that there are only nine non-vanishing Clebsch-Gordan coefficients:

$$\begin{aligned}
C^{1\,-1}_{2\,-2\;1\,1} &= \sqrt{\frac{3}{5}} & C^{1\,-1}_{2\,-1\;1\,0} &= -\sqrt{\frac{3}{10}} & C^{1\,-1}_{2\,0\;1\,-1} &= \frac{1}{\sqrt{10}} \\
C^{1\,0}_{2\,-1\;1\,1} &= \sqrt{\frac{3}{10}} & C^{1\,0}_{2\,0\;1\,0} &= -\sqrt{\frac{2}{5}} & C^{1\,0}_{2\,1\;1\,-1} &= \sqrt{\frac{3}{10}} \\
C^{1\,1}_{2\,0\;1\,1} &= \frac{1}{\sqrt{10}} & C^{1\,1}_{2\,1\;1\,0} &= -\sqrt{\frac{3}{10}} & C^{1\,1}_{2\,2\;1\,-1} &= \sqrt{\frac{3}{5}}
\end{aligned} \tag{D.8}$$

Now we construct the deuteron wave function, e.g. in position space. The notation is $\Psi_{m_s^1 m_s^2\, m_j}$ with m_s^1, $m_s^2 \in \{\uparrow, \downarrow\}$ the spin projections of nucleon 1 and 2, respectively, and m_j the projection of the total angular momentum of the deuteron. Note that we skip the spinors of the nucleons for brevity.

$$\begin{aligned}
\Psi_{\downarrow\downarrow\,-1}(\vec{r}) &= \frac{u(r)}{r}\, Y_{0\,0}(\hat{r}) + \frac{w(r)}{r}\, Y_{2\,0}(\hat{r}) \cdot C^{1\,-1}_{2\,0\;1\,-1} \\
\Psi_{\uparrow\downarrow\,-1}(\vec{r}) &= \Psi_{\downarrow\uparrow\,-1}(\vec{r}) = \frac{w(r)}{r}\, Y_{2\,-1}(\hat{r}) \cdot C^{1\,-1}_{2\,-1\;1\,0} \cdot \frac{1}{\sqrt{2}} \\
\Psi_{\uparrow\uparrow\,-1}(\vec{r}) &= \frac{w(r)}{r}\, Y_{2\,-2}(\hat{r}) \cdot C^{1\,-1}_{2\,-2\;1\,1} \\
\Psi_{\downarrow\downarrow\,0}(\vec{r}) &= \frac{w(r)}{r}\, Y_{2\,1}(\hat{r}) \cdot C^{1\,0}_{2\,1\;1\,-1} \\
\Psi_{\uparrow\downarrow\,0}(\vec{r}) &= \Psi_{\downarrow\uparrow\,0}(\vec{r}) = \left[\frac{u(r)}{r}\, Y_{0\,0}(\hat{r}) + \frac{w(r)}{r}\, Y_{2\,0}(\hat{r}) \cdot C^{1\,0}_{2\,0\;1\,0}\right] \cdot \frac{1}{\sqrt{2}} \\
\Psi_{\uparrow\uparrow\,0}(\vec{r}) &= \frac{w(r)}{r}\, Y_{2\,-1}(\hat{r}) \cdot C^{1\,0}_{2\,-1\;1\,1} \\
\Psi_{\downarrow\downarrow\,1}(\vec{r}) &= \frac{w(r)}{r}\, Y_{2\,2}(\hat{r}) \cdot C^{1\,1}_{2\,2\;1\,-1} \\
\Psi_{\uparrow\downarrow\,1}(\vec{r}) &= \Psi_{\downarrow\uparrow\,1}(\vec{r}) = \frac{w(r)}{r}\, Y_{2\,1}(\hat{r}) \cdot C^{1\,1}_{2\,1\;1\,0} \cdot \frac{1}{\sqrt{2}} \\
\Psi_{\uparrow\uparrow\,1}(\vec{r}) &= \frac{u(r)}{r}\, Y_{0\,0}(\hat{r}) + \frac{w(r)}{r}\, Y_{2\,0}(\hat{r}) \cdot C^{1\,1}_{2\,0\;1\,1}
\end{aligned} \tag{D.9}$$

Finally, in Fig. D.1 we show the radial functions $u(r)$ ($u(p)$) and $w(r)$ ($w(p)$) for two typical wave functions that we use, namely the NNLO chiral wave function with cutoff $\Lambda = 650$ MeV [77] and the AV18-wave function [73]. Significant differences are only visible in the d-state. At large distances (small momenta), both wave functions are dominated by one-pion exchange and therefore lie nearly exactly on top of each other.

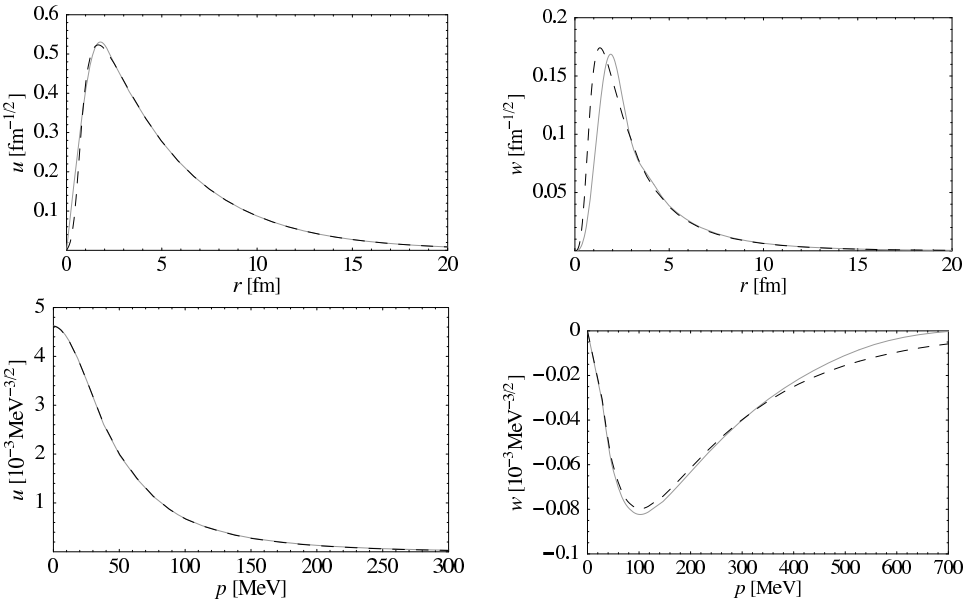

Figure D.1: The radial wave functions generated from the NNLO chiral potential with cut-off $\Lambda = 650$ MeV [77] (grey) and the AV18-potential [73] (dashed). In the upper row we compare the position-space wave functions, in the lower the representation in momentum space. The first column corresponds to the s-state wave function u, the second to w, the radial wave function of the d-state.

Appendix E

Additional Pion-Exchange Diagrams

This appendix, where we give our results for the diagrams shown in Fig. 5.19, refers exclusively to Section 5.4. These pion-exchange diagrams appear at third-order SSE in addition to those of Fig. 5.7, when we count the nucleon propagator as $\mathcal{O}(\epsilon^{-2})$, which is the correct power in the low-energy regime, cf. Section 5.4. As we are only interested in contributions to the static limit, we restrict ourselves to the photon-nucleon coupling given in Eq. (5.27). The full non-relativistic nucleon propagator is included, like in Eqs. (5.29, 5.30). The notation employed can be read off Fig. 5.19. Due to the pion exchange, all diagrams calculated in this appendix contribute to $T^{\gamma NN}(\vec{k}_i, \vec{k}_f; \vec{p}, \vec{p}\,')$, cf. Eq. (5.10).

Using the abbreviations

$$\begin{aligned}
\vec{p}_{ppp} &= \vec{p} + \vec{p}\,' + \frac{\vec{k}_i + \vec{k}_f}{2}, \\
\vec{p}_{mpp} &= \vec{p} - \vec{p}\,' + \frac{\vec{k}_i + \vec{k}_f}{2}, \\
\vec{p}_{mpm} &= \vec{p} - \vec{p}\,' + \frac{\vec{k}_i - \vec{k}_f}{2}, \\
\vec{p}_{mmp} &= \vec{p} - \vec{p}\,' - \frac{\vec{k}_i + \vec{k}_f}{2}
\end{aligned} \tag{E.1}$$

we find:

$$\begin{aligned}
T^{(2a)} &= \frac{e^2\, g_A^2}{4\, f_\pi^2\, m_N}\, \frac{\vec{\epsilon}\,' \cdot \vec{\sigma}_1\, \vec{p}_{mpm} \cdot \vec{\sigma}_2\, \vec{\epsilon} \cdot \vec{p}}{\left[- m_\pi^2 - \vec{p}_{mpm}^{\,2} \right] \left[\omega - B - \frac{\vec{p}^{\,2} + \vec{p} \cdot \vec{k}_i}{m_N} \right]} \\
T^{(2b)} &= \frac{e^2\, g_A^2}{4\, f_\pi^2\, m_N}\, \frac{\vec{\epsilon} \cdot \vec{\sigma}_1\, \vec{p}_{mpm} \cdot \vec{\sigma}_2\, \vec{\epsilon}\,' \cdot \left(\vec{p} - \frac{\vec{k}_i}{2} \right)}{\left[- m_\pi^2 - \vec{p}_{mpm}^{\,2} \right] \left[- \omega - B - \frac{2\vec{p}^{\,2} + \omega^2 + \vec{k}_i \cdot \vec{k}_f - 2\vec{p} \cdot \vec{k}_f}{2 m_N} \right]} \\
T^{(2c)} &= - \frac{e^2\, g_A^2}{4\, f_\pi^2\, m_N}\, \frac{\vec{\epsilon} \cdot \vec{\sigma}_2\, \vec{p}_{mpm} \cdot \vec{\sigma}_1\, \vec{\epsilon}\,' \cdot \vec{p}\,'}{\left[- m_\pi^2 - \vec{p}_{mpm}^{\,2} \right] \left[\omega - B - \frac{\vec{p}\,'^2 + \vec{p}\,' \cdot \vec{k}_f}{m_N} \right]} \\
T^{(2d)} &= - \frac{e^2\, g_A^2}{4\, f_\pi^2\, m_N}\, \frac{\vec{\epsilon}\,' \cdot \vec{\sigma}_1\, \vec{p}_{mpm} \cdot \vec{\sigma}_2\, \vec{\epsilon} \cdot \left(\vec{p}\,' - \frac{\vec{k}_f}{2} \right)}{\left[- m_\pi^2 - \vec{p}_{mpm}^{\,2} \right] \left[- \omega - B - \frac{2\vec{p}\,'^2 + \omega^2 + \vec{k}_i \cdot \vec{k}_f - 2\vec{p}\,' \cdot \vec{k}_i}{2 m_N} \right]}
\end{aligned} \tag{E.2}$$

$$
\begin{aligned}
T^{(3a)} &= -\frac{e^2\, g_A^2}{4\, f_\pi^2\, m_N}\, \frac{\vec{\epsilon}\cdot\vec{\sigma}_2\, \vec{p}_{mmp}\cdot\vec{\sigma}_1\, \vec{\epsilon}\,'\cdot\vec{p}\,'}{\left[\omega^2 - m_\pi^2 - \vec{p}^{\,2}_{mmp}\right]\left[\omega - B - \frac{\vec{p}\,'^2+\vec{p}\,'\cdot\vec{k}_f}{m_N}\right]} \\
T^{(3b)} &= -\frac{e^2\, g_A^2}{4\, f_\pi^2\, m_N}\, \frac{\vec{\epsilon}\,'\cdot\vec{\sigma}_2\, \vec{p}_{mpp}\cdot\vec{\sigma}_1\, \vec{\epsilon}\cdot\left(\vec{p}\,' - \frac{\vec{k}_f}{2}\right)}{\left[\omega^2 - m_\pi^2 - \vec{p}^{\,2}_{mpp}\right]\left[-\omega - B - \frac{2\vec{p}\,'^2+\omega^2+\vec{k}_i\cdot\vec{k}_f-2\vec{p}\,'\cdot\vec{k}_i}{2m_N}\right]} \\
T^{(3c)} &= \frac{e^2\, g_A^2}{4\, f_\pi^2\, m_N}\, \frac{\vec{\epsilon}\,'\cdot\vec{\sigma}_2\, \vec{p}_{mpp}\cdot\vec{\sigma}_1\, \vec{\epsilon}\cdot\vec{p}}{\left[\omega^2 - m_\pi^2 - \vec{p}^{\,2}_{mpp}\right]\left[\omega - B - \frac{\vec{p}^{\,2}+\vec{p}\cdot\vec{k}_i}{m_N}\right]} \\
T^{(3d)} &= \frac{e^2\, g_A^2}{4\, f_\pi^2\, m_N}\, \frac{\vec{\epsilon}\cdot\vec{\sigma}_2\, \vec{p}_{mmp}\cdot\vec{\sigma}_1\, \vec{\epsilon}\,'\cdot\left(\vec{p} - \frac{\vec{k}_i}{2}\right)}{\left[\omega^2 - m_\pi^2 - \vec{p}^{\,2}_{mmp}\right]\left[-\omega - B - \frac{2\vec{p}^{\,2}+\omega^2+\vec{k}_i\cdot\vec{k}_f-2\vec{p}\cdot\vec{k}_f}{2m_N}\right]}
\end{aligned}
\tag{E.3}
$$

$$
\begin{aligned}
T^{(4a)} &= \frac{e^2\, g_A^2}{8\, f_\pi^2\, m_N^2}\, \frac{\vec{p}_{mpm}\cdot\vec{\sigma}_1\, \vec{p}_{mpm}\cdot\vec{\sigma}_2\, \vec{\epsilon}\cdot\vec{p}\,\vec{\epsilon}\,'\cdot\vec{p}\,'}{\left[-m_\pi^2 - \vec{p}^{\,2}_{mpm}\right]\left[\omega - B - \frac{\vec{p}^{\,2}+\vec{p}\cdot\vec{k}_i}{m_N}\right]\left[\omega - B - \frac{\vec{p}\,'^2+\vec{p}\,'\cdot\vec{k}_f}{m_N}\right]} \\
T^{(4b)} &= \frac{e^2\, g_A^2}{8\, f_\pi^2\, m_N^2}\, \frac{\vec{p}_{mpm}\cdot\vec{\sigma}_1\, \vec{p}_{mpm}\cdot\vec{\sigma}_2\, \vec{\epsilon}\cdot\left(\vec{p}\,' - \frac{\vec{k}_f}{2}\right)\, \vec{\epsilon}\,'\cdot\left(\vec{p} - \frac{\vec{k}_i}{2}\right)}{\left[-m_\pi^2 - \vec{p}^{\,2}_{mpm}\right]\left[-\omega - B - \frac{2\vec{p}\,'^2+\omega^2+\vec{k}_i\cdot\vec{k}_f-2\vec{p}\,'\cdot\vec{k}_i}{2m_N}\right]} \\
&\quad\times \frac{1}{\left[-\omega - B - \frac{2\vec{p}^{\,2}+\omega^2+\vec{k}_i\cdot\vec{k}_f-2\vec{p}\cdot\vec{k}_f}{2m_N}\right]}
\end{aligned}
\tag{E.4}
$$

$$
\begin{aligned}
T^{(5a)} &= \frac{e^2\, g_A^2}{4\, f_\pi^2\, m_N^2}\, \frac{\vec{p}_{ppp}\cdot\vec{\sigma}_1\, \vec{p}_{ppp}\cdot\vec{\sigma}_2\, \vec{\epsilon}\cdot\vec{p}\,\vec{\epsilon}\,'\cdot\vec{p}\,'}{\left[\omega^2 - m_\pi^2 - \vec{p}^{\,2}_{ppp}\right]\left[\omega - B - \frac{\vec{p}^{\,2}+\vec{p}\cdot\vec{k}_i}{m_N}\right]\left[\omega - B - \frac{\vec{p}\,'^2+\vec{p}\,'\cdot\vec{k}_f}{m_N}\right]} \\
T^{(5b)} &= -\frac{e^2\, g_A^2}{4\, f_\pi^2\, m_N^2}\, \frac{\vec{p}_{mmp}\cdot\vec{\sigma}_1\, \vec{p}_{mmp}\cdot\vec{\sigma}_2\, \vec{\epsilon}\cdot\left(\vec{p}\,' + \frac{\vec{k}_f}{2}\right)\, \vec{\epsilon}\,'\cdot\left(\vec{p} - \frac{\vec{k}_i}{2}\right)}{\left[\omega^2 - m_\pi^2 - \vec{p}^{\,2}_{mmp}\right]\left[-\omega - B - \frac{2\vec{p}\,'^2+\omega^2+\vec{k}_i\cdot\vec{k}_f+2\vec{p}\,'\cdot\vec{k}_i}{2m_N}\right]} \\
&\quad\times \frac{1}{\left[-\omega - B - \frac{2\vec{p}^{\,2}+\omega^2+\vec{k}_i\cdot\vec{k}_f-2\vec{p}\cdot\vec{k}_f}{2m_N}\right]}
\end{aligned}
\tag{E.5}
$$

$$
\begin{aligned}
T^{(6a)} &= \frac{e^2\, g_A^2}{2\, f_\pi^2\, m_N}\, \frac{\vec{p}_{mpp}\cdot\vec{\sigma}_1\,\vec{p}_{mpm}\cdot\vec{\sigma}_2\,\vec{\epsilon}\cdot\vec{p}\,\vec{\epsilon}\,'\cdot\left(\vec{p}-\vec{p}\,'+\frac{\vec{k}_i}{2}\right)}{\left[\omega^2-m_\pi^2-\vec{p}\,^2_{mpp}\right]\left[-m_\pi^2-\vec{p}\,^2_{mpm}\right]\left[\omega-B-\frac{\vec{p}^{\,2}+\vec{p}\cdot\vec{k}_i}{m_N}\right]} \\
T^{(6b)} &= \frac{e^2\, g_A^2}{2\, f_\pi^2\, m_N}\, \frac{\vec{p}_{mmp}\cdot\vec{\sigma}_1\,\vec{p}_{mpm}\cdot\vec{\sigma}_2\,\vec{\epsilon}\cdot\left(\vec{p}-\vec{p}\,'-\frac{\vec{k}_f}{2}\right)\,\vec{\epsilon}\,'\cdot\left(\vec{p}-\frac{\vec{k}_i}{2}\right)}{\left[\omega^2-m_\pi^2-\vec{p}\,^2_{mmp}\right]\left[-m_\pi^2-\vec{p}\,^2_{mpm}\right]\left[-\omega-B-\frac{2\vec{p}^{\,2}+\omega^2+\vec{k}_i\cdot\vec{k}_f-2\vec{p}\cdot\vec{k}_f}{2m_N}\right]} \\
T^{(6c)} &= -\frac{e^2\, g_A^2}{2\, f_\pi^2\, m_N}\, \frac{\vec{p}_{mmp}\cdot\vec{\sigma}_1\,\vec{p}_{mpm}\cdot\vec{\sigma}_2\,\vec{\epsilon}\cdot\left(\vec{p}-\vec{p}\,'-\frac{\vec{k}_f}{2}\right)\,\vec{\epsilon}\,'\cdot\vec{p}\,'}{\left[\omega^2-m_\pi^2-\vec{p}\,^2_{mmp}\right]\left[-m_\pi^2-\vec{p}\,^2_{mpm}\right]\left[\omega-B-\frac{\vec{p}\,'^2+\vec{p}\,'\cdot\vec{k}_f}{m_N}\right]} \\
T^{(6d)} &= -\frac{e^2\, g_A^2}{2\, f_\pi^2\, m_N}\, \frac{\vec{p}_{mpp}\cdot\vec{\sigma}_1\,\vec{p}_{mpm}\cdot\vec{\sigma}_2\,\vec{\epsilon}\cdot\left(\vec{p}\,'-\frac{\vec{k}_f}{2}\right)\,\vec{\epsilon}\,'\cdot\left(\vec{p}-\vec{p}\,'+\frac{\vec{k}_i}{2}\right)}{\left[\omega^2-m_\pi^2-\vec{p}\,^2_{mpp}\right]\left[-m_\pi^2-\vec{p}\,^2_{mpm}\right]\left[-\omega-B-\frac{2\vec{p}\,'^2+\omega^2+\vec{k}_i\cdot\vec{k}_f-2\vec{p}\,'\cdot\vec{k}_i}{2m_N}\right]}
\end{aligned}
\tag{E.6}
$$

Exchange of the nucleons ($+(1 \leftrightarrow 2)$, cf. Fig. 5.19) has been skipped for brevity.

Appendix F

Multipole Expansion of the Photon Field

The multipole expansion of $\vec{A}$ that we use for the non-perturbative approach to deuteron Compton scattering, described in Chapter 6, has been derived in [24] in analogy to Chapter 7 of Ref. [83]. Nevertheless, it is worthwhile to repeat the derivation here.

We start with the expansion for $\hat{\epsilon}_\lambda \, \mathrm{e}^{i\vec{k}\cdot\vec{r}}$ with $\vec{k} \parallel \vec{e}_z$. For real photons, $\hat{\epsilon}_\lambda \perp \vec{k}$, therefore $\hat{\epsilon}_\lambda \equiv \hat{r}_\lambda$, the unit vector in the spherical basis, with $\lambda = \pm 1$. The spherical basis together with its scalar product is explained in App. L, Eqs. (L.8)-(L.12).

Using the well-known expansion of the exponential function, cf. e.g. [106], we find

$$\begin{aligned} \hat{\epsilon}_\lambda \, \mathrm{e}^{i\vec{k}\cdot\vec{r}}|_{\hat{k}=\hat{z}} = \hat{r}_\lambda \, \mathrm{e}^{i\vec{k}\cdot\vec{r}}|_{\hat{k}=\hat{z}} &= \hat{r}_\lambda \sum_{l=0}^{\infty} \sum_{m=-l}^{l} 4\pi \, i^l \, j_l(\omega r) \, Y^*_{l\,m}(\hat{k}) \, Y_{l\,m}(\hat{r}) \\ &= \hat{r}_\lambda \sum_{l=0}^{\infty} i^l \, \sqrt{4\pi\,(2l+1)} \, j_l(\omega r) \, Y_{l\,0}(\hat{r}), \end{aligned} \tag{F.1}$$

where we have used Eq. (L.28). $j_l(z)$ are the spherical Bessel functions of the first kind, see Eq. (L.29).

The vector spherical harmonic $\vec{T}_{J\,l\,M}(\hat{r})$ is defined as

$$\vec{T}_{J\,l\,M}(\hat{r}) = \sum_{\nu=-1,0,1} (-1)^{1-l-M} \, \sqrt{2J+1} \begin{pmatrix} l & 1 & J \\ M+\nu & -\nu & -M \end{pmatrix} Y_{l\,M+\nu} \, \hat{r}_{-\nu}, \tag{F.2}$$

cf. Eq. (L.42). Eq. (F.2) can be inverted to

$$Y_{l\,m} \, \hat{r}_{-\lambda} = \sum_{J=0}^{\infty} \sum_{M=-J}^{J} (-1)^{-l+M+1} \, \sqrt{2J+1} \begin{pmatrix} l & 1 & J \\ m & -\lambda & -M \end{pmatrix} \vec{T}_{J\,l\,M}(\hat{r}). \tag{F.3}$$

This is easily proven when we use the definition of the Clebsch-Gordan coefficients, Eq. (L.14), to write

$$Y_{l\,m} \, \hat{r}_{-\lambda} = \sum_{J=0}^{\infty} \sum_{M=-J}^{J} C^{J\,M}_{l\,m\;1\,-\lambda} \, \vec{T}_{J\,l\,M}(\hat{r}) \tag{F.4}$$

and

$$\vec{T}_{J\,l\,M}(\hat{r}) = \sum_{\nu=-1,0,1} C^{J\,M}_{l\,M+\nu\;1\,-\nu} \, Y_{l\,M+v} \, \hat{r}_{-\nu} = \sum_{\nu,\tilde{m}} C^{J\,M}_{l\,\tilde{m}\;1\,-\nu} \, Y_{l\,\tilde{m}} \, \hat{r}_{-\nu}, \tag{F.5}$$

where we have used $\tilde{m} - \nu - M = 0$, cf. Eq. (L.16). Inserting (F.5) into (F.4) and making use of the unitarity of the Clebsch-Gordan coefficients (L.22),

$$\sum_{J,M} C^{J\,M}_{l\,m\,1\,-\lambda}\, C^{J\,M}_{l\,\tilde{m}\,1\,-\nu} = \delta_{\lambda,\nu}\,\delta_{m,\tilde{m}}, \tag{F.6}$$

Eq. (F.3) follows immediately and can be used to write Eq. (F.1) as

$$\hat{\epsilon}_\lambda\, \mathrm{e}^{i\vec{k}\cdot\vec{r}}|_{\hat{k}=\hat{z}} = \sum_{l=0}^{\infty} \sum_{J=|l-1|}^{l+1} (-1)^{-l+\lambda+1}\, i^l \sqrt{4\pi\,(2l+1)\,(2J+1)} \begin{pmatrix} l & 1 & J \\ 0 & \lambda & -\lambda \end{pmatrix} j_l(\omega r)\, \vec{T}_{J\,l\,\lambda}(\hat{r}). \tag{F.7}$$

The possible values for J are constrained by the triangular condition of the Clebsch-Gordan coefficients, Eq. (L.15). This condition guarantees that for $l = 0$ only $J = 1$ gives a non-vanishing contribution. Therefore

$$\hat{\epsilon}_\lambda\, \mathrm{e}^{i\vec{k}\cdot\vec{r}}|_{\hat{k}=\hat{z}} = \sum_{l=0}^{\infty} \sum_{J=l-1}^{l+1} (-1)^{-l}\, i^l \sqrt{4\pi\,(2l+1)\,(2J+1)} \begin{pmatrix} l & 1 & J \\ 0 & \lambda & -\lambda \end{pmatrix} j_l(\omega r)\, \vec{T}_{J\,l\,\lambda}(\hat{r}), \tag{F.8}$$

where we have used $(-1)^{\lambda+1} = 1$ as $\lambda = \pm 1$. Explicitly writing out the sum over J yields

$$\begin{aligned} \hat{\epsilon}_\lambda\, \mathrm{e}^{i\vec{k}\cdot\vec{r}}|_{\hat{k}=\hat{z}} = \sum_{l=0}^{\infty} (-1)^{-l}\, i^l \sqrt{4\pi\,(2l+1)}\, j_l(\omega r) \Bigg\{ & \sqrt{2l-1} \begin{pmatrix} l & 1 & l-1 \\ 0 & \lambda & -\lambda \end{pmatrix} \vec{T}_{l-1\,l\,\lambda}(\hat{r}) \\ & + \sqrt{2l+1} \begin{pmatrix} l & 1 & l \\ 0 & \lambda & -\lambda \end{pmatrix} \vec{T}_{l\,l\,\lambda}(\hat{r}) + \sqrt{2l+3} \begin{pmatrix} l & 1 & l+1 \\ 0 & \lambda & -\lambda \end{pmatrix} \vec{T}_{l+1\,l\,\lambda}(\hat{r}) \Bigg\}. \end{aligned} \tag{F.9}$$

The 3-j symbols in Eq. (F.9) are given by

$$\begin{aligned} \begin{pmatrix} l & 1 & l-1 \\ 0 & \lambda & -\lambda \end{pmatrix} &= \frac{(-1)^{-l}\sqrt{l-1}}{\sqrt{2\,(2l-1)\,(2l+1)}}, \\ \begin{pmatrix} l & 1 & l \\ 0 & \lambda & -\lambda \end{pmatrix} &= -\lambda\,\frac{(-1)^{-l}}{\sqrt{2\,(2l+1)}}, \\ \begin{pmatrix} l & 1 & l+1 \\ 0 & \lambda & -\lambda \end{pmatrix} &= \frac{(-1)^{l}\sqrt{l+2}}{\sqrt{2\,(2l+1)\,(2l+3)}}, \end{aligned}$$

so we end up with $((-1)^{2\,l} = 1)$

$$\hat{\epsilon}_\lambda\, \mathrm{e}^{i\vec{k}\cdot\vec{r}}|_{\hat{k}=\hat{z}} = \sum_{l=0}^{\infty} i^l \sqrt{2\pi}\, j_l(\omega r) \left\{ \sqrt{l-1}\, \vec{T}_{l-1\,l\,\lambda}(\hat{r}) - \lambda \sqrt{2\,l+1}\, \vec{T}_{l\,l\,\lambda}(\hat{r}) + \sqrt{l+2}\, \vec{T}_{l+1\,l\,\lambda}(\hat{r}) \right\}. \tag{F.10}$$

For $l = 0$, the first two terms vanish due to the 3-j symbol in the definition of $\vec{T}_{J\,l\,M}(\hat{r})$, cf. Eq. (F.2), for $l = 1$, the first term vanishes due to $\sqrt{l-1}$. Therefore, we can rearrange Eq. (F.10) such that all of the vector spherical harmonics have the same total angular momentum, which we call L. The result is

$$\begin{aligned} \hat{\epsilon}_\lambda\, \mathrm{e}^{i\vec{k}\cdot\vec{r}}|_{\hat{k}=\hat{z}} = \sum_{L=1}^{\infty} i^L \sqrt{2\pi\,(2L+1)} \Bigg\{ & i \sqrt{\frac{L}{2L+1}}\, j_{L+1}(\omega r)\, \vec{T}_{L\,L+1\,\lambda}(\hat{r}) \\ & - \lambda\, j_L(\omega r)\, \vec{T}_{L\,L\,\lambda}(\hat{r}) - i \sqrt{\frac{L+1}{2L+1}}\, j_{L-1}(\omega r)\, \vec{T}_{L\,L-1\,\lambda}(\hat{r}) \Bigg\}. \end{aligned} \tag{F.11}$$

Now we want to generalize this expression to arbitrary directions of $\vec{k}$. This can be achieved by acting with the rotation operator on the angle-dependent quantities on the right-hand side of Eq. (F.11), which are the vector spherical harmonics. The matrix elements of the rotation operator are

$$\langle\, j\, m \mid \hat{D}(\alpha,\beta,\gamma) \mid j'\, m' \,\rangle = \delta_{j,j'}\, D^{j}_{m,m'}(\alpha,\beta,\gamma) \tag{F.12}$$

with the Wigner D-functions $D^{j}_{m,m'}(\alpha,\beta,\gamma)$. These can be written as

$$D^{j}_{m,m'}(\alpha,\beta,\gamma) = \mathrm{e}^{-i\,m\,\alpha}\, d^{j}_{m,m'}(\beta)\, \mathrm{e}^{-i\,m\,\gamma}. \tag{F.13}$$

As we only have to take into account one Euler angle, namely the scattering angle θ, we may choose $\alpha = 0,\ \ \beta = \theta,\ \ \gamma = 0$. Using the well-known relation (see e.g. [107], Chapter 4)

$$\hat{D}(\alpha,\beta,\gamma)\, u(j\, m) = \sum_{m'} u(j\, m')\, D^{j}_{m',m}(\alpha,\beta,\gamma), \tag{F.14}$$

which in our case reduces to

$$\hat{D}(0,\theta,0)\, u(j\, m) = \sum_{m'} u(j\, m')\, d^{j}_{m',m}(\theta), \tag{F.15}$$

we find

$$\begin{aligned}\hat{\epsilon}_\lambda\, \mathrm{e}^{i\vec{k}\cdot\vec{r}} = \sum_{L=1}^{\infty} \sum_{M=-L}^{L} i^L\, \sqrt{2\pi\,(2L+1)}\, \Bigg\{ & i\,\sqrt{\frac{L}{2L+1}}\, j_{L+1}(\omega r)\, \vec{T}_{L\,L+1\,M}(\hat{r}) \\ & - \lambda\, j_L(\omega r)\, \vec{T}_{L\,L\,M}(\hat{r}) - i\sqrt{\frac{L+1}{2L+1}}\, j_{L-1}(\omega r)\, \vec{T}_{L\,L-1\,M}(\hat{r}) \Bigg\}\, d^{L}_{M,\lambda}(\theta).\end{aligned} \tag{F.16}$$

The second term can be simplified via [107]

$$\vec{T}_{L\,L\,M}(\hat{r}) = \frac{1}{\sqrt{L\,(L+1)}}\, \vec{L}\, Y_{L\,M}(\hat{r}) \tag{F.17}$$

with the orbital angular momentum operator $\vec{L}$. In order to simplify the other two terms we show that

$$\begin{aligned}&\sqrt{\frac{L+1}{2L+1}}\, j_{L-1}(\omega r)\, \vec{T}_{L\,L-1\,M}(\hat{r}) - \sqrt{\frac{L}{2L+1}}\, j_{L+1}(\omega r)\, \vec{T}_{L\,L+1\,M}(\hat{r}) \\ =&\frac{1}{\sqrt{L\,(L+1)}} \left\{ \omega\, \vec{r}\, j_L(\omega r)\, Y_{L\,M}(\hat{r}) + \frac{1}{\omega}\, \vec{\nabla}_r \left(1 + r\frac{d}{dr}\right)\, j_L \omega r\, Y_{L\,M}(\hat{r}) \right\}.\end{aligned} \tag{F.18}$$

First we decompose $\vec{r}$ into spherical components via Eqs. (L.11) and (L.13):

$$\vec{r} = \sum_{\nu=-1,0,1} r\,(-1)^{\nu}\, r_\nu\, \hat{r}_{-\nu} = \sum_{\nu=-1,0,1} r\,(-1)^{\nu}\, \sqrt{\frac{4\pi}{3}}\, Y_{1\,\nu}(\hat{r})\, \hat{r}_{-\nu} \tag{F.19}$$

Using this relation we can write the first term on the right-hand side ($RHS1$) of Eq. (F.18) as

$$RHS1 = \sum_{\nu=-1,0,1} \frac{r\,\omega}{\sqrt{L\,(L+1)}}\, j_L(\omega r)\,(-1)^{\nu}\, \sqrt{\frac{4\pi}{3}}\, Y_{1\,\nu}(\hat{r})\, \hat{r}_{-\nu}\, Y_{L\,M}(\hat{r}). \tag{F.20}$$

Now, using Eq. (L.26), the spherical harmonics are combined to

$$RHS1 = \sum_{\nu=-1,0,1} \sum_{\tilde{J}=|L-1|}^{L+1} \sum_{\tilde{M}=-\tilde{J}}^{\tilde{J}} \frac{r\,\omega}{\sqrt{L\,(L+1)}}\, j_L(\omega r)\,(-1)^{\nu+\tilde{M}} \sqrt{(2L+1)\,(2\tilde{J}+1)} \times \begin{pmatrix} 1 & L & \tilde{J} \\ 0 & 0 & 0 \end{pmatrix} \begin{pmatrix} 1 & L & \tilde{J} \\ \nu & M & -\tilde{M} \end{pmatrix} Y_{\tilde{J}\,\tilde{M}}(\hat{r})\,\hat{r}_{-\nu}. \tag{F.21}$$

The spherical harmonic can be replaced by a vector spherical harmonic, making use of Eq. (F.3):

$$RHS1 = \sum_{\nu=-1,0,1} \sum_{\tilde{J}=|L-1|}^{L+1} \sum_{J'=|\tilde{J}-1|}^{\tilde{J}+1} \sum_{\tilde{M},M'} \frac{r\,\omega}{\sqrt{L\,(L+1)}}\, j_L(\omega r)\,(-1)^{\nu+\tilde{M}+\tilde{J}-1+M'} \sqrt{(2L+1)} \times \sqrt{(2\tilde{J}+1)\,(2J'+1)} \begin{pmatrix} 1 & L & \tilde{J} \\ 0 & 0 & 0 \end{pmatrix} \begin{pmatrix} 1 & L & \tilde{J} \\ \nu & M & -\tilde{M} \end{pmatrix} \begin{pmatrix} \tilde{J} & 1 & J' \\ \tilde{M} & -\nu & -M' \end{pmatrix} \vec{T}_{J'\,\tilde{J}\,M'}(\hat{r}) \tag{F.22}$$

The 3-j symbol is symmetric under even permutations of rows and

$$\begin{pmatrix} \tilde{J} & 1 & J' \\ \tilde{M} & -\nu & -M' \end{pmatrix} = (-1)^{\tilde{J}+1+J'} \begin{pmatrix} \tilde{J} & 1 & J' \\ -\tilde{M} & \nu & M' \end{pmatrix},$$

cf. Eq. (L.19). Furthermore $(-1)^{\nu+M'+\tilde{M}} = (-1)^{\nu+M'-\tilde{M}}$, as we are only concerned with integer quantum numbers throughout this work, and $(-1)^{\nu+M'-\tilde{M}} = 1$ due to the 3-j symbols in Eq. (F.22). Therefore we find

$$RHS1 = \sum_{\nu=-1,0,1} \sum_{\tilde{J}=|L-1|}^{L+1} \sum_{J'=|\tilde{J}-1|}^{\tilde{J}+1} \frac{r\,\omega}{\sqrt{L\,(L+1)}}\, j_L(\omega r)\,(-1)^{J'} \sqrt{(2L+1)\,(2\tilde{J}+1)\,(2J'+1)} \times \begin{pmatrix} 1 & L & \tilde{J} \\ 0 & 0 & 0 \end{pmatrix} \vec{T}_{J'\,\tilde{J}\,M'}(\hat{r}) \sum_{\tilde{M},M'} \begin{pmatrix} \tilde{J} & 1 & L \\ -\tilde{M} & \nu & M \end{pmatrix} \begin{pmatrix} \tilde{J} & 1 & J' \\ -\tilde{M} & \nu & M' \end{pmatrix}. \tag{F.23}$$

By use of the unitarity of the 3-j symbols, Eq. (L.22), this becomes

$$RHS1 = \sum_{\tilde{J}=|L-1|}^{L+1} r\,\omega\,(-1)^L\, j_L(\omega r) \sqrt{\frac{2\tilde{J}+1}{L\,(L+1)}} \begin{pmatrix} 1 & L & \tilde{J} \\ 0 & 0 & 0 \end{pmatrix} \vec{T}_{L\,\tilde{J}\,M}(\hat{r}). \tag{F.24}$$

The 3-j symbol takes on the values $\frac{(-1)^{1-L}\sqrt{L+1}}{\sqrt{(2L+1)\,(2L+3)}}$ for $\tilde{J} = L+1$, 0 for $\tilde{J} = L$ and $\frac{(-1)^L\sqrt{L}}{\sqrt{(2L-1)\,(2L+1)}}$ for $\tilde{J} = L-1$. Therefore we get

$$RHS1 = r\,\omega\, j_L(\omega r) \left[\frac{\vec{T}_{L\,L-1\,M}(\hat{r})}{\sqrt{(L+1)\,(2L+1)}} - \frac{\vec{T}_{L\,L+1\,M}(\hat{r})}{\sqrt{L\,(2L+1)}} \right]. \tag{F.25}$$

Now we have to write the second part on the right-hand side of Eq. (F.18) in terms of vector spherical harmonics. This can be achieved using the gradient formula,

Eq. (L.43), which gives

$$\begin{aligned}\vec{\nabla}_r \left(1 + r\frac{d}{dr}\right) j_L(\omega r)\, Y_{L\,M}(\hat{r}) = \\ + \sqrt{\frac{L}{2L+1}} \left((L+3)\,\frac{d}{dr} + r\frac{d^2}{dr^2} + \frac{L+1}{r}\right) j_L(\omega r)\, \vec{T}_{L\,L-1\,M}(\hat{r}) \\ - \sqrt{\frac{L+1}{2L+1}} \left((2-L)\,\frac{d}{dr} + r\frac{d^2}{dr^2} - \frac{L}{r}\right) j_L(\omega r)\, \vec{T}_{L\,L+1\,M}(\hat{r}). \end{aligned} \tag{F.26}$$

Using the recursion relations for spherical Bessel functions, Eq. (L.30), we find

$$\begin{aligned}\frac{1}{r}\, j_L(\omega r) &= \frac{\omega}{2L+1}\, \left[j_{L-1}(\omega r) + j_{L+1}(\omega r)\right], \\ \frac{d}{dr} j_L(\omega r) &= \frac{\omega}{2L+1}\, \left[L\, j_{L-1}(\omega r) - (L+1)\, j_{L+1}(\omega r)\right], \\ r\frac{d^2}{dr^2} j_L(\omega r) &= \frac{r\,\omega}{2L+1}\, \left[\frac{L\,(L-1)}{r}\, j_{L-1}(\omega r) - \omega\,(2L+1)\, j_L(\omega r) + \frac{(L+1)\,(L+2)}{r}\, j_{L+1}(\omega r)\right]. \end{aligned}$$

Inserting these three expressions into Eq. (F.26), which is used to replace the corresponding term in Eq. (F.18), we end up with

$$\begin{aligned} RHS2 = \frac{\vec{T}_{L\,L+1\,M}(\hat{r})}{\sqrt{L\,(2L+1)}}\, \left(r\,\omega\, j_L(\omega r) - L\, j_{L+1}(\omega r)\right) \\ + \frac{\vec{T}_{L\,L-1\,M}(\hat{r})}{\sqrt{(L+1)\,(2L+1)}}\, \left((L+1)\, j_{L-1}(\omega r) - r\,\omega\, j_L(\omega r)\right). \end{aligned} \tag{F.27}$$

Adding Eqs. (F.25) and (F.27) we immediately see the identity (F.18). Combining Eqs. (F.16), (F.17) and (F.18), we get the final result for the multipole expansion:

$$\begin{aligned}\hat{\epsilon}_\lambda\, \mathrm{e}^{i\vec{k}\cdot\vec{r}} = \sum_{L=1}^{\infty} \sum_{M=-L}^{L} d^L_{M,\lambda}(\theta)\, i^L \sqrt{\frac{2\pi\,(2L+1)}{L\,(L+1)}} \\ \times \left\{-\frac{i}{\omega}\, \vec{\nabla}_r \left(1 + r\frac{d}{dr}\right) j_L(\omega r)\, Y_{L\,M}(\hat{r}) - i\,\omega\,\vec{r}\, j_L(\omega r)\, Y_{L\,M}(\hat{r}) - \lambda\, \vec{L}\, Y_{L\,M}(\hat{r})\, j_L(\omega r)\right\} \end{aligned} \tag{F.28}$$

The first two terms correspond to electric, the third to magnetic photons, cf. e.g. [83], Chapter 7.

In our calculation the incoming photon always moves along the z-direction, i.e. $\theta_i = 0$. However, $d^L_{M,\lambda}(\theta = 0) = \delta_{M,\lambda}$, cf. e.g. [108]. Therefore we get for the incoming photon

$$\begin{aligned}\hat{\epsilon}_{\lambda_i}\, \mathrm{e}^{i\vec{k}_i\cdot\vec{r}} = -\sum_{L=1}^{\infty} \sum_{M=-L}^{L} \delta_{M,\lambda_i}\, i^L \sqrt{\frac{2\pi\,(2L+1)}{L\,(L+1)}} \\ \times \left\{\frac{i}{\omega}\, \vec{\nabla}_r \left(1 + r\frac{d}{dr}\right) j_L(\omega r)\, Y_{L\,M}(\hat{r}) + \lambda_i\, \vec{L}\, Y_{L\,M}(\hat{r})\, j_L(\omega r) + i\,\omega\,\vec{r}\, j_L(\omega r)\, Y_{L\,M}(\hat{r})\right\}. \end{aligned} \tag{F.29}$$

Considering the case of an outgoing photon, the expansion would start with

$$\begin{aligned}\hat{\epsilon}^*_\lambda\, \mathrm{e}^{-i\vec{k}\cdot\vec{r}}|_{\hat{k}=\hat{z}} &= \hat{r}^*_\lambda \sum_{l=0}^{\infty} \sum_{m=-l}^{l} 4\pi\,(-1)^l\, i^l\, j_l(\omega r)\, Y^*_{l\,m}(\hat{k})\, Y_{l\,m}(\hat{r}) \\ &= (-1)^\lambda\, \hat{r}_{-\lambda} \sum_{l=0}^{\infty} \sum_{m=-l}^{l} 4\pi\,(-1)^l\, i^l\, j_l(\omega r)\, Y^*_{l\,m}(\hat{k})\, Y_{l\,m}(\hat{r}). \end{aligned} \tag{F.30}$$

The equivalent to Eq. (F.11) therefore is

$$\hat{\epsilon}_\lambda^* \, \mathrm{e}^{-i\vec{k}\cdot\vec{r}}|_{\hat{k}=\hat{z}} = \sum_{L=1}^{\infty} i^L \sqrt{2\pi\,(2L+1)}\,(-1)^{L+\lambda} \left\{ -i\sqrt{\frac{L}{2L+1}}\, j_{L+1}(\omega r)\, \vec{T}_{L\,L+1\,-\lambda}(\hat{r}) \right.$$
$$\left. +\ \lambda\, j_L(\omega r)\, \vec{T}_{L\,L\,-\lambda}(\hat{r}) + i\sqrt{\frac{L+1}{2L+1}}\, j_{L-1}(\omega r)\, \vec{T}_{L\,L-1\,-\lambda}(\hat{r}) \right\}. \quad \text{(F.31)}$$

The signs follow from $\lambda \to -\lambda$ and $(-1)^{L+1} = (-1)^{L-1} = -(-1)^L$. Finally, $d^L_{M,-\lambda}(\theta)$ appears instead of $d^L_{M,\lambda}(\theta)$ in the pendant to Eq. (F.16). Therefore we end up with

$$\hat{\epsilon}_{\lambda_f}^* \, \mathrm{e}^{-i\vec{k}_f\cdot\vec{r}} = \sum_{L'=1}^{\infty} \sum_{M'=-L'}^{L'} d^{L'}_{M',-\lambda_f}(\theta)\, i^{L'} \sqrt{\frac{2\pi\,(2L'+1)}{L'\,(L'+1)}}\,(-1)^{L'+\lambda_f} \quad \text{(F.32)}$$
$$\times \left\{ \frac{i}{\omega}\,\vec{\nabla}_r \left(1 + r\frac{d}{dr}\right) j_{L'}(\omega r)\, Y_{L'\,M'}(\hat{r}) + \lambda_f\, \vec{L}\, Y_{L'\,M'}(\hat{r})\, j_{L'}(\omega r) + i\,\omega\,\vec{r}\, j_{L'}(\omega r)\, Y_{L'\,M'}(\hat{r}) \right\},$$

where we use primed quantities in order to distinguish between outgoing and incoming photons, as we will throughout the whole work.

Appendix G

Calculation of the Dominant Terms with NN-Rescattering

We now evaluate Eqs. (6.23-6.26), which are the amplitudes arising from the replacement $\vec{A} \to \vec{\nabla}\phi$ at both vertices. The results are already given (in the lab frame) in Ref. [24]. We start with the two amplitudes including the intermediate state $\mid C \rangle$ and an energy denominator, $\mathcal{M}_{fi}^{\phi\phi 1}$ and $\mathcal{M}_{fi}^{\phi\phi 2}$.

We write out $\hat{\phi}_i$ and $\hat{\phi}_f$ according to Eq. (6.4) – remember, $\hat{\phi}_{i,f}$ was defined as $e\,\phi_{i,f}(\vec{r}/2)$ – separate the radial from the angular wave function of the intermediate state $\mid C \rangle$ and insert two complete sets of radial states $\mid r \rangle$, $\mid r' \rangle$, as explained in Eq. (6.29). We find

$$\begin{aligned}\mathcal{M}_{fi}^{\phi\phi 1} = \left(\omega + \frac{\omega^2}{2m_d}\right)^2 \sum_{\hat{C}} \iint r^2 dr\, r'^2 dr' \,\langle\, d_f \mid e \sum_{L'=1}^{\infty} \sum_{M'=-L'}^{L'} (-1)^{L'-\lambda_f}\, d^{L'}_{M',-\lambda_f}(\theta) \\ \times \frac{i^{L'+1}}{\omega} \sqrt{\frac{2\pi\,(2L'+1)}{L'\,(L'+1)}}\, \psi_{L'}(\frac{\omega r'}{2})\, Y_{L'\,M'} \mid \hat{C}\, r' \,\rangle\langle\, r' \mid \frac{1}{E_0 - H^{np}_{\hat{C}}} \mid r \,\rangle \\ \times \langle\, r\, \hat{C} \mid -e \sum_{L=1}^{\infty} \sum_{M=-L}^{L} \delta_{M,\lambda_i}\, \frac{i^{L+1}}{\omega} \sqrt{\frac{2\pi\,(2L+1)}{L\,(L+1)}}\, \psi_L(\frac{\omega r}{2})\, Y_{L\,M} \mid d_i \,\rangle. \quad \text{(G.1)}\end{aligned}$$

E_0 is defined as $E_0 = \omega + \frac{\omega^2}{2m_d} - B$, cf. Sect. 6.1.1. We now use the form (D.5) for the deuteron wave functions and introduce the Green's function $G_{\hat{C}}(r, r'; E_0)$ according to Eq. (6.31).

$$\begin{aligned}\mathcal{M}_{fi}^{\phi\phi 1} = \sum_{L=1}^{\infty} \sum_{M=-L}^{L} \sum_{L'=1}^{\infty} \sum_{M'=-L'}^{L'} \sum_{L_C,S_C,J_C,M_C} \sum_{l=0,2} \sum_{l'=0,2} \left(1 + \frac{\omega}{2m_d}\right)^2 2\pi\, e^2\, (-1)^{L'-\lambda_f} \\ \times i^{L+L'}\, \delta_{M,\lambda_i}\, d^{L'}_{M',-\lambda_f}(\theta) \sqrt{\frac{(2L+1)\,(2L'+1)}{L\,(L+1)\,L'\,(L'+1)}} \\ \times \iint r dr\, r' dr'\, u_l(r)\, \psi_L(\frac{\omega r}{2})\, G_{\hat{C}}(r, r'; E_0)\, \psi_{L'}(\frac{\omega r'}{2})\, u_{l'}(r') \quad \text{(G.2)} \\ \times \langle\, l'\,1\,1\,M_f \mid Y_{L'\,M'} \mid L_C\, S_C\, J_C\, M_C \,\rangle\, \langle\, L_C\, S_C\, J_C\, M_C \mid Y_{L\,M} \mid l\,1\,1\,M_i \,\rangle\end{aligned}$$

Now the Wigner-Eckart theorem (L.31) is applied to both matrix elements. The resulting reduced matrix elements are given in Eq. (L.37) and guarantee that $S_C =$

1. Further we know that $M = \lambda_i$. Therefore we read off Eq. (L.16) $M_C = M_i + \lambda_i$ and $M' = M_f - M_i - \lambda_i$, which removes the formal sums over M, M', M_C. The possible values for J_C are determined by the triangular condition (L.15), which the 3-j symbol has to fulfill. L_C of course takes on the values $|J_C - S_C|, \cdots, J_C + S_C$. Therefore we find the final result

$$\begin{aligned}
\mathcal{M}_{fi}^{\phi\phi 1} = & \sum_{L=1}^{\infty}\sum_{L'=1}^{\infty}\sum_{J_C=|L-1|}^{L+1}\sum_{L_C=|J_C-1|}^{J_C+1}\sum_{l,l'}\left(1+\frac{\omega}{2m_d}\right)^2 2\pi\, e^2\,(-1)^{L'-\lambda_f+1-M_f+J_C-M_i-\lambda_i} \\
& \times i^{L+L'}\, d^{L'}_{M_f-M_i-\lambda_i,-\lambda_f}(\theta)\,\sqrt{\frac{(2L+1)\,(2L'+1)}{L\,(L+1)\,L'\,(L'+1)}}\begin{pmatrix} J_C & L & 1 \\ -M_i-\lambda_i & \lambda_i & M_i \end{pmatrix} \\
& \times \iint r dr\, r' dr'\, u_l(r)\,\psi_L(\frac{\omega r}{2})\, G_{\hat{C}}(r,r';E_0)\,\psi_{L'}(\frac{\omega r'}{2})\, u_{l'}(r') \qquad \text{(G.3)} \\
& \times \begin{pmatrix} 1 & L' & J_C \\ -M_f & M_f-M_i-\lambda_i & M_i+\lambda_i \end{pmatrix} \langle\, l'\,1\,1 \,\|\, Y_{L'} \,\|\, L_C\,1\,J_C\,\rangle\,\langle\, L_C\,1\,J_C \,\|\, Y_L \,\|\, l\,1\,1\,\rangle,
\end{aligned}$$

where we used the shortcut $\sum_{l,l'} = \sum_{l=0,2}\sum_{l'=0,2}$ as we always will throughout the whole work. Due to $\psi_1(\frac{\omega r}{2}) \to \frac{1}{3}\,\omega r$ for $\omega \to 0$, we see that the amplitude $\mathcal{M}_{fi}^{\phi\phi 1}$ – as well as $\mathcal{M}_{fi}^{\phi\phi 2}$ and $\mathcal{M}_{fi}^{\phi\phi 3}$ – cannot contribute in the static limit.

The evaluation of $\mathcal{M}_{fi}^{\phi\phi 2}$ is quite similar. Therefore we only give the final result:

$$\begin{aligned}
\mathcal{M}_{fi}^{\phi\phi 2} = & \sum_{L=1}^{\infty}\sum_{L'=1}^{\infty}\sum_{J_C=|L-1|}^{L+1}\sum_{L_C=|J_C-1|}^{J_C+1}\sum_{l,l'}\left(\omega-\frac{\omega^2}{2m_d}+\frac{\vec{P}_C^{\,2}}{2m_C}\right)^2 \frac{2\pi\, e^2}{\omega^2}\,(-1)^{L'-\lambda_f+1+J_C-\lambda_i} \\
& \times i^{L+L'}\, d^{L'}_{M_f-M_i-\lambda_i,-\lambda_f}(\theta)\,\sqrt{\frac{(2L+1)\,(2L'+1)}{L\,(L+1)\,L'\,(L'+1)}}\begin{pmatrix} 1 & L & J_C \\ -M_f & \lambda_i & M_f-\lambda_i \end{pmatrix} \\
& \times \iint r dr\, r' dr'\, u_{l'}(r)\,\psi_L(\frac{\omega r}{2})\, G_{\hat{C}}(r,r';E_0')\,\psi_{L'}(\frac{\omega r'}{2})\, u_l(r') \qquad \text{(G.4)} \\
& \times \begin{pmatrix} J_C & L' & 1 \\ -M_f+\lambda_i & M_f-M_i-\lambda_i & M_i \end{pmatrix} \langle\, l'\,1\,1 \,\|\, Y_L \,\|\, L_C\,1\,J_C\,\rangle\,\langle\, L_C\,1\,J_C \,\|\, Y_{L'} \,\|\, l\,1\,1\,\rangle
\end{aligned}$$

We remind the reader that we use $m_C = 2m_N$. Note that in the u-channel diagrams, the Green's function depends on $E_0' = -\omega - \frac{\vec{P}_C^{\,2}}{2m_C} + \frac{\omega^2}{2m_d} - B$, rather than on E_0 and u_l ($u_{l'}$) depends on r' (r), as we insert the complete set of states $|\, r'\,\rangle$ ($|\, r\,\rangle$) at the vertex of the outgoing (incoming) photon.

How to evaluate the double integrals over r, r' in Eqs. (G.3) and (G.4) is described in Sect. 6.1.1. However, in the u-channel diagrams we do an approximation of the energy denominator as we want to avoid the scattering angle θ entering the denominator via $\vec{P}_C^{\,2}$. The reason is that the numerical effort in solving the double integral is rather high, so we prefer to solve it only once for each energy. The momentum of the intermediate two-nucleon state in the u-channel, calculated in the γd-cm frame is $\vec{P}_C = -\vec{k}_i - \vec{k}_f$. Therefore $\vec{P}_C^{\,2} = (\vec{k}_i + \vec{k}_f)^2 = 2\,\omega^2\,(1+\cos\theta)$. Now we expand the denominator of Eq. (6.24) for $\frac{\vec{P}_C^{\,2}}{2m_C} \ll \omega$ and $m_C \approx m_d$:

$$\frac{1}{-\omega+\frac{\omega^2}{2m_d}-B-E_C-\frac{\vec{P}_C^{\,2}}{2m_C}} \approx \frac{1}{-\omega-\frac{\omega^2}{2m_d}-B-E_C} + \frac{\frac{\omega^2}{m_d}\cos\theta}{\left(-\omega-\frac{\omega^2}{2m_d}-B-E_C\right)^2} \qquad \text{(G.5)}$$

When we assume that the photon energy is the dominant quantity in the denominator, which should be justified as for low energies the diagrams including an energy

denominator become negligible, we can further simplify Eq. (G.5):

$$\frac{1}{-\omega+\frac{\omega^2}{2m_d}-B-E_C-\frac{\vec{P}_C^{\,2}}{2m_C}} \approx \frac{1-\frac{\omega}{m_d}\cos\theta}{-\omega-\frac{\omega^2}{2m_d}-B-E_C} \tag{G.6}$$

Therefore, in this approximation we just have to evaluate the double integral for $\theta = \frac{\pi}{2}$ and multiply the result with $\left(1-\frac{\omega}{m_d}\cos\theta\right)$. Numerical checks, that we performed for all energies at which we calculate the γd cross sections and for $\theta = 5^\circ,\ 180^\circ$ exhibit that the error on the integrals introduced by this approximation is well below 2% in all considered cases.

Evaluation of $\mathcal{M}_{fi}^{\phi\phi 3}$ (Eq. (6.25)) is straightforward. It is suppressed by $\frac{\omega}{m_d}$ and therefore a small correction, as the photon energy which appears in the prefactors of Eqs. (6.23, 6.24) drops out. Inserting the explicit expressions for $\hat{\phi}_i,\ \hat{\phi}_f$ we get

$$\begin{aligned}\mathcal{M}_{fi}^{\phi\phi 3} = &\sum_{L=1}^{\infty}\sum_{M=-L}^{L}\sum_{L'=1}^{\infty}\sum_{M'=-L'}^{L'}\sum_{l,l'}\left(\frac{\vec{P}_C^{\,2}}{2m_C}-\frac{\omega^2}{m_d}\right)\frac{2\pi\,e^2}{\omega^2}\,(-1)^{L'-\lambda_f}\\ &\times i^{L+L'}\,\delta_{M,\lambda_i}\,d^{L'}_{M',-\lambda_f}(\theta)\sqrt{\frac{(2L+1)\,(2L'+1)}{L\,(L+1)\,L'\,(L'+1)}}\\ &\times\int dr\,u_l(r)\,\psi_L(\frac{\omega r}{2})\,\psi_{L'}(\frac{\omega r}{2})\,u_{l'}(r)\,\langle\, l'\,1\,1\,M_f\mid Y_{L\,M}\,Y_{L'\,M'}\mid l\,1\,1\,M_i\,\rangle.\end{aligned} \tag{G.7}$$

We only need one complete set of states $\mid r\,\rangle$ due to the missing intermediate state. The spherical harmonics are combined using Eq. (L.26). We find

$$\begin{aligned}\mathcal{M}_{fi}^{\phi\phi 3} = &\sum_{L=1}^{\infty}\sum_{M=-L}^{L}\sum_{L'=1}^{\infty}\sum_{M'=-L'}^{L'}\sum_{\tilde{L}=|L-L'|}^{L+L'}\sum_{l,l'}\left(\frac{\vec{P}_C^{\,2}}{2m_C}-\frac{\omega^2}{m_d}\right)\frac{\sqrt{\pi}\,e^2}{\omega^2}\,(-1)^{L'-\lambda_f+M+M'}\\ &\times i^{L+L'}\,\delta_{M,\lambda_i}\,d^{L'}_{M',-\lambda_f}(\theta)\,(2L+1)\,(2L'+1)\sqrt{\frac{2\tilde{L}+1}{L\,(L+1)\,L'\,(L'+1)}}\\ &\times\begin{pmatrix}L & L' & \tilde{L}\\ 0 & 0 & 0\end{pmatrix}\begin{pmatrix}L & L' & \tilde{L}\\ M & M' & -M-M'\end{pmatrix}\\ &\times\int dr\,u_l(r)\,\psi_L(\frac{\omega r}{2})\,\psi_{L'}(\frac{\omega r}{2})\,u_{l'}(r)\,\langle\, l'\,1\,1\,M_f\mid Y_{\tilde{L}\,M+M'}\mid l\,1\,1\,M_i\,\rangle.\end{aligned} \tag{G.8}$$

By use of the Wigner-Eckart theorem (L.31) we obtain the final result

$$\begin{aligned}\mathcal{M}_{fi}^{\phi\phi 3} = &\sum_{L=1}^{\infty}\sum_{L'=1}^{\infty}\sum_{\tilde{L}=|L-L'|}^{L+L'}\sum_{l,l'}\left(\frac{\vec{P}_C^{\,2}}{2m_C}-\frac{\omega^2}{m_d}\right)\frac{\sqrt{\pi}\,e^2}{\omega^2}\,(-1)^{L'-\lambda_f+1-M_i}\\ &\times i^{L+L'}\,d^{L'}_{M_f-M_i-\lambda_i,-\lambda_f}(\theta)\,(2L+1)\,(2L'+1)\sqrt{\frac{2\tilde{L}+1}{L\,(L+1)\,L'\,(L'+1)}}\\ &\times\begin{pmatrix}L & L' & \tilde{L}\\ 0 & 0 & 0\end{pmatrix}\begin{pmatrix}L & L' & \tilde{L}\\ \lambda_i & M_f-M_i-\lambda_i & -M_f+M_i\end{pmatrix}\begin{pmatrix}1 & \tilde{L} & 1\\ -M_f & M_f-M_i & M_i\end{pmatrix}\\ &\times\int dr\,u_l(r)\,\psi_L(\frac{\omega r}{2})\,\psi_{L'}(\frac{\omega r}{2})\,u_{l'}(r)\,\langle\, l'\,1\,1\,\|\,Y_{\tilde{L}}\,\|\,l\,1\,1\,\rangle.\end{aligned} \tag{G.9}$$

Now we turn to the amplitude containing the double commutators, Eq. (6.26). We evaluate this contribution by splitting the Hamiltonian H^{np} into a kinetic and a potential energy part. First we discuss the kinetic energy part, denoted by 'kE', i.e.

$H^{np} \to \frac{\vec{p}^{\,2}}{m_N}$ in Eq. (6.26). The momentum operator $\vec{p}$ is

$$\vec{p} = \frac{\vec{p}_p - \vec{p}_n}{2} = \frac{-i\,\vec{\nabla}_{x_p} + i\,\vec{\nabla}_{x_n}}{2} = -i\,\vec{\nabla}_r. \tag{G.10}$$

The only $\vec{r}$-dependent quantities in $\hat{\phi}_i,\ \hat{\phi}_f$ are $\psi_L\,Y_{L\,M}$ and $\psi_{L'}\,Y_{L'\,M'}$, respectively. Therefore we only consider the commutators $-\frac{1}{m_N}\,\Big[[\vec{\nabla}^{\,2}, \psi_L\,Y_{L\,M}], \psi_{L'}\,Y_{L'\,M'}\Big]$ and $-\frac{1}{m_N}\,\Big[[\vec{\nabla}^{\,2}, \psi_{L'}\,Y_{L'\,M'}], \psi_L\,Y_{L\,M}\Big]$. Evaluating the first double commutator yields

$$-\frac{1}{m_N}\,\Big[[\vec{\nabla}^{\,2}, \psi_L\,Y_{L\,M}], \psi_{L'}\,Y_{L'\,M'}\Big] = -\frac{2}{m_N}\,\Big[\vec{\nabla}(\psi_L\,Y_{L\,M})\Big]\cdot\Big[\vec{\nabla}(\psi_{L'}\,Y_{L'\,M'})\Big]. \tag{G.11}$$

The second double commutator in Eq. (6.26) obviously gives the same contribution, as Eq. (G.11) is symmetric under $L \leftrightarrow L'$, $M \leftrightarrow M'$. Now we use $(\vec{\nabla} f)\cdot(\vec{\nabla} g) = \frac{1}{2}\left(\vec{\nabla}^{\,2}(f\,g) - f\,\vec{\nabla}^{\,2} g - g\,\vec{\nabla}^{\,2} f\right)$ to rewrite Eq. (G.11) as

$$\begin{aligned}-\frac{1}{m_N}\,\Big[[\vec{\nabla}^{\,2}, \psi_L\,Y_{L\,M}], \psi_{L'}\,Y_{L'\,M'}\Big] = -\frac{1}{m_N}\,\Big[&\vec{\nabla}^{\,2}(\psi_L\,Y_{L\,M}\,\psi_{L'}\,Y_{L'\,M'}) \\ &- \psi_L\,Y_{L\,M}\,\vec{\nabla}^{\,2}(\psi_{L'}\,Y_{L'\,M'}) - \psi_{L'}\,Y_{L'\,M'}\,\vec{\nabla}^{\,2}(\psi_L\,Y_{L\,M})\Big].\end{aligned} \tag{G.12}$$

The two spherical harmonics in the first term on the right hand side of Eq. (G.12) combine to one. Therefore we only need to evaluate the structure $\vec{\nabla}^{\,2}(f(r)\,Y_{L\,M}(\hat{r}))$. We do so by use of the gradient formula (L.43) and Eqs. (L.48, L.49).

$$\begin{aligned}\vec{\nabla}^{\,2}(f(r)\,Y_{L\,M}(\hat{r})) &= \vec{\nabla}\left\{-\sqrt{\frac{L+1}{2L+1}}\,\left(\frac{\partial}{\partial r} - \frac{L}{r}\right) f(r)\,\vec{T}_{L\,L+1\,M}(\hat{r})\right. \\ &\quad \left. + \sqrt{\frac{L}{2L+1}}\,\left(\frac{\partial}{\partial r} + \frac{L+1}{r}\right) f(r)\,\vec{T}_{L\,L-1\,M}(\hat{r})\right\} \\ &= \frac{L+1}{2L+1}\left(\frac{\partial}{\partial r} + \frac{L+2}{r}\right)\left(\frac{\partial}{\partial r} - \frac{L}{r}\right) f(r)\,Y_{L\,M}(\hat{r}) \\ &\quad + \frac{L}{2L+1}\left(\frac{\partial}{\partial r} - \frac{L-1}{r}\right)\left(\frac{\partial}{\partial r} + \frac{L+1}{r}\right) f(r)\,Y_{L\,M}(\hat{r}) \\ &= \left(\frac{\partial^2}{\partial r^2} + \frac{2}{r}\,\frac{\partial}{\partial r} - \frac{L\,(L+1)}{r^2}\right) f(r)\,Y_{L\,M}(\hat{r}) \\ &= Y_{L\,M}(\hat{r})\,\left(\frac{1}{r}\,\frac{\partial^2}{\partial r^2}\,r - \frac{L\,(L+1)}{r^2}\right) f(r)\end{aligned} \tag{G.13}$$

By the help of Eq. (L.26) we find

$$\begin{aligned}&-\frac{1}{m_N}\,\Big[[\vec{\nabla}^{\,2}, \psi_L\,Y_{L\,M}], \psi_{L'}\,Y_{L'\,M'}\Big] = -\frac{1}{m_N}\sum_J (-1)^{M+M'}\,\sqrt{\frac{(2L+1)\,(2L'+1)\,(2J+1)}{4\pi}} \\ &\times \begin{pmatrix} L & L' & J \\ 0 & 0 & 0 \end{pmatrix}\,\begin{pmatrix} L & L' & J \\ M & M' & -M-M' \end{pmatrix}\,Y_{J\,M+M'}\,\left\{\left(\frac{1}{r}\,\frac{\partial^2}{\partial r^2}\,r - \frac{J\,(J+1)}{r^2}\right)\,\psi_L\,\psi_{L'}\right. \\ &\left. - \psi_L\,\left(\frac{1}{r}\,\frac{\partial^2}{\partial r^2}\,r - \frac{L'\,(L'+1)}{r^2}\right)\,\psi_{L'} - \psi_{L'}\,\left(\frac{1}{r}\,\frac{\partial^2}{\partial r^2}\,r - \frac{L\,(L+1)}{r^2}\right)\,\psi_L\right\}.\end{aligned} \tag{G.14}$$

Including all prefactors and inserting one complete set of radial states $\mid r\,\rangle$, we get for $\mathcal{M}_{fi}^{\phi\phi 4\,\mathrm{kE}}$ (remember, the second double commutator gives exactly the same

contribution):

$$\begin{aligned}\mathcal{M}_{fi}^{\phi\phi 4\,\mathrm{kE}} = &-\sum_{L=1}^{\infty}\sum_{M=-L}^{L}\sum_{L'=1}^{\infty}\sum_{M'=-L'}^{L'}\sum_{J=|L-L'|}^{L+L'}\sum_{l,l'}\frac{\sqrt{\pi}\,e^2}{\omega^2\,m_N}\,(-1)^{L'-\lambda_f+M+M'}\,i^{L+L'}\,(2L+1)\\
&\times(2L'+1)\sqrt{\frac{2J+1}{L\,(L+1)\,L'\,(L'+1)}}\begin{pmatrix} L & L' & J\\ 0 & 0 & 0\end{pmatrix}\begin{pmatrix} L & L' & J\\ M & M' & -M-M'\end{pmatrix}\\
&\times\delta_{M,\lambda_i}\,d^{L'}_{M',-\lambda_f}(\theta)\,\langle\, l'\,1\,1\,M_f\mid Y_{J\,M+M'}\mid l\,1\,1\,M_i\,\rangle\\
&\times\int dr\,u_l(r)\,u_{l'}(r)\,\left\{\left(\frac{1}{r}\,\frac{\partial^2}{\partial r^2}\,r-\frac{J\,(J+1)}{r^2}\right)\psi_L(\frac{\omega r}{2})\,\psi_{L'}(\frac{\omega r}{2})-\psi_L(\frac{\omega r}{2})\,\left(\frac{1}{r}\,\frac{\partial^2}{\partial r^2}\,r\right.\right.\\
&\left.\left.-\,\frac{L'\,(L'+1)}{r^2}\right)\psi_{L'}(\frac{\omega r}{2})-\psi_{L'}(\frac{\omega r}{2})\,\left(\frac{1}{r}\,\frac{\partial^2}{\partial r^2}\,r-\frac{L\,(L+1)}{r^2}\right)\psi_L(\frac{\omega r}{2})\right\}.\end{aligned}\tag{G.15}$$

The derivatives can be written in a more compact form and after using the Wigner-Eckart theorem (L.31) the formal sums over $M,\ M'$ are removed to yield the result

$$\begin{aligned}\mathcal{M}_{fi}^{\phi\phi 4\,\mathrm{kE}} = &\sum_{L=1}^{\infty}\sum_{L'=1}^{\infty}\sum_{J=|L-L'|}^{L+L'}\sum_{l,l'}\frac{\sqrt{\pi}\,e^2}{\omega^2\,m_N}\,(-1)^{L'-\lambda_f-M_i}\,i^{L+L'}\,(2L+1)\,(2L'+1)\\
&\times\sqrt{\frac{2J+1}{L\,(L+1)\,L'\,(L'+1)}}\begin{pmatrix} L & L' & J\\ 0 & 0 & 0\end{pmatrix}\begin{pmatrix} L & L' & J\\ \lambda_i & M_f-M_i-\lambda_i & -M_f+M_i\end{pmatrix}\\
&\times\begin{pmatrix} 1 & J & 1\\ -M_f & M_f-M_i & M_i\end{pmatrix}\,d^{L'}_{M_f-M_i-\lambda_i,-\lambda_f}(\theta)\,\langle\, l'\,1\,1\,\|\,Y_J\,\|\,l\,1\,1\,\rangle\\
&\times\int dr\,u_l(r)\,u_{l'}(r)\,\left\{2\,\left(\frac{\partial}{\partial r}\,\psi_L(\frac{\omega r}{2})\right)\left(\frac{\partial}{\partial r}\,\psi_{L'}(\frac{\omega r}{2})\right)\right.\\
&\left.+\,\frac{L\,(L+1)+L'\,(L'+1)-J\,(J+1)}{r^2}\,\psi_L(\frac{\omega r}{2})\psi_{L'}(\frac{\omega r}{2})\right\}.\end{aligned}\tag{G.16}$$

The final task of this appendix is to calculate Eq. (6.26) with the potential energy part of H^{np} inserted into the commutators. It was shown in Ref. [79] that the correct low-energy limit is a direct consequence from demanding gauge invariance of the calculation. Therefore, in order to fulfill the low-energy theorem, it is necessary to be consistent between the explicitly included exchange particles and the potential used in the double commutator, which is the only part of the two-nucleon reducible amplitude that survives in the static limit. In fact it was proven in Ref. [88], that the pion-exchange diagrams of Fig. 5.7 cancel exactly in the static limit against the double commutator including the one-pion-exchange potential V^{OPE}. The short-distance (hard-core) part of the two-nucleon potential may be interpreted as the exchange of mesons heavier than the pion ($\rho,\ \omega, ...$), see e.g. the CD-Bonn potential [72]. As pointed out in Ref. [22], in order to achieve full consistency one would also have to allow for the explicit exchange of such particles. Nevertheless, below the pion-production threshold our approximation to only include the one-pion exchange explicitly is certainly sufficient, and, consequently, we only include V^{OPE} in the double commutator. The validity of this procedure is further confirmed in Section 6.3.2, where we demonstrate that our calculation is nearly insensitive to features of the *np*-potential which go beyond the one-pion exchange.

The only operators in this potential, which do not commute with $\phi_{i,f}(\vec{x}_p)$, are the isospin operators, because also $\phi(\vec{x}_p)$ depends on the isospin. In the AV18-

notation [73], $V^{\rm OPE}$ reads, cf. Eq. (K.9),

$$\begin{aligned} V_\pi^{AV18}(\vec{r}) &= -f^2\, v_\pi^{AV18}(m_{\pi^0}) + (-1)^{T+1}\, 2\, f^2\, v_\pi^{AV18}(m_{\pi^\pm}) \\ &\approx \left(2\,(-1)^{T+1} - 1\right)\, f^2\, v_\pi^{AV18}(m_\pi) \\ &= f^2\, v_\pi^{AV18}(m_\pi) \cdot \begin{cases} -3 & T=0 \\ 1 & T=1, \end{cases} \end{aligned} \tag{G.17}$$

where we neglect the mass difference between charged and neutral pions. The isospin dependence can be written as

$$V_\pi^{AV18}(\vec{r}) = f^2\, v_\pi^{AV18}(m_\pi)\ (\vec{\tau}_1 \cdot \vec{\tau}_2)\,, \tag{G.18}$$

because

$$\begin{aligned} \frac{1}{2}\,\langle\, p\,n - n\,p \mid (\vec{\tau}_1 \cdot \vec{\tau}_2) \mid p\,n - n\,p\,\rangle &= -3, \\ \frac{1}{2}\,\langle\, p\,n + n\,p \mid (\vec{\tau}_1 \cdot \vec{\tau}_2) \mid p\,n + n\,p\,\rangle &= 1. \end{aligned} \tag{G.19}$$

Here we used the isospin-0 (deuteron) wave function $\frac{1}{\sqrt{2}} \mid p\,n - n\,p\,\rangle$ and the isospin-1 wave function $\frac{1}{\sqrt{2}} \mid p\,n + n\,p\,\rangle$, respectively. The potential $v_\pi^{AV18}(m_\pi)$ is given as, cf. [73] and Eq. (K.10),

$$v_\pi^{AV18}(m_\pi) = \frac{1}{3}\, m_\pi\ \left[Y^{AV18}(r)\, \vec{\sigma}_1 \cdot \vec{\sigma}_2 + T^{AV18}(r)\, S_{12}\right], \tag{G.20}$$

where we set $m_{\pi^\pm} = m_{\pi^0} = m_\pi$, like in Eq. (G.17). The functions $Y^{AV18}(r)$, $T^{AV18}(r)$ are (see Eqs. (K.11, K.12))

$$\begin{aligned} Y^{AV18}(r) &= \frac{{\rm e}^{-m_\pi r}}{m_\pi r}\ \left(1 - {\rm e}^{-cr^2}\right), \\ T^{AV18}(r) &= \left(1 + \frac{3}{m_\pi r} + \frac{3}{(m_\pi r)^2}\right)\ \frac{{\rm e}^{-m_\pi r}}{m_\pi r}\ \left(1 - {\rm e}^{-cr^2}\right)^2, \end{aligned} \tag{G.21}$$

with the cutoff parameter c assigned the value $c = 2.1$ fm^{-2} in [73], and the operator S_{12} is defined via

$$S_{12} = 3\ (\vec{\sigma}_1\ \cdot \hat{r})\ (\vec{\sigma}_2\ \cdot \hat{r}) - \vec{\sigma}_1 \cdot \vec{\sigma}_2. \tag{G.22}$$

However, it is known [88, 24] that the one-pion-exchange potential[1]

$$V_\pi(\vec{r}) = f^2\, m_\pi\ (\vec{\tau}_1 \cdot \vec{\tau}_2)\ \left[S_{12}\ \left(\frac{1}{3} + \frac{1}{m_\pi r} + \frac{1}{(m_\pi r)^2}\right) \frac{{\rm e}^{-m_\pi r}}{m_\pi r} + \vec{\sigma}_1 \cdot \vec{\sigma}_2\, \frac{{\rm e}^{-m_\pi r}}{3\, m_\pi r}\right], \tag{G.23}$$

cf. e.g. [57], Section 3.2, together with the pion-exchange diagrams of Fig. 5.7 generates the correct Thomson limit, cf. Section 6.2. Therefore we remove the cutoff factors $\left(1 - {\rm e}^{-cr^2}\right)$, $\left(1 - {\rm e}^{-cr^2}\right)^2$, which are introduced in [73] in order to have a finite potential at the origin, and rather use the potential (G.23) instead of (G.18). We mark the difference between the thus defined functions and the ones used in [73] by skipping the index '$AV18$'. We are aware that this procedure is strictly speaking not consistent, as we are using $V_\pi^{AV18}(\vec{r})$ in all other parts of this work, but our aim is to achieve the exact static limit on the one hand and to use a modern *np*-potential as far as possible on the other.

[1] We omit the term proportional to $\delta(\vec{r})$, wich gives no contribution due to the vanishing deuteron wave function at the origin.

In order to evaluate the double commutators $\Big[[V_\pi,\hat\phi_i],\hat\phi_f\Big]$ and $\Big[[V_\pi,\hat\phi_f],\hat\phi_i\Big]$, we explicitly write the isospin dependence of $\hat\phi_{i,f}$ (cf. Eq. (6.9)):

$$\hat\phi_{i,f} = e\,\phi_{i,f}(\vec x_p) = \sum_{j=n,p} e_j\,\phi_{i,f}(\vec x_j) = \sum_{j=n,p} \frac{1}{2}\left(1+\tau_j^z\right)\,e\,\phi_{i,f}(\vec x_j) \tag{G.24}$$

Therefore, we have

$$\begin{aligned}\Big[[(\vec\tau_1\cdot\vec\tau_2)\,,\hat\phi_i],\hat\phi_f\Big] &= \frac{e^2}{4}\sum_{l,m=n,p}\left[[(\vec\tau_1\cdot\vec\tau_2)\,,(1+\tau_l^z)],(1+\tau_m^z)\right]\,\phi_i(\vec x_l)\,\phi_f(\vec x_m)\\ &= \frac{e^2}{4}\sum_{l,m=n,p}\left[[\tau_p^i\,\tau_n^i,\tau_l^z],\tau_m^z\right]\,\phi_i(\vec x_l)\,\phi_f(\vec x_m)\\ &= \frac{e^2}{4}\left\{\left[[\tau_p^i\,\tau_n^i,\tau_p^z],\tau_p^z\right]\,\phi_i(\vec x_p)\,\phi_f(\vec x_p)+\left[[\tau_p^i\,\tau_n^i,\tau_p^z],\tau_n^z\right]\,\phi_i(\vec x_p)\,\phi_f(\vec x_n)\right.\\ &+\left.\left[[\tau_p^i\,\tau_n^i,\tau_n^z],\tau_p^z\right]\,\phi_i(\vec x_n)\,\phi_f(\vec x_p)+\left[[\tau_p^i\,\tau_n^i,\tau_n^z],\tau_n^z\right]\,\phi_i(\vec x_n)\,\phi_f(\vec x_n)\right\}.\end{aligned} \tag{G.25}$$

Using the commutator relation $[\tau_i,\tau_j]=2\,i\,\varepsilon_{ijk}\,\tau_k$ we find

$$\begin{aligned}\Big[[(\vec\tau_1\cdot\vec\tau_2)\,,\hat\phi_i],\hat\phi_f\Big] &= e^2\left\{(\vec\tau_1\cdot\vec\tau_2-\tau_1^z\,\tau_2^z)\,\phi_i(\vec x_p)\,\phi_f(\vec x_p)-(\vec\tau_1\cdot\vec\tau_2-\tau_1^z\,\tau_2^z)\,\phi_i(\vec x_p)\,\phi_f(\vec x_n)\right.\\ &-\left.(\vec\tau_1\cdot\vec\tau_2-\tau_1^z\,\tau_2^z)\,\phi_i(\vec x_n)\,\phi_f(\vec x_p)+(\vec\tau_1\cdot\vec\tau_2-\tau_1^z\,\tau_2^z)\,\phi_i(\vec x_n)\,\phi_f(\vec x_n)\right\}.\end{aligned} \tag{G.26}$$

From this equation it is obvious that $\Big[[(\vec\tau_1\cdot\vec\tau_2)\,,\hat\phi_f],\hat\phi_i\Big] = \Big[[(\vec\tau_1\cdot\vec\tau_2)\,,\hat\phi_i],\hat\phi_f\Big]$. Evaluating the isospin operator $(\vec\tau_1\cdot\vec\tau_2-\tau_1^z\,\tau_2^z)$ between two deuteron ($T=0$) wave functions gives

$$\frac{1}{2}\langle\, p\,n-n\,p\mid\vec\tau_1\cdot\vec\tau_2-\tau_1^z\,\tau_2^z\mid p\,n-n\,p\,\rangle=-2. \tag{G.27}$$

Therefore we can rewrite the potential energy part of Eq. (6.26) as

$$\begin{aligned}\mathcal{M}_{fi}^{\phi\phi4\,\mathrm{pot}} &= \langle\, d_f\mid -2\,e^2\,f^2\,v_\pi(m_\pi)\,[\phi_i(\vec x_p)\,\phi_f(\vec x_p)-\phi_i(\vec x_p)\,\phi_f(\vec x_n)\\ &-\phi_i(\vec x_n)\,\phi_f(\vec x_p)+\phi_i(\vec x_n)\,\phi_f(\vec x_n)]\mid d_i\,\rangle.\end{aligned} \tag{G.28}$$

We replace $\vec x_p\to\frac{\vec r}{2}$, $\vec x_n\to-\frac{\vec r}{2}$ as in Eq. (6.16). Inserting one complete set of radial states and the explicit expressions for $\phi_i(\pm\vec r/2)$, $\phi_f(\pm\vec r/2)$, cf. Eq. (6.4), we find

$$\begin{aligned}\mathcal{M}_{fi}^{\phi\phi4\,\mathrm{pot}} &= \sum_{L=1}^{\infty}\sum_{M=-L}^{L}\sum_{L'=1}^{\infty}\sum_{M'=-L'}^{L'}\sum_{l,l'}\frac{4\pi\,e^2\,f^2\,m_\pi}{3\,\omega^2}\,(-1)^{1+L'-\lambda_f}\,i^{L+L'}\,\delta_{M,\lambda_i}\,d^{L'}_{M',-\lambda_f}(\theta)\\ &\times\sqrt{\frac{(2L+1)\,(2L'+1)}{L\,(L+1)\,L'\,(L'+1)}}\left\{\int dr\,u_l(r)\,u_{l'}(r)\,\psi_L(\frac{\omega r}{2})\,\psi_{L'}(\frac{\omega r}{2})\,Y(r)\right.\\ &\times\langle\, l'\,1\,1\,M_f\mid\vec\sigma_1\cdot\vec\sigma_2\,Y_{L\,M}(\hat r)\,Y_{L'\,M'}(\hat r)\mid l\,1\,1\,M_i\,\rangle\\ &+\int dr\,u_l(r)\,u_{l'}(r)\,\psi_L(\frac{\omega r}{2})\,\psi_{L'}(\frac{\omega r}{2})\,T(r)\\ &\times\left.\langle\, l'\,1\,1\,M_f\mid S_{12}\,Y_{L\,M}(\hat r)\,Y_{L'\,M'}(\hat r)\mid l\,1\,1\,M_i\,\rangle\right\}\left(1-(-1)^{L'}-(-1)^{L}+(-1)^{L+L'}\right).\end{aligned} \tag{G.29}$$

Here we used Eq. (L.27), i.e. $Y_{L\,M}(-\hat r)=(-1)^L\,Y_{L\,M}(\hat r)$. As explained before, $T(r)$, $Y(r)$ are identical to $T^{AV18}(r)$, $Y^{AV18}(r)$ with the cutoff functions removed.

We rewrite Eq. (G.29), separating the two operators $\vec{\sigma}_1 \cdot \vec{\sigma}_2$ and $(\vec{\sigma}_1 \cdot \hat{r})\ (\vec{\sigma}_2 \cdot \hat{r})$ from each other. The sum over M may already be removed.

$$\begin{aligned}
\mathcal{M}_{fi}^{\phi\phi 4\,\mathrm{pot}} = & \sum_{L=1}^{\infty}\sum_{L'=1}^{\infty}\sum_{M'=-L'}^{L'}\sum_{l,l'}\sum_{i} \frac{4\pi\, e^2\, f^2\, m_\pi}{3\,\omega^2}\,(-1)^{1+L'-\lambda_f+i}\, i^{L+L'}\, d^{L'}_{M',-\lambda_f}(\theta) \\
& \times \sqrt{\frac{(2L+1)\,(2L'+1)}{L\,(L+1)\,L'\,(L'+1)}} \Bigg\{ \int dr\, u_l(r)\, u_{l'}(r)\, \psi_L(\frac{\omega r}{2})\, \psi_{L'}(\frac{\omega r}{2})\,(Y(r)-T(r)) \\
& \times \langle\, l'\,1\,1\,M_f \mid \sigma_{2\,i}\,\sigma_{1\,-i}\, Y_{L\,\lambda_i}\, Y_{L'\,M'} \mid l\,1\,1\,M_i\,\rangle \\
& + \sum_j 3\,(-1)^j \int dr\, u_l(r)\, u_{l'}(r)\, \psi_L(\frac{\omega r}{2})\, \psi_{L'}(\frac{\omega r}{2})\, T(r) \\
& \times \langle\, l'\,1\,1\,M_f \mid \sigma_{2\,j}\,\sigma_{1\,i}\, r_{-j}\, r_{-i}\, Y_{L\,\lambda_i}\, Y_{L'\,M'} \mid l\,1\,1\,M_i\,\rangle \Bigg\} \\
& \times \left(1-(-1)^{L'}-(-1)^{L}+(-1)^{L+L'}\right) \qquad \text{(G.30)}
\end{aligned}$$

In this step we also expanded the scalar products into spherical components, according to Eq. (L.12). $\sum_i$ is a shortcut for $\sum_{i=-1,0,1}$, which we will use throughout this work. Now we replace $r_{-j},\ r_{-i}$ according to Eq. (L.13) and afterwards combine $Y_{1\,-j}\, Y_{1\,-i}$ and $Y_{L\,\lambda_i}\, Y_{L'\,M'}$ in the second matrix element, using Eq. (L.26). We get

$$\begin{aligned}
\mathcal{M}_{fi}^{\phi\phi 4\,\mathrm{pot}} = & \sum_{L=1}^{\infty}\sum_{L'=1}^{\infty}\sum_{M'=-L'}^{L'}\sum_{l,l'}\sum_{i} \frac{4\pi\, e^2\, f^2\, m_\pi}{3\,\omega^2}\,(-1)^{1+L'-\lambda_f+i}\, i^{L+L'}\, d^{L'}_{M',-\lambda_f}(\theta) \\
& \times \sqrt{\frac{(2L+1)\,(2L'+1)}{L\,(L+1)\,L'\,(L'+1)}} \Bigg\{ \int dr\, u_l(r)\, u_{l'}(r)\, \psi_L(\frac{\omega r}{2})\, \psi_{L'}(\frac{\omega r}{2})\,(Y(r)-T(r)) \\
& \times \langle\, l'\,1\,1\,M_f \mid \sigma_{2\,i}\,\sigma_{1\,-i}\, Y_{L\,\lambda_i}\, Y_{L'\,M'} \mid l\,1\,1\,M_i\,\rangle \\
& + \sum_j \sum_{J=0,2} \sum_{\tilde{J}=|L-L'|}^{L+L'} (-1)^{-i+\lambda_i+M'}\, 3\,\sqrt{(2J+1)\,(2L+1)\,(2L'+1)\,(2\tilde{J}+1)} \\
& \times \begin{pmatrix} 1 & 1 & J \\ 0 & 0 & 0 \end{pmatrix} \begin{pmatrix} 1 & 1 & J \\ -j & -i & i+j \end{pmatrix} \begin{pmatrix} L & L' & \tilde{J} \\ 0 & 0 & 0 \end{pmatrix} \begin{pmatrix} L & L' & \tilde{J} \\ \lambda_i & M' & -\lambda_i - M' \end{pmatrix} \\
& \times \int dr\, u_l(r)\, u_{l'}(r)\, \psi_L(\frac{\omega r}{2})\, \psi_{L'}(\frac{\omega r}{2})\, T(r) \qquad \text{(G.31)} \\
& \times \langle\, l'\,1\,1\,M_f \mid \sigma_{2\,j}\,\sigma_{1\,i}\, Y_{J\,-i-j}\, Y_{\tilde{J}\,\lambda_i+M'} \mid l\,1\,1\,M_i\,\rangle \Bigg\} \left(1-(-1)^{L'}-(-1)^{L}+(-1)^{L+L'}\right),
\end{aligned}$$

where the possible values for $J,\ \tilde{J}$ are given by the 3-j symbols, cf. Eqs. (L.15) and (L.21). Therefore we need to evaluate the matrix-element structure $\langle\, l'\,1\,1\,M_f \mid \sigma_{2\,j}\,\sigma_{1\,i}\, Y_{L\,M}\, Y_{L'\,M'} \mid l\,1\,1\,M_i\,\rangle$. However, as we will be faced with further combinations of spin and orbital angular momenta in the initial and final state in App. I, we derive the element $\langle\, L_1\, S_1\, J_1\, M_1 \mid \sigma_{2\,j}\,\sigma_{1\,i}\, Y_{l\,m}\, Y_{l'\,m'} \mid L_2\, S_2\, J_2\, M_2\,\rangle$.

First we write $\sigma_{2\,j}\,\sigma_{1\,i}$ as sum over tensor products, using Eq. (L.33) and the fact that the vector operator $\vec{\sigma}$ is of rank 1.

$$\begin{aligned}
\sigma_{2\,j}\,\sigma_{1\,i} &= \sum_{S'=0}^{2}\sum_{M'=-S'}^{S'} (-1)^{M'}\,\sqrt{2S'+1}\, \begin{pmatrix} 1 & 1 & S' \\ j & i & -M' \end{pmatrix} (\sigma_2 \otimes \sigma_1)_{S'\,M'} \\
&= \sum_{S'=0}^{2} (-i)^{i+j}\,\sqrt{2S'+1}\, \begin{pmatrix} 1 & 1 & S' \\ j & i & -i-j \end{pmatrix} (\sigma_2 \otimes \sigma_1)_{S'\,i+j} \qquad \text{(G.32)}
\end{aligned}$$

Combining the two spherical harmonics via Eq. (L.26) and making use of Eq. (L.33) once more we find

$$\sigma_{2\,j}\,\sigma_{1\,i}\,Y_{l\,m}\,Y_{l'\,m'} = \sum_{S'=0}^{2}\sum_{L''=|l-l'|}^{l+l'}\sum_{\tilde{J}=|L''-S'|}^{L''+S'}(-1)^{S'-L''}\begin{pmatrix} l & l' & L'' \\ 0 & 0 & 0 \end{pmatrix} \tag{G.33}$$
$$\times\begin{pmatrix} l & l' & L'' \\ m & m' & -m-m' \end{pmatrix}\begin{pmatrix} 1 & 1 & S' \\ j & i & -i-j \end{pmatrix}\begin{pmatrix} S' & L'' & \tilde{J} \\ i+j & m+m' & -i-j-m-m' \end{pmatrix}$$
$$\times\sqrt{\frac{(2l+1)\,(2l'+1)\,(2L''+1)\,(2S'+1)\,(2\tilde{J}+1)}{4\pi}}\;[(\sigma_2\otimes\sigma_1)_{S'}\otimes Y_{L''}]_{\tilde{J}\,i+j+m+m'}\,.$$

Now we use the Wigner-Eckart theorem.

$$\langle\, L_1\,S_1\,J_1\,M_1 \mid \sigma_{2\,j}\,\sigma_{1\,i}\,Y_{l\,m}\,Y_{l'\,m'} \mid L_2\,S_2\,J_2\,M_2\,\rangle$$
$$=\sum_{S'}\sum_{L''}\sum_{\tilde{J}}(-1)^{S'-L''+J_1-M_1}\begin{pmatrix} l & l' & L'' \\ 0 & 0 & 0 \end{pmatrix}\begin{pmatrix} l & l' & L'' \\ m & m' & -m-m' \end{pmatrix}$$
$$\times\begin{pmatrix} 1 & 1 & S' \\ j & i & -i-j \end{pmatrix}\begin{pmatrix} S' & L'' & \tilde{J} \\ i+j & m+m' & -i-j-m-m' \end{pmatrix}$$
$$\times\begin{pmatrix} J_1 & \tilde{J} & J_2 \\ -M_1 & i+j+m+m' & M_2 \end{pmatrix}\sqrt{\frac{(2l+1)\,(2l'+1)\,(2L''+1)\,(2S'+1)\,(2\tilde{J}+1)}{4\pi}}$$
$$\times\,\langle\, L_1\,S_1\,J_1 \,\|\, [(\sigma_2\otimes\sigma_1)_{S'}\otimes Y_{L''}]_{\tilde{J}} \,\|\, L_2\,S_2\,J_2\,\rangle \tag{G.34}$$

We separate this matrix element into spin and orbital angular momentum parts, according to Eqs. (L.40) and (L.41).

$$\langle\, L_1\,S_1\,J_1\,M_1 \mid \sigma_{2\,j}\,\sigma_{1\,i}\,Y_{l\,m}\,Y_{l'\,m'} \mid L_2\,S_2\,J_2\,M_2\,\rangle$$
$$=\sum_{S'}\sum_{L''}\sum_{\tilde{J}}(-1)^{S'-L''+J_1-M_1}\sqrt{\frac{(2l+1)\,(2l'+1)\,(2L''+1)\,(2S'+1)\,(2J_1+1)\,(2J_2+1)}{4\pi}}$$
$$\times\,(2\tilde{J}+1)\begin{pmatrix} l & l' & L'' \\ 0 & 0 & 0 \end{pmatrix}\begin{pmatrix} l & l' & L'' \\ m & m' & -m-m' \end{pmatrix}\begin{pmatrix} 1 & 1 & S' \\ j & i & -i-j \end{pmatrix}$$
$$\times\begin{pmatrix} S' & L'' & \tilde{J} \\ i+j & m+m' & -i-j-m-m' \end{pmatrix}\begin{pmatrix} J_1 & \tilde{J} & J_2 \\ -M_1 & i+j+m+m' & M_2 \end{pmatrix}$$
$$\times\begin{Bmatrix} S_1 & L_1 & J_1 \\ S_2 & L_2 & J_2 \\ S' & L'' & \tilde{J} \end{Bmatrix}\langle\, S_1 \,\|\, (\sigma_2\otimes\sigma_1)_{S'} \,\|\, S_2\,\rangle\,\langle\, L_1 \,\|\, Y_{L''} \,\|\, L_2\,\rangle$$
$$=\sum_{S'}\sum_{L''}\sum_{\tilde{J}}(-1)^{-L''+J_1-M_1+S_1+S_2}\,(2\tilde{J}+1)\,(2S'+1)\begin{pmatrix} J_1 & \tilde{J} & J_2 \\ -M_1 & i+j+m+m' & M_2 \end{pmatrix}$$
$$\times\begin{pmatrix} 1 & 1 & S' \\ j & i & -i-j \end{pmatrix}\begin{pmatrix} l & l' & L'' \\ m & m' & -m-m' \end{pmatrix}\begin{pmatrix} S' & L'' & \tilde{J} \\ i+j & m+m' & -i-j-m-m' \end{pmatrix}$$
$$\times\begin{pmatrix} l & l' & L'' \\ 0 & 0 & 0 \end{pmatrix}\begin{Bmatrix} S_1 & L_1 & J_1 \\ S_2 & L_2 & J_2 \\ S' & L'' & \tilde{J} \end{Bmatrix}\sqrt{\frac{(2l+1)\,(2l'+1)\,(2L''+1)\,(2J_1+1)\,(2J_2+1)}{4\pi}}$$
$$\times\,\langle\, L_1 \,\|\, Y_{L''} \,\|\, L_2\,\rangle\sum_{s}\begin{Bmatrix} 1 & 1 & S' \\ S_2 & S_1 & s \end{Bmatrix}\langle\, S_1 \,\|\, S-t \,\|\, s\,\rangle\,\langle\, s \,\|\, S+t \,\|\, S_2\,\rangle \tag{G.35}$$

In the last line we defined $\vec{S}=\frac{\vec{\sigma}_1+\vec{\sigma}_2}{2}$ and $\vec{t}=\frac{\vec{\sigma}_1-\vec{\sigma}_2}{2}$ in analogy to Eq. (6.65). The reduced matrix elements for S and t are given in App. L, Eqs. (L.35, L.36), and we

find S spin-conserving, t spin-changing, which we also see in Eqs. (L.38, L.39). For evaluating Eq. (G.31) we need a spin-conserving operator; thus only two of the four combinations $\langle S_1 \| S-t \| s \rangle \langle s \| S+t \| S_2 \rangle$ survive:

$$\langle S_1 \| S-t \| s \rangle \langle s \| S+t \| S_2 \rangle \to \langle S_1 \| S \| s \rangle \langle s \| S \| S_2 \rangle - \langle S_1 \| t \| s \rangle \langle s \| t \| S_2 \rangle \tag{G.36}$$

These products of matrix elements can be evaluated according to Eqs. (L.35,L.36), however we rather keep the compact notation of Eq. (G.31) for the final result. Nevertheless, in order to simplify the last bracket in Eq. (G.31), we show that $L+L'$ has to be an even number. First we note that J is even in Eq. (G.31). The index L'', which is summed over in Eq. (G.35), has to be even due to $\langle l' \| Y_{L''} \| l \rangle$ with even l, l', cf. Eqs. (L.34) and (L.21). Therefore also $J+\tilde{J}$ is an even number, which follows from Eq. (G.35). With J even also $\tilde{J}$ has to be even and the 3-j symbol $\begin{pmatrix} L & L' & \tilde{J} \\ 0 & 0 & 0 \end{pmatrix}$ guarantees $L+L'$ even. This is also true for the first matrix element in Eq. (G.31), as again the index L'' in Eq. (G.35) is even and therefore $L+L'$ has to be even, i.e. $(-1)^{L+L'}=1$ and $(-1)^{L'}=(-1)^{L}$. Finally we read $M'=M_f-M_i-\lambda_i$ off Eq. (G.35), which enables us to remove the sum over M' and write down the final result:

$$\begin{aligned}
\mathcal{M}_{fi}^{\phi\phi 4\,\mathrm{pot}} = & \sum_{L=1}^{\infty}\sum_{L'=1}^{\infty}\sum_{l,l'}\sum_{i} \frac{4\pi\, e^2\, f^2\, m_\pi}{3\,\omega^2}\,(-1)^{1+L'-\lambda_f+i}\, i^{L+L'}\, d^{L'}_{M_f-M_i-\lambda_i,-\lambda_f}(\theta) \\
& \times \sqrt{\frac{(2L+1)\,(2L'+1)}{L\,(L+1)\,L'\,(L'+1)}} \Bigg\{ \int dr\, u_l(r)\, u_{l'}(r)\, \psi_L(\tfrac{\omega r}{2})\, \psi_{L'}(\tfrac{\omega r}{2})\,(Y(r)-T(r)) \\
& \times \langle\, l'\,1\,1\,M_f \mid \sigma_{2\,i}\,\sigma_{1\,-i}\, Y_{L\,\lambda_i}\, Y_{L'\,M_f-M_i-\lambda_i} \mid l\,1\,1\,M_i \,\rangle \\
& + \sum_{j}\sum_{J=0,2}\sum_{\tilde{J}=|L-L'|}^{L+L'} (-1)^{-i+M_f-M_i}\, 3\sqrt{(2J+1)\,(2L+1)\,(2L'+1)\,(2\tilde{J}+1)} \\
& \times \begin{pmatrix} 1 & 1 & J \\ 0 & 0 & 0 \end{pmatrix} \begin{pmatrix} 1 & 1 & J \\ -j & -i & i+j \end{pmatrix} \begin{pmatrix} L & L' & \tilde{J} \\ 0 & 0 & 0 \end{pmatrix} \\
& \times \begin{pmatrix} L & L' & \tilde{J} \\ \lambda_i & M_f-M_i-\lambda_i & -M_f+M_i \end{pmatrix} \int dr\, u_l(r)\, u_{l'}(r)\, \psi_L(\tfrac{\omega r}{2})\, \psi_{L'}(\tfrac{\omega r}{2})\, T(r) \\
& \times \langle\, l'\,1\,1\,M_f \mid \sigma_{2\,j}\,\sigma_{1\,i}\, Y_{J\,-i-j}\, Y_{\tilde{J}\,M_f-M_i} \mid l\,1\,1\,M_i \,\rangle \Bigg\}\, 2\left(1-(-1)^L\right)
\end{aligned} \tag{G.37}$$

We never show results beyond $L, L'=2$, which we found to be a sufficiently good approximation in all amplitudes. Therefore we may restrict ourselves to $L=L'=1$, as the $L=2$-contribution vanishes and our result demands $L+L'$ even, i.e. $L=1,\ L'=2$ is forbidden.

Now all amplitudes with the photon field replaced by $\vec{\nabla}\phi$ at both vertices have been evaluated. In the next appendix we calculate the amplitudes where this replacement is made only once. We also give the results for the non-negligible contributions obtained from $\vec{A}\to\vec{A}^{(1)}$, $\vec{A}^{(2)}$ at both vertices.

Appendix H

Calculation of further Terms with NN-Rescattering

This appendix contains the evaluation of the amplitudes given in Eq. (6.56), with $\vec{J}(\vec{\xi})$ replaced by $\vec{J}^{(\sigma)}(\vec{\xi})$, cf. Eq. (6.59). We also calculated the amplitudes including $\vec{J}^{(p)}(\vec{\xi})$ (Eq. (6.60)), but found these contributions invisibly small. Therefore we abstain from writing down those results. The amplitudes (6.56) were derived by replacing $\vec{A} \to \vec{\nabla}\phi$ at one interaction vertex, but there are also non-negligible contributions which do not include the $\vec{\nabla}\phi$-term. These are calculated at the end of this appendix. All following amplitudes can also be found in Ref. [24], albeit in the lab frame.

Before we turn to evaluating Eq. (6.56), we prove the relation $\vec{T}_{J\,L\,M}(\hat{r}) \cdot \vec{V} = [Y_L \otimes V]_{J\,M}$, cf. Eq. (6.66), making use of Eqs. (L.32) and (L.42). First we decompose the scalar product into spherical components, cf. Eq. (L.12):

$$\vec{T}_{J\,L\,M} \cdot \vec{V} = \sum_{\nu=-1,0,1} (-1)^{\nu}\, T_{J\,L\,M\;\nu}\, V_{1\,-\nu} \tag{H.1}$$

Now we replace $T_{J\,L\,M\;\nu}$ according to Eqs. (L.11) and (L.42) by

$$T_{J\,L\,M\;\nu} = \vec{T}_{J\,L\,M} \cdot \hat{r}_\nu = (-1)^{\nu}\,(-1)^{-L-M+1}\,\sqrt{2J+1}\begin{pmatrix} L & 1 & J \\ M+\nu & -\nu & -M \end{pmatrix} Y_{L\,M+\nu}. \tag{H.2}$$

Therefore,

$$\begin{aligned} \vec{T}_{J\,L\,M} \cdot \vec{V} &= \sum_{\nu=-1,0,1} (-1)^{-L-M+1}\,\sqrt{2J+1}\begin{pmatrix} L & 1 & J \\ M+\nu & -\nu & -M \end{pmatrix} Y_{L\,M+\nu}\, V_{1\,-\nu} \\ &= \sum_{\nu=-1,0,1} (-1)^{-L-M+1}\,\sqrt{2J+1}\begin{pmatrix} L & 1 & J \\ M-\nu & \nu & -M \end{pmatrix} Y_{L\,M-\nu}\, V_{1\,\nu}, \end{aligned} \tag{H.3}$$

where we replaced $\nu \to -\nu$ which does not change the sum over ν. On the other hand, Eq. (L.32) gives

$$\begin{aligned} [Y_L \otimes V]_{J\,M} &= \sum_{\mu,\nu} (-1)^{-L+1-M}\,\sqrt{2J+1}\begin{pmatrix} L & 1 & J \\ \mu & \nu & -M \end{pmatrix} Y_{L\,\mu}\, V_{1\,\nu} \\ &= \sum_{\nu} (-1)^{-L+1-M}\,\sqrt{2J+1}\begin{pmatrix} L & 1 & J \\ M-\nu & \nu & -M \end{pmatrix} Y_{L\,M-\nu}\, V_{1\,\nu}, \end{aligned} \tag{H.4}$$

which is identical to Eq. (H.3).

Eq. (6.56) consists of eight amplitudes, however we found that four of them cancel exactly. Only the amplitudes including an energy denominator remain. These are

$$\begin{aligned}
\mathcal{M}_{fi}^{\phi\,\sigma\,a} &= -i\,\left(\omega+\frac{\omega^2}{2m_d}\right)\sum_C \frac{\langle\, d_f \mid \hat{\phi}_f \mid C\,\rangle\langle\, C \mid \int \vec{J}^{(\sigma)}(\vec{\xi})\cdot\vec{A}(\vec{\xi})\,d^3\xi \mid d_i\,\rangle}{\omega+\frac{\omega^2}{2m_d}-B-E_C},\\
\mathcal{M}_{fi}^{\phi\,\sigma\,b} &= i\,\left(\omega+\frac{\omega^2}{2m_d}\right)\sum_C \frac{\langle\, d_f \mid \int \vec{J}^{(\sigma)}(\vec{\xi})\cdot\vec{A}(\vec{\xi})\,d^3\xi \mid C\,\rangle\langle\, C \mid \hat{\phi}_i \mid d_i\,\rangle}{\omega+\frac{\omega^2}{2m_d}-B-E_C},\\
\mathcal{M}_{fi}^{\phi\,\sigma\,c} &= i\,\left(\omega-\frac{\omega^2}{2m_d}+\frac{\vec{P}_C^{\,2}}{2m_C}\right)\sum_C \frac{\langle\, d_f \mid \hat{\phi}_i \mid C\,\rangle\langle\, C \mid \int \vec{J}^{(\sigma)}(\vec{\xi})\cdot\vec{A}(\vec{\xi})\,d^3\xi \mid d_i\,\rangle}{-\omega+\frac{\omega^2}{2m_d}-\frac{\vec{P}_C^{\,2}}{2m_C}-B-E_C},\\
\mathcal{M}_{fi}^{\phi\,\sigma\,d} &= -i\,\left(\omega-\frac{\omega^2}{2m_d}+\frac{\vec{P}_C^{\,2}}{2m_C}\right)\sum_C \frac{\langle\, d_f \mid \int \vec{J}^{(\sigma)}(\vec{\xi})\cdot\vec{A}(\vec{\xi})\,d^3\xi \mid C\,\rangle\langle\, C \mid \hat{\phi}_f \mid d_i\,\rangle}{-\omega+\frac{\omega^2}{2m_d}-\frac{\vec{P}_C^{\,2}}{2m_C}-B-E_C}.
\end{aligned} \tag{H.5}$$

The photon field $\vec{A}(\vec{\xi})$ is replaced either by $\vec{A}^{(1)}(\vec{\xi})$ or $\vec{A}^{(2)}(\vec{\xi})$ (Eqs. (6.57, 6.58)). We start with $\vec{A}^{(1)}(\vec{\xi})$ and use the expression derived for $\int \vec{J}^{(\sigma)}(\vec{\xi})\cdot\vec{A}^{(1)}(\vec{\xi})\,d^3\xi$ in Eq. (6.67). The corresponding amplitudes are denoted by $\mathcal{M}_{fi}^{\phi\,\sigma 1}$, whereas we use the notation $\mathcal{M}_{fi}^{\phi\,\sigma 2}$ when we replace $\vec{A}(\vec{\xi})\to\vec{A}^{(2)}(\vec{\xi})$ later on.

In order to calculate $\mathcal{M}_{fi}^{\phi\,\sigma 1}$, we insert two complete sets of radial states $\mid r\,\rangle$, $\mid r'\,\rangle$, as we did in Eq. (G.1). From the explicit expressions for $\hat{\phi}_f$ and $\int \vec{J}^{(\sigma)}(\vec{\xi})\cdot\vec{A}^{(1)}(\vec{\xi})\,d^3\xi$, Eqs. (6.4) and (6.67), we get

$$\begin{aligned}
\mathcal{M}_{fi}^{\phi\,\sigma 1\,a} = -i\,&\left(\omega+\frac{\omega^2}{2m_d}\right)\sum_{\hat{C}}\iint r^2dr\,r'^2dr'\,\langle\, d_f \mid e\sum_{L'=1}^{\infty}\sum_{M'=-L'}^{L'}(-1)^{L'-\lambda_f}\\
&\times d^{L'}_{M',-\lambda_f}(\theta)\,\frac{i^{L'+1}}{\omega}\sqrt{\frac{2\pi\,(2L'+1)}{L'\,(L'+1)}}\,\psi_{L'}(\frac{\omega r'}{2})\,Y_{L'\,M'}\mid \hat{C}\,r'\,\rangle\\
&\times\langle\, r' \mid \frac{1}{E_0-H^{np}_{\hat{C}}}\mid r\,\rangle\,\langle\, r\,\hat{C}\mid -\sum_{L=1}^{\infty}\sum_{M=-L}^{L}\lambda_i\,\sqrt{2\pi\,(L+1)}\,\frac{e\,\omega}{2\,m_N}\,i^{L+1}\\
&\times j_{L-1}(\frac{\omega r}{2})\,\left(\mu_p-(-1)^L\,\mu_n\right)\,[Y_{L-1}\otimes S]_{L\,M}\,\delta_{M,\lambda_i}\mid d_i\,\rangle.
\end{aligned} \tag{H.6}$$

The term proportional to $[Y_{L-1}\otimes t]_{L\,M}$ in Eq. (6.67) changes the spin of the two-nucleon state, cf. Eq. (L.39). Therefore it gives no contribution as $Y_{L'\,M'}$ demands $S_C=S_d=1$, as can be seen from Eq. (L.37), and has been dropped.

We rewrite Eq. (H.6) as

$$\begin{aligned}
\mathcal{M}_{fi}^{\phi\,\sigma 1\,a} = &\sum_{L=1}^{\infty}\sum_{L'=1}^{\infty}\sum_{M'=-L'}^{L'}\sum_{L_C,J_C,M_C}\sum_{l,l'}\frac{\pi\,e^2\,\lambda_i}{m_N}\,\left(\omega+\frac{\omega^2}{2m_d}\right)\,(-1)^{L'-\lambda_f+1}\\
&\times i^{L+L'+1}\,d^{L'}_{M',-\lambda_f}(\theta)\,\sqrt{\frac{(L+1)\,(2L'+1)}{L'\,(L'+1)}}\,\left(\mu_p-(-1)^L\,\mu_n\right)\\
&\times\iint r dr\,r'dr'\,u_l(r)\,j_{L-1}(\frac{\omega r}{2})\,G_{\hat{C}}(r,r';E_0)\,\psi_{L'}(\frac{\omega r'}{2})\,u_{l'}(r')\\
&\times\langle\, l'\,1\,1\,M_f \mid Y_{L'\,M'}\mid L_C\,1\,J_C\,M_C\,\rangle\,\langle\, L_C\,1\,J_C\,M_C\mid [Y_{L-1}\otimes S]_{L\,M}\mid l\,1\,1\,M_i\,\rangle.
\end{aligned} \tag{H.7}$$

Applying the Wigner-Eckart theorem (L.31) twice and removing the formal sums over M' and M_C, we get the final result

$$\begin{aligned}
\mathcal{M}_{fi}^{\phi\,\sigma 1\,a} = & \sum_{L=1}^{\infty}\sum_{L'=1}^{\infty}\sum_{J_C=|L-1|}^{L+1}\sum_{L_C=|J_C-1|}^{J_C+1}\sum_{l,l'}\frac{\pi\,e^2\,\lambda_i}{m_N}\left(\omega+\frac{\omega^2}{2m_d}\right)(-1)^{L'-\lambda_f-\lambda_i-M_f-M_i+J_C} \\
& \times i^{L+L'+1}\,d^{L'}_{M_f-M_i-\lambda_i,-\lambda_f}(\theta)\sqrt{\frac{(L+1)\,(2L'+1)}{L'\,(L'+1)}}\,\left(\mu_p-(-1)^L\,\mu_n\right) \\
& \times \iint r dr\,r' dr'\,u_l(r)\,j_{L-1}(\frac{\omega r}{2})\,G_{\hat{C}}(r,r';E_0)\,\psi_{L'}(\frac{\omega r'}{2})\,u_{l'}(r') \\
& \times \begin{pmatrix} 1 & L' & J_C \\ -M_f & M_f-M_i-\lambda_i & M_i+\lambda_i \end{pmatrix}\begin{pmatrix} J_C & L & 1 \\ -M_i-\lambda_i & \lambda_i & M_i \end{pmatrix} \\
& \times \langle\, l'\,1\,1 \,\|\, Y_{L'} \,\|\, L_C\,1\,J_C\,\rangle\,\langle\, L_C\,1\,J_C \,\|\, [Y_{L-1}\otimes S]_L \,\|\, l\,1\,1\,\rangle. \qquad \text{(H.8)}
\end{aligned}$$

The values possible for J_C are determined by the second (or, as well, first) 3-j symbol, and L_C takes on the values $|J_C-S_C|,\cdots,J_C+S_C$. The reduced matrix elements can be found in Eqs. (L.37, L.38).

$\mathcal{M}_{fi}^{\phi\,\sigma 1\,b,c,d}$ are calculated quite similarly. Therefore we only give the results.

$$\begin{aligned}
\mathcal{M}_{fi}^{\phi\,\sigma 1\,b} = & \sum_{L=1}^{\infty}\sum_{L'=1}^{\infty}\sum_{J_C=|L-1|}^{L+1}\sum_{L_C=|J_C-1|}^{J_C+1}\sum_{l,l'}\frac{\pi\,e^2\,\lambda_f}{m_N}\left(\omega+\frac{\omega^2}{2m_d}\right)(-1)^{L'-\lambda_f-\lambda_i-M_f-M_i+J_C+1} \\
& \times i^{L+L'+1}\,d^{L'}_{M_f-M_i-\lambda_i,-\lambda_f}(\theta)\sqrt{\frac{(2L+1)\,(L'+1)}{L\,(L+1)}}\,\left(\mu_p-(-1)^{L'}\,\mu_n\right) \\
& \times \iint r dr\,r' dr'\,u_l(r)\,\psi_L(\frac{\omega r}{2})\,G_{\hat{C}}(r,r';E_0)\,j_{L'-1}(\frac{\omega r'}{2})\,u_{l'}(r') \\
& \times \begin{pmatrix} 1 & L' & J_C \\ -M_f & M_f-M_i-\lambda_i & M_i+\lambda_i \end{pmatrix}\begin{pmatrix} J_C & L & 1 \\ -M_i-\lambda_i & \lambda_i & M_i \end{pmatrix} \\
& \times \langle\, l'\,1\,1 \,\|\, [Y_{L'-1}\otimes S]_{L'} \,\|\, L_C\,1\,J_C\,\rangle\,\langle\, L_C\,1\,J_C \,\|\, Y_L \,\|\, l\,1\,1\,\rangle \qquad \text{(H.9)}
\end{aligned}$$

$$\begin{aligned}
\mathcal{M}_{fi}^{\phi\,\sigma 1\,c} = & \sum_{L=1}^{\infty}\sum_{L'=1}^{\infty}\sum_{J_C=|L-1|}^{L+1}\sum_{L_C=|J_C-1|}^{J_C+1}\sum_{l,l'}\frac{\pi\,e^2\,\lambda_f}{m_N}\left(\omega-\frac{\omega^2}{2m_d}+\frac{\vec{P}_C^{\,2}}{2m_C}\right)(-1)^{L'-\lambda_f-\lambda_i+J_C+1} \\
& \times i^{L+L'+1}\,d^{L'}_{M_f-M_i-\lambda_i,-\lambda_f}(\theta)\sqrt{\frac{(2L+1)\,(L'+1)}{L\,(L+1)}}\,\left(\mu_p-(-1)^{L'}\,\mu_n\right) \\
& \times \iint r dr\,r' dr'\,u_{l'}(r)\,\psi_L(\frac{\omega r}{2})\,G_{\hat{C}}(r,r';E_0')\,j_{L'-1}(\frac{\omega r'}{2})\,u_l(r') \\
& \times \begin{pmatrix} 1 & L & J_C \\ -M_f & \lambda_i & M_f-\lambda_i \end{pmatrix}\begin{pmatrix} J_C & L' & 1 \\ -M_f+\lambda_i & M_f-M_i-\lambda_i & M_i \end{pmatrix} \\
& \times \langle\, l'\,1\,1 \,\|\, Y_L \,\|\, L_C\,1\,J_C\,\rangle\,\langle\, L_C\,1\,J_C \,\|\, [Y_{L'-1}\otimes S]_{L'} \,\|\, l\,1\,1\,\rangle \qquad \text{(H.10)}
\end{aligned}$$

$$\mathcal{M}_{fi}^{\phi\,\sigma 1\,d} = \sum_{L=1}^{\infty}\sum_{L'=1}^{\infty}\sum_{J_C=|L-1|}^{L+1}\sum_{L_C=|J_C-1|}^{J_C+1}\sum_{l,l'} \frac{\pi\, e^2\,\lambda_i}{m_N}\left(\omega - \frac{\omega^2}{2m_d} + \frac{\vec{P}_C^{\,2}}{2m_C}\right)(-1)^{L'-\lambda_f-\lambda_i+J_C}$$
$$\times\, i^{L+L'+1}\, d^{L'}_{M_f-M_i-\lambda_i,-\lambda_f}(\theta)\sqrt{\frac{(L+1)\,(2L'+1)}{L'\,(L'+1)}}\,\left(\mu_p - (-1)^L\,\mu_n\right)$$
$$\times \iint r dr\, r' dr'\, u_{l'}(r)\, j_{L-1}(\frac{\omega r}{2})\, G_{\hat{C}}(r,r';E_0')\, \psi_{L'}(\frac{\omega r'}{2})\, u_l(r')$$
$$\times \begin{pmatrix} 1 & L & J_C \\ -M_f & \lambda_i & M_f-\lambda_i \end{pmatrix}\begin{pmatrix} J_C & L' & 1 \\ -M_f+\lambda_i & M_f-M_i-\lambda_i & M_i \end{pmatrix}$$
$$\times \langle\, l'\,1\,1 \,\|\, [Y_{L-1}\otimes S]_L \,\|\, L_C\,1\,J_C\,\rangle\,\langle\, L_C\,1\,J_C \,\|\, Y_{L'}\,\|\, l\,1\,1\,\rangle \qquad \text{(H.11)}$$

Now we calculate the amplitudes $\mathcal{M}_{fi}^{\phi\,\sigma 2}$ which we get from replacing $\vec{A}(\vec{\xi})$ by $\vec{A}^{(2)}(\vec{\xi})$ in Eq. (H.5). As there are no further difficulties in the calculation, once we have the formulae for $\hat{\phi}_{i,f}$ (Eq. (6.4)) and for $\int \vec{J}^{(\sigma)}(\vec{\xi})\cdot\vec{A}^{(2)}(\vec{\xi})\,d^3\xi$ (Eq. (6.72)) at hand, we can immediately write down the results.

$$\mathcal{M}_{fi}^{\phi\,\sigma 2\,a} = \sum_{L=1}^{\infty}\sum_{L'=1}^{\infty}\sum_{J_C=|L-1|}^{L+1}\sum_{L_C=|J_C-1|}^{J_C+1}\sum_{l,l'} \frac{\pi\, e^2}{m_N}\left(\omega + \frac{\omega^2}{2m_d}\right)(-1)^{L'-\lambda_f-\lambda_i-M_f-M_i+J_C}$$
$$\times\, i^{L+L'}\, d^{L'}_{M_f-M_i-\lambda_i,-\lambda_f}(\theta)\sqrt{\frac{(2L+1)\,(2L'+1)}{L'\,(L'+1)}}\,\left(\mu_p + (-1)^L\,\mu_n\right)$$
$$\times \iint r dr\, r' dr'\, u_l(r)\, j_L(\frac{\omega r}{2})\, G_{\hat{C}}(r,r';E_0)\, \psi_{L'}(\frac{\omega r'}{2})\, u_{l'}(r')$$
$$\times \begin{pmatrix} 1 & L' & J_C \\ -M_f & M_f-M_i-\lambda_i & M_i+\lambda_i \end{pmatrix}\begin{pmatrix} J_C & L & 1 \\ -M_i-\lambda_i & \lambda_i & M_i \end{pmatrix}$$
$$\times \langle\, l'\,1\,1 \,\|\, Y_{L'}\,\|\, L_C\,1\,J_C\,\rangle\,\langle\, L_C\,1\,J_C \,\|\, [Y_L\otimes S]_L\,\|\, l\,1\,1\,\rangle \qquad \text{(H.12)}$$

$$\mathcal{M}_{fi}^{\phi\,\sigma 2\,b} = \sum_{L=1}^{\infty}\sum_{L'=1}^{\infty}\sum_{J_C=|L-1|}^{L+1}\sum_{L_C=|J_C-1|}^{J_C+1}\sum_{l,l'} \frac{\pi\, e^2}{m_N}\left(\omega + \frac{\omega^2}{2m_d}\right)(-1)^{L'-\lambda_f-\lambda_i-M_f-M_i+J_C+1}$$
$$\times\, i^{L+L'}\, d^{L'}_{M_f-M_i-\lambda_i,-\lambda_f}(\theta)\sqrt{\frac{(2L+1)\,(2L'+1)}{L\,(L+1)}}\,\left(\mu_p + (-1)^{L'}\,\mu_n\right)$$
$$\times \iint r dr\, r' dr'\, u_l(r)\, \psi_L(\frac{\omega r}{2})\, G_{\hat{C}}(r,r';E_0)\, j_{L'}(\frac{\omega r'}{2})\, u_{l'}(r')$$
$$\times \begin{pmatrix} 1 & L' & J_C \\ -M_f & M_f-M_i-\lambda_i & M_i+\lambda_i \end{pmatrix}\begin{pmatrix} J_C & L & 1 \\ -M_i-\lambda_i & \lambda_i & M_i \end{pmatrix}$$
$$\times \langle\, l'\,1\,1 \,\|\, [Y_{L'}\otimes S]_{L'}\,\|\, L_C\,1\,J_C\,\rangle\,\langle\, L_C\,1\,J_C \,\|\, Y_L\,\|\, l\,1\,1\,\rangle \qquad \text{(H.13)}$$

$$\mathcal{M}_{fi}^{\phi\,\sigma 2\,c} = \sum_{L=1}^{\infty}\sum_{L'=1}^{\infty}\sum_{J_C=|L-1|}^{L+1}\sum_{L_C=|J_C-1|}^{J_C+1}\sum_{l,l'} \frac{\pi\, e^2}{m_N}\left(\omega - \frac{\omega^2}{2m_d} + \frac{\vec{P}_C^{\,2}}{2m_C}\right)(-1)^{L'-\lambda_f-\lambda_i+J_C+1}$$
$$\times\, i^{L+L'}\, d^{L'}_{M_f-M_i-\lambda_i,-\lambda_f}(\theta)\sqrt{\frac{(2L+1)\,(2L'+1)}{L\,(L+1)}}\,\left(\mu_p + (-1)^{L'}\,\mu_n\right)$$
$$\times \iint r dr\, r' dr'\, u_{l'}(r)\, \psi_L(\frac{\omega r}{2})\, G_{\hat{C}}(r,r';E_0')\, j_{L'}(\frac{\omega r'}{2})\, u_l(r')$$
$$\times \begin{pmatrix} 1 & L & J_C \\ -M_f & \lambda_i & M_f-\lambda_i \end{pmatrix}\begin{pmatrix} J_C & L' & 1 \\ -M_f+\lambda_i & M_f-M_i-\lambda_i & M_i \end{pmatrix}$$
$$\times \langle\, l'\,1\,1 \,\|\, Y_L\,\|\, L_C\,1\,J_C\,\rangle\,\langle\, L_C\,1\,J_C \,\|\, [Y_{L'}\otimes S]_{L'}\,\|\, l\,1\,1\,\rangle \qquad \text{(H.14)}$$

$$\mathcal{M}_{fi}^{\phi\,\sigma 2\,d} = \sum_{L=1}^{\infty}\sum_{L'=1}^{\infty}\sum_{J_C=|L-1|}^{L+1}\sum_{L_C=|J_C-1|}^{J_C+1}\sum_{l,l'}\frac{\pi\,e^2}{m_N}\left(\omega-\frac{\omega^2}{2m_d}+\frac{\vec{P}_C^{\,2}}{2m_C}\right)(-1)^{L'-\lambda_f-\lambda_i+J_C}$$
$$\times\, i^{L+L'}\,d^{L'}_{M_f-M_i-\lambda_i,-\lambda_f}(\theta)\sqrt{\frac{(2L+1)\,(2L'+1)}{L'\,(L'+1)}}\,\left(\mu_p+(-1)^L\,\mu_n\right)$$
$$\times\iint r dr\,r' dr'\,u_{l'}(r)\,j_L(\frac{\omega r}{2})\,G_{\hat{C}}(r,r';E_0')\,\psi_{L'}(\frac{\omega r'}{2})\,u_l(r')$$
$$\times\begin{pmatrix}1 & L & J_C\\ -M_f & \lambda_i & M_f-\lambda_i\end{pmatrix}\begin{pmatrix}J_C & L' & 1\\ -M_f+\lambda_i & M_f-M_i-\lambda_i & M_i\end{pmatrix}$$
$$\times\,\langle\, l'\,1\,1\,\|\,[Y_L\otimes S]_L\,\|\,L_C\,1\,J_C\,\rangle\,\langle\, L_C\,1\,J_C\,\|\,Y_{L'}\,\|\,l\,1\,1\,\rangle \qquad \text{(H.15)}$$

The amplitudes $\mathcal{M}_{fi}^{\phi\,\sigma 1}$ ($\mathcal{M}_{fi}^{\phi\,\sigma 2}$) *alone* are numerically large. Their size is a correction of about 5%-10% at 94.2 MeV. However, they partly cancel each other. Therefore the net effect of the contributions $\mathcal{M}_{fi}^{\phi\,\sigma 1}$, $\mathcal{M}_{fi}^{\phi\,\sigma 2}$ is well below 5% for all angles at 94.2 MeV, see Fig. 6.7.

Numerically more important than the amplitudes calculated so far in this appendix are those, where we replace $\vec{J}(\vec{\xi})\cdot\vec{A}(\vec{\xi})$ by $\vec{J}^{(\sigma)}(\vec{\xi})\cdot\vec{A}^{(1,2)}(\vec{\xi})$ at both vertices. However, we found that the mixed contributions, i.e. $H^{\rm int}=-\int\vec{J}^{(\sigma)}(\vec{\xi})\cdot\vec{A}^{(1)}(\vec{\xi})\,d^3\xi$ at one vertex and $H^{\rm int}=-\int\vec{J}^{(\sigma)}(\vec{\xi})\cdot\vec{A}^{(2)}(\vec{\xi})\,d^3\xi$ at the other are negligibly small. The reason for this suppression is the product of matrix elements occuring in these amplitudes, which forbids the leading contribution $L=L'=1$. It is given by Eq. (L.38) with $L'=0$ and $L'=1$, respectively. However, it follows from Eq. (L.21) and the fact that l, l' are even numbers that L_C must be even, odd for $L'=0,\,1$. Therefore, this product vanishes for the leading contribution and we only need to calculate the following four amplitudes:

$$\mathcal{M}_{fi}^{\sigma 1\,\sigma 1\,a}=\sum_C\frac{\langle\, d_f\,|\int\vec{J}^{(\sigma)}(\vec{\xi})\cdot\vec{A}^{(1)}(\vec{\xi})\,d^3\xi\,|\,C\,\rangle\langle\,C\,|\int\vec{J}^{(\sigma)}(\vec{\xi})\cdot\vec{A}^{(1)}(\vec{\xi})\,d^3\xi\,|\,d_i\,\rangle}{\omega+\frac{\omega^2}{2m_d}-B-E_C}$$
$$\mathcal{M}_{fi}^{\sigma 1\,\sigma 1\,b}=\sum_C\frac{\langle\, d_f\,|\int\vec{J}^{(\sigma)}(\vec{\xi})\cdot\vec{A}^{(1)}(\vec{\xi})\,d^3\xi\,|\,C\,\rangle\langle\,C\,|\int\vec{J}^{(\sigma)}(\vec{\xi})\cdot\vec{A}^{(1)}(\vec{\xi})\,d^3\xi\,|\,d_i\,\rangle}{-\omega+\frac{\omega^2}{2m_d}-\frac{\vec{P}_C^{\,2}}{2m_C}-B-E_C}$$
$$\mathcal{M}_{fi}^{\sigma 2\,\sigma 2\,a}=\sum_C\frac{\langle\, d_f\,|\int\vec{J}^{(\sigma)}(\vec{\xi})\cdot\vec{A}^{(2)}(\vec{\xi})\,d^3\xi\,|\,C\,\rangle\langle\,C\,|\int\vec{J}^{(\sigma)}(\vec{\xi})\cdot\vec{A}^{(2)}(\vec{\xi})\,d^3\xi\,|\,d_i\,\rangle}{\omega+\frac{\omega^2}{2m_d}-B-E_C}$$
$$\mathcal{M}_{fi}^{\sigma 2\,\sigma 2\,b}=\sum_C\frac{\langle\, d_f\,|\int\vec{J}^{(\sigma)}(\vec{\xi})\cdot\vec{A}^{(2)}(\vec{\xi})\,d^3\xi\,|\,C\,\rangle\langle\,C\,|\int\vec{J}^{(\sigma)}(\vec{\xi})\cdot\vec{A}^{(2)}(\vec{\xi})\,d^3\xi\,|\,d_i\,\rangle}{-\omega+\frac{\omega^2}{2m_d}-\frac{\vec{P}_C^{\,2}}{2m_C}-B-E_C} \qquad \text{(H.16)}$$

The evaluation of these amplitudes is straightforward, using Eqs. (6.67) and (6.72). The main difference to $\mathcal{M}_{fi}^{\phi\,\sigma 1}$ and $\mathcal{M}_{fi}^{\phi\,\sigma 2}$ is the fact that now the intermediate state may have total spin $S_C=1$ *or* $S_C=0$. In fact, the singlet ($S_C=0$) part of $\mathcal{M}_{fi}^{\sigma 1\,\sigma 1\,a}$, which is the amplitude with two $M1$-interactions, is the dominant contribution to the total deuteron-photodisintegration cross section at threshold, cf. Section 6.4 and Fig. 6.11. Among the amplitudes (H.16), it is also the singlet transition of $\mathcal{M}_{fi}^{\sigma 1\,\sigma 1}$ which gives the most important contribution to the deuteron Compton cross sections, whereas the triplet amplitude and $\mathcal{M}_{fi}^{\sigma 2\,\sigma 2}$ are only minor

corrections. The results are:

$$
\begin{aligned}
\mathcal{M}_{fi}^{\sigma 1\,\sigma 1\,a} = & \sum_{L=1}^{\infty}\sum_{L'=1}^{\infty}\sum_{J_C=|L-1|}^{L+1}\sum_{S_C=0,1}\sum_{L_C=|J_C-S_C|}^{J_C+S_C}\sum_{l,l'}\frac{\pi\,e^2\,\omega^2}{2\,m_N^2}\,(-1)^{L'-\lambda_f-\lambda_i-M_f-M_i+J_C+1} \\
& \times i^{L+L'}\,\lambda_i\,\lambda_f\,d^{L'}_{M_f-M_i-\lambda_i,-\lambda_f}(\theta)\,\sqrt{(L+1)\,(L'+1)} \\
& \times \begin{pmatrix} 1 & L' & J_C \\ -M_f & M_f-M_i-\lambda_i & M_i+\lambda_i \end{pmatrix}\begin{pmatrix} J_C & L & 1 \\ -M_i-\lambda_i & \lambda_i & M_i \end{pmatrix} \\
& \times \Big\{(\mu_p-(-1)^{L'}\,\mu_n)\,(\mu_p-(-1)^{L}\,\mu_n)\,\langle\, l'\,1\,1 \,\|\, [Y_{L'-1}\otimes S]_{L'}\,\|\, L_C\,S_C\,J_C\,\rangle \\
& \times \langle\, L_C\,S_C\,J_C \,\|\, [Y_{L-1}\otimes S]_{L}\,\|\, l\,1\,1\,\rangle + (\mu_p+(-1)^{L'}\,\mu_n)\,(\mu_p+(-1)^{L}\,\mu_n) \\
& \times \langle\, l'\,1\,1 \,\|\, [Y_{L'-1}\otimes t]_{L'}\,\|\, L_C\,S_C\,J_C\,\rangle\,\langle\, L_C\,S_C\,J_C \,\|\, [Y_{L-1}\otimes t]_{L}\,\|\, l\,1\,1\,\rangle\Big\} \\
& \times \iint r dr\,r' dr'\,u_l(r)\,j_{L-1}(\frac{\omega r}{2})\,G_{\hat{C}}(r,r';E_0)\,j_{L'-1}(\frac{\omega r'}{2})\,u_{l'}(r') \qquad \text{(H.17)}
\end{aligned}
$$

$$
\begin{aligned}
\mathcal{M}_{fi}^{\sigma 1\,\sigma 1\,b} = & \sum_{L=1}^{\infty}\sum_{L'=1}^{\infty}\sum_{J_C=|L-1|}^{L+1}\sum_{S_C=0,1}\sum_{L_C=|J_C-S_C|}^{J_C+S_C}\sum_{l,l'}\frac{\pi\,e^2\,\omega^2}{2\,m_N^2}\,(-1)^{L'-\lambda_f-\lambda_i+J_C+1} \\
& \times i^{L+L'}\,\lambda_i\,\lambda_f\,d^{L'}_{M_f-M_i-\lambda_i,-\lambda_f}(\theta)\,\sqrt{(L+1)\,(L'+1)} \\
& \times \begin{pmatrix} 1 & L & J_C \\ -M_f & \lambda_i & M_f-\lambda_i \end{pmatrix}\begin{pmatrix} J_C & L' & 1 \\ -M_f+\lambda_i & M_f-M_i-\lambda_i & M_i \end{pmatrix} \\
& \times \Big\{(\mu_p-(-1)^{L}\,\mu_n)\,(\mu_p-(-1)^{L'}\,\mu_n)\,\langle\, l'\,1\,1 \,\|\, [Y_{L-1}\otimes S]_{L}\,\|\, L_C\,S_C\,J_C\,\rangle \\
& \times \langle\, L_C\,S_C\,J_C \,\|\, [Y_{L'-1}\otimes S]_{L'}\,\|\, l\,1\,1\,\rangle + (\mu_p+(-1)^{L}\,\mu_n)\,(\mu_p+(-1)^{L'}\,\mu_n) \\
& \times \langle\, l'\,1\,1 \,\|\, [Y_{L-1}\otimes t]_{L}\,\|\, L_C\,S_C\,J_C\,\rangle\,\langle\, L_C\,S_C\,J_C \,\|\, [Y_{L'-1}\otimes t]_{L'}\,\|\, l\,1\,1\,\rangle\Big\} \\
& \times \iint r dr\,r' dr'\,u_{l'}(r)\,j_{L-1}(\frac{\omega r}{2})\,G_{\hat{C}}(r,r';E_0')\,j_{L'-1}(\frac{\omega r'}{2})\,u_{l}(r') \qquad \text{(H.18)}
\end{aligned}
$$

$$
\begin{aligned}
\mathcal{M}_{fi}^{\sigma 2\,\sigma 2\,a} = & \sum_{L=1}^{\infty}\sum_{L'=1}^{\infty}\sum_{J_C=|L-1|}^{L+1}\sum_{S_C=0,1}\sum_{L_C=|J_C-S_C|}^{J_C+S_C}\sum_{l,l'}\frac{\pi\,e^2\,\omega^2}{2\,m_N^2}\,(-1)^{L'-M_f-M_i+J_C-\lambda_i-\lambda_f} \\
& \times i^{L+L'}\,d^{L'}_{M_f-M_i-\lambda_i,-\lambda_f}(\theta)\,\sqrt{(2L+1)\,(2L'+1)} \\
& \times \begin{pmatrix} 1 & L' & J_C \\ -M_f & M_f-M_i-\lambda_i & M_i+\lambda_i \end{pmatrix}\begin{pmatrix} J_C & L & 1 \\ -M_i-\lambda_i & \lambda_i & M_i \end{pmatrix} \\
& \times \Big\{(\mu_p+(-1)^{L'}\,\mu_n)\,(\mu_p+(-1)^{L}\,\mu_n)\,\langle\, l'\,1\,1 \,\|\, [Y_{L'}\otimes S]_{L'}\,\|\, L_C\,S_C\,J_C\,\rangle \\
& \times \langle\, L_C\,S_C\,J_C \,\|\, [Y_{L}\otimes S]_{L}\,\|\, l\,1\,1\,\rangle + (\mu_p-(-1)^{L'}\,\mu_n)\,(\mu_p-(-1)^{L}\,\mu_n) \\
& \times \langle\, l'\,1\,1 \,\|\, [Y_{L'}\otimes t]_{L'}\,\|\, L_C\,S_C\,J_C\,\rangle\,\langle\, L_C\,S_C\,J_C \,\|\, [Y_{L}\otimes t]_{L}\,\|\, l\,1\,1\,\rangle\Big\} \\
& \times \iint r dr\,r' dr'\,u_l(r)\,j_{L}(\frac{\omega r}{2})\,G_{\hat{C}}(r,r';E_0)\,j_{L'}(\frac{\omega r'}{2})\,u_{l'}(r') \qquad \text{(H.19)}
\end{aligned}
$$

$$
\begin{aligned}
\mathcal{M}_{fi}^{\sigma_2\,\sigma_2\,b} = & \sum_{L=1}^{\infty}\sum_{L'=1}^{\infty}\sum_{J_C=|L-1|}^{L+1}\sum_{S_C=0,1}\sum_{L_C=|J_C-S_C|}^{J_C+S_C}\sum_{l,l'}\frac{\pi\,e^2\,\omega^2}{2\,m_N^2}\,(-1)^{L'-\lambda_f-\lambda_i+J_C} \\
& \times i^{L+L'}\,d^{L'}_{M_f-M_i-\lambda_i,-\lambda_f}(\theta)\,\sqrt{(2L+1)\,(2L'+1)} \\
& \times \begin{pmatrix} 1 & L & J_C \\ -M_f & \lambda_i & M_f-\lambda_i \end{pmatrix} \begin{pmatrix} J_C & L' & 1 \\ -M_f+\lambda_i & M_f-M_i-\lambda_i & M_i \end{pmatrix} \\
& \times \Big\{ (\mu_p+(-1)^L\,\mu_n)\,(\mu_p+(-1)^{L'}\,\mu_n)\,\langle\, l'\,1\,1 \,\|\, [Y_L\otimes S]_L \,\|\, L_C\,S_C\,J_C\,\rangle \\
& \times \langle\, L_C\,S_C\,J_C \,\|\, [Y_{L'}\otimes S]_{L'} \,\|\, l\,1\,1\,\rangle + (\mu_p-(-1)^L\,\mu_n)\,(\mu_p-(-1)^{L'}\,\mu_n) \\
& \times \langle\, l'\,1\,1 \,\|\, [Y_L\otimes t]_L \,\|\, L_C\,S_C\,J_C\,\rangle\,\langle\, L_C\,S_C\,J_C \,\|\, [Y_{L'}\otimes t]_{L'} \,\|\, l\,1\,1\,\rangle \Big\} \\
& \times \iint r dr\, r' dr'\, u_{l'}(r)\, j_L(\frac{\omega r}{2})\, G_{\hat{C}}(r,r';E_0')\, j_{L'}(\frac{\omega r'}{2})\, u_l(r') \qquad \text{(H.20)}
\end{aligned}
$$

The reduced matrix elements are given in Eqs. (L.38, L.39). The operator $[Y_l \otimes t]_l$ corresponds to $S_C = 0$ (singlet), $[Y_l \otimes S]_l$ to $S_C = 1$ (triplet).

In this appendix we calculated diagrams where only one-body currents are explicitly involved. In the next one we allow for explicit coupling of the photon to two-body, i.e. to meson-exchange currents.

Appendix I

Diagrams with Explicit Two-Body Currents

In this appendix we calculate diagrams explicitly including the two-body currents shown in Fig. 6.2. However, it turned out from our calculation that the only non-negligible of these currents is the Kroll-Ruderman (pair) current, Fig. 6.2(a). Therefore the pion-pole current, Fig. 6.2(b), is only included via charge conservation, cf. Eq. (6.10).

First we derive the Kroll-Ruderman current, including corrections due to the photon energy. We then calculate several contributions with one of the photons coupling to this current. Diagrams with explicit pion exchange at both vertices were found to be small and are not considered in this work.

In order to calculate the interaction Hamiltonian, from which we derive the Kroll-Ruderman current, we first sketch the relevant time-ordered diagrams in Fig. I.1.

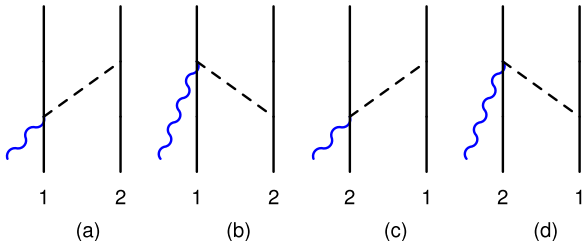

Figure I.1: Possible time-orderings for an incoming photon coupling to the Kroll-Ruderman current.

Now we need to define the Hamiltonians for the $\gamma\pi N$ and the πNN coupling. These are given in Eqs. (L.3, L.4) and can be used, together with Eqs. (L.2) and (L.5-L.7) to write down the amplitude for the process Fig. I.1(a):

$$\mathcal{M}_{fi}^{\mathrm{KR}\,a} = \sum_B \sum_{\pm} \int \frac{d^3q}{(2\pi)^3} \frac{2\pi}{E_\pi} \langle\, C \mid -\frac{f}{m_\pi} (\vec{\sigma}_2 \cdot \vec{\nabla}_2) \frac{1}{\sqrt{2}} \tau_2^{\pm}\, \mathrm{e}^{i\vec{q}\cdot\vec{x}_2} \mid B \,\rangle \tag{I.1}$$
$$\times \frac{1}{\omega + \frac{\omega^2}{2m_d} - B - E_B - E_\pi} \langle\, B \mid \frac{i\,e\,f}{m_\pi} (\vec{\sigma}_1 \cdot \vec{A}(\vec{x}_1)) \frac{1}{\sqrt{2}} (\mp\tau_1^{\mp})\, \mathrm{e}^{-i\vec{q}\cdot\vec{x}_1} \mid d_i \,\rangle$$

E_B is the energy of the two-nucleon state $\mid B \,\rangle$ while the pion is in flight. In order to derive the expression given for the Kroll-Ruderman current in Eq. (6.73) one would

have to make the assumption that $E_\pi = \sqrt{m_\pi^2 + \vec{q}^{\,2}}$ is the by far dominant term in the energy denominator of Eq. (I.1). However, for $\omega \sim 100$ MeV, this is a rather crude approximation. Therefore we keep the photon energy in the denominator and do the approximation $\omega + \frac{\omega^2}{2m_d} - B - E_B - E_\pi \approx \omega - E_\pi$. Nevertheless, we first approximate the denominator by the negative pion energy $-E_\pi$, i.e. we set $\omega = 0$, to check whether we get the correct result for $\vec{J}^{\,\rm KR}_{\rm stat}$.

Neglecting the energy of the intermediate state $\mid B \,\rangle$ in the denominator, one can collapse the sum over B and we find

$$M^{{\rm KR}\,a}_{fi\,{\rm stat}} = \frac{\pi\, e\, f^2}{i\, m_\pi^2} \,\langle\, C \mid (\tau_2^+\,\tau_1^- - \tau_2^-\,\tau_1^+) \int \frac{d^3q}{(2\pi)^3}\,(\vec{\sigma}_2\cdot\vec{\nabla}_2)\,\frac{{\rm e}^{i\vec{q}\cdot(\vec{x}_2-\vec{x}_1)}}{m_\pi^2+\vec{q}^{\,2}}\,(\vec{\sigma}_1\cdot\vec{A}(\vec{x}_1)) \mid d_i\,\rangle. \tag{I.2}$$

From our definition for $\tau_\pm$ (Eq. (L.5)) follows $\tau_2^+\,\tau_1^- - \tau_2^-\,\tau_1^+ = 2\,i\,(\vec{\tau}_1\times\vec{\tau}_2)_z$. Furthermore we define, as in Section 8.3 of [57], $\vec{x}_1 - \vec{x}_2 = \vec{r}$. Therefore $\vec{\nabla}_2 = \vec{\nabla}_{x_2-x_1} = \vec{\nabla}_{-r} = -\vec{\nabla}_r$. The integral over d^3q can easily be evaluated, yielding

$$\int \frac{d^3q}{(2\pi)^3}\,\frac{{\rm e}^{-i\vec{q}\cdot\vec{r}}}{m_\pi^2+\vec{q}^{\,2}} = \frac{{\rm e}^{-m_\pi r}}{4\pi\, r}. \tag{I.3}$$

Therefore we find

$$\begin{aligned} M^{{\rm KR}\,a}_{fi\,{\rm stat}} &= -\frac{e\,f^2}{2\,m_\pi^2}\,\langle\, C \mid (\vec{\tau}_1\times\vec{\tau}_2)_z\,(\vec{\sigma}_2\cdot\vec{\nabla}_r)\,\frac{{\rm e}^{-m_\pi r}}{r}\,(\vec{\sigma}_1\cdot\vec{A}(\vec{x}_1)) \mid d_i\,\rangle \\ &= -\frac{e\,f^2}{2\,m_\pi^2}\,\langle\, C \mid (\vec{\tau}_1\times\vec{\tau}_2)_z\,(\vec{\sigma}_2\cdot\hat{r})\,\frac{\partial}{\partial r}\frac{{\rm e}^{-m_\pi r}}{r}\,(\vec{\sigma}_1\cdot\vec{A}(\vec{x}_1)) \mid d_i\,\rangle. \end{aligned} \tag{I.4}$$

The calculation of diagram I.1(b), where the pion is destroyed rather than created at the $\gamma\pi N$ vertex, is very similar to the derivation of Eq. (I.4). The amplitude is

$$\begin{aligned} \mathcal{M}^{{\rm KR}\,b}_{fi} = \sum_B \sum_\pm \int \frac{d^3q}{(2\pi)^3}\,\frac{2\pi}{E_\pi}\,\langle\, C \mid \frac{i\,e\,f}{m_\pi}\,(\vec{\sigma}_1\cdot\vec{A}(\vec{x}_1))\,\frac{1}{\sqrt{2}}\,(\mp\tau_1^\mp)\,{\rm e}^{i\vec{q}\cdot\vec{x}_1} \mid B\,\rangle \\ \times\,\frac{1}{-B-E_B-E_\pi}\,\langle\, B \mid -\frac{f}{m_\pi}\,(\vec{\sigma}_2\cdot\vec{\nabla}_2)\,\frac{1}{\sqrt{2}}\,\tau_2^\pm\,{\rm e}^{-i\vec{q}\cdot\vec{x}_2} \mid d_i\,\rangle, \end{aligned} \tag{I.5}$$

so the only differences are that $\vec{\nabla}_2 \to -i\,\vec{q}$ rather than $i\,\vec{q}$ and the interchange of $\vec{\tau}_1$, $\vec{\tau}_2$, which gives an additional sign. These two signs cancel and therefore $\mathcal{M}^{{\rm KR}\,b}_{fi} = \mathcal{M}^{{\rm KR}\,a}_{fi}$. Diagrams I.1(c), (d) are identical to diagrams (a), (b) with the nucleons exchanged. This exchange leads to $(\vec{\tau}_1\times\vec{\tau}_2)_z \to -\,(\vec{\tau}_1\times\vec{\tau}_2)_z$ and $\hat{r}\to-\hat{r}$ in Eq. (I.4), so we get for diagram I.1(c) (which is, of course, identical to diagram I.1(d))

$$M^{{\rm KR}\,c}_{fi\,{\rm stat}} = -\frac{e\,f^2}{2\,m_\pi^2}\,\langle\, C \mid (\vec{\tau}_1\times\vec{\tau}_2)_z\,(\vec{\sigma}_1\cdot\hat{r})\,\frac{\partial}{\partial r}\frac{{\rm e}^{-m_\pi r}}{r}\,(\vec{\sigma}_2\cdot\vec{A}(\vec{x}_2)) \mid d_i\,\rangle. \tag{I.6}$$

Adding the four amplitudes I.1(a)-(d), we find for the corresponding interaction Hamiltonian, by removing the initial and final state,

$$H^{{\rm int\,KR}}_{\rm stat} = -\frac{e\,f^2}{m_\pi^2}\,(\vec{\tau}_1\times\vec{\tau}_2)_z\,\Big[(\vec{\sigma}_2\cdot\hat{r})\,(\vec{\sigma}_1\cdot\vec{A}(\vec{x}_1)) + (\vec{\sigma}_1\cdot\hat{r})\,(\vec{\sigma}_2\cdot\vec{A}(\vec{x}_2))\Big]\,\frac{\partial}{\partial r}\frac{{\rm e}^{-m_\pi r}}{r}, \tag{I.7}$$

which is identical to $-\int \vec{J}^{\,\rm KR}_{\rm stat}(\vec{\xi};\vec{x}_1,\vec{x}_2)\cdot\vec{A}(\vec{\xi}\,)$ with $\vec{J}^{\,\rm KR}_{\rm stat}(\vec{\xi};\vec{x}_1,\vec{x}_2)$ given in Eq. (6.73).

Now we discuss how this result changes when we retain the photon energy in the denominator. Again we start with diagram (a) of Fig. I.1 and find instead of

Eq. (I.2)

$$M_{fi}^{\mathrm{KR}\,a} = -\frac{\pi\, e\, f^2}{i\, m_\pi^2}\, \langle\, C \mid (\tau_2^+\, \tau_1^- - \tau_2^-\, \tau_1^+) \times \int \frac{d^3q}{(2\pi)^3}\, (\vec{\sigma}_2 \cdot \vec{\nabla}_2)\, \frac{\mathrm{e}^{i\vec{q}\cdot(\vec{x}_2-\vec{x}_1)}}{\sqrt{m_\pi^2+\vec{q}^{\,2}}\,(\omega-\sqrt{m_\pi^2+\vec{q}^{\,2}})}\, (\vec{\sigma}_1 \cdot \vec{A}(\vec{x}_1)) \mid d_i\,\rangle. \tag{I.8}$$

In order to perform the integral, we do an expansion of the integrand in ω. This expansion is possible to any order, and it converges quite fast. We found that our results achieved with an expansion up to $\mathcal{O}(\omega^7)$ only deviate by about 0.1% from analogous results using the expansion up to $\mathcal{O}(\omega^6)$. Therefore the error introduced by cutting off the expansion at $\mathcal{O}(\omega^7)$ is certainly negligibly small. The resulting interaction Hamiltonian is

$$\begin{aligned} H^{\mathrm{int\,KR}\,a} \approx -\frac{e\, f^2}{m_\pi^2}\, (\vec{\tau}_1 \times \vec{\tau}_2)_z\, (\vec{\sigma}_2 \cdot \hat{r})\, (\vec{\sigma}_1 \cdot \vec{A}(\vec{x}_1))\, \frac{\partial}{\partial r} \Bigg\{ & \frac{\mathrm{e}^{-m_\pi r}}{2\, r} + \frac{K_0(m_\pi r)}{\pi}\, \omega \\ & + \frac{\mathrm{e}^{-m_\pi r}}{4\, m_\pi}\, \omega^2 + \frac{r\, K_1(m_\pi r)}{3\, m_\pi\, \pi}\, \omega^3 + \frac{\mathrm{e}^{-m_\pi r}\,(1+m_\pi r)}{16\, m_\pi^3}\, \omega^4 + \frac{r^2\, K_2(m_\pi r)}{15\, m_\pi^2\, \pi}\, \omega^5 \\ & + \frac{\mathrm{e}^{-m_\pi r}\,(3+3\, m_\pi r + m_\pi^2\, r^2)}{96\, m_\pi^5}\, \omega^6 + \frac{r^3\, K_3(m_\pi r)}{105\, m_\pi^3\, \pi}\, \omega^7 \Bigg\}, \end{aligned} \tag{I.9}$$

$K_i(z)$ being the modified Bessel functions of the second kind.

The photon energy ω does not appear in the denominator of diagram I.1(b). Therefore we find the same interaction Hamiltonian as in the static case. Exchange of the nucleons is treated as before, leaving us with

$$H_s^{\mathrm{int\,KR}} = -\frac{e\, f^2}{m_\pi^2}\, (\vec{\tau}_1 \times \vec{\tau}_2)_z\, \Big[(\vec{\sigma}_2 \cdot \hat{r})\, (\vec{\sigma}_1 \cdot \vec{A}(\vec{x}_1)) + (\vec{\sigma}_1 \cdot \hat{r})\, (\vec{\sigma}_2 \cdot \vec{A}(\vec{x}_2))\Big]\, \frac{\partial}{\partial r} f_s^{\mathrm{KR}}(r), \tag{I.10}$$

with

$$\begin{aligned} f_s^{\mathrm{KR}}(r) = & \frac{\mathrm{e}^{-m_\pi r}}{r} + \frac{K_0(m_\pi r)}{\pi}\, \omega + \frac{\mathrm{e}^{-m_\pi r}}{4\, m_\pi}\, \omega^2 \\ & + \frac{r\, K_1(m_\pi r)}{3\, m_\pi\, \pi}\, \omega^3 + \frac{\mathrm{e}^{-m_\pi r}\,(1+m_\pi r)}{16\, m_\pi^3}\, \omega^4 + \frac{r^2\, K_2(m_\pi r)}{15\, m_\pi^2\, \pi}\, \omega^5 \\ & + \frac{\mathrm{e}^{-m_\pi r}\,(3+3\, m_\pi r + m_\pi^2\, r^2)}{96\, m_\pi^5}\, \omega^6 + \frac{r^3\, K_3(m_\pi r)}{105\, m_\pi^3\, \pi}\, \omega^7. \end{aligned} \tag{I.11}$$

The index s signals that Eq. (I.10) is only valid for s-channel diagrams. In the u-channel, the both time orderings correspond to the (approximate) energy denominators $\frac{1}{-E_\pi}$ and $\frac{1}{-\omega-E_\pi}$, respectively. The net effect is an alternating sign in $f^{\mathrm{KR}}(r)$, say

$$\begin{aligned} f_u^{\mathrm{KR}}(r) = & \frac{\mathrm{e}^{-m_\pi r}}{r} - \frac{K_0(m_\pi r)}{\pi}\, \omega + \frac{\mathrm{e}^{-m_\pi r}}{4\, m_\pi}\, \omega^2 \\ & - \frac{r\, K_1(m_\pi r)}{3\, m_\pi\, \pi}\, \omega^3 + \frac{\mathrm{e}^{-m_\pi r}\,(1+m_\pi r)}{16\, m_\pi^3}\, \omega^4 - \frac{r^2\, K_2(m_\pi r)}{15\, m_\pi^2\, \pi}\, \omega^5 \\ & + \frac{\mathrm{e}^{-m_\pi r}\,(3+3\, m_\pi r + m_\pi^2\, r^2)}{96\, m_\pi^5}\, \omega^6 - \frac{r^3\, K_3(m_\pi r)}{105\, m_\pi^3\, \pi}\, \omega^7. \end{aligned} \tag{I.12}$$

We note that the amplitudes which we calculate in this appendix deviate by about 25%, depending on whether we use the static interaction Hamiltonian (I.7) or a corrected one, including Eq. (I.11) or (I.12), respectively.

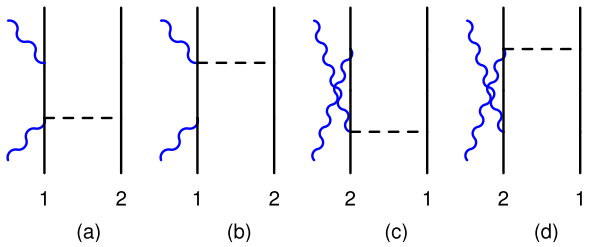

Figure I.2: Diagrams with one photon coupling to the Kroll-Ruderman current.

We are now able to use the Kroll-Ruderman interaction Hamiltonian to calculate the diagrams displayed in Fig. I.2. As explained in Sect. 6.1.2, there are only a few combinations to be taken into account. These are $\mathcal{M}_{fi}^{\mathrm{KR\,full}\,\sigma 1}$, $\mathcal{M}_{fi}^{\phi\,\mathrm{KR1}}$ and $\mathcal{M}_{fi}^{\phi\,\mathrm{KR2}}$. The indices 'full', '1', '2' denote the coupling of the full photon field $\vec{A}$ or of $\vec{A}^{(1)}$, $\vec{A}^{(2)}$, respectively. First we compute the contributions $\mathcal{M}_{fi}^{\mathrm{KR\,full}\,\sigma 1}$, where we skip the index 'full' for brevity. These four amplitudes have already been calculated in [24], however using the static Kroll-Ruderman Hamiltonian (I.7). They read

$$\begin{aligned}
\mathcal{M}_{fi}^{\mathrm{KR}\,\sigma 1\,a} &= -\sum_C \frac{\langle\, d_f \mid \int \vec{J}^{(\sigma)}(\vec{\xi}\,)\cdot\vec{A}^{(1)}(\vec{\xi}\,)\,d^3\xi \mid C\,\rangle\langle\, C \mid H_s^{\mathrm{int\,KR}} \mid d_i\,\rangle}{\omega + \frac{\omega^2}{2m_d} - B - E_C}, \\
\mathcal{M}_{fi}^{\mathrm{KR}\,\sigma 1\,b} &= -\sum_C \frac{\langle\, d_f \mid H_s^{\mathrm{int\,KR}} \mid C\,\rangle\langle\, C \mid \int \vec{J}^{(\sigma)}(\vec{\xi}\,)\cdot\vec{A}^{(1)}(\vec{\xi}\,)\,d^3\xi \mid d_i\,\rangle}{\omega + \frac{\omega^2}{2m_d} - B - E_C}, \\
\mathcal{M}_{fi}^{\mathrm{KR}\,\sigma 1\,c} &= -\sum_C \frac{\langle\, d_f \mid \int \vec{J}^{(\sigma)}(\vec{\xi}\,)\cdot\vec{A}^{(1)}(\vec{\xi}\,)\,d^3\xi \mid C\,\rangle\langle\, C \mid H_u^{\mathrm{int\,KR}} \mid d_i\,\rangle}{-\omega + \frac{\omega^2}{2m_d} - \frac{\vec{P}_C^{\,2}}{2m_C} - B - E_C}, \\
\mathcal{M}_{fi}^{\mathrm{KR}\,\sigma 1\,d} &= -\sum_C \frac{\langle\, d_f \mid H_u^{\mathrm{int\,KR}} \mid C\,\rangle\langle\, C \mid \int \vec{J}^{(\sigma)}(\vec{\xi}\,)\cdot\vec{A}^{(1)}(\vec{\xi}\,)\,d^3\xi \mid d_i\,\rangle}{-\omega + \frac{\omega^2}{2m_d} - \frac{\vec{P}_C^{\,2}}{2m_C} - B - E_C},
\end{aligned} \tag{I.13}$$

which follows immediately from Eq. (6.1). As explained in Section 6.1.2, we only consider that part of $\int \vec{J}^{(\sigma)}(\vec{\xi}\,)\cdot\vec{A}^{(1)}(\vec{\xi}\,)\,d^3\xi$, which contains the operator $[Y_{L-1}\otimes t]_L$, cf. Eq. (6.67). Plugging this expression and the Kroll-Ruderman-Hamiltonian into the first amplitude of Eq. (I.13) we find

$$\begin{aligned}
\mathcal{M}_{fi}^{\mathrm{KR}\,\sigma 1\,a} = -\sum_C \langle\, d_f \mid -\sum_{L'=1}^{\infty}\sum_{M'=-L'}^{L'} & \lambda_f \sqrt{2\pi\,(L'+1)}\,\frac{e\,\omega}{2m_d}\,i^{L'+1}\,j_{L'-1}(\frac{\omega r}{2}) \\
\times \Big(\mu_p + (-1)^{L'}\,\mu_n\Big)\; & [Y_{L'-1}\otimes t]_{L'\,M'}\;\Big(-(-1)^{L'+\lambda_f}\,d^{L'}_{M',-\lambda_f}(\theta)\Big) \mid C\,\rangle \frac{1}{\omega + \frac{\omega^2}{2m_d} - B - E_C} \\
\times \langle\, C \mid -\frac{e\,f^2}{m_\pi^2}\;(\vec{\tau}_1\times\vec{\tau}_2)_z\;\Big\{(\vec{\sigma}_1\cdot\hat{\epsilon}_{\lambda_i})\,(\vec{\sigma}_2\cdot\hat{r})\,\mathrm{e}^{i\vec{k}_i\vec{x}_1} + (\vec{\sigma}_2\cdot\hat{\epsilon}_{\lambda_i})\,(\vec{\sigma}_1\cdot\hat{r})\,\mathrm{e}^{i\vec{k}_i\vec{x}_2}\Big\}\;\frac{\partial}{\partial r} f_s^{\mathrm{KR}}(r) \mid d_i\,\rangle.
\end{aligned} \tag{I.14}$$

We decompose the exponentials into multipoles according to Eq. (F.1), replacing $\vec{x}_1 \to \frac{\vec{r}}{2}$, $\vec{x}_2 \to -\frac{\vec{r}}{2}$ as usual, and use

$$\frac{1}{\sqrt{2}}\langle\, p\,n + n\,p \mid (\vec{\tau}_1\times\vec{\tau}_2)_z\;\frac{1}{\sqrt{2}} \mid p\,n - n\,p\,\rangle = -2\,i, \tag{I.15}$$

cf. Eq. (6.76). Therefore,

$$\begin{aligned}\mathcal{M}^{\mathrm{KR}\,\sigma 1\,a}_{fi} = &-\sum_{\hat{C}}\sum_{L'=1}^{\infty}\sum_{M'=-L'}^{L'}\sum_{L=0}^{\infty}\sum_{M=-L}^{L}\sum_{l,l'}\frac{4\pi\,\lambda_f\,e^2\,f^2\,\omega}{m_N\,m_\pi^2}\,i^{L+L'}\,(-1)^{L'+\lambda_f}\,Y^*_{L\,M}(\hat{k}_i)\\
&\times\Big(\mu_p+(-1)^{L'}\,\mu_n\Big)\;d^{L'}_{M',-\lambda_f}(\theta)\sqrt{2\pi\,(L'+1)}\,\langle\,l'\,1\,1\,M_f\mid[Y_{L'-1}\otimes t]_{L'\,M'}\mid L_C\,S_C\,J_C\,M_C\,\rangle\\
&\times\langle\,L_C\,S_C\,J_C\,M_C\mid\big\{(\vec{\sigma}_1\cdot\hat{\epsilon}_{\lambda_i})\,(\vec{\sigma}_2\cdot\hat{r})+(-1)^L(\vec{\sigma}_2\cdot\hat{\epsilon}_{\lambda_i})\,(\vec{\sigma}_1\cdot\hat{r})\big\}\;Y_{L\,M}(\hat{r})\mid l\,1\,1\,M_i\,\rangle\\
&\times\iint r\,dr\,r'\,dr'\,u_{l'}(r')\,j_{L'-1}(\frac{\omega r'}{2})\,G_{\hat{C}}(r,r';E_0)\,j_L(\frac{\omega r}{2})\,u_l(r)\,\frac{\partial}{\partial r}f^{\mathrm{KR}}_s(r).\quad\text{(I.16)}\end{aligned}$$

We now apply the Wigner-Eckart theorem (L.31), the identity $Y^*_{L\,M}(\hat{k}_i)=\frac{1}{2}\sqrt{\frac{2L+1}{\pi}}\,\delta_{M,0}$ and decompose the scalar products into spherical components, using $r_j=\sqrt{\frac{4\pi}{3}}\,Y_{1\,j}(\hat{r})$. We further put $S_C=0$ due to Eq. (L.39).

$$\begin{aligned}\mathcal{M}^{\mathrm{KR}\,\sigma 1\,a}_{fi} = &\sum_{\hat{C}}\sum_{L'=1}^{\infty}\sum_{M'=-L'}^{L'}\sum_{L=0}^{\infty}\sum_{l,l'}\sum_{i,j}\frac{4\pi\,\lambda_f\,e^2\,f^2\,\omega}{m_N\,m_\pi^2}\sqrt{\frac{\pi}{3}}\,i^{L+L'}\,(-1)^{L'+\lambda_f+1-M_f+i+j}\\
&\times\Big(\mu_p+(-1)^{L'}\,\mu_n\Big)\;(\hat{\epsilon}_{\lambda_i})_{-i}\,d^{L'}_{M',-\lambda_f}(\theta)\sqrt{2\,(L'+1)\,(2L+1)}\\
&\times\iint r\,dr\,r'\,dr'\,u_{l'}(r')\,j_{L'-1}(\frac{\omega r'}{2})\,G_{\hat{C}}(r,r';E_0)\,j_L(\frac{\omega r}{2})\,u_l(r)\,\frac{\partial}{\partial r}f^{\mathrm{KR}}_s(r)\\
&\times\begin{pmatrix}1 & L' & J_C\\ -M_f & M' & M_C\end{pmatrix}\langle\,l'\,1\,1\,\|\,[Y_{L'-1}\otimes t]_{L'}\,\|\,J_C\,0\,J_C\,\rangle\\
&\times\langle\,J_C\,0\,J_C\,M_C\mid\sigma_{2\,j}\,\sigma_{1\,i}\,Y_{1\,-j}\,Y_{L\,0}+(-1)^L\,\sigma_{1\,j}\,\sigma_{2\,i}\,Y_{1\,-j}\,Y_{L\,0}\mid l\,1\,1\,M_i\,\rangle\quad\text{(I.17)}\end{aligned}$$

The second matrix element in Eq. (I.17) is evaluated according to Eq. (G.35). From $\langle\,S_1\,\|\,S-t\,\|\,s\,\rangle\,\langle\,s\,\|\,S+t\,\|\,S_2\,\rangle$ and the definitions of $\vec{S}$, $\vec{t}$, cf. Eq. (G.35), we see that the product $\sigma_{2\,j}\,\sigma_{1\,i}$ is antisymmetric under the interchange $1\leftrightarrow 2$ in the spin-changing, symmetric in the spin-conserving case. In Eq. (I.17) we have $S_1=0$ and $S_2=1$. Therefore only two of the four combinations are possible:

$$\langle\,S_1\,\|\,S-t\,\|\,s\,\rangle\,\langle\,s\,\|\,S+t\,\|\,S_2\,\rangle\to\langle\,S_1\,\|\,S\,\|\,s\,\rangle\,\langle\,s\,\|\,t\,\|\,S_2\,\rangle-\langle\,S_1\,\|\,t\,\|\,s\,\rangle\,\langle\,s\,\|\,S\,\|\,S_2\,\rangle\quad\text{(I.18)}$$

From Eqs. (L.35, L.36) we find that the only non-vanishing product of spin matrix elements is

$$\langle\,0\,\|\,t\,\|\,s\,\rangle\,\langle\,s\,\|\,S\,\|\,1\,\rangle=-3\sqrt{2}\,\delta_{s,1}.\quad\text{(I.19)}$$

The 9-j symbol guarantees that $S'=1$, cf. Eq. (L.25). Therefore we can easily evaluate the sum over s and find

$$\sum_s\begin{Bmatrix}1 & 1 & 1\\ 1 & 0 & s\end{Bmatrix}\langle\,0\,\|\,S-t\,\|\,s\,\rangle\,\langle\,s\,\|\,S+t\,\|\,1\,\rangle=-\sqrt{2}.\quad\text{(I.20)}$$

Nevertheless, we keep the compact notation of Eq. (I.17) to write down the final

result:

$$\mathcal{M}^{\mathrm{KR}\,\sigma 1\,a}_{fi} = \sum_{L=0}^{\infty}\sum_{L'=1}^{\infty}\sum_{J_C=|L'-1|}^{L'+1}\sum_{l,l'}\sum_{i,j}\frac{4\pi\,\lambda_f\,e^2\,f^2\,\omega}{m_N\,m_\pi^2}\sqrt{\frac{\pi}{3}}\,i^{L+L'}\,(-1)^{L'+\lambda_f+1-M_f+i+j}$$
$$\times\left(\mu_p+(-1)^{L'}\,\mu_n\right)\,(\hat{\epsilon}_{\lambda_i})_{-i}\,d^{L'}_{M_f-M_i-i,-\lambda_f}(\theta)\,\sqrt{2\,(L'+1)\,(2L+1)}$$
$$\times\iint r\,dr\,r'\,dr'\,u_{l'}(r')\,j_{L'-1}(\frac{\omega r'}{2})\,G_{\hat{C}}(r,r';E_0)\,j_L(\frac{\omega r}{2})\,u_l(r)\,\frac{\partial}{\partial r}f^{\mathrm{KR}}_s(r)$$
$$\times\begin{pmatrix}1 & L' & J_C\\ -M_f & M_f-M_i-i & M_i+i\end{pmatrix}\,\langle\,l'\,1\,1\,\|\,[Y_{L'-1}\otimes t]_{L'}\,\|\,J_C\,0\,J_C\,\rangle$$
$$\times\langle\,J_C\,0\,J_C\,M_i+i\,|\,\sigma_{2\,j}\,\sigma_{1\,i}\,Y_{1\,-j}\,Y_{L\,0}\,|\,l\,1\,1\,M_i\,\rangle\,\left(1-(-1)^L\right) \tag{I.21}$$

Obviously the leading orbital angular momenta are $L = L' = 1$. As $|\mu_p - \mu_n| \gg |\mu_p + \mu_n|$, one may restrict oneself to this contribution.

The evaluation of $\mathcal{M}^{\mathrm{KR}\,\sigma 1\,b\text{-}d}_{fi}$ is quite similar to the derivation of Eq. (I.21). Therefore we only give the results:

$$\mathcal{M}^{\mathrm{KR}\,\sigma 1\,b}_{fi} = \sum_{L=1}^{\infty}\sum_{L'=0}^{\infty}\sum_{J_C=|L-1|}^{L+1}\sum_{l,l'}\sum_{i,j}\frac{8\pi\,\lambda_i\,e^2\,f^2\,\omega}{m_N\,m_\pi^2}\sqrt{\frac{\pi}{3}}\,i^{L+L'}\,(-1)^{J_C-M_i-\lambda_i+i+j}$$
$$\times\left(\mu_p+(-1)^{L}\,\mu_n\right)\,(\hat{\epsilon}^*_{\lambda_f})_{-i}\,Y^*_{L'\,M_f-M_i-\lambda_i-i}(\hat{k}_f)\,\sqrt{2\pi\,(L+1)}$$
$$\times\iint r\,dr\,r'\,dr'\,u_l(r)\,j_{L-1}(\frac{\omega r}{2})\,G_{\hat{C}}(r,r';E_0)\,j_{L'}(\frac{\omega r'}{2})\,u_{l'}(r')\,\frac{\partial}{\partial r'}f^{\mathrm{KR}}_s(r')$$
$$\times\langle\,l'\,1\,1\,M_f\,|\,\sigma_{2\,j}\,\sigma_{1\,i}\,Y_{1\,-j}\,Y_{L'\,M_f-M_i-\lambda_i-i}\,|\,J_C\,0\,J_C\,M_i+\lambda_i\,\rangle$$
$$\times\langle\,J_C\,0\,J_C\,\|\,[Y_{L-1}\otimes t]_L\,\|\,l\,1\,1\,\rangle\,\begin{pmatrix}J_C & L & 1\\ -M_i-\lambda_i & \lambda_i & M_i\end{pmatrix}\,\left((-1)^{L'}-1\right) \tag{I.22}$$

$$\mathcal{M}^{\mathrm{KR}\,\sigma 1\,c}_{fi} = \sum_{L=1}^{\infty}\sum_{L'=0}^{\infty}\sum_{J_C=|L-1|}^{L+1}\sum_{l,l'}\sum_{i,j}\frac{8\pi\,\lambda_i\,e^2\,f^2\,\omega}{m_N\,m_\pi^2}\sqrt{\frac{\pi}{3}}\,i^{L+L'}\,(-1)^{-M_f+i+j}$$
$$\times\left(\mu_p+(-1)^{L}\,\mu_n\right)\,(\hat{\epsilon}^*_{\lambda_f})_{-i}\,Y^*_{L'\,M_f-M_i-\lambda_i-i}(\hat{k}_f)\,\sqrt{2\pi\,(L+1)}$$
$$\times\iint r\,dr\,r'\,dr'\,u_{l'}(r)\,j_{L-1}(\frac{\omega r}{2})\,G_{\hat{C}}(r,r';E'_0)\,j_{L'}(\frac{\omega r'}{2})\,u_l(r')\,\frac{\partial}{\partial r'}f^{\mathrm{KR}}_u(r')$$
$$\times\begin{pmatrix}1 & L & J_C\\ -M_f & \lambda_i & M_f-\lambda_i\end{pmatrix}\,\langle\,l'\,1\,1\,\|\,[Y_{L-1}\otimes t]_L\,\|\,J_C\,0\,J_C\,\rangle \tag{I.23}$$
$$\times\langle\,J_C\,0\,J_C\,M_f-\lambda_i\,|\,\sigma_{2\,j}\,\sigma_{1\,i}\,Y_{1\,-j}\,Y_{L'\,M_f-M_i-\lambda_i-i}\,|\,l\,1\,1\,M_i\,\rangle\,\left((-1)^{L'}-1\right)$$

$$\mathcal{M}^{\mathrm{KR}\,\sigma 1\,d}_{fi} = \sum_{L=0}^{\infty}\sum_{L'=1}^{\infty}\sum_{J_C=|L'-1|}^{L'+1}\sum_{l,l'}\sum_{i,j}\frac{4\pi\,\lambda_f\,e^2\,f^2\,\omega}{m_N\,m_\pi^2}\sqrt{\frac{\pi}{3}}\,i^{L+L'}\,(-1)^{L'-\lambda_f+1+j+J_C-M_f}$$
$$\times\left(\mu_p+(-1)^{L'}\,\mu_n\right)\,(\hat{\epsilon}_{\lambda_i})_{-i}\,d^{L'}_{M_f-M_i-i,-\lambda_f}(\theta)\,\sqrt{2\,(L'+1)\,(2L+1)}$$
$$\times\iint r\,dr\,r'\,dr'\,u_l(r')\,j_{L'-1}(\frac{\omega r'}{2})\,G_{\hat{C}}(r,r';E'_0)\,j_L(\frac{\omega r}{2})\,u_{l'}(r)\,\frac{\partial}{\partial r}f^{\mathrm{KR}}_u(r)$$
$$\times\langle\,l'\,1\,1\,M_f\,|\,\sigma_{2\,j}\,\sigma_{1\,i}\,Y_{1\,-j}\,Y_{L\,0}\,|\,J_C\,0\,J_C\,M_f-i\,\rangle \tag{I.24}$$
$$\times\langle\,J_C\,0\,J_C\,\|\,[Y_{L'-1}\otimes t]_{L'}\,\|\,l\,1\,1\,\rangle\,\begin{pmatrix}J_C & L' & 1\\ -M_f+i & M_f-M_i-i & M_i\end{pmatrix}\,\left(1-(-1)^L\right)$$

In $\mathcal{M}_{fi}^{\mathrm{KR}\,\sigma 1\,b,d}$ we used

$$\frac{1}{2}\langle\, p\,n - n\,p \mid (\vec{\tau}_1 \times \vec{\tau}_2)_z \mid p\,n + n\,p\,\rangle = 2\,i. \tag{I.25}$$

We turn now to the calculation of $\mathcal{M}_{fi}^{\phi\,\mathrm{KR1}}$ and $\mathcal{M}_{fi}^{\phi\,\mathrm{KR2}}$, going beyond Ref. [24]. First we demonstrate the isospin-changing character of $\phi(\vec{x}_p)$. Therefore, we explicitly write the isospin-dependence of ϕ, as we did in Eq. (G.24) and evaluate this operator between two isospin wave functions with $T = 0$ and $T = 1$, respectively.

$$\begin{aligned}
&\frac{1}{2}\,\langle\, p\,n - n\,p \mid \sum_{j=1,2} \frac{1}{2}\,(1+\tau_z^j)\,\phi(\vec{x}_j) \mid p\,n + n\,p\,\rangle \\
=&\frac{1}{4}\,\langle\, p\,n - n\,p \mid \tau_z^1\,\phi(\vec{x}_1) + \tau_z^2\,\phi(\vec{x}_2) \mid p\,n + n\,p\,\rangle \\
=&\frac{1}{2}\,(\phi(\vec{x}_1) - \phi(\vec{x}_2)) = \frac{1}{2}\,(\phi(\vec{r}/2) - \phi(-\vec{r}/2))
\end{aligned} \tag{I.26}$$

The last step reflects our usual choice $\vec{x}_1 = \frac{\vec{r}}{2},\ \vec{x}_2 = -\frac{\vec{r}}{2}$. The only angular operator contained in ϕ is Y_L. As we need an isospin-changing matrix element, L has to be odd, which follows from Eq. (L.38), see also Section 6.1.2. Due to this observation and the definition of $\phi(\vec{r})$, Eq. (6.4), which implies $\phi_{L\,\mathrm{odd}}(-\vec{r}/2) = -\phi_{L\,\mathrm{odd}}(\vec{r}/2)$, we may replace $\frac{1}{2}\,(\phi(\vec{r}/2) - \phi(-\vec{r}/2)) \to \phi(\vec{r}/2)$ in the following. An explicit proof of our claim L odd is given after Eq. (I.30).

We start with the calculation of $\mathcal{M}_{fi}^{\phi\,\mathrm{KR1}}$. The four amplitudes follow immediately from Eq. (6.56):

$$\begin{aligned}
\mathcal{M}_{fi}^{\phi\,\mathrm{KR1}\,a} &= i\,\left(\omega + \frac{\omega^2}{2m_d}\right) \sum_C \frac{\langle\, d_f \mid \hat{\phi}_f \mid C\,\rangle\langle\, C \mid H_s^{\mathrm{int}\,\mathrm{KR1}} \mid d_i\,\rangle}{\omega + \frac{\omega^2}{2m_d} - B - E_C} \\
\mathcal{M}_{fi}^{\phi\,\mathrm{KR1}\,b} &= -i\,\left(\omega + \frac{\omega^2}{2m_d}\right) \sum_C \frac{\langle\, d_f \mid H_s^{\mathrm{int}\,\mathrm{KR1}} \mid C\,\rangle\langle\, C \mid \hat{\phi}_i \mid d_i\,\rangle}{\omega + \frac{\omega^2}{2m_d} - B - E_C} \\
\mathcal{M}_{fi}^{\phi\,\mathrm{KR1}\,c} &= -i\,\left(\omega - \frac{\omega^2}{2m_d} + \frac{\vec{P}_C^{\,2}}{2m_C}\right) \sum_C \frac{\langle\, d_f \mid \hat{\phi}_i \mid C\,\rangle\langle\, C \mid H_u^{\mathrm{int}\,\mathrm{KR1}} \mid d_i\,\rangle}{-\omega + \frac{\omega^2}{2m_d} - \frac{\vec{P}_C^{\,2}}{2m_C} - B - E_C} \\
\mathcal{M}_{fi}^{\phi\,\mathrm{KR1}\,d} &= i\,\left(\omega - \frac{\omega^2}{2m_d} + \frac{\vec{P}_C^{\,2}}{2m_C}\right) \sum_C \frac{\langle\, d_f \mid H_u^{\mathrm{int}\,\mathrm{KR1}} \mid C\,\rangle\langle\, C \mid \hat{\phi}_f \mid d_i\,\rangle}{-\omega + \frac{\omega^2}{2m_d} - \frac{\vec{P}_C^{\,2}}{2m_C} - B - E_C}
\end{aligned} \tag{I.27}$$

Now we have to specify $H^{\mathrm{int}\,\mathrm{KR1}}$, which is achieved by replacing $\vec{A}$ by $\vec{A}^{(1)}$ in Eq. (I.10). We find, using Eq. (F.17),

$$\begin{aligned}
H_{s,u}^{\mathrm{int}\,\mathrm{KR1}} = &\sum_{\vec{k},\lambda} \sum_{L=1}^{\infty} \sum_{M=-L}^{L} \frac{e\,f^2}{m_\pi^2}\,(\vec{\tau}_1 \times \vec{\tau}_2)_z\,\lambda\,\sqrt{2\pi\,(2L+1)}\,i^L\,j_L(\frac{\omega r}{2})\,\Big[a_{\vec{k},\lambda}\,\delta_{M,\lambda} \\
&- a_{\vec{k},\lambda}^\dagger\,(-1)^{L+\lambda}\,d_{M,-\lambda}^L(\theta)\Big]\,\Big\{(\vec{\sigma}_1 \cdot \vec{T}_{L\,L\,M}(\vec{x}_1))\,(\vec{\sigma}_2 \cdot \hat{r}) + (\vec{\sigma}_2 \cdot \vec{T}_{L\,L\,M}(\vec{x}_2))\,(\vec{\sigma}_1 \cdot \hat{r})\Big\}\,\frac{\partial}{\partial r} f_{s,u}^{\mathrm{KR}}(r).
\end{aligned} \tag{I.28}$$

The scalar products are expanded into spherical components, according to Eq. (H.2).

$$\begin{aligned}
H_{s,u}^{\mathrm{int}\,\mathrm{KR1}} = &-\sum_{\vec{k},\lambda} \sum_{L=1}^{\infty} \sum_{M=-L}^{L} \sum_{i,j} \frac{2\pi\,e\,f^2}{m_\pi^2}\,(\vec{\tau}_1 \times \vec{\tau}_2)_z\,(-1)^{j-L-M}\,i^L\,\sqrt{\frac{2}{3}}\,\lambda\,(2L+1)\,j_L(\frac{\omega r}{2}) \\
&\times \Big[a_{\vec{k},\lambda}\,\delta_{M,\lambda} - a_{\vec{k},\lambda}^\dagger\,(-1)^{L+\lambda}\,d_{M,-\lambda}^L(\theta)\Big]\,\begin{pmatrix} L & 1 & L \\ M-i & i & -M \end{pmatrix} \\
&\times \sigma_{2\,j}\,\sigma_{1\,i}\,Y_{1\,-j}\,Y_{L\,M-i}\,\left(1 + (-1)^L\right)\,\frac{\partial}{\partial r} f_{s,u}^{\mathrm{KR}}(r)
\end{aligned} \tag{I.29}$$

Here we used the fact that the matrix element arising from ϕ does not change the spin, i.e. $S_C = 1$ in the following amplitudes, and the symmetry of $\sigma_{2\,j}\,\sigma_{1\,i}$ under $1 \leftrightarrow 2$ for spin-conserving matrix elements, as observed in Eq. (G.35). Therefore, the Hamiltonian (I.29) only holds for spin-conserving matrix elements.

Now the evaluation of the amplitudes (I.27) is straightforward and very similar to the calculation of $\mathcal{M}_{fi}^{\mathrm{KR}\,\sigma 1}$. Therefore we only give the results.

$$\begin{aligned}
\mathcal{M}_{fi}^{\phi\,\mathrm{KR}1\,a} = &\sum_{L=1}^{\infty}\sum_{L'=1}^{\infty}\sum_{J_C=|L'-1|}^{L'+1}\sum_{L_C=|J_C-1|}^{J_C+1}\sum_{l,l'}\sum_{i,j}\frac{8\pi\,e^2\,f^2}{m_\pi^2}\left(1+\frac{\omega}{2m_d}\right)\\
&\times(-1)^{L'-L-\lambda_f-\lambda_i+j-M_f}\,i^{L+L'+1}\,\lambda_i\,d^{L'}_{M_f-M_i-\lambda_i,-\lambda_f}(\theta)\,(2L+1)\sqrt{\frac{\pi\,(2L'+1)}{3\,L'\,(L'+1)}}\\
&\times\iint r\,dr\,r'\,dr'\,u_{l'}(r')\,\psi_{L'}(\frac{\omega r'}{2})\,G_{\hat{C}}(r,r';E_0)\,j_L(\frac{\omega r}{2})\,u_l(r)\,\frac{\partial}{\partial r'}f_s^{\mathrm{KR}}(r)\\
&\times\begin{pmatrix} L & 1 & L\\ \lambda_i-i & i & -\lambda_i\end{pmatrix}\begin{pmatrix} 1 & L' & J_C\\ -M_f & M_f-M_i-\lambda_i & M_i+\lambda_i\end{pmatrix}\langle\, l'\,1\,1\,\|\,Y_{L'}\,\|\,L_C\,1\,J_C\,\rangle\\
&\times\langle\, L_C\,1\,J_C\,M_i+\lambda_i\,|\,\sigma_{2\,j}\,\sigma_{1\,i}\,Y_{1\,-j}\,Y_{L\,\lambda_i-i}\,|\,l\,1\,1\,M_i\,\rangle\,\left(1+(-1)^L\right)
\end{aligned}\tag{I.30}$$

Before we write down the remaining amplitudes we prove explicitly our claim in the context of Eq. (I.26) that L' has to be an odd number. The last bracket of Eq. (I.30) demands L even. From Eq. (L.21) we know that the index L'', which is summed over in Eq. (G.35), has to be odd and from $\langle\, L_C\,\|\,Y_{L''}\,\|\,l\,\rangle$ follows that L_C has to be an odd number too, cf. Eq. (L.34), because l is even. That is exactly what we need, as $L_C + S_C + T_C$ has to be odd (cf. Section 6.1.2) and $S_C = T_C = 1$. Eq. (L.37) then tells us that in fact L', the orbital angular momentum number of ϕ, has to be an odd number. This also holds in the following three amplitudes, albeit we don't show it explicitly. These are

$$\begin{aligned}
\mathcal{M}_{fi}^{\phi\,\mathrm{KR}1\,b} = &\sum_{L=1}^{\infty}\sum_{L'=1}^{\infty}\sum_{J_C=|L-1|}^{L+1}\sum_{L_C=|J_C-1|}^{J_C+1}\sum_{l,l'}\sum_{i,j}\frac{8\pi\,e^2\,f^2}{m_\pi^2}\left(1+\frac{\omega}{2m_d}\right)\\
&\times(-1)^{1-\lambda_f+j-M_f+J_C}\,i^{L+L'+1}\,\lambda_f\,d^{L'}_{M_f-M_i-\lambda_i,-\lambda_f}(\theta)\,(2L'+1)\sqrt{\frac{\pi\,(2L+1)}{3\,L\,(L+1)}}\\
&\times\iint r\,dr\,r'\,dr'\,u_l(r)\,\psi_L(\frac{\omega r}{2})\,G_{\hat{C}}(r,r';E_0)\,j_{L'}(\frac{\omega r'}{2})\,u_{l'}(r')\,\frac{\partial}{\partial r'}f_s^{\mathrm{KR}}(r')\\
&\times\begin{pmatrix} L' & 1 & L'\\ M_f-M_i-\lambda_i-i & i & -M_f+M_i+\lambda_i\end{pmatrix}\begin{pmatrix} J_C & L & 1\\ -M_i-\lambda_i & \lambda_i & M_i\end{pmatrix}\left(1+(-1)^{L'}\right)\\
&\times\langle\, l'\,1\,1\,M_f\,|\,\sigma_{2\,j}\,\sigma_{1\,i}\,Y_{1\,-j}\,Y_{L'\,M_f-M_i-\lambda_i-i}\,|\,L_C\,1\,J_C\,M_i+\lambda_i\,\rangle\,\langle\, L_C\,1\,J_C\,\|\,Y_L\,\|\,l\,1\,1\,\rangle,
\end{aligned}\tag{I.31}$$

$$\begin{aligned}
\mathcal{M}_{fi}^{\phi\,\mathrm{KR}1\,c} = &\sum_{L=1}^{\infty}\sum_{L'=1}^{\infty}\sum_{J_C=|L-1|}^{L+1}\sum_{L_C=|J_C-1|}^{J_C+1}\sum_{l,l'}\sum_{i,j}\frac{8\pi\,e^2\,f^2}{m_\pi^2\,\omega}\left(\omega-\frac{\omega^2}{2m_d}+\frac{\vec{P}_C^{\,2}}{2m_C}\right)\\
&\times(-1)^{1-\lambda_f+\lambda_i+j+M_i}\,i^{L+L'+1}\,\lambda_f\,d^{L'}_{M_f-M_i-\lambda_i,-\lambda_f}(\theta)\,(2L'+1)\sqrt{\frac{\pi\,(2L+1)}{3\,L\,(L+1)}}\\
&\times\iint r\,dr\,r'\,dr'\,u_{l'}(r)\,\psi_L(\frac{\omega r}{2})\,G_{\hat{C}}(r,r';E_0')\,j_{L'}(\frac{\omega r'}{2})\,u_l(r')\,\frac{\partial}{\partial r'}f_u^{\mathrm{KR}}(r')\\
&\times\begin{pmatrix} L' & 1 & L'\\ M_f-M_i-\lambda_i-i & i & -M_f+M_i+\lambda_i\end{pmatrix}\begin{pmatrix} 1 & L & J_C\\ -M_f & \lambda_i & M_f-\lambda_i\end{pmatrix}\left(1+(-1)^{L'}\right)\\
&\times\langle\, l'\,1\,1\,\|\,Y_L\,\|\,L_C\,1\,J_C\,\rangle\,\langle\, L_C\,1\,J_C\,M_f-\lambda_i\,|\,\sigma_{2\,j}\,\sigma_{1\,i}\,Y_{1\,-j}\,Y_{L'\,M_f-M_i-\lambda_i-i}\,|\,l\,1\,1\,M_i\,\rangle,
\end{aligned}\tag{I.32}$$

$$\mathcal{M}_{fi}^{\phi\,\mathrm{KR1}\,d} = \sum_{L=1}^{\infty}\sum_{L'=1}^{\infty}\sum_{J_C=|L'-1|}^{L'+1}\sum_{L_C=|J_C-1|}^{J_C+1}\sum_{l,l'}\sum_{i,j}\frac{8\pi\,e^2\,f^2}{m_\pi^2\,\omega}\left(\omega-\frac{\omega^2}{2m_d}+\frac{\vec{P}_C^{\,2}}{2m_C}\right)$$
$$\times(-1)^{j-L+L'-\lambda_f+J_C-M_f}\,i^{L+L'+1}\,\lambda_i\,d^{L'}_{M_f-M_i-\lambda_i,-\lambda_f}(\theta)\,(2L+1)\sqrt{\frac{\pi\,(2L'+1)}{3\,L'\,(L'+1)}}$$
$$\times\iint r\,dr\,r'\,dr'\,u_l(r')\,\psi_{L'}(\frac{\omega r'}{2})\,G_{\hat{C}}(r,r';E_0')\,j_L(\frac{\omega r}{2})\,u_{l'}(r)\,\frac{\partial}{\partial r}f_u^{\mathrm{KR}}(r) \qquad \text{(I.33)}$$
$$\times\begin{pmatrix} L & 1 & L\\ \lambda_i-i & i & -\lambda_i\end{pmatrix}\begin{pmatrix} J_C & L' & 1\\ -M_f+\lambda_i & M_f-M_i-\lambda_i & M_i\end{pmatrix}\left(1+(-1)^L\right)$$
$$\times\langle\,l'\,1\,1\,M_f\mid\sigma_{2\,j}\,\sigma_{1\,i}\,Y_{1\,-j}\,Y_{L\,\lambda_i-i}\mid L_C\,1\,J_C\,M_f-\lambda_i\,\rangle\,\langle\,L_C\,1\,J_C\parallel Y_{L'}\parallel l\,1\,1\,\rangle.$$

Finally, we need $H_{s,u}^{\mathrm{int\,KR2}}$ in order to calculate the amplitudes $\mathcal{M}_{fi}^{\phi\,\mathrm{KR2}}$. We replace $\vec{A}$ by $\vec{A}^{(2)}$ in Eq. (I.10) and find

$$H_{s,u}^{\mathrm{int\,KR2}} = \sum_{\vec{k},\lambda}\sum_{L=1}^{\infty}\sum_{M=-L}^{L}\frac{e\,f^2\,\omega}{m_\pi^2}\,(\vec{\tau}_1\times\vec{\tau}_2)_z\,\sqrt{\frac{2\pi\,(2L+1)}{L\,(L+1)}}\,i^{L+1}\,j_L(\frac{\omega r}{2})\,\Big[a_{\vec{k},\lambda}\,\delta_{M,\lambda}$$
$$-\,a^\dagger_{\vec{k},\lambda}\,(-1)^{L+\lambda}\,d^L_{M,-\lambda}(\theta)\Big]\,\{(\vec{\sigma}_1\cdot\vec{x}_1)\,(\vec{\sigma}_2\cdot\hat{r})\,Y_{L\,M}(\vec{x}_1)+(\vec{\sigma}_2\cdot\vec{x}_2)\,(\vec{\sigma}_1\cdot\hat{r})\,Y_{L\,M}(\vec{x}_2)\}\,\frac{\partial}{\partial r}f_{s,u}^{\mathrm{KR}}(r). \qquad \text{(I.34)}$$

We substitute $\vec{x}_1\to\frac{\vec{r}}{2}=\frac{r}{2}\cdot\hat{r}$, $\vec{x}_2\to-\frac{r}{2}\cdot\hat{r}$ and combine the two spherical harmonics resulting from $(\vec{\sigma}_1\cdot\hat{r})\,(\vec{\sigma}_2\cdot\hat{r})$ via Eq. (L.26). The result is, again assuming spin conservation,

$$H_{s,u}^{\mathrm{int\,KR2}} = \sum_{\vec{k},\lambda}\sum_{L=1}^{\infty}\sum_{M=-L}^{L}\sum_{J=0,2}\sum_{i,j}\frac{2\pi\,e\,f^2\,\omega}{m_\pi^2}\,(\vec{\tau}_1\times\vec{\tau}_2)_z\,i^{L+1}\,\sqrt{\frac{(2L+1)\,(2J+1)}{2\,L\,(L+1)}}\,j_L(\frac{\omega r}{2})$$
$$\times\Big[a_{\vec{k},\lambda}\,\delta_{M,\lambda}-a^\dagger_{\vec{k},\lambda}\,(-1)^{L+\lambda}\,d^L_{M,-\lambda}(\theta)\Big]\begin{pmatrix}1&1&J\\0&0&0\end{pmatrix}\begin{pmatrix}1&1&J\\-i&-j&i+j\end{pmatrix}$$
$$\times\sigma_{2\,j}\,\sigma_{1\,i}\,Y_{J\,-i-j}\,Y_{L\,M}\,\left(1-(-1)^L\right)\,r\frac{\partial}{\partial r}f_{s,u}^{\mathrm{KR}}(r). \qquad \text{(I.35)}$$

The amplitudes are identical to Eq. (I.27), except for $H^{\mathrm{int\,KR1}}\to H^{\mathrm{int\,KR2}}$. Therefore we can immediately write down the results:

$$M_{fi}^{\phi\,\mathrm{KR2}\,a} = \sum_{L=1}^{\infty}\sum_{L'=1}^{\infty}\sum_{J_C=|L'-1|}^{L'+1}\sum_{L_C=|J_C-1|}^{J_C+1}\sum_{J=0,2}\sum_{l,l'}\sum_{i,j}\frac{4\pi\,e^2\,f^2}{m_\pi^2}\left(\omega+\frac{\omega^2}{2m_d}\right)$$
$$\times(-1)^{L'-\lambda_f-M_f}\,i^{L+L'}\,d^{L'}_{M_f-M_i-\lambda_i,-\lambda_f}(\theta)\sqrt{\frac{\pi\,(2L+1)\,(2L'+1)\,(2J+1)}{L\,(L+1)\,L'\,(L'+1)}}$$
$$\times\iint r\,dr\,r'\,dr'\,u_{l'}(r')\,\psi_{L'}(\frac{\omega r'}{2})\,G_{\hat{C}}(r,r';E_0)\,j_L(\frac{\omega r}{2})\,u_l(r)\,r\frac{\partial}{\partial r}f_s^{\mathrm{KR}}(r)$$
$$\times\begin{pmatrix}1&L'&J_C\\-M_f&M_f-M_i-\lambda_i&M_i+\lambda_i\end{pmatrix}\begin{pmatrix}1&1&J\\0&0&0\end{pmatrix}\begin{pmatrix}1&1&J\\-i&-j&i+j\end{pmatrix}\left(1-(-1)^L\right)$$
$$\times\langle\,l'\,1\,1\parallel Y_{L'}\parallel L_C\,1\,J_C\,\rangle\,\langle\,L_C\,1\,J_C\,M_i+\lambda_i\mid\sigma_{2\,j}\,\sigma_{1\,i}\,Y_{J\,-i-j}\,Y_{L\,\lambda_i}\mid l\,1\,1\,M_i\,\rangle \qquad \text{(I.36)}$$

Obviously, L has to be an odd number. J is even, which means L_C has to be odd, as well as L'. Therefore our prediction of odd angular quantum numbers for ϕ still holds.

The remaining three amplitudes are:

$$
\begin{aligned}
M_{fi}^{\phi\,\mathrm{KR2}\,b} = & \sum_{L=1}^{\infty}\sum_{L'=1}^{\infty}\sum_{J_C=|L-1|}^{L+1}\sum_{L_C=|J_C-1|}^{J_C+1}\sum_{J=0,2}\sum_{l,l'}\sum_{i,j}\frac{4\pi\,e^2\,f^2}{m_\pi^2}\left(\omega+\frac{\omega^2}{2m_d}\right)\\
&\times(-1)^{1+L'-\lambda_f-\lambda_i+J_C-M_i}\,i^{L+L'}\,d^{L'}_{M_f-M_i-\lambda_i,-\lambda_f}(\theta)\sqrt{\frac{\pi\,(2L+1)\,(2L'+1)\,(2J+1)}{L\,(L+1)\,L'\,(L'+1)}}\\
&\times\iint r\,dr\,r'\,dr'\,u_l(r)\,\psi_L(\frac{\omega r}{2})\,G_{\hat{C}}(r,r';E_0)\,j_{L'}(\frac{\omega r'}{2})\,u_{l'}(r')\,r'\frac{\partial}{\partial r'}f_s^{\mathrm{KR}}(r')\\
&\times\begin{pmatrix} J_C & L & 1\\ -M_i-\lambda_i & \lambda_i & M_i\end{pmatrix}\begin{pmatrix}1&1&J\\0&0&0\end{pmatrix}\begin{pmatrix}1&1&J\\-i&-j&i+j\end{pmatrix}\left(1-(-1)^{L'}\right)\\
&\times\langle\,l'\,1\,1\,M_f\mid\sigma_{2\,j}\,\sigma_{1\,i}\,Y_{J\,-i-j}\,Y_{L'\,M_f-M_i-\lambda_i}\mid L_C\,1\,J_C\,M_i+\lambda_i\,\rangle\,\langle\,L_C\,1\,J_C\parallel Y_L\parallel l\,1\,1\,\rangle
\end{aligned}
\tag{I.37}
$$

$$
\begin{aligned}
M_{fi}^{\phi\,\mathrm{KR2}\,c} = & \sum_{L=1}^{\infty}\sum_{L'=1}^{\infty}\sum_{J_C=|L-1|}^{L+1}\sum_{L_C=|J_C-1|}^{J_C+1}\sum_{J=0,2}\sum_{l,l'}\sum_{i,j}\frac{4\pi\,e^2\,f^2}{m_\pi^2}\left(\omega-\frac{\omega^2}{2m_d}+\frac{\vec{P}_C^{\,2}}{2m_C}\right)\\
&\times(-1)^{1+L'-\lambda_f-M_f}\,i^{L+L'}\,d^{L'}_{M_f-M_i-\lambda_i,-\lambda_f}(\theta)\sqrt{\frac{\pi\,(2L+1)\,(2L'+1)\,(2J+1)}{L\,(L+1)\,L'\,(L'+1)}}\\
&\times\iint r\,dr\,r'\,dr'\,u_{l'}(r)\,\psi_L(\frac{\omega r}{2})\,G_{\hat{C}}(r,r';E_0')\,j_{L'}(\frac{\omega r'}{2})\,u_l(r')\,r'\frac{\partial}{\partial r'}f_u^{\mathrm{KR}}(r')\\
&\times\begin{pmatrix} 1 & L & J_C\\ -M_f & \lambda_i & M_f-\lambda_i\end{pmatrix}\begin{pmatrix}1&1&J\\0&0&0\end{pmatrix}\begin{pmatrix}1&1&J\\-i&-j&i+j\end{pmatrix}\left(1-(-1)^{L'}\right)\\
&\times\langle\,l'\,1\,1\parallel Y_L\parallel L_C\,1\,J_C\,\rangle\,\langle\,L_C\,1\,J_C\,M_f-\lambda_i\mid\sigma_{2\,j}\,\sigma_{1\,i}\,Y_{J\,-i-j}\,Y_{L'\,M_f-M_i-\lambda_i}\mid l\,1\,1\,M_i\,\rangle
\end{aligned}
\tag{I.38}
$$

$$
\begin{aligned}
M_{fi}^{\phi\,\mathrm{KR2}\,d} = & \sum_{L=1}^{\infty}\sum_{L'=1}^{\infty}\sum_{J_C=|L'-1|}^{L'+1}\sum_{L_C=|J_C-1|}^{J_C+1}\sum_{J=0,2}\sum_{l,l'}\sum_{i,j}\frac{4\pi\,e^2\,f^2}{m_\pi^2}\left(\omega-\frac{\omega^2}{2m_d}+\frac{\vec{P}_C^{\,2}}{2m_C}\right)\\
&\times(-1)^{L'-\lambda_f+\lambda_i+J_C-M_f}\,i^{L+L'}\,d^{L'}_{M_f-M_i-\lambda_i,-\lambda_f}(\theta)\sqrt{\frac{\pi\,(2L+1)\,(2L'+1)\,(2J+1)}{L\,(L+1)\,L'\,(L'+1)}}\\
&\times\iint r\,dr\,r'\,dr'\,u_l(r')\,\psi_{L'}(\frac{\omega r'}{2})\,G_{\hat{C}}(r,r';E_0')\,j_L(\frac{\omega r}{2})\,u_{l'}(r)\,r\frac{\partial}{\partial r}f_u^{\mathrm{KR}}(r)\\
&\times\begin{pmatrix} J_C & L' & 1\\ -M_f+\lambda_i & M_f-M_i-\lambda_i & M_i\end{pmatrix}\begin{pmatrix}1&1&J\\0&0&0\end{pmatrix}\begin{pmatrix}1&1&J\\-i&-j&i+j\end{pmatrix}\left(1-(-1)^{L}\right)\\
&\times\langle\,l'\,1\,1\,M_f\mid\sigma_{2\,j}\,\sigma_{1\,i}\,Y_{J\,-i-j}\,Y_{L\,\lambda_i}\mid L_C\,1\,J_C\,M_f-\lambda_i\,\rangle\,\langle\,L_C\,1\,J_C\parallel Y_{L'}\parallel l\,1\,1\,\rangle
\end{aligned}
\tag{I.39}
$$

Appendix J

Corrections to the Charge Density

In this appendix we give an estimate which shows that we do not need to take into account corrections to the charge density due to meson exchange, cf. Sect. 6.1.1. As we found that only the Kroll-Ruderman current (Fig. 6.2) gives non-negligible contributions, we assume that we may also neglect the charge density corresponding to the pion-pole current. Nevertheless we briefly demonstrate the small size of this term.

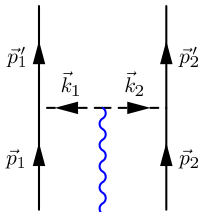

Figure J.1: Momenta in the coupling of a photon to the pion-pole current.

The pion-pole current is proportional to $\vec{k}_1 - \vec{k}_2$, with $\vec{k}_1$, $\vec{k}_2$ the momenta transferred to nucleon 1 and 2, see Fig. J.1. Therefore, $\rho_{\rm ex}^{\rm pion-pole} \propto k_1^0 - k_2^0 = p_1'^0 - p_1^0 - (p_2'^0 - p_2^0) = p_1'^0 - p_2'^0 - (p_1^0 - p_2^0)$ with $p_i^0 = \sqrt{m_N^2 + \vec{p}_i^{\,2}} \approx m_N + \frac{\vec{p}_i^{\,2}}{2m_N}$. In the limit of a static deuteron, which is assumed throughout the whole work, except for energy denominators, the kinetic energies of the two nucleons are equal and $k_1^0 - k_2^0$ vanishes. We therefore conclude that we only have to take care of $\rho_{\rm ex}^{\rm KR}$, which is the charge density corresponding to the Kroll-Ruderman current.

First we derive an explicit expression for $\rho_{\rm ex}^{\rm KR}$. The $\gamma\pi N$-vertex is proportional to $\epsilon \cdot S$ with the Pauli-Lubanski spin vector defined as, see e.g. [35],

$$S^\mu = \frac{i}{2}\,\gamma_5\,\sigma^{\mu\nu}\,v_\nu, \tag{J.1}$$

where $\sigma^{\mu\nu} = \frac{i}{2}\,[\gamma^\mu, \gamma^\nu]$. We use $\gamma_5 = \begin{pmatrix} 0 & 1 \\ 1 & 0 \end{pmatrix}$ and $\sigma^{0i} = i \begin{pmatrix} 0 & \sigma^i \\ \sigma^i & 0 \end{pmatrix}$, cf. e.g. [36]. The four-velocity v^ν is [109]

$$v^\nu = \begin{pmatrix} \frac{1}{\sqrt{1-v^2/c^2}} \\ \frac{\vec{v}}{c\sqrt{1-v^2/c^2}} \end{pmatrix}, \tag{J.2}$$

which in the static limit reduces to

$$v_\nu^{\text{stat}} = \begin{pmatrix} 1 \\ 0 \\ 0 \\ 0 \end{pmatrix}. \tag{J.3}$$

In this limit we find for the spin vector

$$S^\mu = \frac{i}{2}\,\gamma_5\,\sigma^{\mu 0} = \frac{1}{2}\begin{pmatrix} 0 & \\ \begin{pmatrix} \vec{\sigma} & 0 \\ 0 & \vec{\sigma} \end{pmatrix} & \end{pmatrix}, \tag{J.4}$$

which means that in the non-relativistic reduction we may replace $\vec{S} \to \frac{1}{2}\,\vec{\sigma}$, i.e. $\vec{J}^{\text{KR}} \propto \vec{\sigma}$, in agreement with Eq. (6.73). Our task is therefore to calculate the leading contribution to S^0. Approximating $\frac{v^2}{c^2} \approx 0$ and returning to units with $c = 1$, we find

$$S^0 = \frac{i}{2}\,\gamma_5\,\sigma^{0\nu}\,v_\nu = -\frac{i}{2}\,\gamma_5\,\sigma^{0i}\,v_i \approx \frac{1}{2}\begin{pmatrix} \vec{\sigma}\cdot\vec{v} & 0 \\ 0 & \vec{\sigma}\cdot\vec{v} \end{pmatrix}. \tag{J.5}$$

Therefore we have to replace

$$S^0 \to \frac{1}{2}\,\vec{\sigma}\cdot\vec{v} = \frac{1}{2}\,\vec{\sigma}\cdot\frac{\vec{p}}{m_N}, \tag{J.6}$$

which leads us to [57]

$$\rho_{\text{ex}}^{\text{KR}}(\vec{k}_1,\vec{k}_2) = -i\,e\left(\frac{4\pi\,f^2}{m_N\,m_\pi^2}\right)(\vec{\tau}_1\times\vec{\tau}_2)_z\left\{\frac{(\vec{\sigma}_1\cdot\vec{p}_1)\,(\vec{\sigma}_2\cdot\vec{k}_2)}{\vec{k}_2^{\,2}+m_\pi^2} - \frac{(\vec{\sigma}_2\cdot\vec{p}_2)\,(\vec{\sigma}_1\cdot\vec{k}_1)}{\vec{k}_1^{\,2}+m_\pi^2}\right\}, \tag{J.7}$$

or, in position space,

$$\begin{aligned}\rho_{\text{ex}}^{\text{KR}}(\vec{\xi};\vec{x}_1,\vec{x}_2) = \frac{e\,f^2}{m_N\,m_\pi^2}\,(\vec{\tau}_1\times\vec{\tau}_2)_z\,\Big\{&\delta(\vec{x}_1-\vec{\xi})\,(\vec{\sigma}_2\cdot\hat{r})\,(\vec{\sigma}_1\cdot\vec{p}_1)\\ &+\,\delta(\vec{x}_2-\vec{\xi})\,(\vec{\sigma}_1\cdot\hat{r})\,(\vec{\sigma}_2\cdot\vec{p}_2)\Big\}\,\frac{\partial}{\partial r}\frac{\mathrm{e}^{-m_\pi r}}{r}.\end{aligned} \tag{J.8}$$

We neglect the correction to $\frac{\mathrm{e}^{-m_\pi r}}{r}$ described in App. I, as we only want to give an estimate for the size of corrections due to the meson-exchange charge density.

Now we have to think about how to include ρ^{ex} into the calculation. In the long-wavelength limit, the photon cannot resolve the deuteron, i.e. the deuteron appears as a charged, pointlike, static object to the photon. Therefore also the nucleons appear to be static in this limit and Siegert's hypothesis [84] guarantees that the γd scattering amplitude is described by $\rho^0(\vec{\xi})$ only, whereas meson-exchange effects cannot be resolved. Thus ρ^{ex} does not contribute in the static limit. However this does not need to be the case for non-zero photon energies. In the high-energy regime of our calculation, say in the order of $\omega \sim 100$ MeV, we found the amplitudes containing the structure $\langle\, d_f \mid \hat{\phi} \mid C\,\rangle\langle\, C \mid \hat{\phi} \mid d_i\,\rangle$ to be the dominant terms arising from $\vec{\nabla}\cdot\vec{J} = -i\,[H,\rho]$ (cf. Sect. 6.1.1 and App. G). Therefore we assume that for a numerical estimate of the importance of ρ^{ex} we may replace $\vec{\nabla}\cdot\vec{J} \to -i\,[H,\rho^0]$ at one interaction vertex and $\vec{\nabla}\cdot\vec{J} \to -i\,[H,\rho^{\text{ex}}]$ at the other. Repeating the steps

described in Eqs. (6.11-6.22) we find

$$\mathcal{M}_{fi}^{\rho^{\rm ex}\,a} = \left(\omega + \frac{\omega^2}{2m_d}\right)^2 \sum_C \frac{\langle\, d_f \mid \hat{\phi}_f \mid C\,\rangle\langle\, C \mid \int \rho^{\rm ex}(\vec{\xi};\vec{x}_1,\vec{x}_2)\,\phi_i(\vec{\xi})\,d^3\xi \mid d_i\,\rangle}{\omega + \frac{\omega^2}{2m_d} - B - E_C},$$

$$\mathcal{M}_{fi}^{\rho^{\rm ex}\,b} = \left(\omega + \frac{\omega^2}{2m_d}\right)^2 \sum_C \frac{\langle\, d_f \mid \int \rho^{\rm ex}(\vec{\xi};\vec{x}_1,\vec{x}_2)\,\phi_f(\vec{\xi})\,d^3\xi \mid C\,\rangle\langle\, C \mid \hat{\phi}_i \mid d_i\,\rangle}{\omega + \frac{\omega^2}{2m_d} - B - E_C},$$

$$\mathcal{M}_{fi}^{\rho^{\rm ex}\,c} = \left(\omega - \frac{\omega^2}{2m_d} + \frac{\vec{P}_C^{\,2}}{2m_C}\right)^2 \sum_C \frac{\langle\, d_f \mid \hat{\phi}_i \mid C\,\rangle\langle\, C \mid \int \rho^{\rm ex}(\vec{\xi};\vec{x}_1,\vec{x}_2)\,\phi_f(\vec{\xi})\,d^3\xi \mid d_i\,\rangle}{-\omega + \frac{\omega^2}{2m_d} - \frac{\vec{P}_C^{\,2}}{2m_C} - B - E_C},$$

$$\mathcal{M}_{fi}^{\rho^{\rm ex}\,d} = \left(\omega - \frac{\omega^2}{2m_d} + \frac{\vec{P}_C^{\,2}}{2m_C}\right)^2 \sum_C \frac{\langle\, d_f \mid \int \rho^{\rm ex}(\vec{\xi};\vec{x}_1,\vec{x}_2)\,\phi_i(\vec{\xi})\,d^3\xi \mid C\,\rangle\langle\, C \mid \hat{\phi}_f \mid d_i\,\rangle}{-\omega + \frac{\omega^2}{2m_d} - \frac{\vec{P}_C^{\,2}}{2m_C} - B - E_C}. \tag{J.9}$$

The index 'KR' has been skipped for convenience as we are only concerned with the Kroll-Ruderman charge density. So we need to calculate $\int \rho^{\rm ex}(\vec{\xi};\vec{x}_1,\vec{x}_2)\,\phi_{i,f}(\vec{\xi})\,d^3\xi$, which is trivial due to the δ-functions in $\rho^{\rm ex}$.

$$\int \rho^{\rm ex}(\vec{\xi};\vec{x}_1,\vec{x}_2)\,\phi_{i,f}(\vec{\xi})\,d^3\xi = \frac{e\,f^2}{m_N\,m_\pi^2}\,(\vec{\tau}_1\times\vec{\tau}_2)_z\left(\frac{\partial}{\partial r}\frac{{\rm e}^{-m_\pi r}}{r}\right) \tag{J.10}$$
$$\times\left\{\phi_{i,f}(\vec{x}_1)\,(\vec{\sigma}_2\cdot\hat{r})\,(\vec{\sigma}_1\cdot\vec{p}_1) + \phi_{i,f}(\vec{x}_2)\,(\vec{\sigma}_1\cdot\hat{r})\,(\vec{\sigma}_2\cdot\vec{p}_2)\right\}$$

We now replace $\vec{x}_1 \to \frac{\vec{r}}{2}$, $\vec{x}_2 \to -\frac{\vec{r}}{2}$, $\vec{p}_1 \to -i\,\vec{\nabla}_1 = -i\,\vec{\nabla}_r$ and $\vec{p}_2 \to -i\,\vec{\nabla}_2 = i\,\vec{\nabla}_r$ with $\vec{\nabla}_r$ acting on the deuteron wave function. For our estimate we restrict ourselves to the s-wave part of this wave function, cf. Eq. (D.5), which is by far ($\sim 95\%$) dominating over the d-wave function. The reason is that in this approximation $\vec{\nabla}_r$ reduces to $\hat{r}\frac{\partial}{\partial r}$, as the s-wave function is spherically symmetric. We therefore may rewrite Eq. (J.10) as

$$\int \rho^{\rm ex}(\vec{\xi};\vec{x}_1,\vec{x}_2)\,\phi_{i,f}(\vec{\xi})\,d^3\xi = -\frac{i\,e\,f^2}{m_N\,m_\pi^2}\,(\vec{\tau}_1\times\vec{\tau}_2)_z\left(\frac{\partial}{\partial r}\frac{{\rm e}^{-m_\pi r}}{r}\right) \tag{J.11}$$
$$\times\,(\vec{\sigma}_1\cdot\hat{r})\,(\vec{\sigma}_2\cdot\hat{r})\,\left(\phi_{i,f}(\vec{r}/2) - \phi_{i,f}(-\vec{r}/2)\right)\,\frac{\partial}{\partial r}.$$

Under these assumptions it is easy to evaluate the amplitudes (J.9). However, we found them to be about a factor of 4 smaller than e.g. the amplitudes $\mathcal{M}_{fi}^{\phi\,\rm KR2}$, which are small corrections themselves – their contributions account for less than 5% of the differential cross sections for all energies and angles under consideration. Therefore we claim that contributions due to $\rho^{\rm ex}$ may well be neglected in our calculation and thus abstain from showing the final results for the amplitudes (J.9).

Appendix K

The AV18 Neutron-Proton Potential

Here we sketch the neutron-proton potential that we use in our Schrödinger-like differential equation, Eq. (6.41). It is the so-called AV18-potential as published in [73]. This potential consists of an electromagnetic part (em), a one-pion-exchange part (π), and an intermediate- and short-distance part (sd):

$$V(np) = V^{em}(np) + V^{\pi}(np) + V^{sd}(np) \tag{K.1}$$

The electromagnetic part is very small for the neutron-proton system, and therefore nearly invisible in Fig. K.2. Nevertheless, we include it for completeness although we do not expect any significant influence on our cross sections. It is composed of a Coulomb term, arising from the neutron charge distribution, and of the interaction between the magnetic moments of the two nucleons,

$$V^{em}(np) = V_C(np) + V_{mm}(np) \tag{K.2}$$

with

$$V_C(np) = \alpha\,\beta_n\,\frac{F_{np}(r)}{r}. \tag{K.3}$$

α is the fine-structure constant and β_n the slope of the neutron electric form factor. The authors of [73] use $\beta_n = 0.0189\ \mathrm{fm}^2$, which is the value determined experimentally in [110]. The function $F_{np}(r)$ is defined as

$$F_{np}(r) = b^2\,\left(15\,br + 15\,(br)^2 + 6\,(br)^3 + (br)^4\right)\,\frac{\mathrm{e}^{-br}}{384} \tag{K.4}$$

with $b = 4.27\ \mathrm{fm}^{-1}$ and is shown in Fig. K.1, together with several other functions contained in the AV18-potential.

The magnetic-moment interaction is given by

$$\begin{aligned} V_{mm}(np) = &-\frac{\alpha}{4\,m_n\,m_p}\,\mu_n\,\mu_p\,\left[\frac{2}{3}\,F_\delta(r)\,\vec{\sigma}_i\cdot\vec{\sigma}_j + \frac{F_t(r)}{r^3}\,S_{ij}\right] \\ &-\frac{\alpha}{2\,m_n\,m_r}\,\mu_n\,\frac{F_{ls}(r)}{r^3}\,\left(\vec{L}\cdot\vec{S} + \vec{L}\cdot\vec{t}\right). \end{aligned} \tag{K.5}$$

$\mu_n,\ \mu_p$ are the magnetic moments of the neutron and proton, respectively, $m_n,\ m_p$ their masses. m_r is the reduced nucleon mass $m_r = \frac{m_n\,m_p}{m_n+m_p}$. The spin operators

S_{ij}, $\vec{S}$ and $\vec{t}$ are

$$\begin{aligned} S_{ij} &= 3\,(\vec{\sigma}_i \cdot \hat{r})\,(\vec{\sigma}_j \cdot \hat{r}) - \vec{\sigma}_i \cdot \vec{\sigma}_j, \\ \vec{S} &= \frac{1}{2}\,(\vec{\sigma}_i + \vec{\sigma}_j), \\ \vec{t} &= \frac{1}{2}\,(\vec{\sigma}_i - \vec{\sigma}_j). \end{aligned} \tag{K.6}$$

However, the operator $\vec{t}$ is designated to be very small, cf. [73], and therefore is neglected in our calculation, as also the other contributions to $V^{em}(np)$ are tiny, see Fig. K.2. $\vec{L} = \vec{r} \times \vec{p}$ is the orbital angular momentum operator and the functions $F_\delta(r)$, $F_t(r)$ and $F_{ls}(r)$ – for their derivation cf. [73] and references therein – are given by

$$\begin{aligned} F_\delta(r) &= b^3 \left(\frac{1}{16} + \frac{1}{16}\,br + \frac{1}{48}\,(br)^2 \right) \mathrm{e}^{-br}, \\ F_t(r) &= 1 - \left(1 + br + \frac{1}{2}\,(br)^2 + \frac{1}{6}\,(br)^3 + \frac{1}{24}\,(br)^4 + \frac{1}{144}\,(br)^5 \right) \mathrm{e}^{-br}, \\ F_{ls}(r) &= 1 - \left(1 + br + \frac{1}{2}\,(br)^2 + \frac{7}{48}\,(br)^3 + \frac{1}{48}\,(br)^4 \right) \mathrm{e}^{-br} \end{aligned} \tag{K.7}$$

and are shown in Fig. K.1, divided by the same power of r as they appear in Eq. (K.5).

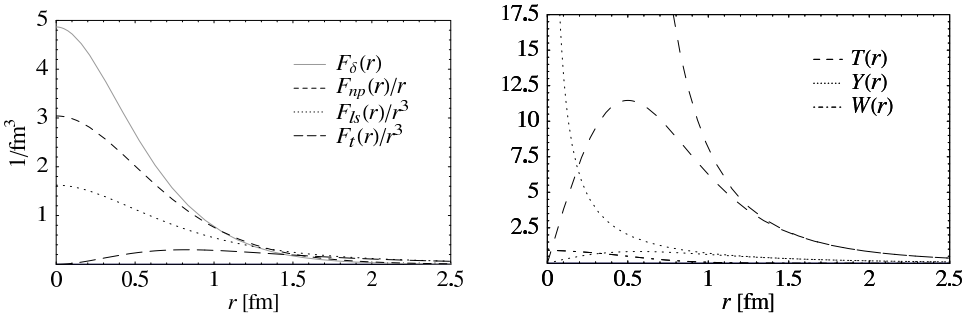

Figure K.1: Various functions used in the AV18-potential. Those which appear in Eq. (K.5) are divided by the corresponding power of r. In the divergent functions on the right-hand side the cutoff functions, cf. Eqs. (K.11, K.12), have been removed.

The tensor operator S_{ij} only contributes in the triplet state ($S = 1$) [57]. The values of its matrix elements $\langle\, L\,1\,J \mid S_{ij} \mid L'\,1\,J \,\rangle$ are given in Table K.1, cf. Appendix 10 of [57][1], for all possible orbital angular momentum numbers L, L' at given total angular momentum J.

The eigenvalues of the spin-orbit operator $\vec{L}\cdot\vec{S}$, which obviously only contributes in the triplet case due to the total spin $\vec{S}$, are given in Table K.2, those of $\vec{\sigma}_i \cdot \vec{\sigma}_j$ are

$$\vec{\sigma}_i \cdot \vec{\sigma}_j \mid S \,\rangle = 2\,[S\,(S+1) - 3/2] \mid S \,\rangle. \tag{K.8}$$

The next component of the potential to be discussed is the one-pion-exchange potential, which is the dominant part at large distances, cf. Fig. K.2. It reads

$$V^\pi(np) = -f^2\,v_\pi(m_{\pi^0}) + (-1)^{T+1}\,2\,f^2\,v_\pi(m_{\pi^\pm}), \tag{K.9}$$

[1] We note that there is a typo in [57] for $L = L' = J + 1$, namely an erroneous factor J.

	L'		
L	$J+1$	J	$J-1$
$J+1$	$-\frac{2\,(J+2)}{2J+1}$	0	$\frac{6\sqrt{J\,(J+1)}}{2J+1}$
J	0	2	0
$J-1$	$\frac{6\sqrt{J\,(J+1)}}{2J+1}$	0	$-\frac{2\,(J-1)}{2J+1}$

Table K.1: Matrix elements of the tensor operator $\langle\, L\,1\,J \mid S_{ij} \mid L'\,1\,J\,\rangle$.

L		
$J+1$	J	$J-1$
$-(L+1)$	-1	L

Table K.2: Matrix elements of the spin-orbit operator $\langle\, L\,1\,J \mid \vec{L}\cdot\vec{S} \mid L\,1\,J\,\rangle$.

where T is the total isospin of the np-system, f the pion-nucleon coupling ($f^2 = 0.075$), cf. Section 6.1.1 and Appendix A, and

$$v_\pi(m) = \left(\frac{m}{m_{\pi^\pm}}\right)^2 \frac{1}{3}\, m\, \left[Y_m^{AV18}(r)\,\vec{\sigma}_i\cdot\vec{\sigma}_j + T_m^{AV18}(r)\,S_{ij}\right]. \tag{K.10}$$

We mark the Yukawa and tensor functions $Y_m(r)$, $T_m(r)$ by the index $AV18$, as we use slightly different functions $Y(r)$, $T(r)$ in App. G. The AV18-functions are defined as

$$Y_m^{AV18}(r) = \frac{\mathrm{e}^{-mr}}{mr}\,\left(1-\mathrm{e}^{-cr^2}\right), \tag{K.11}$$

$$T_m^{AV18}(r) = \left(1+\frac{3}{mr}+\frac{3}{(mr)^2}\right)\,\frac{\mathrm{e}^{-mr}}{mr}\,\left(1-\mathrm{e}^{-cr^2}\right)^2 \tag{K.12}$$

and are plotted in the right panel of Fig. K.1, where we set $m \equiv \mu \equiv \frac{1}{3}\,(m_{\pi^0} + 2\,m_{\pi^\pm})$, which is the average over the pion masses. The cutoff parameter c is assigned the value $c = 2.1$ fm^{-2} in [73]. The cutoff functions $\left(1-\mathrm{e}^{-cr^2}\right)$, $\left(1-\mathrm{e}^{-cr^2}\right)^2$ are introduced in [73] in order to avoid the $\frac{1}{r^n}$-divergency for $r\to 0$. However, in App. G we remove the cutoff functions for calculating one certain amplitude. The thus truncated functions are also displayed in Fig. K.1.

The remaining part of the potential is the so-called intermediate- and short-distance phenomenological potential (sd), which is expressed as a sum of central (c), $\vec{L}^2$ ($l2$), tensor (t), spin-orbit (ls) and quadratic spin-orbit ($ls2$) terms. The parameters of the short-distance potential depend on the total spin S and isospin T of the system.

$$V_{ST}^{sd}(np) = v_{ST}^{c}(r) + v_{ST}^{l2}(r)\;\vec{L}^{\,2} + v_{ST}^{t}(r)\,S_{ij} + v_{ST}^{ls}\,\vec{L}\cdot\vec{S} + v_{ST}^{ls2}(r)\,\left(\vec{L}\cdot\vec{S}\right)^2 \tag{K.13}$$

This part of the potential is the dominant one for short distances, see Fig. K.2. Each of the functions $v_{ST}^i(r)$ in Eq. (K.13) has the general form

$$v_{ST}^i(r) = I_{ST}^i\;\left(T_\mu^{AV18}(r)\right)^2 + \left[P_{ST}^i + \mu r\,Q_{ST}^i + (\mu r)^2\,R_{ST}^i\right]\;W(r), \tag{K.14}$$

where μ is the averaged pion mass as before. $T_\mu^{AV18}(r)$ is defined in Eq. (K.12), the Woods-Saxon function

$$W(r) = \frac{1}{1 + \mathrm{e}^{(r-r_0)/a}} \tag{K.15}$$

is plotted in Fig. K.1; it dampens out the square bracket in Eq. (K.14) for large distances and therefore ensures the short-range character of V^{sd}. The parameters of the Woods-Saxon function chosen in [73] are $r_0 = 0.5$ fm and $a = 0.2$ fm. The spin- and isospin-dependent parameters $I,\ P,\ Q,\ R$ are listed in [73]. The eigenvalues of $\vec{L}^{\,2}$ are $L\,(L+1)$ and those of $(\vec{L}\cdot\vec{S})^2$ are the squares of the numbers given in Table K.2.

The only remaining subtlety is the question, which combinations of $S,\ T$ and L are allowed by Pauli's principle. This principle guarantees that the total wave function of the two-nucleon system has to be antisymmetric under exchange of the two nucleons due to their fermionic nature, i.e. the wave function has to fulfill $(-1)^{S+T+L} = -1$. Therefore, for $S = 1,\ T = 0$, which is the deuteron case, and for $S = 0,\ T = 1$ we find L even, for $S = 0,\ T = 0$ and $S = 1,\ T = 1$ we have L odd.

Four examples of the resulting potentials for the various combinations of $L,\ S,\ J$ are shown in the first column of Fig. K.2, together with a comparison of the full potential with the three parts separated from each other, cf. Eq. (K.1). This comparison is done at short distances (middle column) and at larger distances (right column). At short distances the contribution *sd* (dotted) dominates, whereas above about 4 fm the potential is made up nearly entirely by the one-pion-exchange (dashed) potential. The electromagnetic part (dotdashed) is negligible in all cases considered. It only gives sizeable contributions when we look at the proton-proton rather than the proton-neutron interaction [73]. The first row in Fig. K.2 corresponds to the deuteron s-state, the second to the deuteron d-state, which are both triplet ($S = 1$) states. The lower two rows show singlet states.

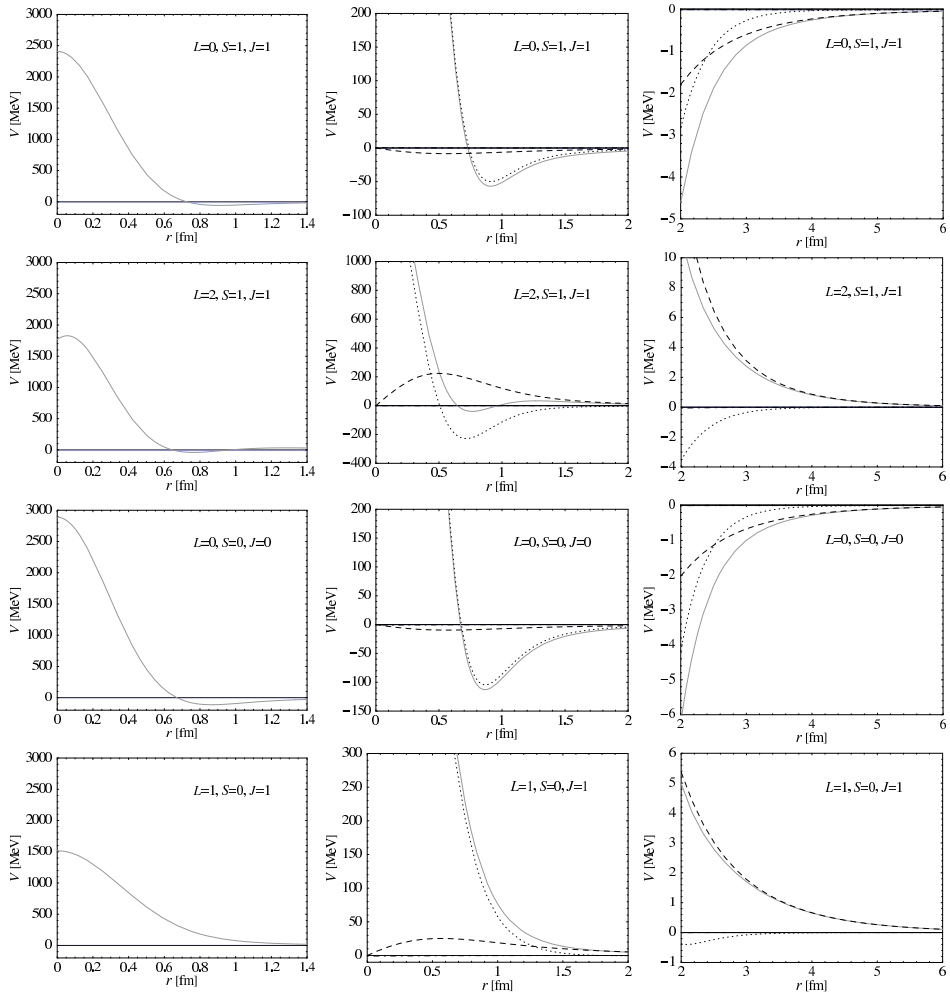

Figure K.2: The AV18-potential for four different combinations of L, S, J. In the left panels we show the full potential, in the middle column we compare the full potential (solid) with the three contributions *em* (dotdashed), π (dashed) and *sd* (dotted) at short distances, in the right panel we give this comparison for larger distances.

Appendix L

Formulae

Photon field $\vec{A}(\vec{x})$ and (charged) pion field $\phi(\vec{x})$, normalized according to Ref. [24]:

$$\vec{A}(\vec{x}) = \sum_{\vec{k},\lambda} \left(a_{\vec{k}}\, \hat{\epsilon}_\lambda\, \mathrm{e}^{i\vec{k}\cdot\vec{x}} + a^\dagger_{\vec{k}}\, \hat{\epsilon}^*_\lambda\, \mathrm{e}^{-i\vec{k}\cdot\vec{x}} \right) \tag{L.1}$$

$$\phi_\pm(\vec{x}) = \sum_{\vec{q}} \sqrt{\frac{2\pi}{E_\pi}} \left(a_{\mp,\vec{q}}\, \mathrm{e}^{i\vec{q}\cdot\vec{x}} + a^\dagger_{\pm,\vec{q}}\, \mathrm{e}^{-i\vec{q}\cdot\vec{x}} \right) \tag{L.2}$$

$a^\dagger_\pm$ ($a_\pm$) creates (annihilates) a $\pi^\pm$, $E_\pi = \sqrt{\vec{q}^{\,2} + m_\pi^2}$.

Hamiltonians for πN and $\gamma\pi N$ coupling, cf. e.g. [57], Section 8.2:

$$H^{\pi NN} = -\frac{f}{m_\pi}\, (\vec{\sigma}\cdot\vec{\nabla})\, (\vec{\tau}\cdot\vec{\phi}(\vec{x})) \tag{L.3}$$

$$H^{\gamma\pi N} = \frac{e\, f}{m_\pi}\, (\vec{\sigma}\cdot\vec{A}(\vec{x}))\, (\vec{\tau}\times\vec{\phi}(\vec{x}))_z \tag{L.4}$$

Definitions:

$$\begin{aligned} \phi_\pm &= \frac{1}{\sqrt{2}}\,(\phi_x \pm i\,\phi_y) & \tau_\pm &= \tau_x \pm i\,\tau_y \\ \Rightarrow \qquad \phi_x &= \frac{1}{\sqrt{2}}\,(\phi_+ + \phi_-) & \tau_x &= \frac{1}{2}\,(\tau_+ + \tau_-) \\ \phi_y &= -\frac{i}{\sqrt{2}}\,(\phi_+ - \phi_-) & \tau_y &= -\frac{i}{2}\,(\tau_+ - \tau_-) \end{aligned} \tag{L.5}$$

$$\Rightarrow \qquad \vec{\tau}\cdot\vec{\phi} = \tau_x\,\phi_x + \tau_y\,\phi_y = \frac{1}{\sqrt{2}}\,(\tau_+\,\phi_- + \tau_-\,\phi_+) \tag{L.6}$$

$$(\vec{\tau}\times\vec{\phi})_z = \tau_x\,\phi_y - \tau_y\,\phi_x = \frac{i}{\sqrt{2}}\,(\tau_+\,\phi_- - \tau_-\,\phi_+) \tag{L.7}$$

The following formulae can all be found in textbooks on the quantum theory of angular momentum, e.g. [108, 107, 83].

The spherical basis:

$$\begin{aligned} \hat{r}_{+1} &= -\frac{1}{\sqrt{2}}\,(\vec{e}_x + i\,\vec{e}_y) \\ \hat{r}_0 &= \vec{e}_z \\ \hat{r}_{-1} &= \frac{1}{\sqrt{2}}\,(\vec{e}_x - i\,\vec{e}_y) \end{aligned} \tag{L.8}$$

$$\Rightarrow \hat{r}_i \cdot \hat{r}_j = (-1)^i\,\delta_{i,-j} \tag{L.9}$$

Polarization vectors in the spherical basis:

$$\begin{aligned} \hat{\epsilon}_{+1} = \hat{r}_{+1} &= -\frac{1}{\sqrt{2}}\begin{pmatrix}1\\ i\\ 0\end{pmatrix} & \hat{\epsilon}'^{*}_{+1} &= \frac{1}{\sqrt{2}}\begin{pmatrix}-\cos\theta\\ i\\ \sin\theta\end{pmatrix} \\ \hat{\epsilon}_{-1} = \hat{r}_{-1} &= \frac{1}{\sqrt{2}}\begin{pmatrix}1\\ -i\\ 0\end{pmatrix} & \hat{\epsilon}'^{*}_{-1} &= \frac{1}{\sqrt{2}}\begin{pmatrix}\cos\theta\\ i\\ -\sin\theta\end{pmatrix} \end{aligned} \tag{L.10}$$

Expansion of a vector $\vec{V}$ into spherical components:

$$\vec{V} = \sum_{\nu=-1,0,1} (-1)^\nu\, V_\nu\, \hat{r}_{-\nu}\;; \qquad V_\nu = \vec{V}\cdot\hat{r}_\nu \tag{L.11}$$

Scalar product in spherical coordinates:

$$\vec{U}\cdot\vec{V} = \sum_{j=-1,0,1} (-1)^j\, U_j\, V_{-j} \tag{L.12}$$

Useful identity for r_ν:

$$r_\nu = \hat{r}\cdot\hat{r}_\nu = \sqrt{\frac{4\pi}{3}}\, Y_{1\,\nu}(\hat{r}) \tag{L.13}$$

Clebsch-Gordan coefficients:

$$C^{j_3\,m_3}_{j_1\,m_1\;j_2\,m_2} = (-1)^{j_1-j_2+m_3}\,\sqrt{2j_3+1}\begin{pmatrix} j_1 & j_2 & j_3 \\ m_1 & m_2 & -m_3 \end{pmatrix} \tag{L.14}$$

$\begin{pmatrix} j_1 & j_2 & j_3 \\ m_1 & m_2 & -m_3 \end{pmatrix}$ is the Wigner 3-j symbol and the angular momenta $j_1,\ j_2,\ j_3$ have to fulfill the triangular condition

$$j_1 \le j_2 + j_3, \qquad j_2 \le j_1 + j_3, \qquad j_3 \le j_1 + j_2. \tag{L.15}$$

The projections on the quantization axis have to add up to zero:

$$m_1 + m_2 - m_3 = 0 \tag{L.16}$$

Further properties of the 3-j symbol:
The 3-j symbol is symmetric under even permutations of rows,

$$\begin{pmatrix} j_1 & j_2 & j_3 \\ m_1 & m_2 & m_3 \end{pmatrix} = \begin{pmatrix} j_2 & j_3 & j_1 \\ m_2 & m_3 & m_1 \end{pmatrix} = \begin{pmatrix} j_3 & j_1 & j_2 \\ m_3 & m_1 & m_2 \end{pmatrix}. \tag{L.17}$$

Under odd permutations it behaves like

$$\begin{pmatrix} j_1 & j_2 & j_3 \\ m_1 & m_2 & m_3 \end{pmatrix} = (-1)^{j_1+j_2+j_3} \begin{pmatrix} j_2 & j_1 & j_3 \\ m_2 & m_1 & m_3 \end{pmatrix}. \tag{L.18}$$

Further:

$$\begin{pmatrix} j_1 & j_2 & j_3 \\ m_1 & m_2 & m_3 \end{pmatrix} = (-1)^{j_1+j_2+j_3} \begin{pmatrix} j_1 & j_2 & j_3 \\ -m_1 & -m_2 & -m_3 \end{pmatrix} \tag{L.19}$$

$$\Rightarrow \quad \begin{pmatrix} j_1 & j_2 & j_3 \\ 0 & 0 & 0 \end{pmatrix} = (-1)^{j_1+j_2+j_3} \begin{pmatrix} j_1 & j_2 & j_3 \\ 0 & 0 & 0 \end{pmatrix} \tag{L.20}$$

$$\Rightarrow \quad \begin{pmatrix} j_1 & j_2 & j_3 \\ 0 & 0 & 0 \end{pmatrix} = 0 \text{ for } j_1 + j_2 + j_3 \text{ odd} \tag{L.21}$$

Unitarity of the Clebsch-Gordan-coefficients:

$$\begin{aligned} \sum_{j,m} C^{j\,m}_{j_1\,m'_1\;j_2\,m'_2} C^{j\,m}_{j_1\,m_1\;j_2\,m_2} &= \delta_{m'_1,m_1}\,\delta_{m'_2,m_2} \\ \sum_{m_1,m_2} C^{j'\,m'}_{j_1\,m_1\;j_2\,m_2} C^{j\,m}_{j_1\,m_1\;j_2\,m_2} &= \delta_{j',j}\,\delta_{m',m} \end{aligned} \tag{L.22}$$

Properties of the 6-j and 9-j symbols:
In a non-vanishing 6-j symbol $\left\{ \begin{matrix} j_1 & j_2 & j_3 \\ l_1 & l_2 & l_3 \end{matrix} \right\}$ the four triads $(j_1\,j_2\,j_3)$, $(l_1\,l_2\,j_3)$, $(j_1\,l_2\,l_3)$, $(l_1\,j_2\,l_3)$ fulfill the triangular condition Eq. (L.15).
The 9-j symbol can be written in terms of the 6-j symbols [111]:

$$\begin{aligned} \left\{ \begin{matrix} j_{11} & j_{12} & j_{13} \\ j_{21} & j_{22} & j_{23} \\ j_{31} & j_{32} & j_{33} \end{matrix} \right\} &= \sum_j (-1)^{2j}\,(2j+1) \\ &\times \left\{ \begin{matrix} j_{11} & j_{21} & j_{31} \\ j_{32} & j_{33} & j \end{matrix} \right\} \left\{ \begin{matrix} j_{12} & j_{22} & j_{32} \\ j_{21} & j & j_{23} \end{matrix} \right\} \left\{ \begin{matrix} j_{13} & j_{23} & j_{33} \\ j & j_{11} & j_{12} \end{matrix} \right\} \end{aligned} \tag{L.23}$$

The upper limit for j is determined by the triangular condition on the triads of the various 6-j symbols:

$$j \leq \mathrm{Min}[j_{11} + j_{33},\, j_{21} + j_{32},\, j_{12} + j_{23}] \tag{L.24}$$

We calculate 9-j symbols via Eq. (L.23), 3-j and 6-j symbols are standard functions in programs like *Mathematica*.
The 9-j symbol is symmetric under even permutations of rows or columns. Any 9-j symbol with one null entry can be simplified using

$$\left\{ \begin{matrix} L_f & S_f & J_f \\ L_i & S_i & J_i \\ L & 0 & L' \end{matrix} \right\} = \delta_{S_f,S_i}\,\delta_{L,L'}\,\frac{(-1)^{L_f+S_f+J_i+L'}}{\sqrt{(2S_i+1)\,(2L+1)}} \left\{ \begin{matrix} L_i & J_i & S_i \\ J_f & L_f & L \end{matrix} \right\}. \tag{L.25}$$

Product of two spherical harmonics:

$$\begin{aligned} Y_{j\,m}\,Y_{j'\,m'} &= \sum_J (-1)^{m+m'} \sqrt{\frac{(2j+1)\,(2j'+1)\,(2J+1)}{4\pi}} \\ &\times \begin{pmatrix} j & j' & J \\ 0 & 0 & 0 \end{pmatrix} \begin{pmatrix} j & j' & J \\ m & m' & -m-m' \end{pmatrix} Y_{J\,m+m'} \end{aligned} \tag{L.26}$$

Some properties of the spherical harmonics:

$$Y_{l\,m}(-\hat{r}) = (-1)^l\, Y_{l\,m}(\hat{r}) \tag{L.27}$$

$$Y_{l\,m}(\vec{e}_z) = \delta_{m,0}\sqrt{\frac{2l+1}{4\pi}} \tag{L.28}$$

Definition of the spherical Bessel functions (we use the same convention as e.g. Ref. [57]):

$$j_l(z) = \sqrt{\frac{\pi}{2z}} J_{l+\frac{1}{2}}(z) \tag{L.29}$$

$J_l(z)$ is the Bessel function of the first kind.
Recursion relations for the spherical Bessel functions:

$$\begin{aligned} \frac{2l+1}{x}\, j_l(x) &= j_{l-1}(x) + j_{l+1}(x) \\ (2l+1)\, j_l'(x) &= l\, j_{l-1}(x) - (l+1)\, j_{l+1}(x) \end{aligned} \tag{L.30}$$

Wigner-Eckart theorem:

$$\langle\, J_f\, M_f \mid T_{J\,M} \mid J_i\, M_i \,\rangle = (-1)^{J_f - M_f} \begin{pmatrix} J_f & J & J_i \\ -M_f & M & M_i \end{pmatrix} \langle\, J_f \parallel T_J \parallel J_i \,\rangle \tag{L.31}$$

The matrix element on the right-hand side is called "reduced matrix element".

Tensor product ($\otimes$) definition:

$$[T_{k_1} \otimes T_{k_2}]_{k\,m} = \sum_{m_1,m_2} \sqrt{2k+1}\,(-1)^{-k_1+k_2-m} \begin{pmatrix} k_1 & k_2 & k \\ m_1 & m_2 & -m \end{pmatrix} T_{k_1\,m_1}\, T_{k_2\,m_2} \tag{L.32}$$

Inversion:

$$T_{k_1\,m_1}\, T_{k_2\,m_2} = \sum_{k,m} (-1)^{k_1-k_2+m} \sqrt{2k+1} \begin{pmatrix} k_1 & k_2 & k \\ m_1 & m_2 & -m \end{pmatrix} [T_{k_1} \otimes T_{k_2}]_{k\,m} \tag{L.33}$$

Reduced matrix elements:

$$\langle\, l' \parallel Y_L \parallel l \,\rangle = (-1)^{l'} \sqrt{\frac{(2l'+1)\,(2L+1)\,(2l+1)}{4\pi}} \begin{pmatrix} l' & L & l \\ 0 & 0 & 0 \end{pmatrix} \tag{L.34}$$

$$\langle\, S_f \parallel S \parallel S_i \,\rangle = \sqrt{6}\, \delta_{S_i,1}\, \delta_{S_f,1} \tag{L.35}$$

$$\langle\, S_f \parallel t \parallel S_i \,\rangle = \sqrt{3}\, (\delta_{S_i,0}\, \delta_{S_f,1} - \delta_{S_i,1}\, \delta_{S_f,0}) \tag{L.36}$$

$$\begin{aligned} \langle\, L_f\, S_f\, J_f \parallel Y_L \parallel L_i\, S_i\, J_i \,\rangle = (2L+1) &\sqrt{\frac{(2L_i+1)\,(2L_f+1)\,(2J_i+1)\,(2J_f+1)\,(2S_f+1)}{4\pi}} \\ &\times (-1)^{L_f}\, \delta_{S_f,S_i} \begin{Bmatrix} L_f & S_f & J_f \\ L_i & S_i & J_i \\ L & 0 & L \end{Bmatrix} \begin{pmatrix} L_f & L & L_i \\ 0 & 0 & 0 \end{pmatrix} \end{aligned} \tag{L.37}$$

$$\begin{aligned} \langle\, L_f\, S_f\, J_f \parallel [Y_{L'} \otimes S]_L \parallel L_i\, S_i\, J_i \,\rangle = &\sqrt{\frac{3\,(2L_i+1)\,(2L_f+1)\,(2J_i+1)\,(2J_f+1)}{2\pi}} \\ &\times \sqrt{(2L+1)\,(2L'+1)}\,(-1)^{L_f}\, \delta_{S_f,S_i}\, \delta_{S_i,1} \begin{Bmatrix} L_f & S_f & J_f \\ L_i & S_i & J_i \\ L' & 1 & L \end{Bmatrix} \begin{pmatrix} L_f & L' & L_i \\ 0 & 0 & 0 \end{pmatrix} \end{aligned} \tag{L.38}$$

$$\langle\, L_f\, S_f\, J_f \,\|\, [Y_{L'} \otimes t]_L \,\|\, L_i\, S_i\, J_i \,\rangle = \sqrt{\frac{3\,(2L_i+1)\,(2L_f+1)\,(2J_i+1)\,(2J_f+1)}{16\pi}}$$
$$\times \sqrt{(2L+1)\,(2L'+1)}\,(-1)^{L_f}\,[(-1)^{S_i} - (-1)^{S_f}] \left\{ \begin{array}{ccc} L_f & S_f & J_f \\ L_i & S_i & J_i \\ L' & 1 & L \end{array} \right\} \left(\begin{array}{ccc} L_f & L' & L_i \\ 0 & 0 & 0 \end{array} \right) \tag{L.39}$$

S and t are related to $\vec{S} = \frac{\vec{\sigma}_1 + \vec{\sigma}_2}{2}$, $\vec{t} = \frac{\vec{\sigma}_1 - \vec{\sigma}_2}{2}$; $\vec{L}$ is the angular momentum operator.

Formulae for uncoupling tensor products:

$$\langle\, j_1\, j_2\, j \,\|\, [T_{k_1} \otimes T_{k_2}]_k \,\|\, j_1'\, j_2'\, j' \,\rangle = \sqrt{(2j+1)\,(2j'+1)\,(2k+1)} \tag{L.40}$$
$$\times \left\{ \begin{array}{ccc} j_1 & j_2 & j \\ j_1' & j_2' & j' \\ k_1 & k_2 & k \end{array} \right\} \langle\, j_1 \,\|\, T_{k_1} \,\|\, j_1' \,\rangle\, \langle\, j_2 \,\|\, T_{k_2} \,\|\, j_2' \,\rangle$$
$$\langle\, j \,\|\, [T_{k_1} \otimes T_{k_2}]_k \,\|\, j' \,\rangle = (-1)^{k+j+j'}\, \sqrt{2k+1} \tag{L.41}$$
$$\times \sum_J \left\{ \begin{array}{ccc} k_1 & k_2 & k \\ j' & j & J \end{array} \right\} \langle\, j \,\|\, T_{k_1} \,\|\, J \,\rangle\, \langle\, J \,\|\, T_{k_2} \,\|\, j' \,\rangle$$

Definition of the vector spherical harmonic:

$$\vec{T}_{J\,L\,M}(\hat{r}) = \sum_{\nu=-1,0,1} (-1)^{-L-M+1}\, \sqrt{2J+1} \left(\begin{array}{ccc} L & 1 & J \\ M+\nu & -\nu & -M \end{array} \right) \hat{r}_{-\nu}\, Y_{L\,M+\nu}(\hat{r}) \tag{L.42}$$

The gradient formula:

$$\vec{\nabla}\, f(r)\, Y_{L\,M}(\hat{r}) = -\sqrt{\frac{L+1}{2L+1}} \left(\frac{\partial}{\partial r} - \frac{L}{r} \right) f(r)\, \vec{T}_{L\,L+1\,M}(\hat{r})$$
$$+ \sqrt{\frac{L}{2L+1}} \left(\frac{\partial}{\partial r} + \frac{L+1}{r} \right) f(r)\, \vec{T}_{L\,L-1\,M}(\hat{r}) \tag{L.43}$$

Curl version of the gradient formula:

$$\vec{\nabla} \times \left[f(r)\, \vec{T}_{L\,L\,M}(\hat{r}) \right] = i \left(\frac{\partial}{\partial r} - \frac{L}{r} \right) f(r) \sqrt{\frac{L}{2L+1}}\, \vec{T}_{L\,L+1\,M}(\hat{r}) \tag{L.44}$$
$$+ i \left(\frac{\partial}{\partial r} + \frac{L+1}{r} \right) f(r) \sqrt{\frac{L+1}{2L+1}}\, \vec{T}_{L\,L-1\,M}(\hat{r})$$
$$\vec{\nabla} \times \left[f(r)\, \vec{T}_{L\,L+1\,M}(\hat{r}) \right] = i \left(\frac{\partial}{\partial r} + \frac{L+2}{r} \right) f(r) \sqrt{\frac{L}{2L+1}}\, \vec{T}_{L\,L\,M}(\hat{r}) \tag{L.45}$$
$$\vec{\nabla} \times \left[f(r)\, \vec{T}_{L\,L-1\,M}(\hat{r}) \right] = i \left(\frac{\partial}{\partial r} - \frac{L-1}{r} \right) f(r) \sqrt{\frac{L+1}{2L+1}}\, \vec{T}_{L\,L\,M}(\hat{r}) \tag{L.46}$$

Divergence version of the gradient formula:

$$\vec{\nabla} \cdot \left[f(r)\, \vec{T}_{L\,L\,M}(\hat{r}) \right] = 0 \tag{L.47}$$
$$\vec{\nabla} \cdot \left[f(r)\, \vec{T}_{L\,L+1\,M}(\hat{r}) \right] = -\sqrt{\frac{L+1}{2L+1}} \left(\frac{\partial}{\partial r} + \frac{L+2}{r} \right) f(r)\, Y_{L\,M}(\hat{r}) \tag{L.48}$$
$$\vec{\nabla} \cdot \left[f(r)\, \vec{T}_{L\,L-1\,M}(\hat{r}) \right] = \sqrt{\frac{L}{2L+1}} \left(\frac{\partial}{\partial r} - \frac{L-1}{r} \right) f(r)\, Y_{L\,M}(\hat{r}) \tag{L.49}$$

Bibliography

[1] J.L. Powell, Phys. Rev. 75, 32 (1949).

[2] A. M. Baldin, Nucl. Phys. 18, 310 (1960).

[3] M. Gell-Mann and M.L. Goldberger, Phys. Rev. 96, 1433 (1954); F.E. Low, Phys. Rev. 96, 1428 (1954).

[4] D. Babusci, G. Giordano, A.I. L'vov, G. Matone and A.M. Nathan, Phys. Rev. C 58, 1013 (1998).

[5] Olmos de Leon et al., Eur. Phys. J. A 10, 207 (2001).

[6] E.L. Hallin et al., Phys. Rev. C 48, 1497 (1993).

[7] F.J. Federspiel et al., Phys. Rev. Lett. 67, 1511 (1991).

[8] B.E. MacGibbon et al., Phys. Rev. C 52, 2097 (1995).

[9] G. Galler et al., Phys. Lett. B 503, 245 (2001).

[10] M. Schumacher, Prog. Part. Nucl. Phys. 55, 567 (2005).

[11] K. Kossert et al., Eur. Phys. J. A 16, 259 (2003).

[12] J. Schmiedmayer et al., Phys. Rev. Lett. 66, 1015 (1991).

[13] T.L. Enik et al., Sov. J. Nucl. Phys. 60, 567 (1997).

[14] L. Koester et al., Phys. Rev. C 51, 3363 (1995).

[15] V. Bernard, N. Kaiser, J. Kambor and U.-G. Meißner, Nucl. Phys. B 388, 315 (1992).

[16] V. Bernard, N. Kaiser, U.-G. Meißner and A. Schmidt, Phys. Lett. B 319, 269 (1993); Z. Phys. A 348, 317 (1994).

[17] M. Lucas, Ph.D. thesis, University of Illinois (1994).

[18] M. Lundin et al., Phys. Rev. Lett. 90, 192501 (2003).

[19] D.L. Hornidge et al., Phys. Rev. Lett. 84, 2334 (2000).

[20] H. Gao, private communication (2002, 2003).

[21] B. Schröder, private communication (2004).

[22] M.I. Levchuk and A.I. L'vov, Nucl. Phys. A 674, 449 (2000).

[23] J. Chen, X. Ji and Y. Li, Phys. Rev. C 71, 044321 (2005).

[24] J.J. Karakowski and G.A. Miller, Phys. Rev. C 60, 014001 (1999); J.J. Karakowski, Ph.D. thesis, preprint nt@uw-99-6, (1999). [nucl-th/9901011].

[25] S.R. Beane, M. Malheiro, J.A. McGovern, D.R. Phillips and U. van Kolck, Phys. Lett. B 567, 200 (2003); erratum ibid. B 607, 320 (2005) and Nucl. Phys. A 747, 311 (2005).

[26] R.P. Hildebrandt, H.W. Grießhammer, T.R. Hemmert and B. Pasquini, Eur. Phys. J. A 20, 293 (2004).

[27] R.P. Hildebrandt, H.W. Grießhammer and T.R. Hemmert, Eur. Phys. J. A 20, 329 (2004).

[28] R.P. Hildebrandt, H.W. Grießhammer, T.R. Hemmert and D.R. Phillips, Nucl. Phys. A 748, 573 (2005).

[29] R.P. Hildebrandt, "Chirale Dynamik und Compton-Streuung am Nukleon", diploma thesis, TU München (2002).

[30] T. Muta, Foundations of Quantum Chromodynamics, World Scientific, Singapore · New Jersey · London · Hong Kong, ISBN 981-02-2674-8 (1998).

[31] A.W. Thomas and W. Weise, The Structure of the Nucleon, WILEY-VCH Verlag, Berlin, ISBN 3-527-40297-7 (2001).

[32] J. Gasser and H. Leutwyler, Ann. Phys. 158, 142 (1984).

[33] E. Jenkins and A.V. Manohar, Phys. Lett. B 255, 558 (1991).

[34] S. Weinberg, Physica 96 A, 327 (1979).

[35] V. Bernard, N. Kaiser and U.-G. Meißner, Int. J. Mod. Phys. E 4, 193 (1995).

[36] C. Itzykson and J.-B. Zuber, Quantum Field Theory, McGraw-Hill Book Company, New York et al., ISBN 0-07-032071-3 (1980).

[37] M.E. Peskin and D.V. Schroeder, An Introduction to Quantum Field Theory, Addison-Wesley Publishing Company, Reading, Massachusetts, ISBN 0-201-50397-2 (1995).

[38] E. Jenkins and A.V. Manohar, Phys. Lett. B 259, 353 (1991); E. Jenkins and A.V. Manohar, in Proceedings of Effective Field Theories of the Standard Model, edited by U.-G. Meißner, World Scientific, Singapore (1992).

[39] M. Procura, B. Musch, T. Wollenweber, T.R. Hemmert and W. Weise, in preparation.

[40] T.R. Hemmert and W. Weise, Eur. Phys. J. A 15, 487 (2002).

[41] T.R. Hemmert, B.R. Holstein and J. Kambor, Phys. Lett. B 395, 89 (1997).

[42] T.R. Hemmert, B.R. Holstein and J. Kambor, J. Phys. G 24, 1831 (1998).

[43] V. Pascalutsa and D.R. Phillips, Phys. Rev. C 67, 055202 (2003).

[44] N. Fettes, U.-G. Meißner, M. Mojzis and S. Steininger, Ann. Phys. 283, 273 (2000).

[45] V.I. Ritus, Sov. Phys. JETP 5, 1249 (1957); A.P. Contogouris, Nuovo Cimento 25, 104 (1962); Y. Nagashima, Prog. Theor. Phys. 33, 828 (1965).

[46] H.W. Grießhammer and T.R. Hemmert, Phys. Rev. C 65, 045207 (2002).

[47] B.R. Holstein, D. Drechsel, B. Pasquini and M. Vanderhaeghen, Phys. Rev. C 61, 034316 (2000).

[48] See e.g. S. Ragusa, Phys. Rev. D 47, 3757 (1993).

[49] T.R. Hemmert, in Proceedings of GDH 2000, edited by L. Tiator and D. Drechsel, (Mainz 2001) [nucl-th/0101055].

[50] D. Drechsel, B. Pasquini and M. Vanderhaeghen, Phys. Rep. 378, 99 (2003).

[51] O. Hanstein, D. Drechsel and L. Tiator, Nucl. Phys. A 632, 561 (1998).

[52] B.R. Holstein "Chiral Perturbation Theory and Nucleon Polarizabilities", in Chiral Dynamics 1997: Theory and Experiment, Editors: A.M. Bernstein, D. Drechsel and T. Walcher, Springer-Verlag, Berlin (1998). [hep-ph/9710548].

[53] See e.g. T.R. Hemmert "Nucleon Compton Scattering in Chiral Effective Field Theories" in Chiral Dynamics 2000: Theory and Experiment, Editors: A.M. Bernstein, J.L. Goity and U.-G. Meißner, World Scientific, Singapore (2001). [nucl-th/0101054].

[54] J.A. McGovern, Phys. Rev. C 63, 064608 (2001), Erratum ibid. C 66, 039902 (2002).

[55] T.R. Hemmert, B.R. Holstein and J. Kambor, Phys. Rev. D 55, 5598 (1997).

[56] T.R. Hemmert, B.R. Holstein, J. Kambor and G. Knöchlein: Phys. Rev. D 57, 5746 (1998).

[57] T. Ericson and W. Weise, Pions and Nuclei, Clarendon Press, Oxford, ISBN 0-19-852008-5 (1988).

[58] N.C. Mukhopadhyay, A.M. Nathan and L. Zhang, Phys. Rev. D 47, 7 (1993).

[59] A. Hünger, et al., Nucl. Phys. A 620, 385 (1997).

[60] S.R. Beane and M.J. Savage, Nucl. Phys. A 694, 511 (2001); H.W. Grießhammer and G. Rupak, Phys. Lett. B 529, 57 (2002).

[61] P.A.M. Guichon, B. Pasquini and W. Weise, private communication.

[62] M.N. Butler, M.J. Savage and R.P. Springer, Nucl. Phys. B 399, 69 (1993).

[63] T.R. Hemmert and B.R. Holstein, in preparation.

[64] J. Ahrens et al. [GDH Collaboration], Phys. Rev. Lett. 87, 022003 (2001).

[65] P.A.M. Guichon, G.Q. Liu and A.W. Thomas, Nucl. Phys. A 591, 606 (1995).

[66] for χEFT calculations of generalized polarizabilities see T.R. Hemmert, B.R. Holstein, G. Knöchlein and D. Drechsel, Phys. Rev. D 62, 014013 (2000).

[67] for DR calculations of generalized polarizabilities see B. Pasquini, D. Drechsel, M. Gorchtein, A. Metz and M. Vanderhaeghen, Phys. Rev. C 62, 052201 (2000).

[68] J. Tonnison, A.M. Sandorfi, S. Hoblit and A.M. Nathan, Phys. Rev. Lett. 80, 4382 (1998).

[69] S.R. Beane, M. Malheiro, D.R. Phillips and U. van Kolck, Nucl. Phys. A 656, 367 (1999).

[70] S. Weinberg, Phys. Lett. B 251, 288 (1990); Nucl. Phys. B 363, 3 (1991).

[71] V.G. Stoks, R.A. Klomp, C.P. Terheggen and J.J. de Swart, Phys. Rev. C 49, 2950 (1994).

[72] R. Machleidt, F. Sammarruca and Y. Song, Phys. Rev. C 53, 1483 (1996).

[73] R.B. Wiringa, V.G. Stoks and R. Schiavilla, Phys. Rev. C 51, 38 (1995).

[74] T.-S. Park, K. Kubodera, D.-P. Min and M. Rho, Nucl. Phys. A 646, 83 (1999).

[75] S.R. Beane, V. Bernard, E. Epelbaum, U.-G. Meißner and D.R. Phillips, Nucl. Phys. A 720, 399 (2003).

[76] D.R. Phillips, Phys. Lett. B 567, 12 (2003).

[77] E. Epelbaum, W. Glöckle and U.-G. Meissner, Eur. Phys. J. A 19, 125 (2004); ibid. 19, 401 (2004).

[78] A. Nogga, R.G.E. Timmermans and U. van Kolck (2005). `[nucl-th/0506005]`.

[79] J.L. Friar, Ann. of Phys. 95, 170 (1975).

[80] D. Choudhury and D.R. Phillips, Phys. Rev. C 71, 044002 (2005).

[81] E. Epelbaum, W. Glöckle and U.-G. Meißner, Nucl. Phys. A 671, 295 (2000).

[82] R.P. Hildebrandt, H.W. Grießhammer and T.R. Hemmert, forthcoming.

[83] M.E. Rose, Elementary Theory of Angular Momentum, John Wiley & Sons, inc., New York · London · Sydney (1957).

[84] A.J.F. Siegert, Phys. Rev. 52, 787 (1937).

[85] F. Schwabl, Quantum Mechanics I, Springer-Verlag Berlin · Heidelberg · New York, ISBN 3-540-63779-6 (1998).

[86] J.J. Sakurai, Modern Quantum Mechanics, Addison-Wesley Publishing Company, ISBN 0-201-53929-2 (1994).

[87] P.M. Morse and H. Feshbach, Methods of Theoretical Physics, McGraw-Hill Book Company, inc., New York · Toronto · London (1953).

[88] H. Arenhövel, Z. Phys. A 297, 129 (1980).

[89] M. Weyrauch and H. Arenhövel, Nucl. Phys. A 408, 425 (1983).

[90] F. Partovi, Ann. Phys. 27, 79 (1964).

[91] M.I. Levchuk, Few Body Syst. 19, 77 (1995).

[92] H. Arenhövel and M. Sanzone, Photodisintegration of the Deuteron, Few Body Systems Suppl. 3, Springer-Verlag Wien·New York, ISBN 3-211-82276-3 (1991).

[93] P. Marin, G.R. Bishop and H. Halban, Proc. Phys. Soc. 67A, 1113 (1954).

[94] Y. Birenbaum et al., Phys. Rev. C 32, 1825 (1985).

[95] R. Bernabei et al., Phys. Rev. Lett. 57, 1542 (1986).

[96] H.O. Meyer et al., Phys. Rev. C 31, 309 (1985).

[97] E. de Sanctis et al., Phys. Rev. C 34, 413 (1986).

[98] R. Moreh, T.J. Kennett and W.V. Prestwick, Phys. Rev. C 39, 1247 (1989); erratum ibid. C 40, 1548 (1989).

[99] A.H. Snell, E.C. Barker and R.L. Sternberg, Phys. Rev. 80, 637 (1950).

[100] W.R. McMurray and C.H. Collie, Proc. Phys. Soc. 68A, 181 (1955).

[101] G.E. Brown and A.D. Jackson, The Nucleon-Nucleon Interaction, North-Holland Publishing Company, Amsterdam · Oxford, ISBN 0 7204 03359 (1976).

[102] H.A. Bethe, Phys. Rev. 76, 38 (1949).

[103] H.A. Bethe and C. Longmire, Phys. Rev. 77, 647 (1950).

[104] Particle Data Group, Phys. Lett. B 592, 1 (2004).

[105] M.L. Goldberger and S.B. Treiman, Phys. Rev. 110, 1178 (1958).

[106] J.D. Jackson, Classical Electrodynamics, W. de Gruyter, Berlin · New York, ISBN 3-11-016502-3 (2002).

[107] A.R. Edmonds, Angular Momentum in Quantum Mechanics, University Press, Princeton, ISBN 0-691-07912-9 (1996).

[108] D.A. Varshalovich, A.N. Moskalev and V.K. Khersonskii, Quantum Theory of Angular Momentum, World Scientific, Singapore, ISBN 9971-50-107-4 (1988).

[109] L.D. Landau and E.M. Lifshitz, Course of Theoretical Physics II, The Classical Theory of Fields, Akademie-Verlag, Berlin, ISBN 3-05-500066-8 (1987).

[110] V.E. Krohn and G.R. Ringo, Phys. Rev. D 8, 1305 (1973).

[111] M. Rotenberg, R. Bivins, N. Metropolis and J.K. Wooten jr., the 3-j and 6-j symbols, Crosby Lockwood & Son Ltd, London (1959).

Acknowledgments

There are many people who supported me – in one way or the other – in the development of this thesis. Especially I would like to thank

- Prof. Dr. W. Weise for giving me the opportunity to graduate at his chair and for numerous valuable discussions and comments.
- my advisors Dr. habil. H.W. Grießhammer and Dr. T.R. Hemmert for all their patience and help.
- my second assessor Prof. Dr. H. Friedrich and chairman Prof. Dr. R. Krücken
- my parents for their support in all non-physical matters.
- Estelle for the nice coffee breaks and her friendship in general.
- D.R. Phillips for his kind invitation to the Ohio University, Athens, and for providing us with his deuteron Compton code.
- many physicists for interesting and helpful discussions, especially D.R. Phillips, N. Kaiser, B. Pasquini, H. Gao and A. Nogga.
- all members of T39 for the nice working climate, especially my room mate and friend M. Procura.

This work was supported in part by the Bundesministerium für Forschung und Technologie, and by the Deutsche Forschungsgemeinschaft under contracts GR1887/2-1 and GR1887/2-2.